7-14-2020

Coupled Inflow and Structural Dynamics of Rotors with Time Delays and Adjoint Variables

Cory Andrew Seidel
Washington University in St. Louis

WASHINGTON UNIVERSITY IN ST. LOUIS

McKelvey School of Engineering

Department of Mechanical Engineering and Materials Science

Dissertation Examination Committee:
David A. Peters, Chair
Swami Karunamoorthy
Dale Pitt
Palghat Ramachandran
Shankar Sastry

Coupled Inflow and Structural Dynamics of Rotors
with Time Delays and Adjoint Variables

by

Cory Seidel

A dissertation presented to
The Graduate School
of Washington University in
partial fulfillment of the
requirements for the degree
of Doctor of Philosophy

August 2020
Saint Louis, Missouri

Table of Contents

List of Figures

List of Tables

Nomenclature

Roman

$\{A\},\{A\}_2,\{A\}_3$ pitch angle coupling

a slope of lift curve, (1/rad)

a_n^m, b_n^m cosine and sine induced inflow expansion coefficients

$\bar{a}_n^m, \bar{b}_n^m$ real and imaginary part for cosine induced inflow expansion coefficients

$[B], [B_2]$ on-disk inflow coupling

$\{\tilde{B}\},\{\tilde{B}_2\}$ on-disk blade flapping coupling

$\{b_q\}_k$ blade flapping state variable

$[C], [CC_2]$ off-disk inflow coupling

$\{\tilde{C}\},\{\tilde{C}_2\}$ off-disk blade flapping coupling

c chord length (m)

C_T thrust coefficient

$[D]$ damping matrix

d rotor spacing, (z/R)

$\bar{d}$ time delay, (d/υ)

E	error norm
$\vec{f}$	external body forces
h	cross feedback parameter
I_y	flapping inertia, (kg-m^2)
K_n^m	Legendre constant, $(\pi/2)^{(-1)^{n+m}} H_n^m$
k	inflow feedback parameter
$\left[\tilde{L}^c\right], [\tilde{L}^s]$	cosine, sine form of influence coefficient matrix
L_q	total lift on blade, (N)
LR	learning rate
$[M]$	mass matrix
MD	max depth
NT	number of trees
P	nondimensional pressure, p$/V_\infty^2\rho$
$\overline{P}_n^m(i\eta)$	normalized Legendre function of first kind
p	nondimensional flapping frequency
$\overline{Q}_n^m(i\eta)$	normalized Legendre function of second kind
Q	number of blades
q	inter-rotor feedback

R	rotor radius, (m)
$\overline{r}$	nondimensional radial distance, (x/R)
t	time, (s)
$\overline{t}$	nondimensional time, Ωt
U	in-plane component of flow, (m/s)
U_p	perpendicular component of flow, (m/s)
U_T	tangential component of flow, (m/s)
$\overline{V}_L$	total nondimensional velocity on lower rotor, $\overline{V}_{LL} + \overline{V}_{LU}$
$\overline{V}_{LL}$	nondimensional velocity on lower rotor due to lower rotor
$\overline{V}_{LU}$	nondimensional velocity on lower rotor due to upper rotor
$\overline{V}_U$	total nondimensional velocity on upper rotor, $\overline{V}_{UU} + \overline{V}_{UL}$
$\overline{V}_{UL}$	nondimensional velocity on upper rotor due to lower rotor
ϑ	flow perpendicular to the disk, (m/s)
$\overline{V}_{UU}$	nondimensional velocity on upper rotor due to upper rotor
$\overline{V}_\infty$	freestream velocity, (m/s)
w_k	induced velocity, (m/s)
x	radial distance from blade root, (m)
z	distance off rotor disk plane, (m)

Greek

α_n^m	cosine velocity state variable
β_n^m	sine velocity state variable
γ	Lock number
δ_n^m	cosine velocity co-state variable
ε_n^m	sine velocity co-state variable
η	climb rate, $\vartheta/\Omega R$
$\theta_{q,k}$	pitch angle of rotor blade
κ_β	root spring
λ	characteristic eigenvalue
ρ	air density, (kg/m^3)
μ	advance ratio, $U/\Omega R$
σ	rotor solidity
τ_n^{mc}, τ_n^{ms}	cosine and sine part of pressure coefficients$_n^s$
υ	nondimensional freestream velocity, $V_\infty/\Omega R$
$\bar{\Phi}$	viscosity dissipation function
Φ_n^{mc}, Φ_n^{mc}	cosine and sine part of pressure potentials
ϕ_n^m	radial expansion shape function

xx

χ	skew angle
Ψ_n^{mc}, Ψ_n^{ms}	cosine and sine part of velocity potentials$_n^s$
$\psi_{q,k}$	angular position from rotor aft, (rad)
$\psi_{q,k}^*$	adjoint angular position from rotor aft, $\psi_{q,k} + \pi$ (rad)
Ω	rotor speed, rad/sec
ω	reduced frequency, $\omega = \Omega R / V_\infty$
$\overline{\nu}, \overline{\eta}, \overline{\psi}$	ellipsoidal coordinates
$\nu^*, \eta^*, \overline{\psi}^*$	ellipsoidal coordinates of centro-symmetric point of the current position
ν_{on}, η_{on}	on-disk ellipsoidal coordinates
ν_{off}, η_{off}	off-disk ellipsoidal coordinates

Subscripts and Special Characters

m, r	harmonic numbers
n, j	polynomial numbers
$()_k$	on k rotor (U or L)
$()_q$	on q-th blade
$\dot{()}$	derivative in time, $\partial/\partial t$
$()^*$	derivative in nondimensional time, $\partial/\partial\overline{t}$

$$
\begin{bmatrix}
\ddots & & & \\
& (\ ) & & \\
& & \ddots &
\end{bmatrix}
\qquad \text{diagonal matrix}
$$

$\vec{\nabla}$ \qquad\qquad\qquad Laplacian operator

Acknowledgments

I would like to start out by thanking Dr. David A. Peters for all of his guidance to help me reach this point in my research. He has taken me from a limited understanding of rotary systems to developing methods for solving complex problems that I never imagined could be modeled mathematically. Through his dedication to the development of understanding rotorcraft systems, I have gained a greater appreciation for the work behind the governing equations of fluid dynamics that are simply accepted as fact by students.

Thank you to my committee members, Dr. Swami Karunamoorthy, Dr. Dale Pitt, Dr. Palghat Ramachandran, and Dr. Shankar Sastry for their commitment and guidance throughout the process of this work.

Cory Seidel

Washington University in Saint Louis

August 2020

Dedicated to my family.

ABSTRACT OF THE DISSERTATION

Coupled Inflow and Structural Dynamics of Rotors

with Time Delays and Adjoint Variables

by

Cory Seidel

Doctor of Philosophy in Mechanical Engineering

Washington University in St. Louis, August 2020

Research Advisor: Professor David A. Peters

In this work, the finite-state models of Morillo-Duffy and Fei (including the Adjoint Theorem) are expanded to calculate the coupled inflow and rotor dynamics of a coaxial rotor system. Because the Adjoint Theorem involves coupling of rotor and inflow states with adjoint rotor states (including pure time delays in both types of variables), the resultant coupled dynamics experiences characteristics heretofore not studied in a dynamic system. It is the purpose of this work to study these new and interesting dynamic behaviors that can occur in the physically meaningful context of a coaxial rotor. The work is also interested in how this interesting behavior can be found in real time for applications to flight simulators for coaxial rotors.

In order to study this new behavior, this present work first introduces a dynamic inflow model that does more than just compute the flow on a given rotor (as is done with most inflow models). Rather the model must compute for each of two interacting rotors: 1.) the flow above each rotor and 2.) the flow below the upper rotor. This must be done so that the

effect of the lower rotor on the upper (and of the upper rotor on the lower) can be found in a flight simulation. The dynamic models of the two rotors are simple blade flapping, no in plane motion or torsion, for both an infinite and a finite number of rotor blades in axial flow. This model will be sufficient for understanding the most significant dynamics of the type of systems in which we are interested. In particular two rotors will be coupled in interesting ways. First, the upper rotor will be affected by the flow due to the lower rotor. This is a standard, state-variable coupling that involves neither adjoint variables nor time delays. However, the upper rotor also affects the dynamics of the lower rotor. In that case, the flow on the lower rotor due to the upper rotor will involve both adjoint states and pure time delays, giving the new and interesting behavior.

Chapter 1

Introduction

The aerodynamics of rotary wing systems can be described through several methods including computational fluid dynamics (CFD), vortex methods (fixed and free wake), vortex particle method (VPM), and finite-state methods. While very powerful and important to the understanding of multi-rotor systems, CFD methods are not presently developed to the point that they could be used in real-time flight simulation or in control systems designs. Fixed wake vortex methods do not require significant computational power, but also are not as close to the true wake geometry as they do not allow distortion. Free wake, or prescribed wake methods better account for distortions in the wake, but require significant computation because the induced velocity throughout the wake must be calculated, rather than just on the disk [1]. VPM solves for rotor wake vorticity transportation and diffusion through a Lagrangian formulation rather than a numerical solution over a grid. VPM performs faster than CFD methods but is also unable to perform in real-time. The finite-state approach provides a computationally less expensive approach that can be used for real-time analysis. The development of the finite-state inflow models over the last 50 years has seen them advance from momentum theory approximations to three dimensional solutions to potential flow equations. In addition, inflow models are ideal solutions for induced flow in rotorcraft

because they explain the physics of the dynamic behavior of the rotor and are designed in a hierarchical nature to incorporate previous models.

In [2], Peters describes the three characteristics that make a theory a dynamic inflow model as:

1. Provided the time history of blade loads, the theory must be a mathematical model that determines induced flow normal to the rotor as a function of time and position.

2. The mathematical model must be made up of a finite number of time-based ordinary differential equations following the form:

$$[M] \{\dot{\alpha}_n^m\} + [L] \{\alpha_n^m\} = \{\tau_n^m\} \tag{1.1}$$

   where the α_n^m are states that define the flow field, $[M]$ is the mass matrix, $[L]$ is a matrix of influence coefficients, and τ_n^m is the loading on the blades. It follows that α are state variables for the flow field that are driven by the blade loads.

3. The number of states chosen is user determined based on the application being solved and hierarchical in that it can handle varying numbers of states.

Until the recent work of Fei [3,4], the developed models only accounted for flow on and above the rotor disk. Fei introduced an approach to find the flow below the rotor disk using the adjoint theorem. The adjoint theorem introduces velocity co-state variables and time delays into the coupled solution. The main focus of this work is to use the models developed by Morillo, Duffy and Fei to investigate the dynamics of the coupled system.

1.1 Previous Work with Inflow Models

In the early 1980s, the Pitt-Peters model was developed to satisfy the need for a physics-based unsteady dynamic theory for helicopter rotor systems [5]. This model relates transient rotor loads (thrust, roll moment, and pitch moment) to the overall transient response of the rotor induced flow field. The basis of the Pitt-Peters model was Mangler's actuator-disc theory [6]. The Pitt-Peters model describes the perturbed induced inflow and pressure distribution as:

$$\lambda = \lambda_0 + \bar{r}\lambda_s sin\left(\bar{\psi}\right) + \bar{r}\lambda_c \cos\left(\bar{\psi}\right) \tag{1.2}$$

$$P = \sum_{m=0}^{1} \sum_{n=m+1}^{m+3} P_n^m\left(\nu\right) Q_n^m\left(i\eta\right) \left[C_n^m \cos\left(m\bar{\psi}\right) + D_n^m \sin\left(m\bar{\psi}\right)\right)] \tag{1.3}$$

where ν, η, and $\bar{\psi}$ are the ellipsoidal coordinates (Appendix A). P_n^m and Q_n^m are the associated Legendre functions of the first and second kinds, respectively. C_n^m and D_n^m are coefficients which are functions of time and are governed by a set of ordinary differential equations. The Pitt-Peters model assumes superposition of pressure, which states that superimposing the unsteady pressure and static pressure of the field results in the total pressure due to the velocity field. In turn, developing the equation for dynamic inflow derivatives for a rotor with unsteady loading and induced flow distribution, which is written as:

$$[M] \begin{Bmatrix} \dot{\lambda}_0 \\ \lambda_s \\ \lambda_c \end{Bmatrix} + [L]^{-1} \begin{Bmatrix} \lambda_0 \\ \lambda_s \\ \lambda_c \end{Bmatrix} = \begin{Bmatrix} C_T \\ -C_L \\ -C_M \end{Bmatrix} \tag{1.4}$$

where $[M]$ is the apparent mass matrix and $[L]$ is the dynamic inflow gain matrix. These matrices were found in closed form to be:

$$[M] = \begin{bmatrix} \frac{128}{75\pi} & 0 & 0 \\ 0 & \frac{16}{45\pi} & 0 \\ 0 & 0 & \frac{16}{45\pi} \end{bmatrix} \tag{1.5}$$

$$[L] = \frac{1}{V} \begin{bmatrix} \frac{1}{2} & 0 & -\frac{15}{64}\sqrt{\frac{1-\sin(\alpha)}{1+\sin(\alpha)}} \\ 0 & \frac{4}{1+\sin(\alpha)} & 0 \\ \frac{15}{64}\sqrt{\frac{1-\sin(\alpha)}{1+\sin(\alpha)}} & 0 & \frac{4\sin(\alpha)}{1+\sin(\alpha)} \end{bmatrix} \tag{1.6}$$

where V is the flow velocity and α is the skew angle of the streamline at the disk. As depicted in Eq. 1.4, the Pitt-Peters model describes three states. The first state, λ_0, describes the uniform flow over the disk whereas the other two states, λ_s and λ_c, describe the side-to-side and fore-to-aft gradient, respectively. The theory behind the Pitt-Peters model has been validated experimentally [7]. The Pitt-Peters model is only able to provide a crude wake description of the uniform flow due to a lack of higher harmonic terms (one harmonic and one radial shape function).

David Peters and Chengjian He expanded on the work of the Pitt-Peters model by improving the accuracy through the development of a higher harmonic theory [8,9]. The Peters-He generalized dynamic wake model was able to accomplish that by extending the pressure distribution of the Pitt-Peters model to include higher harmonic terms and an arbitrary number of radial functions for each harmonic. The expanded pressure distributions were modeled as:

$$P = -\frac{1}{2}\sum_{m=0}^{\infty}\sum_{n=m+1,m+3,...}^{\infty} \bar{P}_n^m(\nu)\,\bar{Q}_n^m(i\eta)\left[\tau_n^{mc}\cos\left(m\bar{\psi}\right) + \tau_n^{ms}\sin\left(m\bar{\psi}\right)\right] \tag{1.7}$$

4

where τ_n^{mc} and τ_n^{ms} are the new pressure coefficients for the side-to-side and fore-to-aft gradients. Similarly, the inflow distribution was expanded to include an arbitrary number of harmonics and radial functions:

$$v_z = \sum_{m=0}^{\infty} \sum_{n=m+1,m+3,\ldots}^{\infty} \frac{\bar{P}_n^m(\nu)}{\nu} \left[\alpha_n^m \cos\left(m\bar{\psi}\right) + \beta_n^m \sin\left(m\bar{\psi}\right) \right] \tag{1.8}$$

Here, $\bar{P}_n^m(\nu)$ and $\bar{Q}_n^m(i\eta)$ are the normalized associated Legendre functions of the first and second kind, respectively. The derivations of normalized Legendre functions are outlined in Appendix B.

The Peters-He model also assumes superposition of pressures, which excludes inflow models with no induced velocity on the disk. This model has a similar form to the Pitt-Peters model in Eq. 1.4:

$$[M]\{\dot{\alpha}_n^m\} + V\left[\tilde{L}^c\right]^{-1}\{\alpha_n^m\} = \frac{1}{2}\{\tau_n^{mc}\} \tag{1.9}$$

$$[M]\{\dot{\beta}_n^m\} + V\left[\tilde{L}^s\right]^{-1}\{\beta_n^m\} = \frac{1}{2}\{\tau_n^{ms}\} \tag{1.10}$$

except that the pressure coefficients, τ_n^{mc} and τ_n^{ms}, are updated for a coaxial rotor system and V is the velocity normal to the disk. The Peters-He model has been validated with wind-tunnel data [9].

The Peters-He model cannot describe inflow distribution that is caused by mass-injection. It disregards the $m + n = even$ terms for Legendre polynomials and therefore only considers $m + n = odd$ terms which represent pressure discontinuities at the disk. Additionally, the Peters-He model only treats the normal components of flow on the disk.

Following the work by He, the focus shifted to finding the flow throughout the field, primarily above the rotor disk. Wen-Ming Cao and David Peters set out to find the flow off the disk as well as on the disk and determined that a second set of wake states must exist for the flow off

the disk, but were unable to determine what the state should be [10]. Later, Jorge Morillo and David Peters discovered that these states could be solved for rigorously with no need for the assumption of superposition of pressures [11]. This was completed by including the mass source terms in the expansions and using the gradient of velocity potentials to compose the velocity field. The Peters-Morillo model was now able to account for $m + n = odd$ and $m + n = even$ Legendre polynomials. Morillo's pressure and velocity distributions are:

$$P = -\sum_{m=0}^{\infty} \sum_{n=m+1}^{\infty} \left[\tau_n^{mc} \Phi_n^{mc} + \tau_n^{ms} \Phi_n^{ms} \right] \tag{1.11}$$

$$\overrightarrow{v} = \sum_{m=0}^{\infty} \sum_{n=m+1}^{\infty} \left[\hat{a}_n^m \overrightarrow{\Psi}_n^{mc} + \hat{b}_n^m \overrightarrow{\Psi}_n^{ms} \right] \tag{1.12}$$

where Φ_n^m and Ψ_n^m are the pressure and velocity potentials, respectively. The Morillo pressure and velocity potentials differ from the Pitt and He potentials in that they incorporated even and odd functions and considered all velocity components, not just the normal component. Morillo and Peters solved for the inflow states using a Galerkin approach to obtain a closed form solution and solve for all three components of the velocity potential. They were able to solve for the velocity potential on the rotor disk and the velocity field above the rotor disk. The closed form solutions using the Galerkin approach are:

$$[M^c] \{\dot{a}_n^m\} + [D^c] \left[\tilde{L}^c \right]^{-1} [M^c] \{a_n^m\} = [D^c] \{\tau_n^{mc}\} \tag{1.13}$$

$$[M^s] \left\{ \dot{b}_n^m \right\} + [D^s] \left[\tilde{L}^s \right]^{-1} [M^s] \{b_n^m\} = [D^s] \{\tau_n^{ms}\} \tag{1.14}$$

where $[D]$ is the damping matrix and a_n^m and b_n^m are the velocity state variables relative to the side-to-side and fore-to-aft gradients. Compared to closed-form solutions for step response and frequency response above the rotor disk, the Peters-Morillo model proved to be accurate, but slow to converge. This is due to ill-conditioned matrices. In addition, the Peters-Morillo model could not handle non-zero flux mass sources, which are the fundamental

6

mass-source terms (the terms with $m = n$) because they were unable to find the potential function associated with those velocity distributions.

Hsieh and Peters later found the potential functions for $m = n$ and approximated the solution for the special case of $m = n = 0$ [12]. The approximate solution for the special case still involved a singularity, but they replaced the infinite integral with an approximate solution for the infinite kinetic energy that converged as the number of terms was increased. Garcia-Duffy and Peters then incorporated the Hsieh solutions into a dynamic inflow model for all components of flow above the rotor disk [13].

Although the work of Morillo extended the models from normal flow at the disk to all three components of flow through a volume in space, that volume only included the disk plane and the infinite hemisphere above the disk plane. Velocities below the plane were not capable of being found. Fei and Peters expanded on the Morillo-Duffy model to include all three components of induced flow everywhere in the flow field—including below the plane of the rotor disk and in the rotor wake itself [4][14]. In order to find the flow below the disk Fei used the adjoint theorem to compute the adjoint of the velocity based on co-state variables. The adjoint theorem provides that the flow below the disk converges at least as well as the flow above the disk. Fei further validated the adjoint theorem for both step responses and frequency response with a varying range of skew angles.

1.2 Relevant Research for Coaxial Rotors

While the model developed in this paper is for multi-rotor systems, the immediate results and applications are for coaxial rotor systems. Therefore, the survey of literature on current methods for multi-rotor systems primarily focuses on coaxial rotor helicopters. Notable work in the field that is relevant to this research is primarily conducted using CFD, VPM,

or some form of finite state methods. In some cases, these methods are combined to for a hybrid model. In addition, this literature survey extends to machine learning algorithms (MLA) and the current work within the rotor industry involving varying MLAs. In the CFD realm Chen et al. extract dynamic inflow models from CFD investigations to evaluate the computed induced flow with test data [15]. Meanwhile, Lakshminarayan and Baeder use Reynolds-averaged Navier-Stokes solvers to investigate microscale coaxial rotors in hover [16]. Their work highlights the predictive capabilities of the computational approach, the development of the wake below each rotor, and the impact of rotor interactions on power and thrust. In [17], Rajmohan et. al develop a hybrid CFD/VPM method to study rotor dynamics in a coaxial rotor system. The method uses CFD airloads to generate vorticity in VPM simulations and uses VPM to simulate far wake in the CFD solution.

Singh and Friedmann study coaxial rotor interactions in hover using VPM in [18] and outline the blade passage frequency as a source for oscillations in the loading profile. In [19] Singh and Friedmann also used VPM to analyze the wake development, performance, and loads from the vortex wake interaction of a coaxial rotor system in hover. He and Zhao modeled rotor wake dynamics in hover and forward flight using viscous vortex particle method in [20]. The model is also able to capture wake contraction and tip-vortex roll-up without the empirical modeling parameters other models rely on. Zhao and He expanded their work with VPM to identify essential modeling parameters and advance the Peters-He model [21].

In [22] Prasad et. al propose two coaxial rotor models for hover conditions. The first model extends the Peters-He model by superimposing two pressure fields to create a dual actuator scenario. The second model uses Galerkin weighted residuals for the finite state inflow theory and wake contraction developed from incompressible flow equations. In [23-24] Prassad et al. used superposition with single rotor models to develop solutions for coaxial rotor systems

while removing the need for backward time marching, which is required under the adjoint theorem. In [25] Cardito et. al present a linear finite-state dynamic perturbation model for coaxial rotor systems that provides good correlation for hover conditions but struggles with forward flight. Cardito et al. further investigated finite-state models for coaxial rotor systems with rational approximation of corresponding transfer functions [26].

Juhasz et. al present three different models in [27] that are developed through blade-element theory, free-vortex wake model, and CFD. The work finds that the best solution is a combination of all three models. In [28] Obayashi et. al compare a commercial Navier-Stokes solver with a hybrid Navier-Stokes free-wake analysis for a trimmed rotor with equal but opposite torques on the rotors. The hybrid method proved to be more efficient at producing acceptable results for lower settings but overestimates the figure of merit and underestimates the power required as thrust increases. Silwal and Raghav use high-speed particle image velocimetry to study the interactions between rotors in a coaxial system [29]. The study focuses on impact of rotor spacing on tip vortex structures and observed that rotor spacing heavily influences the trajectories of tip vortices.

Some other applications of models for different types of rotor systems include the work by Tsushim and Su in [30]. Here they combine finite-state methods with dynamic structural equations for highly flexible wings to combine energy harvesting and piezoelectric actuation in a UAV. Henriksen et. al present three models for wind turbines in [31] that are based on blade element momentum theory to estimate the free mean wind speed. Two of the models use dynamic states to illustrate the physics within the wake.

Within the realm of machine learning for helicopter applications, a large portion of the research focus has been on controls—especially through reinforcement learning [32-34] and autonomous flight—with aerobatic maneuvers being one of the key focuses [35-36]. However,

9

other overlaps with machine learning for helicopter applications exist as well, including the work by Pawar and Jung [37] which focuses on the use of support vector machines to predict damage to composite helicopter rotor blades and how much fatigue life is left in the blades. Kumar and Ben-Tzvi [38] use machine learning for estimating ambient air turbulence for RC helicopters.

Outside of the helicopter realm, machine learning is being utilized in almost every field imaginable. In data sciences one particular framework, XGBoost^{TM}, is gaining a lot of attention for its ability to perform efficiently and accurately. XGBoost^{TM} is a gradient boosted tree framework that is scalable for large and small data sets [39]. XGBoost^{TM} is used throughout a wide range of applications including short-term load forecasting of power systems [40][41], price forecasting [42], and image classification [43].

1.3   Objective and Approach

The aim of this research is broken down into five main goals: 1) develop a single inflow state proof of concept solution for a system with adjoint variables and time-delayed terms; 2) expand the approach of the proof of concept solution to a coaxial rotor system that is an extension of the work of Morillo and Fei with multiple inflow states and an infinite number of blades; 3) adapt the multiple inflow-state solution for a system with a finite number of blades; 4) apply the finite blade model to wind turbines to investigate optimal rotor spacing; and 5) design machine learning algorithm methods for regression analysis across the lower rotor disk.

In this work, we first discuss the underlying physics of a single lifting rotor system and the corresponding governing equations. This provides a basis for the work that is expanded into the final coupled coaxial rotor model and bridges the gap between Fei's investigations of

flow below the rotor disk and coupled feedback of the coaxial system. The addition of a second rotor brings modifications to existing equations through coupling terms, new state (and co-state) variables for velocity, and time-delayed terms. However, a co-state variable for the lower rotor is not included because the flow below the lower rotor is not of interest in this work. The makeup of the governing inflow state equations will be discussed in the following chapters. It is important to know that the velocity state and co-state variables for both rotors are coupled, some of the coupled terms are time delayed (a result of the adjoint theorem), and the co-state terms are solved through reverse time marching due to an instability that occurs when forward time marching.

The expansion from the proof of concept model to the infinite and finite blade models is accomplished by expanding the pressure coefficients of Morillo with the adjoint theorem utilized in Fei's work. The new pressure coefficients contain on-disk and off-disk terms along with coupling matrices, time-delayed terms, and co-state variables. The off-disk terms are a new development in this work. The solution containing the finite number of blades provides a higher fidelity analysis of the blade dynamics and velocity profile development with varying degrees of rotor spacing. These methods are then expanded to wind turbine applications through minimal adjustments to the model to account for the change to power generation.

The finite-blade model is used to create a dataset for the development of machine learning algorithms with regression analysis. Gradient boosted trees within XGBoost$^{\text{TM}}$ are utilized here to model the velocity across the lower rotor. The models are fit by tuning hyperparameters for the gradient boosted tree to obtain a good fit with the model without overfitting to the training data. The models are used to predict values within the dataset and intermediate values as a feasibility study towards future use with predicting higher harmonic solutions. The machine learning algorithms cannot replace the finite-state models because they rely on

them for training data, but hopefully in the future can used to obtain real-time analysis for higher harmonic simulations.

Chapter 2

Fundamental Concepts for Inflow Models and the Adjoint Theorem

2.1 Fluid Dynamics Equations

The equations used in this work apply to a rotor in a Newtonian fluid and are governed by the conservation laws: conservation of mass, conservation of momentum, and conservation of energy, as well as the boundary condition of no-slip at solid-fluid interfaces [44]. The conservation of mass is given as:

$$\frac{\partial \rho}{\partial t} + \overrightarrow{\nabla} \cdot (\rho \overrightarrow{v}_t) = 0 \tag{2.1}$$

where ρ is the fluid density and $\overrightarrow{v}_t$ is the total velocity vector. For this application, it is assumed that the helicopter is flying at standard atmospheric conditions and therefore the inflow is incompressible and inviscid. The conservation of mass further reduces to:

$$\overrightarrow{\nabla} \cdot \overrightarrow{v}_t = 0 \tag{2.2}$$

By Newton's laws, the conservation of momentum, is described by the Navier-Stokes equations, which, for a viscous fluid, are:

$$\rho \left(\frac{\partial \vec{v}_t}{\partial t} + \vec{v}_t \cdot \vec{\nabla} \vec{v}_t \right) = -\vec{\nabla} p + \vec{\nabla} \left(\bar{\lambda} \, \vec{\nabla} \cdot \vec{v}_t \right) + \bar{\mu} \left(\vec{\nabla} \left(\vec{\nabla} \cdot \vec{v}_t \right) + \left(\vec{\nabla} \cdot \vec{\nabla} \right) \vec{v}_t \right) + \rho \vec{f} \quad (2.3)$$

where p is the pressure, $\bar{\lambda}$ is the second viscosity coefficient, $\bar{\mu}$ is the dynamic viscosity coefficient, and $\vec{f}$ represents the external forces. Under the assumptions of incompressible and inviscid flow (and the understanding that there are no significant body forces on the disk), it follows that:

$$\rho \left(\frac{\partial \vec{v}_t}{\partial t} + \vec{v}_t \cdot \vec{\nabla} \vec{v}_t \right) = -\vec{\nabla} p \quad (2.4)$$

Finally, conservation of energy can be expressed in the form:

$$\rho \left(\frac{\partial e}{\partial t} + \vec{v}_t \cdot \vec{\nabla} e \right) = -\vec{\nabla} p \cdot \vec{v}_t + \vec{\nabla} \left(k \vec{\nabla} T \right) + \bar{\Phi} \quad (2.5)$$

where e is the internal energy per unit mass, k is the thermal conductivity of the fluid (air), T is temperature, and $\bar{\Phi}$ is the viscous dissipation function (which is zero in this case). In a system where ρ and μ are constant, the conservation of mass and momentum become uncoupled from the conservation of energy (and temperature). Under the assumption of adiabatic flow, energy can be neglected.

In the following derivation for velocity about a steady free-stream, only linearized equations are considered because this work only utilizes linear equations. The steady free-stream velocity is represented as V_∞ in the total velocity equation:

$$\vec{v}_t = V_\infty \vec{\xi} + \delta \vec{v} \quad (2.6)$$

14

where $\vec{\xi}$ is a unit vector along the streamline. Here, $\delta\vec{v}$ is defined as:

$$\delta\vec{v} = \delta\vec{v}_x \, \vec{i} + \delta\vec{v}_y \, \vec{j} + \delta\vec{v}_z \, \vec{k} \tag{2.7}$$

As demonstrated in Figure 2-1, the skew of the streamline, χ, is measured with respect to the positive z axis such that:

$$\vec{\xi} = -\sin(\chi) \, \vec{i} + \cos(\chi) \, \vec{k} \tag{2.8}$$
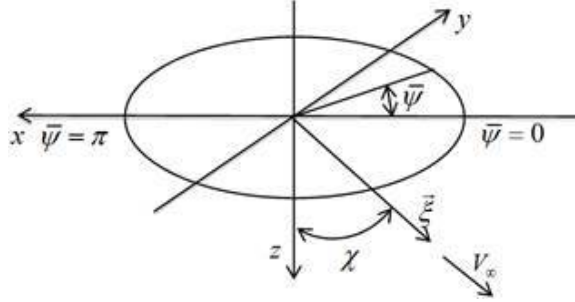
Figure 2-1: Cartesian coordinate system

Here the unit vectors $\vec{i}$, $\vec{j}$, and $\vec{k}$ are in the x, y, and z directions, respectively. Equation 2.6 is then substituted into Eqs. 2.2 and 2.4, the momentum and continuity equations, with the assumption that V_∞ is constant to obtain:

$$\nabla \cdot \delta v = 0 \tag{2.9}$$

$$\rho \frac{\partial \delta\vec{v}}{\partial t} + \rho V_\infty \frac{\partial \delta\vec{v}}{\partial \xi} = -\vec{\nabla}p \tag{2.10}$$

Throughout this work all variables for length and velocity are made nondimensional on the length scale of the rotor radius R, the velocity scale of the ΩR, and the mass scale associated with density ρ. In addition, the time component is also nondimensionalized as $\bar{t} = \Omega t$. The Laplacian operator ∇ is redefined to represent the gradient with respect to nondimensional

15

coordinates. Nondimensionalization simplifies the momentum and continuity equations in Eqs. 2.9 and 2.10 down to:

$$\nabla \cdot \vec{v} = 0 \tag{2.11}$$

$$\frac{\partial \vec{v}}{\partial \tau} + \overline{V}\frac{\partial \vec{v}}{\partial \overline{\xi}} = -\vec{\nabla}P \tag{2.12}$$

where $\vec{v} = \delta\vec{v}/\Omega R$, $\overline{V} = V_\infty/\Omega R$, $\overline{\xi} = \xi/R$, and $P = p/\rho\Omega^2 R^2$. These terms are the nondimensional terms for pressure P, induced velocity v, and the nondimensional coordinate on the streamline ξ.

If we assume that the velocity can be written as the gradient of a potential function Ψ, then continuity is automatically fulfilled.

$$\vec{v} = \vec{\nabla}\Psi \tag{2.13}$$

$$\vec{\nabla} \cdot \vec{v} = \vec{\nabla} \cdot \vec{\nabla}\Psi = 0 \tag{2.14}$$

Now to determine the pressure potential, Eq. 2.13 is substituted into Eq. 2.12, resulting in:

$$\frac{\partial \vec{\nabla}\Psi}{\partial \overline{t}} + \overline{V}\frac{\partial \vec{\nabla}\Psi}{\partial \xi} = -\vec{\nabla}P \tag{2.15}$$

The divergence of Eq. 2.15 gives:

$$\frac{\partial \vec{\nabla} \cdot \vec{\nabla}\Psi}{\partial \overline{t}} + \overline{V}\frac{\partial \vec{\nabla} \cdot \vec{\nabla}\Psi}{\partial \xi} = -\vec{\nabla} \cdot \vec{\nabla}P \tag{2.16}$$

Equation 2.14 shows that the divergence of the gradient of the velocity potential function is zero and thus:

$$\vec{\nabla} \cdot \vec{\nabla}P = 0 \tag{2.17}$$

The pressure can be written as a potential function, Φ:

$$\Phi = P \tag{2.18}$$

16

Solutions for the velocity and pressure potentials for this work will be expanded upon in the following sections.

2.2   Pressure Potentials

To solve the governing equations for this work (Eqs. 2.11 and 2.12), the pressure potential, Φ, and velocity potential, v, are expanded in terms of potential functions that satisfy Laplace's equation. These equations must satisfy the boundary conditions for pressure and velocity.

For the pressure field, the boundary conditions are given by a discontinuity across the rotor disk. Ellipsoidal coordinates $(\nu, \eta, \overline{\psi})$ were selected because for any odd function of v there is a resultant discontinuity across the rotor disk. Therefore, any function that satisfies Laplace's equation and is odd can be considered for the expansion functions used in determining Φ. Even functions for v that satisfy Laplace's equation result in discontinuities in the normal derivative of the pressure potential and are relevant to mass source terms (Appendix B). The pressure potential is composed as:

$$\Phi_n^{mc}(\nu, \eta, \overline{\psi}) = \overline{P}_n^m(\nu)\overline{Q}_n^m(i\eta)\cos(m\overline{\psi}) \tag{2.19}$$

$$\Phi_n^{ms}(\nu, \eta, \overline{\psi}) = \overline{P}_n^m(\nu)\overline{Q}_n^m(i\eta)\sin(m\overline{\psi}) \tag{2.20}$$

The analytical solution of the Laplace equations is known for ellipsoidal coordinates (Appendix B). In the plane of the rotor disk, but off the disk $(\nu = 0)$, $\overline{P}_n^m$ odd functions are zero, but for even functions the pressure potential has normal derivatives on the plane. Thus, Legendre functions that are even functions of ν occur when $m + n = even$ and they become odd functions of ν when $m + n = odd$. It is also important to note that the coordinate ν is positive above the disk and negative below the disk, whereas the opposite is true for z. The range of ν is $-1 < \nu < 0$ below the disk and $0 < \nu < 1$ above the disk. The jump in

17

ν across the disk correlates with a jump in pressure across the disk, the boundary condition for Φ at the disk. On the disk, $\eta = 0$ and the odd potentials can be used to describe the pressure jump across the rotor disk. Meanwhile, the even potentials have a discontinuity in slope which is used to describe the mass source in the flow field.

The pressure jump across the disk is written as a summation of the terms that include both pressure discontinuities and mass-source terms.

$$P = -\sum_{m=0}^{\infty}\sum_{n=m}^{\infty}\left(\tau_n^{mc}\Phi_n^{mc} + \tau_n^{ms}\Phi_n^{ms}\right) \tag{2.21}$$

Here τ_n^{mc} and τ_n^{ms} are the cosine and sine forms of the pressure coefficient. The pressure change across the disk is found from:

$$\Delta P = [P_{lower} - P_{upper}]|_{\eta=0} = 2\sum_{m=0}^{\infty}\sum_{n=m+1,m+3,\cdots}^{\infty}\left(\tau_n^{mc}\Phi_n^{mc} + \tau_n^{ms}\Phi_n^{ms}\right)|_{\eta=0} \tag{2.22}$$

where ΔP is the net pressure drop across the disk from above the disk (-z) to below the disk (+z). The injected mass in the system is expressed by:

$$\frac{\Delta \dot{m}}{\rho V_\infty} = [P_{lower} + P_{upper}]|_{\eta=0} = 2\sum_{m=0}^{\infty}\sum_{n=m,m+2,\cdots}^{\infty}\left(\tau_n^{mc}\Phi_n^{mc} + \tau_n^{ms}\Phi_n^{ms}\right)|_{\eta=0} \tag{2.23}$$

$\Delta \dot{m}$ is the net mass per unit time per unit area that is injected at the disk. It is important to note that only $m+n = odd$ will contribute to ΔP and only $m+n = even$ will contribute to $\Delta \dot{m}$.

2.3   Velocity Potentials

In previous work for finite-state models, two sets of velocity potentials are explored, prime potentials and derived potentials. The velocity potentials must satisfy the boundary condition that states the velocity field far upstream from the rotor disk is equal to zero. We

do not expand the flow field below the rotor disk because it is only potential flow between vortex sheets. Rather, we will use the Adjoint Theorem to find flow below the disk in terms of flow on and above the disk.

For flow above the disk, the pressure potentials not only satisfy Laplace's equation, but also are zero at an infinite distance above the rotor and finite on the disk ($z = 0$). As $z \to -\infty$, $\eta \to \infty$, and $\lim\limits_{\eta \to \infty} \bar{Q}_n^m (i\eta) = 0$.

The prime potential functions are defined as integrals along a streamline of pressure potentials. The prime potentials are represented as:

$$\Psi_n^{mc} = \int_{-\infty}^{\xi} \Phi_n^m \cos\left(m\bar{\psi}\right) d\xi \tag{2.24}$$

$$\Psi_n^{ms} = \int_{-\infty}^{\xi} \Phi_n^m \sin\left(m\bar{\psi}\right) d\xi \tag{2.25}$$

Thus, since the prime potentials satisfy the upper boundary layer condition, the flow velocities may be represented by an expansion summation of the gradient of the prime potentials.

$$\vec{v} = \sum_{m=0}^{\infty} \sum_{n=m}^{\infty} \left(\hat{a}_n^m \vec{\nabla} \Psi_n^{mc} + \hat{b}_n^m \vec{\nabla} \Psi_n^{ms}\right) \tag{2.26}$$

The derived potentials, $\hat{\Psi}_n^m$, are chosen such that we can write the gradient in closed form (this is not possible for the prime potentials). We have chosen to define the derived potentials such that their derivative with respect to z is:

$$\frac{d\Psi_n^{mc}}{dz} = \overline{P}_n^m(\nu)\overline{Q}_n^m(i\eta)\cos(m\psi) \tag{2.27}$$

$$\frac{d\Psi_n^{ms}}{dz} = \overline{P}_n^m(\nu)\overline{Q}_n^m(i\eta)\sin(m\psi) \tag{2.28}$$

Peters and Morillo [11] found these derived potentials in the following form:

$$\hat{\Psi}_n^m = \sigma_n^m \Phi_{n+1}^m + \varsigma_n^m \Phi_{n-1}^m \tag{2.29}$$

19

where σ_n^m is:

$$\sigma_n^m = \frac{1}{K_n^m \sqrt{(2n+1)(2n+3)\left[(n+1)^2 - m^2\right]}} \tag{2.30}$$

$$\varsigma_n^m = \frac{1}{K_n^m \sqrt{(4n^2-1)(n^2-m^2)}} \qquad n \neq m \tag{2.31}$$

Here K_n^m is:

$$K_n^m = \left(\frac{\pi}{2}\right)^{(-1)^{n+m}} H_n^m \tag{2.32}$$

and H_n^m is:

$$H_n^m = \frac{(n+m+1)!!\,(n-m-1)!!}{(n+m)!!\,(n-m)!!} \tag{2.33}$$

This definition of the derived potentials is only valid above the rotor plane ($z < 0$). Morillo was only able to find them for cases where $m \neq n$. Peters and Hsieh [12] later were able to find the derived potentials for the special cases where $m = n \neq 0$ and $m = n = 0$. For the former case, a formula in terms of a Legendre function where the subscript is greater than the superscript was developed.

$$\hat{\Psi}_m^{mc} = \left[\sigma_m^m \bar{P}_{m+1}^m(\nu)\,\bar{Q}_{m+1}^m(i\eta) + \bar{P}_{m-1}^m(\nu)\,\bar{Q}_{m-1}^m(i\eta)\right]\cos\left(m\bar{\psi}\right) \tag{2.34}$$

$$\hat{\Psi}_m^{ms} = \left[\sigma_m^m \bar{P}_{m+1}^m(\nu)\,\bar{Q}_{m+1}^m(i\eta) + \bar{P}_{m-1}^m(\nu)\,\bar{Q}_{m-1}^m(i\eta)\right]\sin\left(m\bar{\psi}\right) \tag{2.35}$$

Here the "alternative" Legendre terms contain an $m-1$ subscript. The calculation for these first and second order Legendre terms are:

$$\bar{P}_{m-1}^m(\nu) = \frac{2}{\pi}\frac{\sqrt{(2m)!!}}{\sqrt{(2m+1)!!}}\frac{(1-\nu^2)^{m/2}}{(1+\nu)^m}\sum_{n=0}^{m-1}\frac{(m-1)!\,2^{m-1-n}\,(-1)^n}{n!\,(m-1-n)!\,(n+m)}(1-\nu)^n \tag{2.36}$$

$$\bar{Q}_{m-1}^m(i\eta) = \frac{1}{(1+\eta^2)^{m/2}} \tag{2.37}$$

For the special case of $m = n = 0$ Peters and Hsieh found the derived velocity potential to be:

$$\hat{\Psi}_0^0 = \frac{2}{\pi} \nu \left[1 - \eta \tan^{-1} \left(\frac{1}{\eta} \right) \right] - \frac{2}{\pi} \ln|1 + \nu| - \frac{1}{\pi} \ln\left|1 + \eta^2\right| + \frac{2}{\pi} \ln|Z_{\max}| \quad \nu > 0 \qquad (2.38)$$

where $Z_{\max}$ is a large number representing the radius to which the ξ integral is taken. The exact value of this arbitrary number does not enter our equations. It is strictly a conceptual idea.

The velocity potentials all satisfy Laplace's equation and the conservation of mass. Therefore, the conservation of momentum is the only governing equation of the velocity expansion coefficients. To obtain a finite-state wake model, the momentum equations must be represented in finite state form.

2.4   Equations in Terms of Derived Potentials

The Galerkin method (Appendix C) is used to find the closed form representation of the dynamic equations for the velocity potential expansions in terms of prime potentials. A change of variable is then needed to find the velocity in terms of the derived potentials. The relationship needed to transform between the two bases must obey the following:

$$\{\hat{a}_n^m\}^T [\Psi_n^{mc}] = \{a_n^m\}^T \left\{ \sigma_n^m \Phi_{n+1}^{mc} + \varsigma_n^m \Phi_{n-1}^{mc} \right\} \qquad (2.39)$$

In order to find the transform between the two bases, the prime and derived potential functions are dotted with the gradient of each potential function and integrated over the region above the rotor disk. The resultant relation between the two types of potentials is:

$$\{\hat{a}_n^m\} = \left[\tilde{L}^c \right]^{-1} [M^c] \{a_n^m\} \qquad (2.40)$$

where $[M^c]$ is:

$$[M^c] = \left[\tilde{L}^c\right]_{\chi=0} = \left[\iint_s \frac{\partial \Phi_j^{rc}}{\partial z} \Psi_n^{mc} ds\right] \tag{2.41}$$

A similar relationship exists between $\left\{\hat{b}_n^m\right\}$ and $\{b_n^m\}$ that incorporates the $[L^s]$ and $[M^s]$ terms which relate the sine coefficients. With the appropriate change of variables achieved, the equation of motion in terms of the derived potentials is found to be:

$$[M^c]\left\{\overset{*m}{\hat{a}_n}\right\} + V[D^c][L^c]^{-1}[M^c]\{a_n^m\} = [D^c]\{\tau_n^{mc}\} \tag{2.42}$$

This equation represents the all components of velocity above and on the rotor plane in closed form. Equation 2.42 can be further reduced for the case of axial flow $(\chi = 0)$ where $\left[\tilde{L}^c\right]$ and $[M^c]$ are equivalent. The simplified equation of motion is:

$$[M^c]\left\{\overset{*m}{\hat{a}_n}\right\} + V[D^c]\{a_n^m\} = [D^c]\{\tau_n^{mc}\} \tag{2.43}$$

Amazingly, the transform of Morillo also applied to derived potentials of Hsieh when $m = n$.

2.5   Flow Below the Disk by Adjoint Theorem

At the time of Hsieh's work, only solutions for the velocity on and above the disk were possible because that was the limit of the Galerkin integrals. The Galerkin method is not applicable to the region below the rotor plane because the wake contains complicated boundary conditions. The flow inside the wake is not entirely potential flow because vortex shedding from the blades creates vortex sheets. Between the vortex sheets potential flow exists, but the entire field below the rotor disk is not irrotational and therefore cannot be simplified to be solvable by the Galerkin method.

Although the flow is not irrotational below the rotor disk plane and not potential flow, it still satisfies the conservation of mass and momentum equations. By satisfying the conservation equations, a solution below the disk can be obtained in terms of the flow field on and above the disk. This was the case for Fei's work with the adjoint theorem and adjoint states (also referred to as co-states) [4]. The adjoint theorem resulted from a closed form solution for frequency response below a perturbed disk which was then transformed it into the time domain. A complex conjugate that appeared in the frequency domain translated into an adjoint in the time domain. Time delays also appeared in the transformation to the time domain. The resultant solution for velocity at a location ξ_0 below the rotor disk is represented as:

$$\overrightarrow{v}\left(r_0,\overline{\psi}_0,\xi_0,\overline{t}\right) = \overrightarrow{v}\left(r_0,\overline{\psi}_0,0,\overline{t}-\xi_0\right) + \overrightarrow{v}^*\left(r_0,\widetilde{\psi}_0,0,\overline{t}-\xi_0\right) - \overrightarrow{v}^*(r_0,\widetilde{\psi}_0,-\xi_0,\overline{t}) \quad (2.44)$$

where $\overrightarrow{v}^*$ is the adjoint velocity, $\widetilde{\psi}_0$ is the adjoint azimuth angle, r_0 is the nondimensional radial location of the intersection point of the streamline with the rotor plane, and $\overline{t}-\xi_0$ indicate a time delayed term. The solution in the frequency domain can be generalized to Eq. 2.44 because any general time-domain solution can be expressed as a Fourier Transform in terms of frequency components. Since the frequency domain solution is true for any frequency in the transform, then it is true in general for the inverse transform in time when written in terms of $\overrightarrow{v}^*$ as in Eq. 2.44. It should be noted that the solution in Eq. 2.44 does not include the jump in velocity across the actuator disk due to the mass sources.

Analyzing each velocity component in Eq. 2.44 and illustrated in Fig. 2-2, $\overrightarrow{v}\left(r_0,\overline{\psi}_0,\xi_0,\overline{t}\right)$ is the velocity below the rotor disk at point a along the streamline; $\overrightarrow{v}\left(r_0,\overline{\psi}_0,0,\overline{t}-\xi_0\right)$ is the velocity at point b where the free streamline intersects the rotor plane; $\overrightarrow{v}^*\left(r_0,\widetilde{\psi}_0,0,\overline{t}-\xi_0\right)$ is the adjoint velocity at point c which is centro-symmetric to point b; $\overrightarrow{v}^*(r_0,\widetilde{\psi}_0,-\xi_0,\overline{t})$is the adjoint velocity at point d which is centro-symmetric to point a.
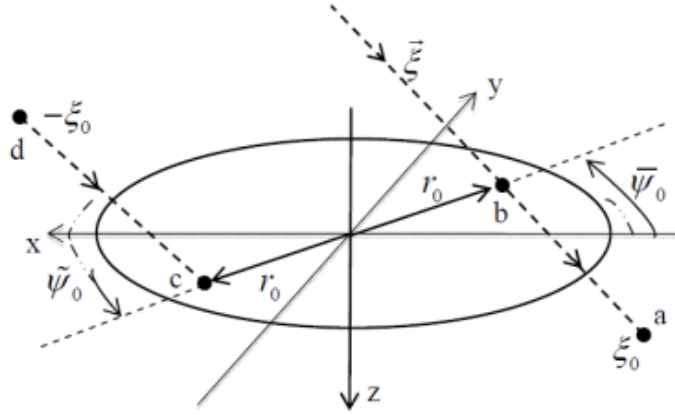
Figure 2-2: 3-D perspective of co-states for the adjoint theorem

The adjoint to the momentum equation is:

$$- [M^c] \left\{ \overset{*}{\overline{\Delta}}{}^m_n \right\} + V [D^c][L^c]^{-1}[M^c]\left\{ \overline{\Delta}{}^m_n \right\} = [D^c] \begin{bmatrix} \ddots & & \\ & (-1)^{n+1} & \\ & & \ddots \end{bmatrix} \{\tau^{mc}_n\} \qquad (2.45)$$

This equation must be solved backwards in time for the co-state variables because the solution is unstable in a forward time marching. The backwards time-marching process is discussed in greater detail in Chapter 3.

The methods outlined in this chapter are used in conjunction with the adjoint theorem for development of a coaxial rotor model. The first model is a simplified proof of concept model using simplified pressure coefficients with the adjoint theorem. Then a more rigorous model based on the Morillo-Duffy model and the adjoint theorem is presented.

24

Chapter 3

Proof of Concept for Single and Coaxial Rotor Systems

Prior to this work, finite-state inflow models with adjoint variables had not been derived for a coaxial rotor system. Before proceeding with the full development of the equations for the coaxial rotor system, a simplified proof of concept was developed to find solution methods for systems of equations with time delays and adjoint variables. In addition, a coaxial rotor system requires the development of coupled terms to describe the rotor interaction. This section explains the process of expansion from a single rotor to coaxial rotors and illustrates three solution methods used to model the proof of concept. The equations in this chapter are nominally presented in nondimensional form. The derivations for nondimensional form are given in chapter 4. As part of the simplification, the developed equations only cover a single harmonic, have a reduced shape function, and do not describe a real wake.

3.1 Derived Equations for Single Inflow State System

The equations in this section consider a single lifting rotor system (a tail rotor is assumed to counter balance the torque of the lifting rotor) and a coaxial lifting rotor system where

the rotors rotate in opposite directions to counterbalance torque. Illustrated in Figure 3-1, each rotor in the coaxial system contains its own set of dynamic equations for states and co-states. The lower rotor does not contain a co-state variable (δ) because we are not interested in the flow below the lower rotor. A simplified single lifting rotor system is discussed first to demonstrate the underlying equations and physics in a simplified case. These methods are then adapted to a coaxial rotor system and finally to a coaxial rotor system with blade flapping.

Upper Rotor: α_U, δ_U, b_U

d

Lower Rotor: α_L, b_L
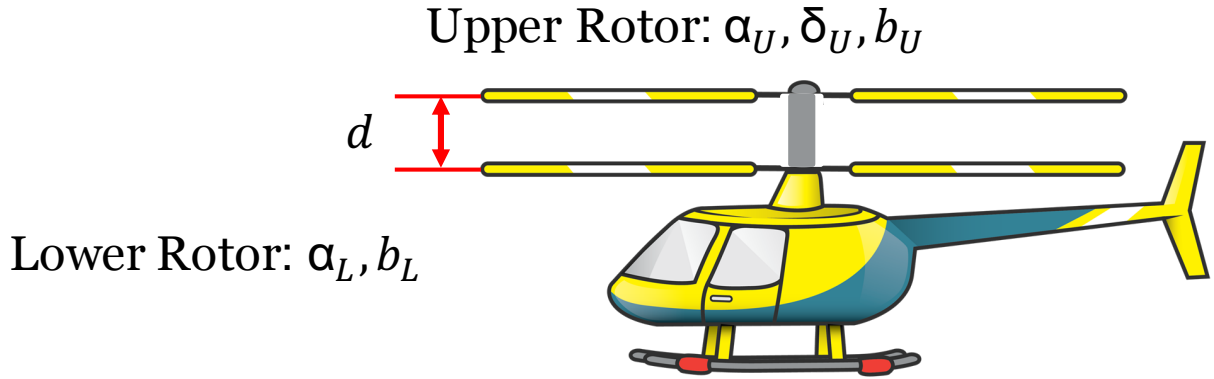
Figure 3-1: Coaxial rotor helicopter

3.1.1 Single Lifting Rotor System in Axial Flow

For a single lifting rotor system, the velocity on and above the rotor disk is found using state variables (α_n^m) where the state variable is found from:

$$[M]\left\{\overset{*}{\alpha}_n^m\right\} + \upsilon\,[D]\,[\tilde{L}]^{-1}\,[M]\,\{_n^m\} = [D]\,\{\tau_n^m\} \tag{3.1}$$

The flow below the rotor is found using the adjoint theorem and requires co-state variables (δ_n^m). The co-state variables are solved for from:

$$-[M]\left\{\overset{*m}{\delta_n}\right\} + \upsilon[D]\left[\tilde{L}\right]^{-1}[M]\{\alpha_n^m\} = [D]\begin{bmatrix} \ddots & & \\ & (-1)^{n+1} & \\ & & \ddots \end{bmatrix}\{\tau_n^m\} \qquad (3.2)$$

In these equations, $[M]$ is the apparent mass matrix, $[D]$ is the damping matrix, $[\overline{L}]$ is the influence coefficient matrix, υ is the nondimensional freestream flow and τ_n^m is the pressure coefficient. The mass, damping, and influence coefficient matrices are found using the Galerkin method, which is discussed in Appendix C. In axial flow, the case throughout all of this work, the relationship holds that $[\tilde{L}]^{-1} = [M]$. Simplifying and rearranging Eqs. 3.1 and 3.2 results in:

$$\left\{\overset{*m}{\alpha_n}\right\} + \upsilon[M]^{-1}[D]\{\alpha_n^m\} = [M]^{-1}[D]\{\tau_n^m\} \qquad (3.3)$$

$$-\left\{\overset{*m}{\delta_n}\right\} + \upsilon[M]^{-1}[D]\{\alpha_n^m\} = [M]^{-1}[D]\begin{bmatrix} \ddots & & \\ & (-1)^{n+1} & \\ & & \ddots \end{bmatrix}\{\tau_n^m\} \qquad (3.4)$$

In the case of a single inflow state, the mass and damping matrices contain only a single term:

$$\lambda = \frac{D}{M} \qquad (3.5)$$

where λ is the characteristic eigenvalue. In addition, $\upsilon = 1$ for the proof of concept. Equations 3.3 and 3.4 are further reduced to form a set of differential equations as:

$$\overset{*}{\alpha}_1 + \lambda\alpha_1 = \lambda\tau_1 \qquad (3.6)$$

$$-\overset{*}{\delta}_1 + \lambda\delta_1 = \lambda\tau_1 \qquad (3.7)$$

27

where the subscript 1 is indicative of the lifting rotor in a single rotor system. For a single lifting rotor system, the pressure coefficient is:

$$\tau_1 = \theta_1 - k\overline{V}_{11} \tag{3.8}$$

where θ_U is the pitch angle of the rotor (which is a step input function), k is the inflow feedback parameter, and $\overline{V}_{11}$ is the nondimensional velocity impact of the rotor on itself. $\overline{V}_{11}$ occurs on the rotor disk plane. In the single lifting rotor system, only on disk terms impact the velocity state and co-state development. In a coaxial rotor system, on-disk and off-disk terms impact the state and co-state development.

For the proof of concept, the pressure potential is reduced to:

$$\Phi(z) = e^{-\lambda z} \tag{3.9}$$

This function still satisfies the boundary condition above the disk (approaches zero as distance above the rotor approaches infinity).

The velocity vector for flow above and on the rotor disk for a single state is:

$$\overline{V}_A(z,\bar{t}) = \alpha(\bar{t})\Phi(z) \tag{3.10}$$

From the adjoint theorem, the velocity below the rotor is:

$$\overline{V}_B(z,\bar{t}) = \overline{V}(0,\bar{t}-\bar{z}) + \overline{V}^*(0,\bar{t}-\bar{z}) - \overline{V}^*(-z,\bar{t}) \tag{3.11}$$

where $\overline{V}^*$ is the adjoint velocity and the $\bar{t} - \bar{z}$ are the time delayed terms. The adjoint velocity in this simplified model is:

$$\overline{V}^*(z,\bar{t}) = \delta(\bar{t})\Phi(z) \tag{3.12}$$

The velocity on the rotor plane is found using Eq. 3.10 and plugging in $z = 0$. From Eq. 3.9, we know that $\Phi(0) = 1$ and therefore $\overline{V}_{11} = \alpha(\overline{t})$. This allows for further modification of Eqs. 3.6 and 3.7, resulting in:

$$\overset{*}{\alpha}_1 + \lambda \alpha_1 = \lambda \left[\theta_1 - k \alpha_1 \right] \tag{3.13}$$

$$-\overset{*}{\delta}_1 + \lambda \delta_1 = \lambda \left[\theta_1 - k \alpha_1 \right] \tag{3.14}$$

It should be noted that the right side of Eqs. 3.13 and 3.14 are identical and that δ_1 is dependent on α_1, but α_1 is independent of δ_1. In addition, F_1 is equivalent to the lifting force of the rotor (only in the proof of concept) and can be denoted as:

$$F_1 = \theta_1 - k \alpha_1 \tag{3.15}$$

3.1.2 Coaxial Rotor System in Axial Flow

The addition of a second lifting rotor to create a coaxial system results in additional terms for Eqs. 3.13 and 3.14, and the addition of a new equation to solve for the velocity state of a second rotor. In this system, the subscript U is used to denote upper rotor variables and L is used to denote the lower rotor variables. The flow below the lower rotor is not of interest for this work and therefore a second co-state variable is not needed. Combined, the coaxial rotor system contains 3 equations and 3 coupled state/co-state variables, α_U, α_L, and δ_U. Equation 3.13, the velocity state variable for a single lifting rotor, is adapted for the upper rotor through inclusion of an additional term to account for the impact of the lower rotor on the upper rotor. The state variable for the upper rotor is modeled as:

$$\overset{*}{\alpha}_U + \lambda \alpha_U = \lambda \left[\theta_U - k \overline{V}_{UU} - h \overline{V}_{UL} \right] \tag{3.16}$$

29

where h is the cross-feedback parameter and $\overline{V}_{UL}$ is the impact of the lower rotor on the upper rotor. Given that the upper rotor is upstream from the lower rotor, the velocity component is simply:

$$\overline{V}_{UL}\left(d,\bar{t}\right) = \alpha_L\left(\bar{t}\right)\Phi\left(-d\right) \tag{3.17}$$

where d is distance between the rotors. This results in:

$$\overset{*}{\alpha}_U + \lambda\alpha_U = \lambda\left[\,\theta_U - k\alpha_U - \mathrm{q}\alpha_L\right] \tag{3.18}$$

where $q = he^{-\lambda d}$. The lift force of the upper rotor is:

$$F_U = \theta_U - k\alpha_U - \mathrm{q}\alpha_L \tag{3.19}$$

In turn, the co-state variable solution from Eq. 3.14 incorporates the same new τ_U as the state variable for the upper rotor and is:

$$-\overset{*}{\delta}_U + \lambda\delta_U = \lambda\left[\,\theta_U - k\alpha_U - \mathrm{q}\alpha_L\right] = \lambda F_U \tag{3.20}$$

For the lower rotor, the velocity state variable, α_L, is modeled by:

$$\overset{*}{\alpha}_L + \lambda\alpha_L = \lambda\left[\theta_L - k\overline{V}_{LL} - h\overline{V}_{LU}\right] \tag{3.21}$$

where $\overline{V}_{LU}$ is the impact of the upper rotor on the lower rotor and $\overline{V}_{LL}$ is the impact of the lower rotor on the lower rotor. $\overline{V}_{LL}$ is solved similar to $\overline{V}_{UU}$, such that:

$$\overline{V}_{LL}\left(0,\bar{t}\right) = \alpha_L\left(\bar{t}\right)\Phi\left(0\right) \tag{3.22}$$

$\overline{V}_{LU}$ requires the adjoint theorem because it is flow on the lower rotor due to the upper rotor (i.e. flow below the upper rotor). It is solved for here as:

$$\overline{V}_{LU}\left(d,\overline{t}\right) = \overline{V}_{UU}\left(0,\overline{t}-\overline{d}\right) + \overline{V}_{UU}^{*}\left(0,\ \overline{t}-\overline{d}\right) - \overline{V}_{UU}^{*}\left(-d,\ \overline{t}\right) \tag{3.23}$$

which results in:

$$\overline{V}_{LU}\left(d,\overline{t}\right) = \alpha_{U}\left(\overline{t}-\overline{d}\right)\Phi\left(0\right) + \delta_{U}\left(\overline{t}-\overline{d}\right)\Phi\left(0\right) - \delta_{U}\left(\overline{t}\right)\Phi\left(-d\right) \tag{3.24}$$

Inserting Eqs. 3.22 and 3.24 into Eq. 3.21 yields:

$$\overset{*}{\alpha}_{L} + \lambda\alpha_{L} = \lambda\left[\theta_{L} - k\alpha_{L}(\overline{t}) - h\alpha_{U}\left(\overline{t}-\overline{d}\right) - h\delta_{U}\left(\overline{t}-\overline{d}\right) + q\delta_{U}\left(\overline{t}\right)\right] \tag{3.25}$$

The lift exerted by the lower rotor is written as:

$$F_{L} = \ \theta_{L} - k\alpha_{L}(\overline{t}) - h\alpha_{U}\left(t-d\right) - h\delta_{U}\left(t-d\right) + q\delta_{U}\left(t\right) \tag{3.26}$$

3.1.3   Blade Flapping in a Coaxial Rotor System

The coaxial rotor system was further modified to account for blade flapping. Each rotor introduces a blade flapping state variable, b, and 4 new equations, for a total of 7 equations and 7 coupled state and co-state variables (the blade flapping equations are second-order ODEs in time and therefore have b and $\overset{*}{b}$ terms). Blade flapping introduces oscillations into all of the other state/co-state variables. The new velocity state equation for the upper rotor with the coupled blade flapping term is:

$$\overset{*}{\alpha}_{U} + \lambda\alpha_{U} = \lambda\left[\theta_{U} - k\overline{V}_{UU} - h\overline{V}_{UL} - \overset{*}{b}_{U}\right] \tag{3.27}$$

where $\overset{*}{b}_U$ is the slope of the blade flapping variable for the upper rotor. The velocity components for Eq. 3.27, $\overline{V}_{UU}$ and $\overline{V}_{UL}$, are the same as for the solution without blade flapping in Eq. 3.25. The new velocity co-state equation for the upper rotor is:

$$-\overset{*}{\delta}_U + \lambda\delta_U = \lambda\left[\theta_U - k\overline{V}_{UU} - h\overline{V}_{UL} - \overset{*}{b}_U\right] \tag{3.28}$$

where F_U is now:

$$F_U = \theta_U - k\alpha_U - h\alpha_L - \overset{*}{b}_U \tag{3.29}$$

The lower rotor velocity state solution is:

$$\overset{*}{\alpha}_L + \lambda\alpha_L = \lambda\left[\theta_L - k\alpha_L(\bar{t}) - h\alpha_U\left(\bar{t} - d\right) - h\delta_U\left(\bar{t} - d\right) + q\delta_U\left(\bar{t}\right) - \overset{*}{b}_L\right] = \lambda F_L \tag{3.30}$$

The blade flapping state variable equations, for the upper rotor, b_U, and the lower rotor, b_L, are dependent on the lift forces of their respective rotors (F_U and F_L), the Lock number (γ), and the flapping frequency p. The blade flapping state equations for their respective rotors are:

$$\overset{**}{b}_U = \frac{\gamma}{8}F_U - p^2 b_U \tag{3.31}$$

$$\overset{**}{b}_L = \frac{\gamma}{8}F_L - p^2 b_L \tag{3.32}$$

3.2   Solution Methods

Three approaches were taken to solve and model the systems of equations: closed form (using Laplace transforms), time marching, and the convolution integral. The closed form solution is only applied to the single rotor system because the coaxial system proved to be too complex due to the time delayed terms.

3.2.1 Closed Form Solution

The closed form solution is the first solution process that was investigated for this work. The closed form solution is based off of Eqs. 3.13 and 3.14 and yields:

$$\alpha_1 = \begin{cases} 0 & \bar{t} < 0 \\ \frac{\theta_1}{k+1}\left(1 - e^{-(k+1)\lambda\bar{t}}\right) & \bar{t} > 0 \end{cases} \tag{3.33}$$

$$\delta_1 = \begin{cases} \frac{2\theta_1}{k+2}\,e^{\lambda\bar{t}} & \bar{t} < 0 \\ \frac{\theta_1}{k+1} + \frac{\theta_1 k}{(k+1)(k+2)}e^{-(k+1)\lambda\bar{t}} & \bar{t} > 0 \end{cases} \tag{3.34}$$

While α and δ are not fully coupled, which is the case with all of the state and co-state variables in the coaxial rotor system, the one way coupling was enough to confidently develop time marching and convolution methods that could be expanded to a coaxial rotor system.

3.2.2 Time Marching Method

The time marching solution utilizes ODE45 in MatLab, which is a Dormand-Prince method that is in the Runge-Kutta family of solution methods. The unique feature of solving the system of equations using a time marching method is that δ must be time marched backwards because it becomes unstable when time marching forward. Given that δ is one way coupled to α in the single lifting rotor system (assuming k $\neq$ 0) the state and co-state variables can be solved separately. In the coaxial system all state and co-state variables are coupled, therefore the equations must be solved simultaneously.

3.2.3 Convolution Integral

The convolution integral method utilizes the time marching process (ODE45) for solving the state variables (α_U, α_L, and later b_U, b_L) and a convolution integral for the co-state variable

δ. The co-state still requires the alternate nondimensional time domain, τ, because δ is dependent on time marched state variables. The convolution integral is defined as:

$$\delta_1 \left(d \right) = \int_0^z f \left(\tau \right) g \left(d - \tau \right) d\tau \tag{3.35}$$

where $f \left(\tau \right)$ is the force from the upper rotor $\left(F_U \right)$ and $g \left(d - \tau \right)$ is the impulse response and is also defined as:

$$g \left(d - \tau \right) = \lambda e^{-\lambda(d-\tau)} \tag{3.36}$$

The integral solution is approximated using the Trapezoidal rule, shown here:

$$Area = \int_a^b f \approx \frac{\Delta x}{2} \left(f \right) + 2 \sum_{i=1}^N \left(f \left(x_i \right) + f \left(x_N \right) \right) \tag{3.37}$$

Other forms of Riemann Sums can be used and provide accurate results, but require a significantly smaller step size than the trapezoidal rule. The time marching method and convolution integral both provided accurate results with a variation in simulation time that was insignificant for one inflow state.

3.2.4 Initial and Terminal Conditions

One of the most important aspects of the solution for coupled rotor inflow dynamics is the set of initial conditions used for the states $\left(\alpha_U, \alpha_L, \; b_U, b_L \right)$ and co-states $\left(\delta_U \right)$. The initial conditions for the state variables are straightforward. At nondimensional time $\bar{t} = 0$, the initial conditions are $\alpha_U = 0$, $\alpha_L = 0$, $b_U = 0$, and $b_L = 0$.

The terminal conditions for the co-state variables are more subtle because the co-state equations are solved in reverse time: $\tau = \bar{t}_{ref} - \bar{t}$, $d\tau = -d\bar{t}$. The terminal conditions apply to the location where $\bar{t} = \bar{t}_{ref}$ and therefore $\tau = 0$, which is equivalent to the current time in the regular nondimensional time domain. The terminal condition for the co-state remains

constant throughout the solution process. However, the development of the co-state profiles are dynamic and the time-delayed co-state values change with each time step. Thus, at every time step in $\bar{t}$, one must stop and time march the co-states backwards as far as the time delay requires.

In either of the above cases, one could ask the question, "How do we know what terminal conditions to put on the co-states?" Fortunately, the Adjoint theorem shows that the velocity below a disk computed by the co-states is independent of the initial and terminal conditions because the Adjoint theorem sweeps out the homogeneous solution, making initial and terminal conditions unobservable in the velocity. Evaluating the vorticity equation:

$$\frac{\partial \overline{V}}{\partial \bar{t}} - \upsilon \frac{\partial \overline{V}}{\partial z} = \Delta P \tag{3.38}$$

the adjoint velocity terms $\overline{V}^* \left(\bar{t} - \bar{d} \right)$ terms can be plugged in to Eq. 3.38 to form:

$$\frac{\partial \overline{V}^* \left(\bar{t} - \bar{d} \right)}{\partial \bar{t}} - \upsilon \frac{\partial \overline{V}^* \left(\bar{t} - \bar{d} \right)}{\partial z} = \Delta P \tag{3.39}$$

Solving by the chain rule, we find that:

$$\frac{\partial \overline{V}^* \left(\bar{t} - \bar{d} \right)}{\partial \bar{t}} = \overline{V}^{*\prime} \times (1) + \overline{V}^{*\prime} \times (-1) = 0 \tag{3.40}$$

and therefore, the velocity solution is independent of the terminal conditions utilized.

Since we are left with the ability to select any terminal conditions, there are two basic methods that make logical sense. One is simply to make the terminal conditions zero at $\tau = 0$. The other approach is to make the terminal conditions at $\tau = 0$ equal to the steady-state values, should the equations be taken to steady-state. The latter method is very advantageous for computation of the required pitch input for load sharing of two rotors,

but the method of zero initial conditions is more advantageous for simplicity. We use both methods here to show that they do result in the identical solution.

Going into the selection of terminal conditions, one of the primary concerns for the zero terminal condition is that the co-state profile develops slower and has a large drop off at the end as shown in Figure 3-2.
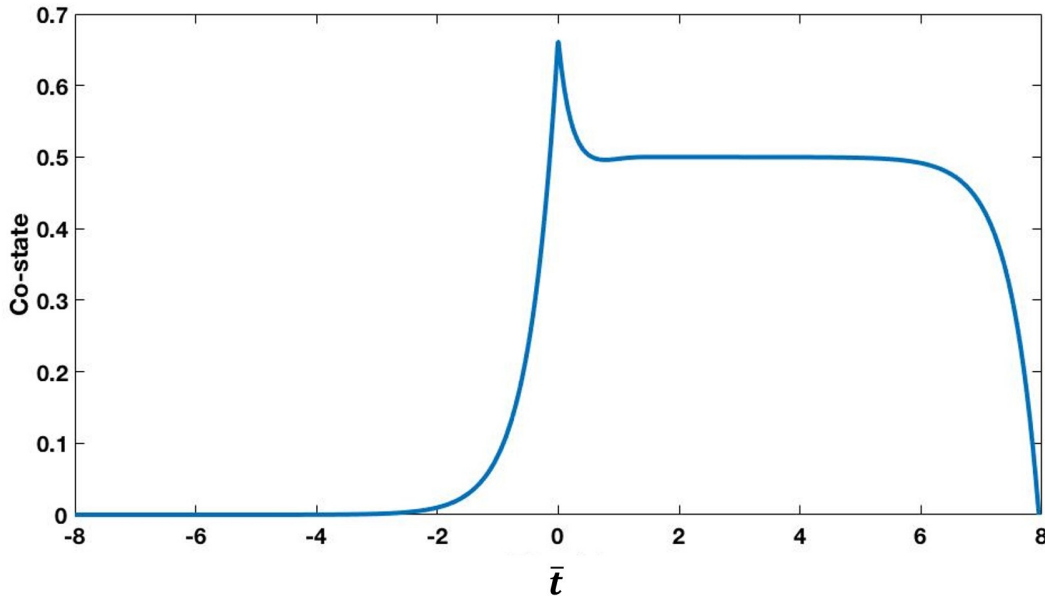
Figure 3-2: δ_U with zero terminal conditions

The steady-state terminal condition has the obvious benefit that the final value is the steady-state value. The initial thought with this approach is that it would take less time for the state and co-state values reach steady state. In order to find the steady-state values, the system of equations must be reduced through known quantities. The approach taken is similar to that used to determine load sharing in Appendix D. Evaluating the system at $\bar{t} = \infty$, it can be said that the time delayed state variables are equivalent to their non-time delayed counterparts (i.e. $\alpha(\infty - \bar{d}) = \alpha(\infty)$). The steady-state terminal condition

36

allows that the equivalence within the state variables is also true for co-state variables (i.e. $\delta(\infty - \overline{d}) = \delta(\infty)$). For load sharing the lifting force for the upper rotor must be equal to the lifting force of the lower rotor ($F_U = F_L$), such that:

$$F_U + F_L = F_{Total} \tag{3.41}$$

$$F_U = F_L = \frac{1}{2}F_{Total} \tag{3.42}$$

For the purposes of the examples in this section, the total lifting force is set to be 1 and therefore, the lifting force on each rotor is 0.5. In a fully converged system, the first order terms go to zero and leave behind the relationships: $\alpha_U = F_U$, $\delta_U = F_U$, and $\alpha_L = F_L$. From load sharing $F_U = F_L$, and therefore we find that $F_U = F_L = \alpha_U = \alpha_L = \delta_U$.

By the previous declaration that $F_{Total} = 1$, all state and co-state values will have a steady-state value of 0.5 and thus, the steady-state terminal conditions are set to $d(\infty) = 0.5$. The co-state profile for steady-state terminal condition is shown in Figure 3-3.
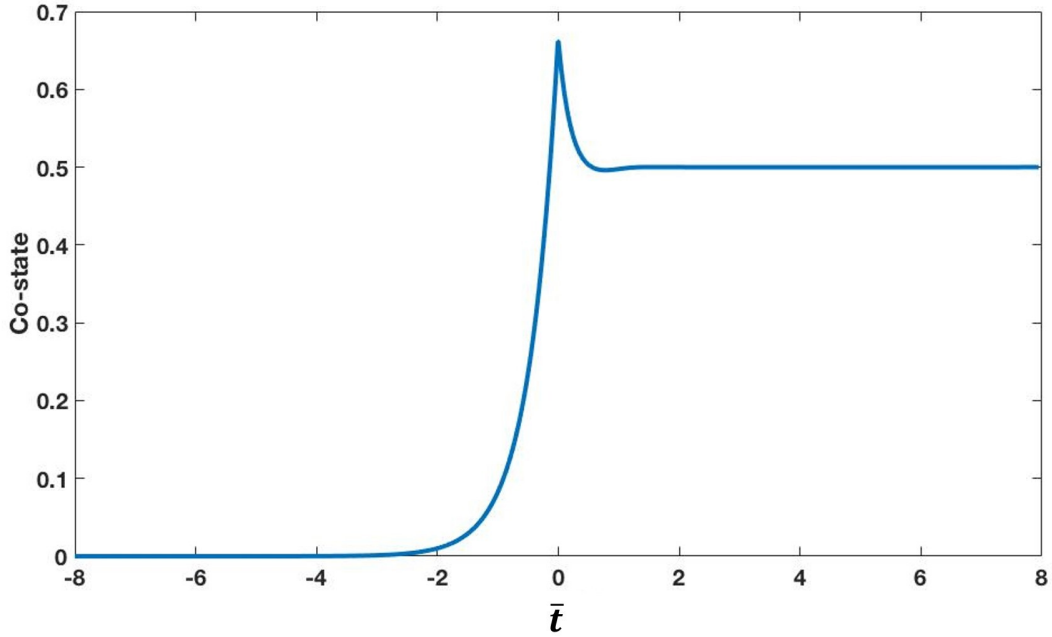
Figure 3-3: δ_U with steady-state terminal conditions

The development of the δ profiles for both sets of terminal conditions are significantly different. Initially, the development of the profiles was demonstrated through short gifs that cycled through every time step. Here, we have selected various nondimensional times in the development that show when different characteristics of the profile develop. It is important to note the values of the user defined input variables for these plots. The rotor spacing is set as $d = 1$, the feedback parameters are also set as $h = k = 1$, and through load sharing, the step input pitch angles for each rotor are $\theta_U = 1.06$ and $\theta_L = 1.94$. For the zero terminal conditions, as shown in Figure 3-4, nine nondimensional times were selected to demonstrate the development of the co-state profiles. The first trend that can be noticed is the peak of the d profile grows significantly and does not reach a stable peak until 1-1.5 nondimensional time. After the peak stabilizes, the steady-state region begins to develop, but it takes until $\bar{t} \sim 4 - 5$ for a respectable amount of the profile to cover a converged region. The drawback

of the zero terminal condition case is that the simulation has to be calculated for a decent amount of time to find the steady-state region of the co-state variable.
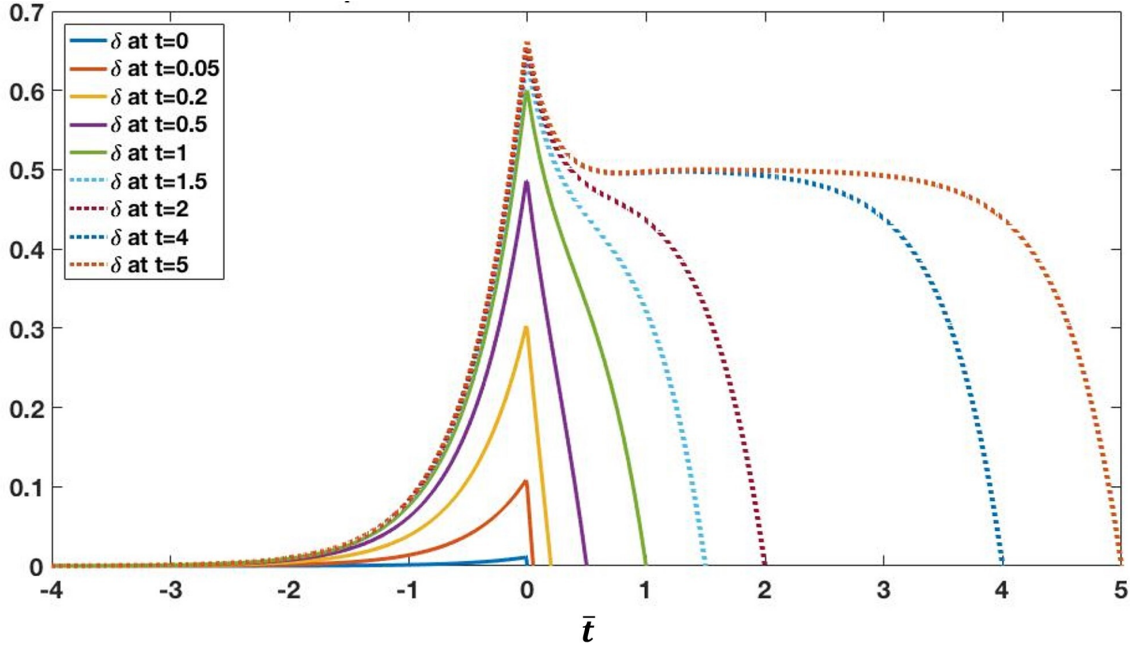
Figure 3-4: Development of δ_U profile with zero terminal conditions

From Fig. 3-5 the development of the δ profile for steady-state terminal conditions proves to be more rapid and contains less variation than that of the zero terminal condition. The peak in the system stabilizes around $\bar{t} = 0.5$. The profile contains a reasonable region of converged values within two seconds. After the peak in the system, there is a minor over correction that causes the profile to dip below the converged value. This exists in the plot of the zero initial conditions but is difficult to notice given the more drastic fluctuations in other regions. There is minor fluctuation in this region as it develops and stabilizes, which occurs between $\bar{t} = 1 - 2$.
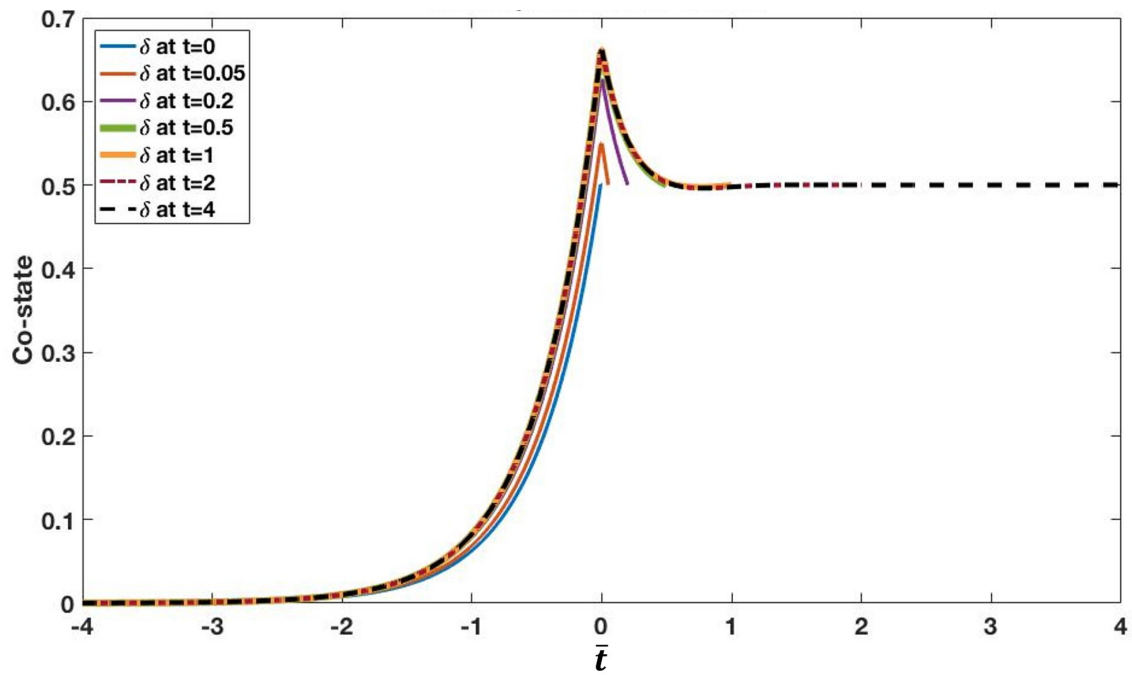
Figure 3-5: Development of δ_U profile with zero terminal conditions

Figure 3-6 demonstrates that at a long enough time the profiles reach similar peaks and steady-state values. As can be seen, the profiles are identical before the zero terminal condition profile begins to trail off towards zero.
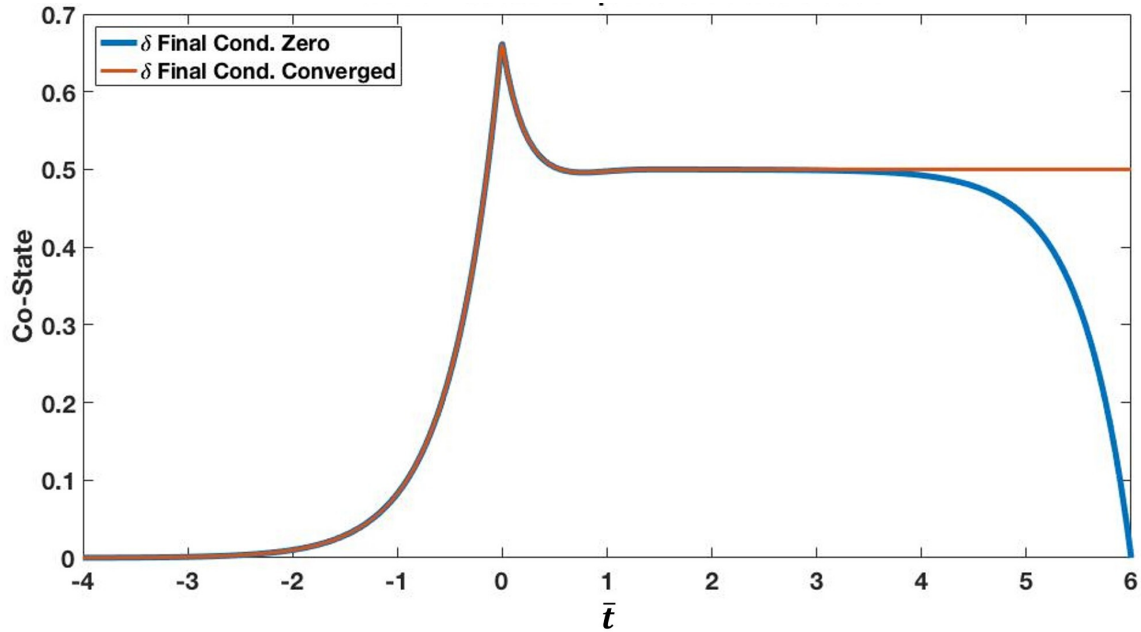
Figure 3-6: Comparison of δ_U profiles for different terminal conditions

3.3 Numeric Illustrations for Single Inflow State

The presented numeric illustrations draw on single inflow state solutions for single lifting rotor and coaxial rotor systems in axial flow. The comparisons between the systems are meant to examine and rationalize trends that appear in one or both rotor systems. For the single inflow state $\lambda = 2.094$, which is determined from D_{11}^{00}/M_{11}^{00} (where $r = 0, m = 0, j = 1, n = 1$).

3.3.1 Trends in Single Rotor System

The purpose of the single lifting rotor system was to provide a starting point for developing solution methods for time marching and convolution integral methods and validate the results from these methods with the closed form solution. In addition, this system provides a general understanding of the velocity state and co-state profile shapes relative to θ and k parameters.

41

First the comparison of methods will be discussed and then impact of k and θ on state profiles are explored.

Comparisons of the velocity profile for the closed form solution and the time marching solution are shown in Figure 3-7 and Figure 3-8 the profiles in each figure have the same inputs ($k = 1, \theta = 1$), but vary in nondimensional time. The nondimensional time step size and displacement step size are both 0.05. The vertical blue line in Fig. 3-7 is to demonstrate the current time in the system ($\bar{t}_0$) and mark the end of the wake. The convolution integral is not illustrated to prevent more overlay in the plots, but the values are approximately the same as the other two methods.
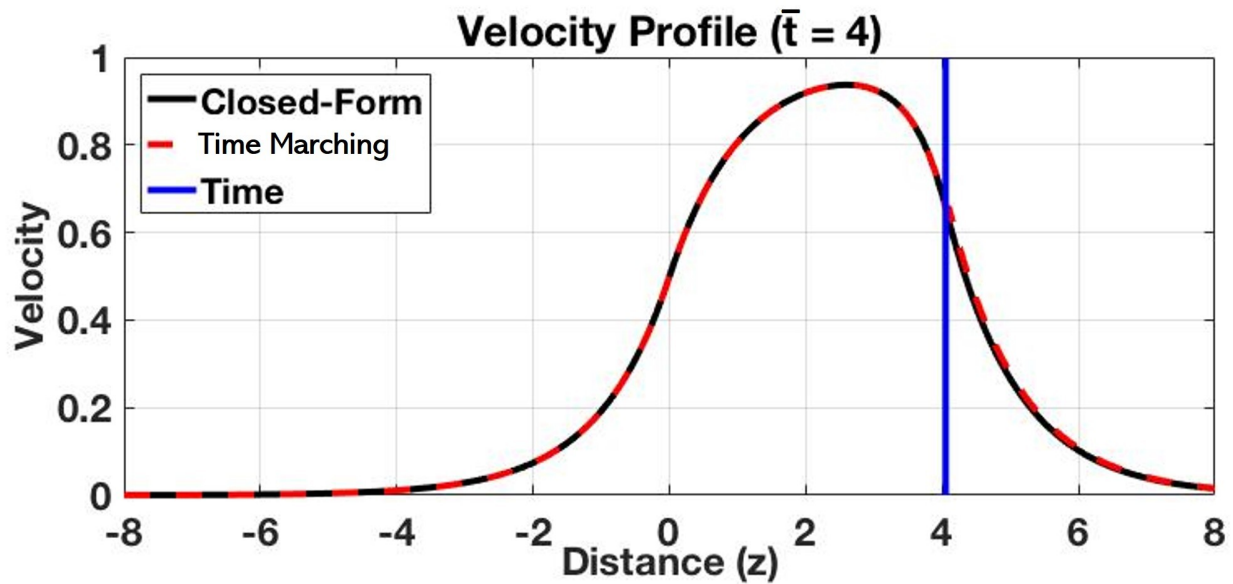
Figure 3-7: Velocity profile for closed form and time marching solutions for single lifting rotor system with $k = 1, \theta = 1$ at $\bar{t} = 4$
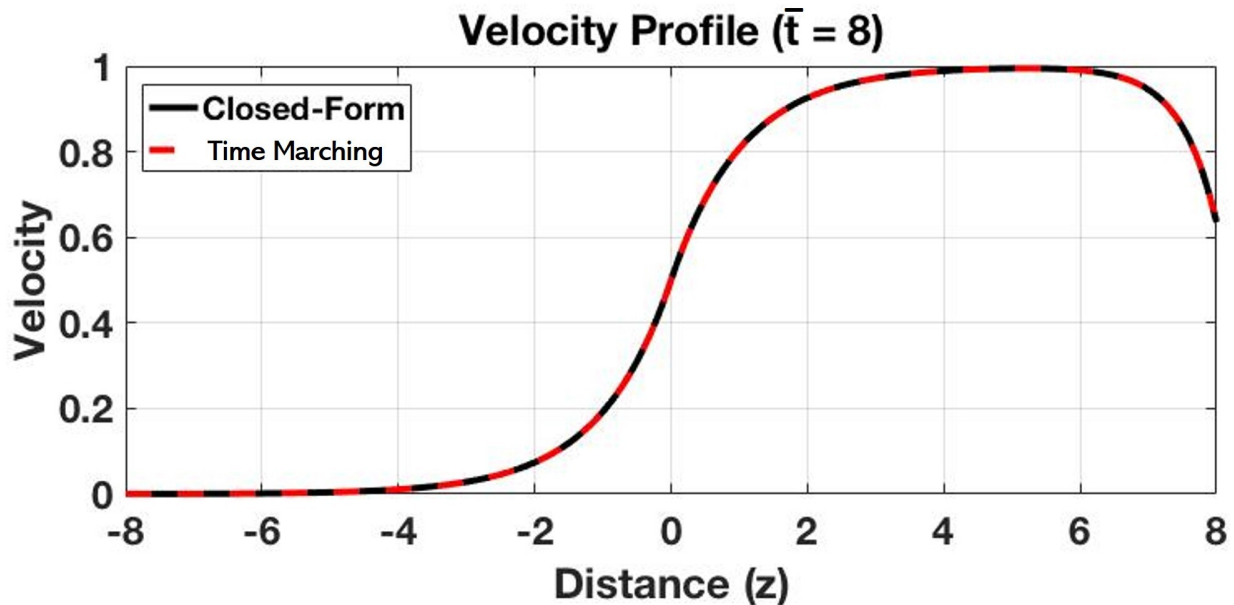
Figure 3-8: Velocity profile for closed form and time marching solutions for single lifting rotor system with $k = 1, \theta_1 = 1$ at $\bar{t} = 8$

The nondimensional time and displacement step sizes are controllable factors that impact the accuracy of the solution methods. For the single lift rotor solution, a sufficient level of accuracy for the nondimensional velocity at critical locations is approximately ± 0.005 and is achieved with a step size of 0.05. The time marched solution was slightly more accurate at any given time step size, but the convolution integral method required less computational time to reach a final solution. To reach the same level of accuracy, a smaller nondimensional time step size for the convolution integral method is required. As a result, the computational time required is approximately the same for both methods to reach the same level of accuracy.

In Eqs. 3.33 and 3.34, the relationship between k and α_1 and δ_1 is displayed, and demonstrates that an increase in k results in a decrease in α_1 and δ_1. Looking at Figure 3-9 and Figure 3-10, when k changes from 0 (Fig. 3-9) to 1 (Fig. 3-10), the converged values of α_1 and δ_1 decrease from 1 to 0.5. For $k > -1$ the exponential terms for α_1 and δ_1 approach

43

zero as time increases, resulting in a converged value of:

$$\alpha_1 \left(\bar{t}_\infty \right) = {}_1 \left(\bar{t}_\infty \right) = \frac{\theta_1}{k+1} \tag{3.43}$$
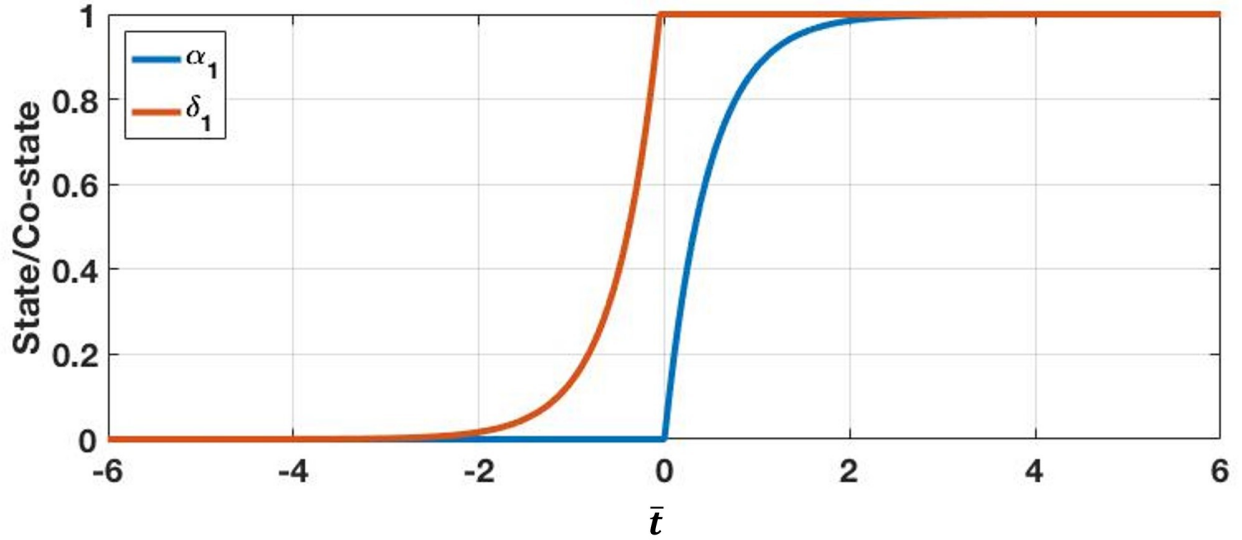
Figure 3-9: α_1 and δ_1 profiles for single lifting rotor system with $k = 0$, $\theta = 1$
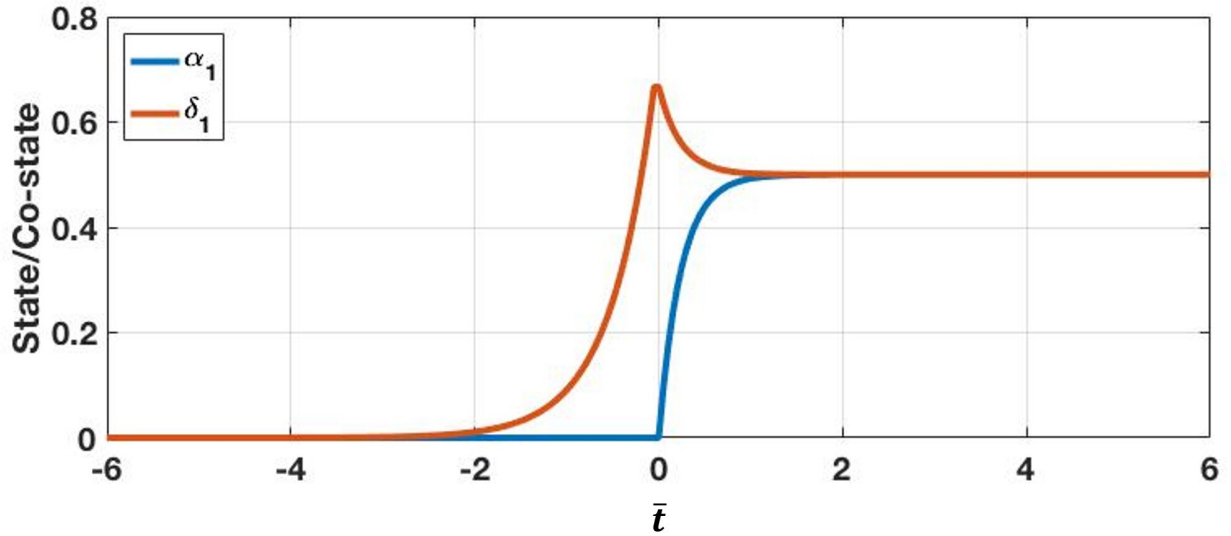
Figure 3-10: α_1 and δ_1 profiles for single lifting rotor system with $k = 1$, $\theta = 1$

While variation in k impacts the steady-state value, it also impacts the rate of convergence through how fast the exponential portion of α_1 and δ_1 approaches 0. The same trend also occurs by varying λ, but the steady-state solution does not vary in magnitude (only the decaying portion of the solution is a function of λ). These trends are illustrated in the α profiles in Figs. 3-9 and 3-10 for variations in k.

For the single lifting rotor system, θ_1 is a unit input. For the case where $k = 0$, the converged α_1 and δ_1 values are solely dependent on θ_1 in that:

$$\alpha_1\left(\bar{t}_\infty\right) = \delta_1\left(\bar{t}_\infty\right) = \theta_1 \tag{3.44}$$

The δ profile in Figure 3-10 contains an additional trend of peak amplitude at $\bar{t} = 0$ along with the convergence rate. The peak amplitude is governed by:

$$\delta\left(0\right) = \frac{2\theta_1}{k+2} \tag{3.45}$$

and is a result of the reverse time march process and sudden inflow from the collective pitch. As stated previously, in a single rotor system θ_1 is defined as 1 throughout this work. The decay of the exponential term follows the same process as for the α equation, but δ converges from above the stable value. This is due to the addition of the exponential term as opposed to the subtraction in the α equations.

While the trends are not exactly the same in the coaxial equations, the impact of these parameters is similar and can be identified. The similarities between the single rotor system and the coaxial rotor system will be discussed further in the next section.

3.3.2   Trends in Coaxial Rotor System

The results in this section are from the time marching method, but results from the con-volution integral are approximately the same. Four cases of varied parameters for systems with and without blade flapping are investigated to study the impact of rotor spacing on step input for each rotor in the system. The parameters for the cases are given in Table 3-1.

Table 3-1: Input value cases for coaxial system investigations.

Input Variable	Case #1	Case #2	Case #3	Case #4
θ_U	1.33	1.06	1.01	1.00
θ_L	1.67	1.94	1.99	2.00
k	1.00	1.00	1.00	1.00
h	1.00	1.00	1.00	1.00
d	0.20	1.00	2.00	4.00

These pitch angles were generated using a load sharing input to ensure that both rotors contribute equally to the total lift in the system. Load sharing occurs when the system stabilizes. Prior to stabilization, the load distribution between rotors is uneven, as can be seen in the Figs. 3-11 through 3-13 for the state and co-state variables. Under load sharing, the torques from each rotor are the same magnitude, but different direction, resulting in a stable system.

First, for systems without blade flapping, it is noticeable from Fig. 3-11 that the α_U states for all input cases reach convergence around $\bar{t} = 2$. There are only small variations between the different cases prior to reaching steady state. All input cases result in the same steady state value because load sharing was applied and the pitch angles adjust to accommodate

46

for the change in rotor spacing. The minor variations are due to the system adjusting to initial startup of the helicopter and the overshoot of the α_L terms on the lower rotor.

Figure 3-12 shows that the size of the overshoot for the α_L terms increases significantly as the rotor spacing increases. This is due to the increased time it takes for the flow from the upper rotor to reach the lower rotor and for system to balance out. The terms all reach the same steady-state value due to load sharing. The large variation in the α_L terms is the most significant trend to notice, especially when observing the velocity terms on the rotors. The variations in the shape of the initial region demonstrate that the rotor spacing has significant impact on α_L.

The co-state variable (δ_U), profiles in Fig. 3-13 show minor variations between the different input cases. This is not surprising as the co-state equation has the same pressure coefficient as the state variable equation for the upper rotor.

Figures 3-14 and 3-15 depict the velocity on the upper and lower rotor disks, respectively. First, Fig. 3-14 shows that the converged velocity on the upper rotor decreases notably as the rotor spacing increases. There are very minor changes in the converged velocity as the distance between the rotors becomes large ($d > 2$). These trends demonstrate that as the rotor spacing increases, the impact of the lower rotor on the upper rotor decreases. This is also demonstrated in Eq. 3.17 and is true of off-disk terms because the exponential in the shape function approaches zero as $d \to \infty$.

For the velocity on the lower rotor in Fig. 3-15, there are two trends to discuss, the change in converged velocity with rotor spacing and the delayed increased to convergence for the cases with larger rotor spacings. As the rotor spacing increases, the converged velocity on the lower rotor increases. This is again related to the off-disk terms. However, the impact of the velocity on the lower rotor due to the upper rotor in Eq. 3.25, the adjoint term

47

above the rotor disk is negative. Therefore, as the spacing increases the impact of this term decreases. The second trend of the delayed time to reach convergence is related to the time delay associated with the flow from the upper rotor reaching the lower rotor.

As discussed previously, the blade flapping equations are second-order ODEs, which introduces a damped oscillation to the state and co-state variables. As is shown in Figs. 3-16 to 3-18 the state and co-state variables converge to the same values as before but take longer to converge due to the blade flapping dynamics. The blade flapping investigations used the same input cases from above to provide a direct comparison of profiles between the systems with and without blade flapping.

Figures 3-16 and 3-18 show minor variations with rotor spacing for α_U and δ_U, respectively. This remains consistent with the previous systems without blade flapping. The blade flapping itself remains consistent in amplitude and frequency in both systems. The profiles for the various α_L terms in Fig.3-17 are more dynamically interesting because the profiles differ with spacing. It is noticeable that the oscillations within all of the cases are similar in frequency, but the peaks occur at different times. This is due to the delay in time for the flow from the upper rotor to reach the lower rotor. The velocity profiles are made up of both on-disk and off-disk terms and thus are a combination of the oscillations in both. The velocity on the lower rotor is heavily driven by the off-disk terms, while to upper rotor is driven by the on-disk terms. This is why the peaks do not vary for the upper rotor but will vary for the lower rotor.

The velocity profiles on the upper and lower rotors in Figs. 3-19 and 3-20 show similar trends of velocity magnitudes versus rotor spacing as systems without blade flapping. The velocity on the upper rotor experiences oscillations from the addition of blade flapping, but the rotor spacing does not impact the frequency or peak location. However, the velocity on

the lower rotor does experience variations in frequency and peak location with changes in rotor spacing. Case #4 provides the most notable variation in peak location, which reaches its maxima near when the other profiles reach their minima, and the peaks are less defined. This is the result of the maxima in the off-disk terms lining up with the minima in the on-disk terms and vice versa.

Finally, Figs. 3-21 and 3-22 show the blade flapping states for the upper and lower rotors, respectively. On the upper rotor, the magnitude of the oscillations decreases as the rotor spacing increases, which falls in line with decreased influence of the lower rotor on the upper rotor. The blade flapping state on the lower rotor shows variations in peak location for the different input cases, a result of increased rotor spacing and the time delay. Case #4 for the lower rotor has inconsistent decay, which is likely a result of the alignment of the on-disk and off-disk velocity terms.
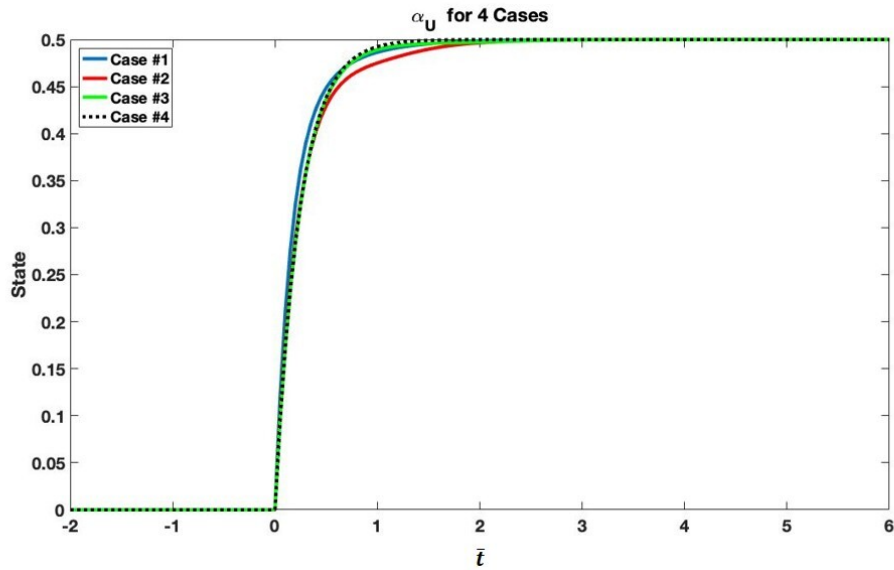
Figure 3-11: α_U profiles vs. nondimensional time for the four test cases
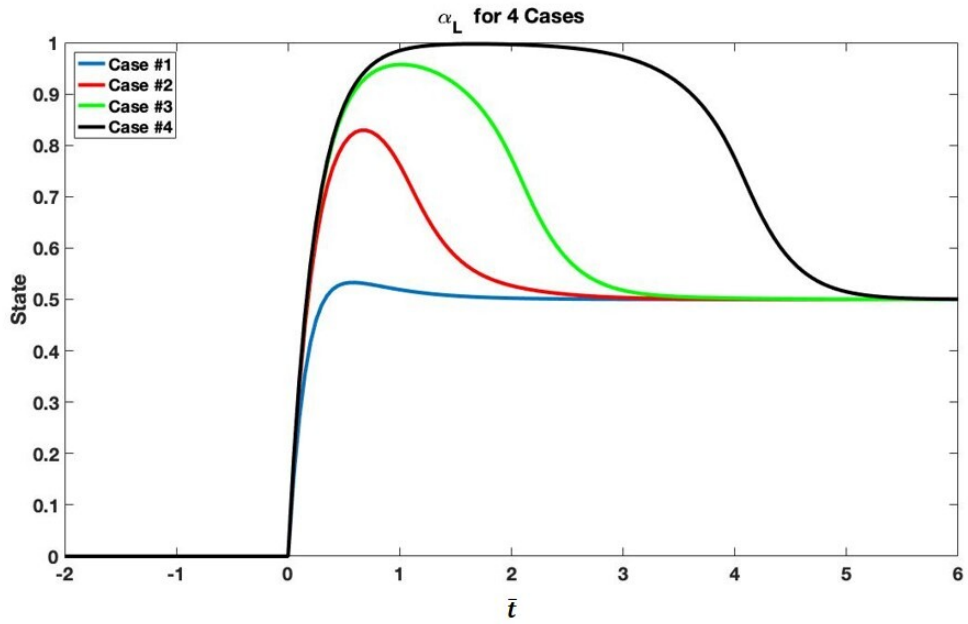
Figure 3-12: α_L profiles vs. nondimensional time for the four test cases
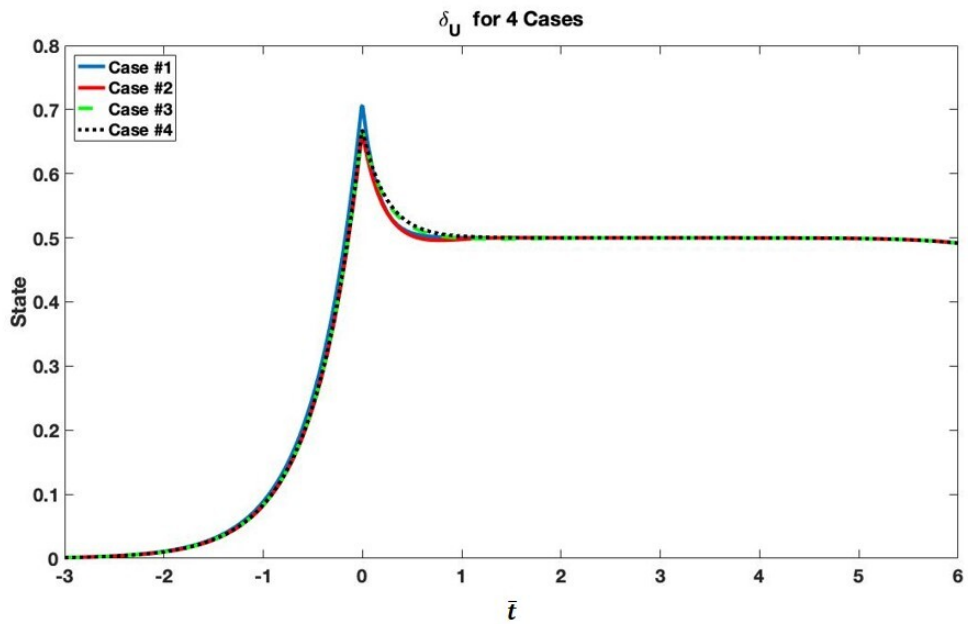
Figure 3-13: δ_U profiles vs. nondimensional time for the four test cases
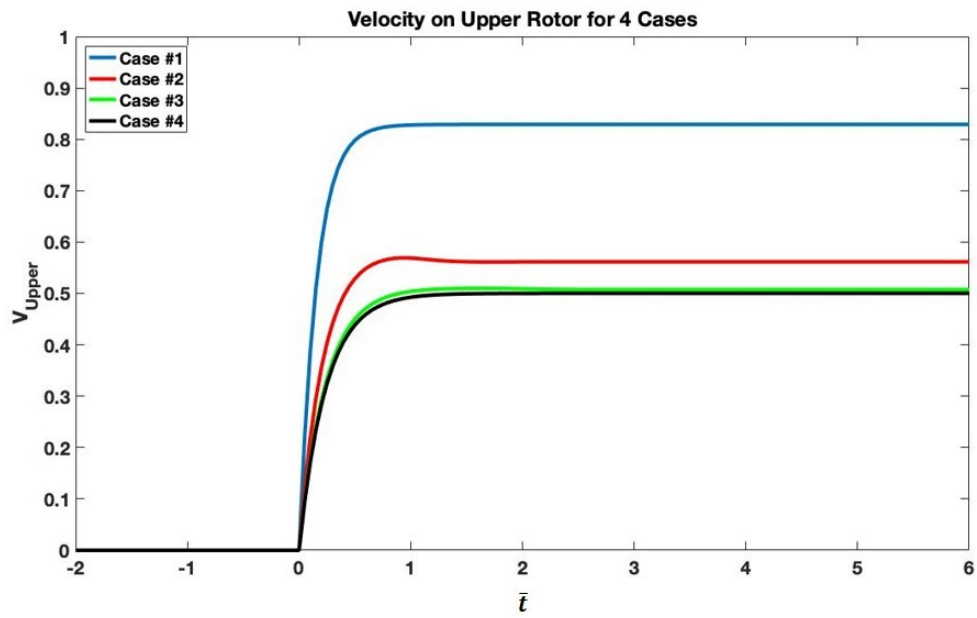
Figure 3-14: Nondimensional velocity on upper rotor vs. $\bar{t}$ for the four test cases
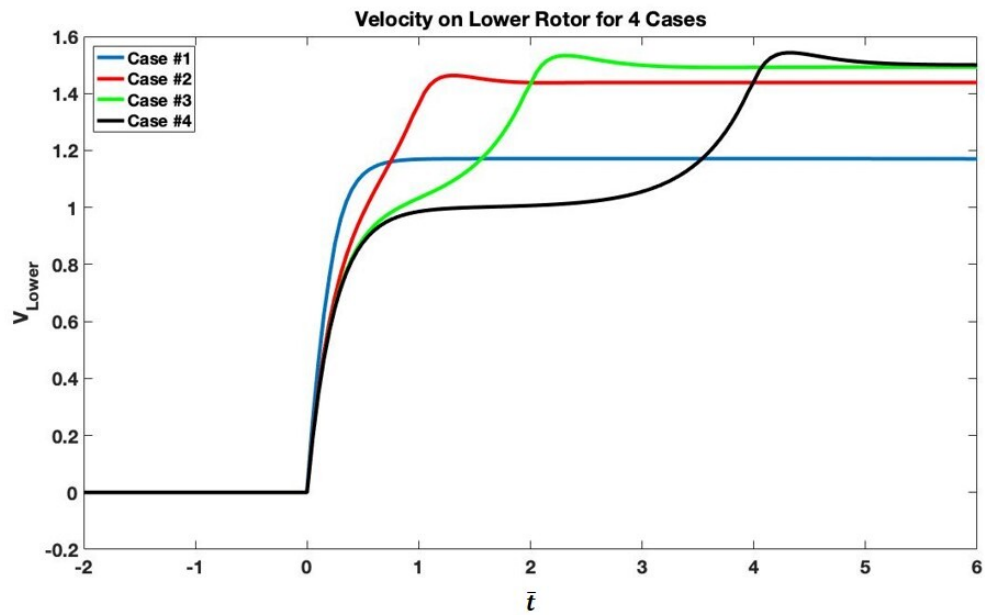
Figure 3-15: Nondimensional velocity on lower rotor vs. $\bar{t}$ for the four test cases

51
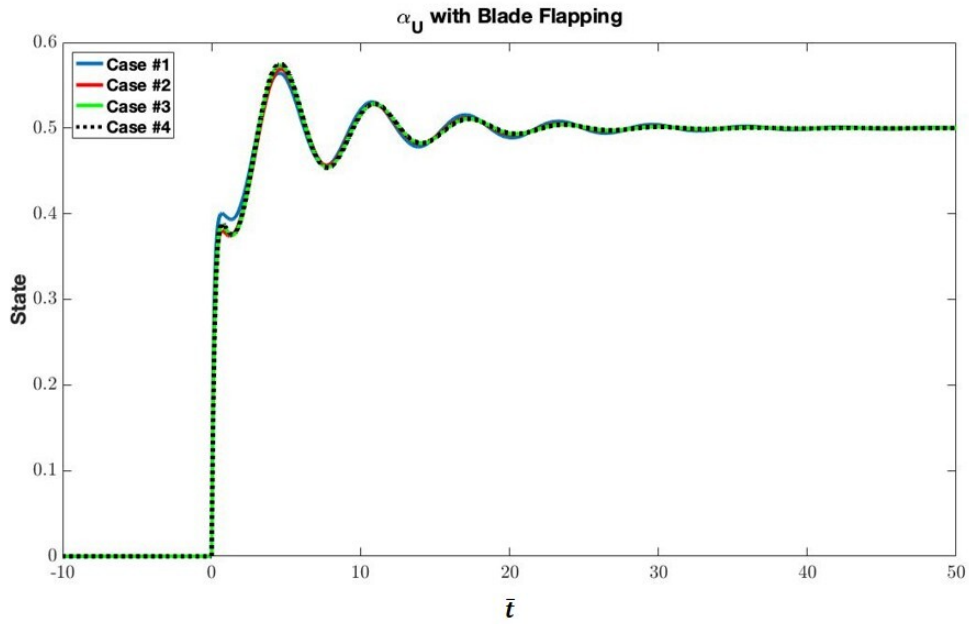
Figure 3-16: α_U profiles vs. $\bar{t}$ for system with blade flapping ($\gamma = 5$ and $p^2 = 1.08$)
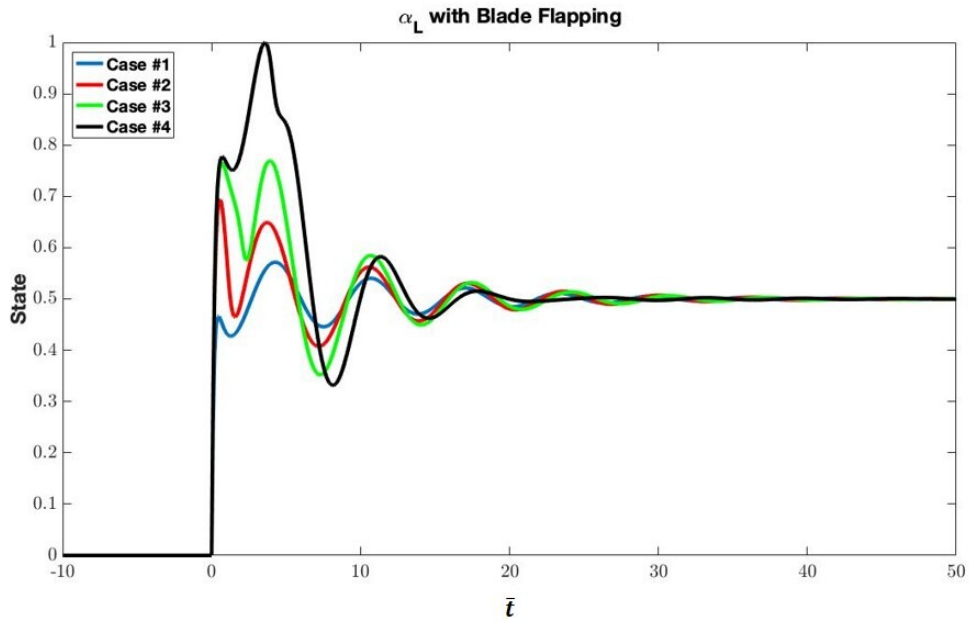
Figure 3-17: α_L profiles vs. $\bar{t}$ for system with blade flapping ($\gamma = 5$ and $p^2 = 1.08$)
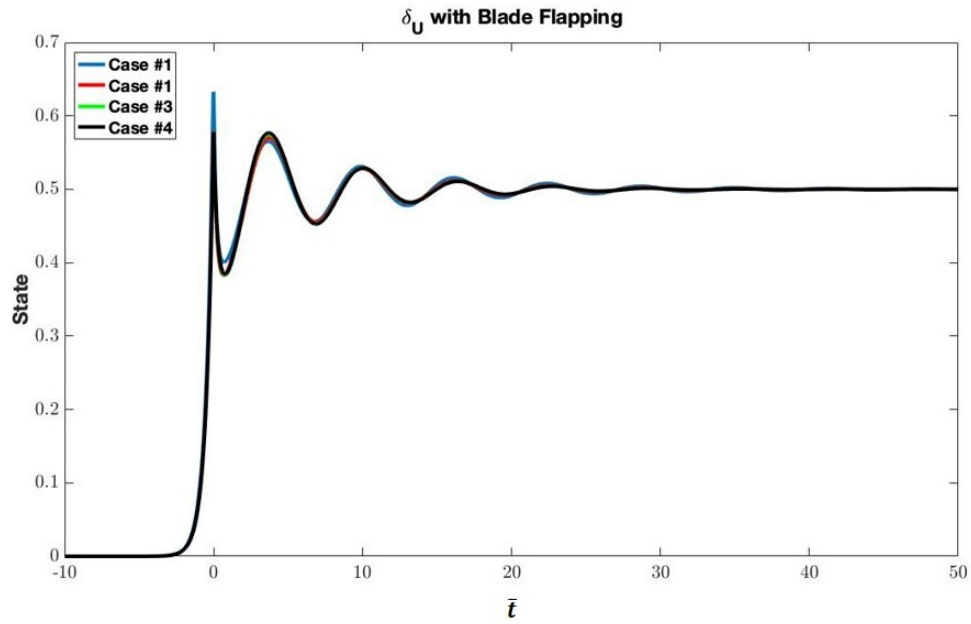
Figure 3-18: δ_U profiles vs. $\bar{t}$ for system with blade flapping ($\gamma = 5$ and $p^2 = 1.08$)
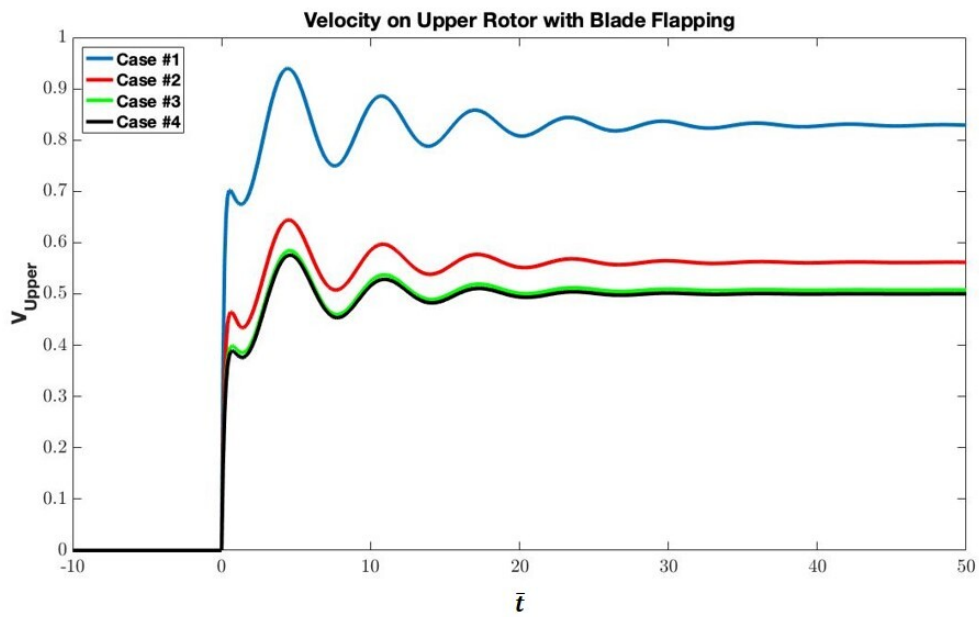
Figure 3-19: Nondimensional velocity on upper rotor vs. $\bar{t}$ for system with blade flapping ($\gamma = 5$ and $p^2 = 1.08$)
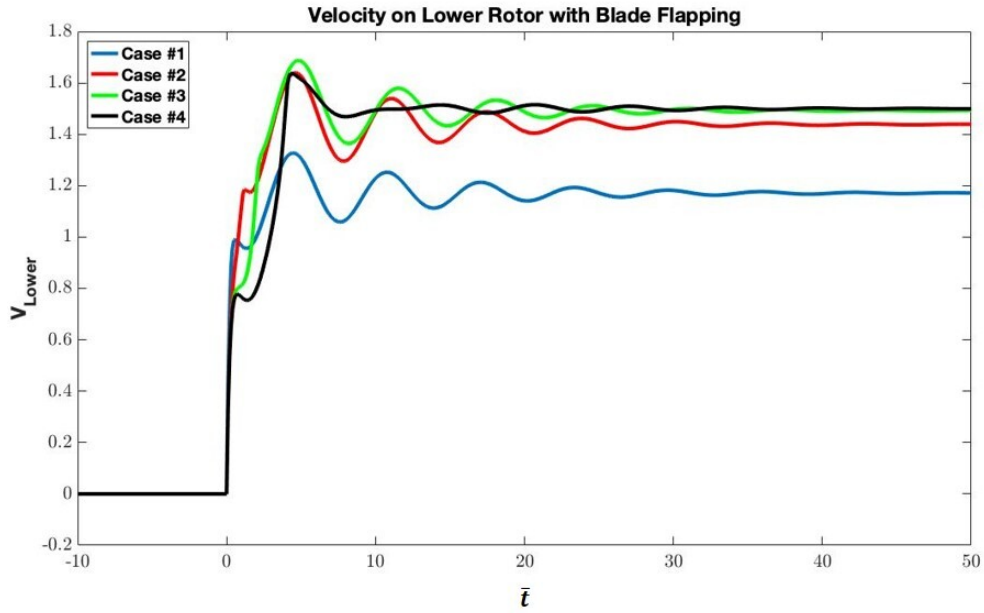
Figure 3-20: Nondimensional velocity on lower rotor vs. $\bar{t}$ for system with blade flapping ($\gamma = 5$ and $p^2 = 1.08$)
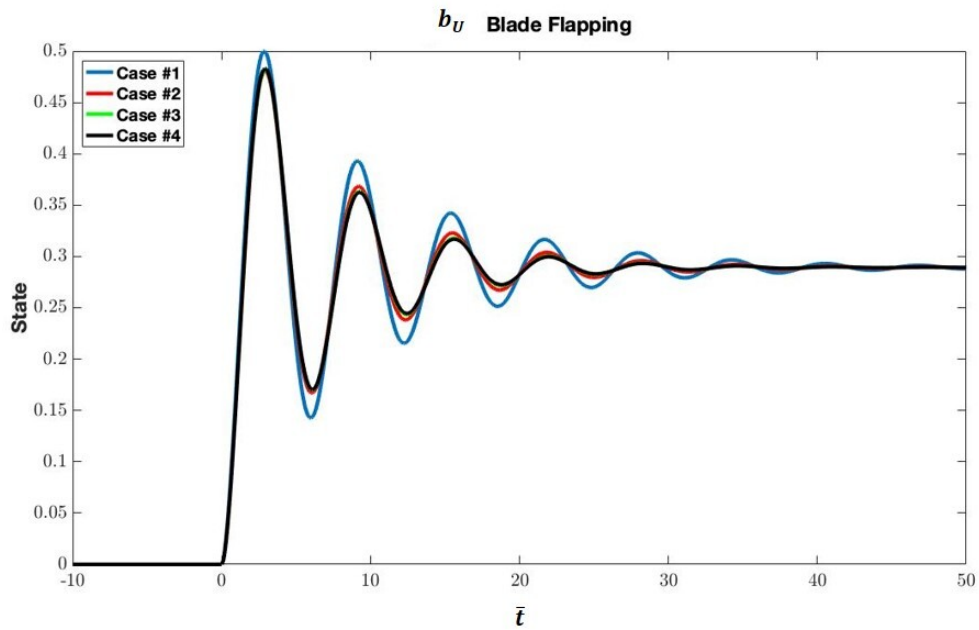
Figure 3-21: Upper rotor blade flapping state profiles vs. $\bar{t}$ ($\gamma = 5$ and $p^2 = 1.08$)
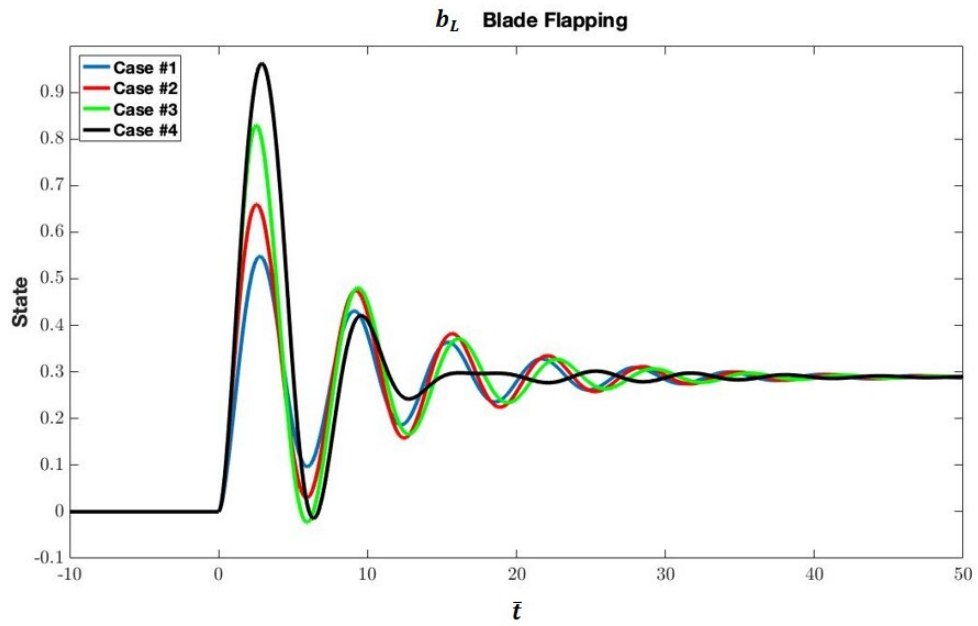
Figure 3-22: Lower rotor blade flapping state profiles vs. $\bar{t}$ ($\gamma = 5$ and $p^2 = 1.08$)

Chapter 4

Multiple Inflow States and an Infinite Number of Blades

4.1 Improved Representation of Governing Equations

In Chapter 3, a simple model for a coaxial rotor helicopter was developed with a single inflow state and simplified shape functions as a proof of concept for a system of coupled equations with adjoint variables and time delays. The simple model was developed based on the work of Morillo [11], Hsieh [12], Garcia-Duffy [13][45], and Fei [3], but was reduced in complexity to compare the time-marching and convolution solution methods with the closed form solution of a single lifting rotor helicopter. The model included simplified rotor feedback terms (k, h, and q) and neglected coefficients from the lift equation (σ, c, a, etc.). It also included a predefined shape function that is now be replaced by a more complete approach that includes Legendre functions. The transition from a single inflow state to multiple inflow states requires updates to the approach for initial and terminal conditions, for load sharing, and for the blade loading. The following sections discuss the updates and process of developing a more complete model, and the correlation to the previous simple model.

4.1.1 Improved Velocity Feedback Terms

To more accurately define the rotor interaction within the coaxial system, more inclusive feedback terms are developed. These are applicable for either a single inflow state or multiple inflow states, the latter of which is discussed in this chapter. For the model developed in this chapter, a solution with a single inflow state is a special case of the multiple inflow state case, which contains fewer equations and unknowns, but is generally less accurate. The simplified equations in chapter 3 for a single inflow state are not equivalent to a single inflow state solution based on this model.

The cross-coupling velocity terms, V_{UU}, V_{UL}, V_{LU}, and V_{LL} from Chapter 3 were developed as a function of nondimensional time and rotor spacing (d). The previous terms are:

$$V_{UU}\left(d,\bar{t}\right) = \alpha_U\left(\bar{t}\right)(0) \tag{4.1}$$

$$V_{UL}\left(d,\bar{t}\right) = \alpha_L\left(\bar{t}\right)(-\mathrm{d}) \tag{4.2}$$

$$V_{LU}\left(d,\bar{t}\right) = \alpha_U\left(\bar{t}-\bar{d}\right)(0) + \delta_U\left(\bar{t}-\bar{d}\right)(0) - \delta_U\left(\bar{t}\right)(-d) \tag{4.3}$$

$$V_{LL}\left(d,t\right) = \alpha_L\left(\bar{t}\right)(0) \tag{4.4}$$

where the previous pressure potential (and shape function) was:

$$\Phi\left(z\right) = e^{-\lambda z}$$

The transition to the multiple inflow state formulation is completed, in part, by a change from the previous notional shape function to the Legendre functions utilized by Pitt [5]. Therefore, the pressure potentials are now those of the Pitt-Peters model:

$$\Phi_n^{0c} = \overline{P}_n^0\left(\nu\right)\overline{Q}_n^0\left(i\eta\right) \tag{4.5}$$

$$\Phi_n^{mc} = \overline{P}_n^m (\nu) \overline{Q}_n^m (i\eta) \cos (m\psi) \tag{4.6}$$

$$\Phi_n^{ms} = \overline{P}_n^m (\nu) \overline{Q}_n^m (i\eta) \sin (m\psi) \tag{4.7}$$

Here, $\overline{P}_n^m$ are normalized Legendre functions of the 1st kind, $\overline{Q}_n^m$ are normalized Legendre functions of the 2nd kind, and ν, η, and $\overline{\psi}$ are ellipsoidal coordinates. In chapter 3, Φ was only a function of z, the distance above or below the rotor. Here, the Legendre functions Φ_n^{mc} and Φ_n^{ms} depend on the exact location off the velocity in three-dimensional space, represented through ellipsoidal coordinates. For this chapter we will only use Eq. 4.5 because we only study the 0th harmonic terms for a system with an infinite number of blades. Generally, the number of harmonics is chosen to be an integer multiple of the number of blades. For an infinite number of blades, only the 0th harmonic can be used.

The next step is to determine the pressure potential on the disk—previously $\Phi(0)$—and off the disk—previously $\Phi(d)$. From the ellipsoidal coordinates illustrated in Appendix A, it can be seen that on the rotor disk ($z = 0$) that $\eta = 0$ and ν varies with location on the disk. Thus, the pressure potential on the disk is:

$$\Phi_n^{0c} = \overline{P}_n^0 (\nu) \overline{Q}_n^0 (0i) \tag{4.8}$$

where it can be shown that $\overline{Q}_n^m (0i) = 1$ and therefore

$$\Phi_n^{0c} = \overline{P}_n^0 (\nu) \tag{4.9}$$

For the off-disk case, where $z < 0$ (above the disk), η and ν both vary and are dependent on location, thus

$$\Phi_n^{0c} = \overline{P}_n^0 (\nu) \overline{Q}_n^0 (i\eta) \tag{4.10}$$

The cross-coupling velocity components are nondimensionalized to put for the state variables in nondimensional form. The nondimensional cross-coupling velocity components are found

through the relationship:

$$\overline{V}_{UU} = \frac{V_{UU}}{\Omega R}; \overline{V}_{LU} = \frac{V_{LU}}{\Omega R}; \overline{V}_{UL} = \frac{V_{UL}}{\Omega R}; \overline{V}_{LL} = \frac{V_{LL}}{\Omega R} \tag{4.11}$$

Therefore, substitution of Eqs. 4.9 and 4.10 into the nondimensional cross-coupling velocity equations yields:

$$\overline{V}_{UU}\left(\bar{t}, \nu, \eta, \psi_{q,U}\right) = \sum \{\alpha_n^m(\bar{t})\}_U \overline{P}_n^m\left(\nu_{on}\right) \cos\left(m\psi_{q,U}\right) \tag{4.12}$$

$$\overline{V}_{LL}\left(\bar{t}, \nu, \eta, \psi_{q,L}\right) = \sum \{\alpha_n^m(\bar{t})\}_L \overline{P}_n^m\left(\nu_{on}\right) \cos\left(m\psi_{q,L}\right) \tag{4.13}$$

$$\overline{V}_{UL}\left(\bar{t}, \nu, \eta, \psi_{q,U}\right) = \sum \{\alpha_n^m(\bar{t})\}_L \overline{P}_n^m\left(\nu_{off}\right) \overline{Q}_n^m\left(i\eta_{off}\right) \cos\left(m\psi_{q,U}\right) \tag{4.14}$$

$$\overline{V}_{LU}\left(\bar{t}, \nu, \eta, \psi_L\right) = \overline{V}\left(\bar{t} - \bar{d}, \nu, 0, \psi_L\right)$$
$$+ \overline{V}^*\left(\bar{t} - \bar{d}, \nu, 0, \psi_L^*\right) - \overline{V}^*\left(\bar{t}, \nu, \eta, \psi_L^*\right) \tag{4.15}$$

where V^* is the adjoint velocity. The adjoint velocity contains co-state terms. For example, the adjoint velocity above the disk:

$$\overline{V}^*\left(\bar{t}, \nu, \eta, \psi_L\right) = \sum \delta_n^m\left(\bar{t}\right) \overline{P}_n^m\left(\nu_{off}\right) \overline{Q}_n^m\left(i\eta_{off}\right) \cos\left(m\psi_L^*\right) \tag{4.16}$$

Therefore, the velocity on the lower rotor caused by the upper rotor is:

$$\overline{V}_{LU}\left(\bar{t}, \nu, \eta, \psi_{q,L}\right) = \sum \{\alpha_n^m(\bar{t} - \bar{d})\}_U \overline{P}_n^m\left(\nu_{on}\right) \cos\left(m\psi_{q,L}\right)$$
$$+ \sum \{\delta_n^m(\bar{t} - \bar{d})\}_L \overline{P}_n^m\left(\nu_{on}\right) \cos\left(m\psi_{q,L}^*\right)$$
$$+ \sum \{\delta_n^m(\bar{t})\}_L \overline{P}_n^m\left(\nu_{off}\right) \overline{Q}_n^m\left(i\eta_{off}\right) \cos\left(m\psi_{q,L}^*\right) \tag{4.17}$$

4.1.2 Lift Equations

To this point the pressure distribution, τ_n^m, has been significantly simplified in several aspects. Previously, the pitch angles of the rotors, θ_U and θ_L, were applied as step inputs of varying

magnitude, dependent only on rotor spacing. In addition, each "pitch angle" absorbed several coefficients, including the rotor solidity (σ) and the slope of the lift curve (a). Through blade element theory, we now discuss the formation of the new τ_n^m in terms of explicit rotor variables and expand to exactly define the inflow feedback. The pressure distribution in terms of blade loading (lifting force) is more accurately represented as:

$$\left\{\tau_n^{0c}\right\}_k = \frac{1}{4\pi} \sum_{q=1}^{Q} \left[\int_0^1 \frac{L_q, k}{\rho \Omega^2 R^3} \phi_n^0(\bar{r}) \, d\bar{r}\right] \tag{4.18}$$

$$\left\{\tau_n^{mc}\right\}_k = \frac{1}{2\pi} \sum_{q=1}^{Q} \left[\int_0^1 \frac{L_q, k}{\rho \Omega^2 R^3} \phi_n^m(\bar{r}) \, d\bar{r}\right] \cos\left(m\psi_{q,k}\right) \tag{4.19}$$

$$\left\{\tau_n^{ms}\right\}_k = \frac{1}{2\pi} \sum_{q=1}^{Q} \left[\int_0^1 \frac{L_q, k}{\rho \Omega^2 R^3} \phi_n^m(\bar{r}) \, d\bar{r}\right] \sin\left(m\psi_{q,k}\right) \tag{4.20}$$

where Q is the number of blades, L_q is the lift on blade q, ρ is the density of the fluid (air), R is the rotor diameter, Ω is the rotor speed, $\bar{r}$ is the nondimensional radial coordinate r/R, and ϕ_n^0 is the radial expansion shape function. These pressure distributions are from the Peters-He model [9]. For this chapter, we will derive the new pressure distributions for the τ_n^{0c} case, as it is the only one that applies for an infinite number of blades. The other two will be discussed in the next chapter for a system with a finite number of blades.

Previously for a single inflow state, it was accepted that the lift on the upper and lower rotor were equivalent to the pressure distribution such that:

$$\tau_U = F_U = \ \theta_U - kV_{UU} - hV_{UL} \tag{4.21}$$

$$\tau_L = F_L = \ \theta_L - kV_{LL} - hV_{LU} \tag{4.22}$$

However, as shown in Eqs. 4.18-4.20 above, the lift force and pressure distributions are no longer directly equivalent and a more complex relationship exists. From blade element

theory, the lift on a rotor is represented as:

$$L_{q,k}dr = dF_1 = \frac{1}{2}\rho ac \left[U_{T,k}{}^2 \theta_{q,k} - U_{P,k}U_{T,k} \right] dr \qquad (4.23)$$

In this equation, c is the chord length, a is the slope of the lift curve, $U_{T,k}$ represents the tangential velocity component on the k-th rotor, and $U_{P,k}$ represents the perpendicular velocity component on the k-th rotor. Figure 4-1 illustrates the components of velocity and lift for an air foil with pitch angle θ.
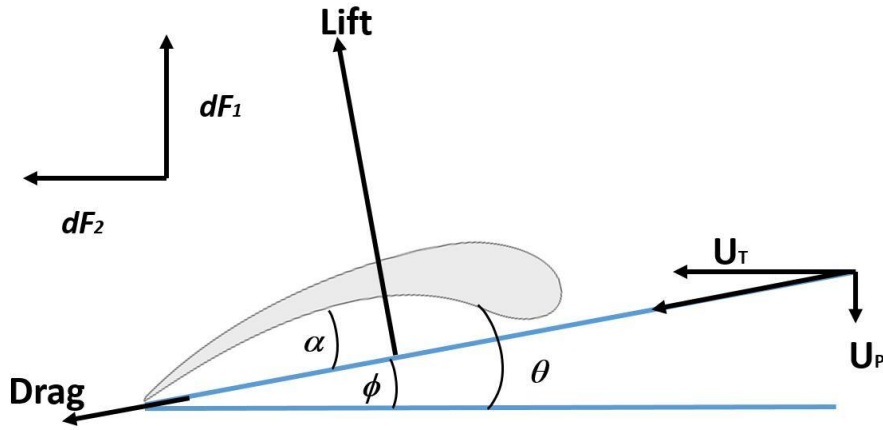
Figure 4-1: Velocity components on rotor blade cross-section

$U_{T,k}$ is a function of the radius of the rotor (r) and the radial velocity (Ω), such that:

$$U_{T,k} = \Omega r \qquad (4.24)$$

The velocity perpendicular to the rotor disk is related to the state equations and through the rotor feedback terms. The representations for the upper and lower rotors are as follows:

$$U_{P,U} = V_{UU} + V_{UL} \qquad (4.25)$$

$$U_{P,L} = V_{LL} + V_{LU} \qquad (4.26)$$

61

Substitution of Eqs. 4.24-4.26 into Eq. 4.23 yields:

$$L_{q,U} = \frac{1}{2}\rho ac \left[\theta_{q,U}\Omega^2 r^2 - \Omega r V_{UU} - \Omega r V_{UL}\right] \tag{4.27}$$

$$L_{q,L} = \frac{1}{2}\rho ac \left[\theta_{q,L}\Omega^2 r^2 - \Omega r V_{LL} - \Omega r V_{LU}\right] \tag{4.28}$$

To further simplify these equations, we substitute the lift equations into Eq. 4.18 and nondimensionalize the components. In addition, we can drop the summation and replace it with a Q outside of the integral because the system contains and infinite number of blades and all blades are identical. From these we obtain:

$$\left\{\tau_j^{0c}\right\}_U = \frac{Q}{4\pi}\int_0^1 \frac{1}{2}\frac{ac}{R}\left[\theta_{q,U}\bar{r}^2 - \overline{V}_{UU}\bar{r} - \overline{V}_{UL}\bar{r}\right]\phi_j^0\left(\bar{r}\right)d\bar{r} \tag{4.29}$$

$$\left\{\tau_j^{0c}\right\}_L = \frac{Q}{4\pi}\int_0^1 \frac{1}{2}\frac{ac}{R}\left[\theta_{q,L}\bar{r}^2 - \overline{V}_{UU}\bar{r} - \overline{V}_{UL}\bar{r}\right]\phi_j^0\left(\bar{r}\right)d\bar{r} \tag{4.30}$$

The final reorganization before integrating the right side of the equations is to pull the constant terms to the front and substitute for the rotor solidity (σ):

$$\sigma = \frac{Qc}{\pi R} \tag{4.31}$$

to obtain $\left\{\tau_j^{0c}\right\}_U$ and $\left\{\tau_j^{0c}\right\}_U$:

$$\left\{\tau_j^{0c}\right\}_U = \frac{\sigma a}{8}\int_0^1 \left[\theta_{q,U}\bar{r}^2 - \overline{V}_{UU}\bar{r} - \overline{V}_{UL}\bar{r}\right]\phi_j^0\left(\bar{r}\right)d\bar{\bar{r}} \tag{4.32}$$

$$\left\{\tau_j^{0c}\right\}_L = \frac{\sigma a}{8}\int_0^1 \left[\theta_{q,L}\bar{r}^2 - \overline{V}_{UU}\bar{r} - \overline{V}_{UL}\bar{r}\right]\phi_j^0\left(\bar{r}\right)d\bar{\bar{r}} \tag{4.33}$$

The rotor solidity must be user defined in this model due to the infinite number of blades (c would be infinitely small and $Q = \infty$). It is desired to find the solution in terms of the ellipsoidal coordinate system. The general relationship for the change of coordinates is:

$$\nu^2 = 1 - \bar{r}^2 \tag{4.34}$$

62

$$\nu d\nu = -\bar{r}d\bar{r} \tag{4.35}$$

From this relationship we find that the new bounds of the integral are:

$$at\ \bar{r} = 0,\ \nu = 1$$

$$at\ \bar{r} = 1,\ \nu = 0$$

These bounds are flipped to put the greater value as the upper limit. ϕ_j^r can now be defined in terms of ν as:

$$\phi_j^r(\bar{r}) = \frac{1}{\nu}\overline{P}_j^r(\nu) \tag{4.36}$$

Substitution of all of these relationships into Eqs. 4.32 and 4.33 yields:

$$\left\{\tau_j^{0c}\right\}_U = \frac{\sigma a}{8}\int_0^1\left[\theta_{q,U}\overline{P}_j^r(\nu)\ \sqrt{1-\nu^2} - \overline{V}_{UU}\overline{P}_j^r(\nu) - \overline{V}_{UL}\overline{P}_j^r(\nu)\right]d\nu \tag{4.37}$$

$$\left\{\tau_j^{0c}\right\}_L = \frac{\sigma a}{8}\int_0^1\left[\theta_{q,L}\overline{P}_j^r(\nu)\ \sqrt{1-\nu^2} - \overline{V}_{LL}\overline{P}_j^r(\nu) - \overline{V}_{LU}\overline{P}_j^r(\nu)\right]d\nu \tag{4.38}$$

The cross-coupling velocity terms in Eqs. 4.12-4.15 are substituted in to form:

$$\left\{\tau_j^{0c}\right\}_U = \frac{\sigma a}{8}\int_0^1\left[\theta_{q,U}\overline{P}_j^0(\nu_{on})\ \sqrt{1-\nu^2}\right.$$

$$- \sum\left\{\alpha_j^0(\bar{t})\right\}_U\overline{P}_j^0(\nu_{on})\,\overline{P}_n^0(\nu_{on}) \tag{4.39}$$

$$\left.- \sum\left\{\alpha_j^0(\bar{t})\right\}_L(t)\,\overline{P}_j^0(\nu_{off})\,\overline{Q}_j^0\left(i\eta_{off}\right)\overline{P}_n^0(\nu_{on})\right]d\nu$$

$$\left\{\tau_j^{0c}\right\}_L = \frac{\sigma a}{8} \int_0^1 \left[\theta_{q,L} \overline{P}_j^0 (\nu) \sqrt{1-\nu^2} \right.$$

$$- \sum \left\{\alpha_j^0 (\bar{t})\right\}_L \overline{P}_j^0 (\nu_{on}) \overline{P}_n^0 (\nu_{on})$$

$$- \sum \left\{\alpha_j^0 (\bar{t} - \bar{d})\right\}_U \overline{P}_j^0 (\nu_{on}) \overline{P}_n^0 (\nu_{on}) \tag{4.40}$$

$$- \sum \left\{\delta_j^0 (\bar{t} - \bar{d})\right\}_U \overline{P}_j^0 (\nu_{on}) \overline{P}_n^0 (\nu_{on})$$

$$\left. + \sum \left\{\delta_j^0 (\bar{t})\right\}_U \overline{P}_j^0 (\nu_{off}) \overline{Q}_j^0 \left(i\eta_{off}\right) \overline{P}_n^0 (\nu_{on}) \right] d\nu$$

The integrals are then separated and the state and co-state variables can be brought outside because they are only a function of nondimensional time. Eqs. 4.39 and 4.40 then become:

$$\left\{\tau_j^{0c}\right\}_U = \frac{\sigma a}{8} \left[\theta_{q,U} \int_0^1 \left[\overline{P}_j^0 (\nu) \sqrt{1-\nu^2} \right] d\nu \right.$$

$$- \sum \left\{\alpha_j^0 (\bar{t})\right\}_U \int_0^1 \left[\overline{P}_j^0 (\nu_{on}) \overline{P}_n^0 (\nu_{on}) \right] d\nu \tag{4.41}$$

$$\left. - \sum \left\{\alpha_j^0 (\bar{t})\right\}_L \int_0^1 \left[\overline{P}_j^0 (\nu_{off}) \overline{Q}_j^0 \left(i\eta_{off}\right) \overline{P}_n^0 (\nu_{on}) \right] d\nu \right]$$

$$\left\{\tau_j^{0c}\right\}_L = \frac{\sigma a}{8} \left[\theta_{q,L} \int_0^1 \left[\overline{P}_j^0 (\nu_{on}) \sqrt{1-\nu^2} \right] d\nu \right.$$

$$- \sum \left\{\alpha_j^0 (\bar{t})\right\}_L \int_0^1 \left[\overline{P}_j^0 (\nu_{on}) \overline{P}_n^0 (\nu_{on}) \right] d\nu$$

$$- \sum \left\{\alpha_j^0 (\bar{t} - \bar{d})\right\}_U \int_0^1 [\overline{P}_j^0 (\nu_{on}) \overline{P}_n^0 (\nu_{on})] d\nu \tag{4.42}$$

$$- \sum \left\{\delta_j^0 (\bar{t} - \bar{d})\right\}_U \int_0^1 [\overline{P}_j^0 (\nu_{on}) \overline{P}_n^0 (\nu_{on})] d\nu$$

$$\left. + \sum \left\{\delta_j^0 (\bar{t})\right\}_U \int_0^1 [\overline{P}_j^0 (\nu_{off}) \overline{Q}_j^0 \left(i\eta_{off}\right) \overline{P}_n^0 (\nu_{on})] d\nu \right]$$

From these equations, we notice three common integrals of Legendre functions. We represent these integrals in matrix form as follows:

$$\left\{A_j^r\right\} = \int_0^1 \sqrt{1 - \nu_{on}^2}\,\overline{P}_j^r\left(\nu_{on}\right) d\nu \tag{4.43}$$

$$\left[B_{nj}^{mr}\right] = \int_0^1 \overline{P}_n^m\left(\nu_{on}\right)\overline{P}_j^r\left(\nu_{on}\right) d\nu \tag{4.44}$$

$$\left[C_{nj}^{mr}\right] = \int_0^1 \overline{P}_n^m\left(\nu_{on}\right)\overline{P}_j^r\left(\nu_{off}\right)\overline{Q}_j^r\left(i\eta_{off}\right) d\nu \tag{4.45}$$

$\left\{A_n^m\right\}$ represents the pitch coupling terms, $\left[B_{nj}^{mr}\right]$ are the on-disk inflow coupling term, and $\left[C_{nj}^{mr}\right]$ are the off-disk inflow coupling term. Now, the pressure distribution for the upper and lower rotors are represented as:

$$\left\{\tau_j^{0c}\right\}_U = \frac{\sigma a}{8}\left[\left\{A_j^0\right\}\theta_{q,U} - [B_{nj}^{00}]\left\{\alpha_j^0\left(\bar{t}\right)\right\}_U - [C_{nj}^{00}]\left\{\alpha_j^0\left(\bar{t}\right)\right\}_L\right] \tag{4.46}$$

$$
\begin{aligned}
\left\{\tau_j^{0c}\right\}_L = \frac{\sigma a}{8}\Big[& \left\{A_j^0\right\}\theta_{q,L} - [B_{nj}^{00}]\left\{\alpha_j^0\left(\bar{t}\right)\right\}_L - [B_{nj}^{00}]\left\{\alpha_j^0\left(\bar{t} - \bar{d}\right)\right\}_U \\
& - [B_{nj}^{00}]\left\{\delta_j^0\left(\bar{t} - \bar{d}\right)\right\}_U + [C_{nj}^{00}]\left\{\delta_j^0\left(\bar{t}\right)\right\}_U\Big]
\end{aligned}
\tag{4.47}
$$

The summations drop out of the equations and are replaced by the product of the new coupling matrices and state and co-state column matrices.

The final forms of the state equations can be represented as follows:

$$
\begin{aligned}
\{\overset{*}{\alpha}_j^0\}_U + v\,[M]^{-1}[D]\{\alpha_j^0\left(\bar{t}\right)\}_U = \frac{\sigma a}{8}\,[M]^{-1}[D]\Big(& \left\{A_j^0\right\}\theta_{q,U} \\
& - \left[B_{nj}^{00}\right]\left\{\alpha_j^0\left(\bar{t}\right)\right\}_L - \left[C_{nj}^{00}\right]\left\{\alpha_j^0\left(\bar{t}\right)\right\}_L\Big)
\end{aligned}
\tag{4.48}
$$

$$\{\overset{*0}{\alpha_j}\}_L + \upsilon[M]^{-1}[D]\{\alpha_j^0(\bar{t})\}_L = \frac{\sigma a}{8}\left(\{A_j^0\}\theta_{q,L} - [B_{nj}^{00}]\{\alpha_j^0(\bar{t})\}_L\right.$$

$$\left. - [B_{nj}^{00}]\{\alpha_j^0(\bar{t}-\bar{d})\}_U - [B_{nj}^{00}]\{\delta_j^0(\bar{t}-\bar{d})\}_U + [C_{nj}^{00}]\{\delta_j^0(\bar{t})\}_U\right) \tag{4.49}$$

$$-\{\overset{*0}{\delta_j}\}_U + \upsilon[M]^{-1}[D]\{\delta_j^0(\bar{t})\}_U = \frac{\sigma a}{8}[M]^{-1}[D]\left(\{A_n^0\}\theta_U\right.$$

$$\left. - [B_{nj}^{00}]\{\alpha_j^0(\bar{t})\}_L - [C_{nj}^{00}]\{\alpha_j^0(\bar{t})\}_L\right) \tag{4.50}$$

4.1.3   Blade Flapping

To include blade flapping in the multiple inflow state solution, the following set of equations must be introduced for each blade on both the upper and lower rotors:

$$I_y\ddot{b}_{q,k} + \left(I_y\Omega^2 + \kappa_\beta\right)b_{q,k} = \int_0^L L_{q,k}rdr \tag{4.51}$$

where b_k is the blade flapping state variable for the k-th blade, I_y is the flapping inertia of the blade, and κ_β is the root spring. In addition to solving Eq. 4.51, $L_{q,k}$ must be updated to include blade flapping terms. Therefore, the perpendicular velocity components from Eqs. 4.25 and 4.26 must be updated to include blade flapping terms. The new U_p components with blade flapping are:

$$U_{P,U} = V_{UU} + V_{UL} + \{\dot{b}\}_{q,U}r \tag{4.52}$$

$$U_{P,L} = V_{LL} + V_{LU} + \{\dot{b}\}_{q,L}r \tag{4.53}$$

The lift equations for each rotor are now:

$$L_{q,U} = \frac{1}{2}\rho ac\left[\theta_{q,U}\Omega^2r^2 - \Omega rV_{UU} - \Omega rV_{UL} - \{\dot{b}\}_{q,U}\Omega r^2\right] \tag{4.54}$$

$$L_{q,L} = \frac{1}{2}\rho ac\left[\theta_{q,L}\Omega^2r^2 - \Omega rV_{LL} - \Omega rV_{LU} - \{\dot{b}\}_{q,L}\Omega r^2\right] \tag{4.55}$$

66

Converting the terms to nondimensional form, and solving Eq. 4.51 for blade flapping of the upper and lower rotors, it is found that:

$$\overset{**}{b}_{q,U} + p^2\{b\,(\bar{t})\}_{q,U} = \frac{\gamma}{2}\left(\frac{1}{4}\theta_{q,U} - \left\{\widetilde{B}_n^0\right\}^T\left\{\alpha_n^0\,(\bar{t})\right\}_U - \left\{\widetilde{C}_n^0\right\}^T\left\{\alpha_n^0\,(\bar{t})\right\}_L - \frac{1}{4}\overset{*}{b}_{q,U}\right) \quad (4.56)$$

$$\overset{**}{b}_{q,L} + p^2\{b\,(\bar{t})\}_{q,L} = \frac{\gamma}{2}\left(\frac{1}{4}\theta_{q,L} - \{\widetilde{B}_n^0\}^T\left\{\alpha_n^0\,(\bar{t})\right\}_L - \left\{\widetilde{B}_n^0\right\}^T\left\{\alpha_n^0\,(\bar{t}-\bar{d})\right\}_U\right.$$
$$\left. - \left\{\widetilde{B}_n^0\right\}^T\left\{\delta_n^0\,(\bar{t}-\bar{d})\right\}_U + \left\{\widetilde{C}_n^0\right\}^T\left\{\delta_n^0\,(\bar{t})\right\}_U - \frac{1}{4}\overset{*}{b}_{q,L}\right) \quad (4.57)$$

In these equations, p is the flapping frequency and γ is the Lock number, both of which are equivalent to:

$$p^2 = \left(1 + \frac{\kappa_\beta}{I_y\Omega^2}\right) \quad (4.58)$$

$$\gamma = \frac{\rho acR^4}{I_y} \quad (4.59)$$

The coupling terms in Eqs. 4.56 and 4.57 are:

$$\left\{\widetilde{B}_j^r\right\} = \int_0^1 \nu_{on}\sqrt{1 - \nu_{on}^2}\,\overline{P}_j^r\,(\nu_{on})\,d\nu \quad (4.60)$$

$$\left\{\widetilde{C}_j^r\right\} = \int_0^1 \nu_{off}\sqrt{1 - \nu_{off}^2}\,\overline{P}_j^r\,(\nu_{off})\,\overline{Q}_j^r\,(i\eta_{off})\,d\nu \quad (4.61)$$

Finally, the state equations are updated to reflect the updated lift and are as follows:

$$\left\{\overset{*}{\alpha}_j^0\right\}_U + \upsilon\,[M]^{-1}[D]\left\{\alpha_j^0\,(\bar{t})\right\}_U = \frac{\sigma a}{8}\,[M]^{-1}[D]\left(\left\{A_j^0\right\}\theta_{q,U}\right.$$
$$\left. - \left[B_{nj}^{00}\right]\left\{\alpha_j^0\,(\bar{t})\right\}_U - \left[C_{nj}^{00}\right]\left\{\alpha_j^0\,(\bar{t})\right\}_L - \left\{A_j^0\right\}\overset{*}{b}_{q,U}\right) \quad (4.62)$$

$$\left\{\overset{*}{\alpha}_j^0\right\}_L + \upsilon[M]^{-1}[D]\left\{\alpha_j^0\,(\bar{t})\right\}_L = \frac{\sigma a}{8}\left(\{A_j^0\}\theta_{q,L} - [B_{nj}^{00}]\left\{\alpha_j^0\,(\bar{t})\right\}_L\right.$$
$$\left. - [B_{nj}^{00}]\left\{\alpha_j^0\,(\bar{t}-\bar{d})\right\}_U - [B_{nj}^{00}]\left\{\delta_j^0\,(\bar{t}-\bar{d})\right\}_U + [C_{nj}^{00}]\left\{\delta_j^0\,(\bar{t})\right\}_U - \{A_j^0\}\overset{*}{b}_{q,L}\right) \quad (4.63)$$

$$-\left\{\overset{*}{\delta^0_j}\right\}_U + \upsilon[M]^{-1}[D]\left\{\delta^0_j\left(\bar{t}\right)\right\}_U = \frac{\sigma a}{8}[M]^{-1}[D]\left(\left\{A^0_n\right\}\theta_{q,U}\right.$$

$$\left. - \left[B^{00}_{nj}\right]\left\{\alpha^0_j\left(\bar{t}\right)\right\}_L - \left[C^{00}_{nj}\right]\left\{\alpha^0_j\left(\bar{t}\right)\right\}_L - \left\{A^0_n\right\}\overset{*}{b}_{q,U}\right) \tag{4.64}$$

4.1.4 Initial and Terminal Conditions for Multiple Inflow States

The initial conditions for the state variables for multiple inflow states are similar to those for a single inflow state. All are zero. For the co-state terms, there are again multiple options for terminal conditions, which are similar to that of the single inflow state. The terminal conditions will again be referred to as the zero terminal condition and the steady-state terminal conditions. The results presented in this chapter use the steady-state terminal conditions. Velocity is independent of the terminal conditions, provided there are enough inflow states and a long enough nondimensional time is simulated to reach convergence.

The process of solving for the converged terminal condition is almost entirely the same as the load sharing process outlined in Appendix D. Therefore, it is not necessary to recompose the entire process. After the pitch angle θ_U of the upper rotor is determined from load sharing, it can be plugged back into:

$$\left\{\begin{array}{c} \left\{\delta^0_j\right\}_U \\ \left\{\delta^0_j\right\}_L \end{array}\right\} = [F]^{-1}[G]\left\{\begin{array}{c} \theta_{q,U} \\ \theta_{q,L} \end{array}\right\} \tag{4.65}$$

to find the terminal conditions. Equation 4.65 is the condensed form of:

$$\left\{\begin{array}{c} \left\{\delta^0_j\right\}_U \\ \left\{\delta^0_j\right\}_L \end{array}\right\} = \left[\begin{array}{cc} I + \frac{\sigma a}{8\upsilon}[B] & \frac{\sigma a}{8\upsilon}[C] \\ 2\frac{\sigma a}{8\upsilon}[B] - \frac{\sigma a}{8\upsilon}[C] & I + \frac{\sigma a}{8\upsilon}[B] \end{array}\right]^{-1}\left[\begin{array}{cc} \frac{\sigma a}{8}\{A\} & 0 \\ 0 & \frac{\sigma a}{8}\{A\} \end{array}\right]\left\{\begin{array}{c} \theta_{q,U} \\ \theta_{q,L} \end{array}\right\} \tag{4.66}$$

The steady-state value for δ^0_{1U}, α^0_{1U}, and α^0_{1L} should be equivalent to $\frac{\sqrt{3}}{4\nu}C_T$ for an equal load sharing case.

68

4.2 Numerical Illustrations of Multiple Inflow States without Blade Flapping

This section presents results for systems with multiple inflow states and illustrates the trends of general solutions when more inflow states are added. The processes presented will also vary the spacing between the two rotors and illustrate changes in the state/co-state profiles and the velocity profiles on the rotor disk. Outside of the variance in the number of inflow states and the rotor spacing, the only other adjustable parameters are σ, γ, p, υ, and C_T, which will not be varied in this work. The values selected for these parameters are $\sigma = 0.1$, $\gamma = 5$, $p^2 = 1.08$, $\upsilon = 0.01$, and $C_T = 0.01$. All graphs of velocity vs. nondimensional time occur at location $\bar{r} = 0.8$. In addition, all presented results are for systems with steady-state terminal conditions and utilize load sharing, therefore θ_U and θ_L vary with rotor spacing.

4.2.1 Velocity State and Co-state Variable Profiles

The development of the velocity state and co-state variable profiles depict several notable trends in relation to number of harmonics and rotor spacing. For these plots, equal load sharing is utilized, which results in the same steady-state value for the first odd state and co-state values ($\{\alpha_1^0\}_U = \{\alpha_1^0\}_L = \{\delta_1^0\}_U$), regardless of number of harmonics and rotor spacing. However, dynamic portions of the first odd profiles at small values of time vary with rotor spacing and number of harmonics. For this section, the overall trends of the state, co-state, and velocity profiles will be discussed along with the early dynamics and dynamics when the flow form the upper rotor hits the lower rotor.

Figures 4-2 to 4-7 illustrate the profile development for $\{\alpha_n^0\}_U$ state variables in arrangements of 2, 4, and 6 states and rotor spacings of $d = 0.2$ and $d = 1.0$. It is noticeable in all of the figures that the even inflow states converge to a steady-state value of zero, which was

expected because they are mass source terms. As was discussed earlier, $\{\alpha_1^0\}_U = \frac{1}{\nu}\frac{\sqrt{3}}{4}C_T$ at steady-state, which is depicted in Figs. 4-2 to 4-7. As more inflow states are added, it takes longer for the states to reach their steady-state values, as is evident in Figs. 4-3,4-4, 4-6, and 4-7. For the $\{\alpha_n^0\}_U$ state variables, smaller rotor spacings generally result in larger peaks in the early dynamics of the system. Increasing the number of states also impacts the early dynamics because all of the states are reacting to the inflow when the system starts up.

The $\{\alpha_n^0\}_L$ profiles in Figs. 4-8 to 4-13 demonstrate similar overall trends to the $\{\alpha_n^0\}_U$ profiles. However, the impact of when the flow from the upper rotor hits the lower rotor can be seen. In these plots the time delay is $\bar{d} = 2$ for a rotor spacing $d = 0.2$ and $\bar{d} = 10$ for a rotor spacing $d = 1.0$. Therefore, the change in dynamics due to the flow from the upper rotor hitting the lower rotor occurs at $\bar{t} = 2$ and $\bar{t} = 10$, respectively. For brevity, we will refer to the change in dynamics when the flow from the upper rotor hits the lower rotor as time-delay dynamics because they occur when $\bar{t} = \bar{d}$. For the $\{\alpha_n^0\}_L$ profiles with $d = 0.2$ rotor spacing in Figs. 4-8 to 4-10, it is difficult to see time-delay dynamics in the 2-state and 4-state results because the dynamics occur early in the profiles when the states are close to their steady-state values. However, for the 6-state profiles the time-delays are more evident because the profiles are much farther from steady-state. When $d = 1.0$ in Figs. 4-11 to 4-13, the time-delay dynamics are evident in the profiles for 2, 4, and 6 state solutions. These changes are more noticeable because they cause a change in direction for many of the profiles.

The development of the co-state profile is described by two different formats. First the time-delayed co-state profiles are shown in Figs. 4-14 to 4-19 and then the full co-state profiles developed after the entire simulation is run in Figs. 4-20 to 4-25. The former case are the

values used for the calculations with each time step. The purpose of the latter is to simply demonstrate how the profile develops when calculated over the entire time domain.

As is illustrated in Figs. 4-14 to 4-19, the time-delayed co-state, $\{\delta_n^0(\bar{t} - \bar{d})\}_U$, profiles change dynamically when $\bar{t} = \bar{d}$ and then decay to the steady-state value. These profiles vary with terminal conditions but will converge to the same steady-state value. The number of states has a significant impact on the profile development, especially prior to $\bar{t} = \bar{d}$. This part of the $\{\delta_n^0(\bar{t} - \bar{d})\}_U$ profile occurs at $\bar{t} < 0$, which contains no blade loading.

The co-state profiles in Figs. 4-20 to 4-25 provide a clearer illustration of how the time-delayed terms are formed and an overall picture of what the $\{\delta_n^0(\bar{t} - \bar{d})\}_U$ profiles would look like for larger rotor spacings. Rotor spacing itself has little impact on the shape of the $\{\delta_n^0\}_U$ profile. The full $\{\delta_n^0\}_U$ profile also demonstrates that co-states converge to zero as $\bar{t} \to -\infty$. It is worth noting that for a solution with more co-states, it takes longer to converge to zero as $\bar{t} \to -\infty$, but this does not impact the accuracy of the velocity profiles.
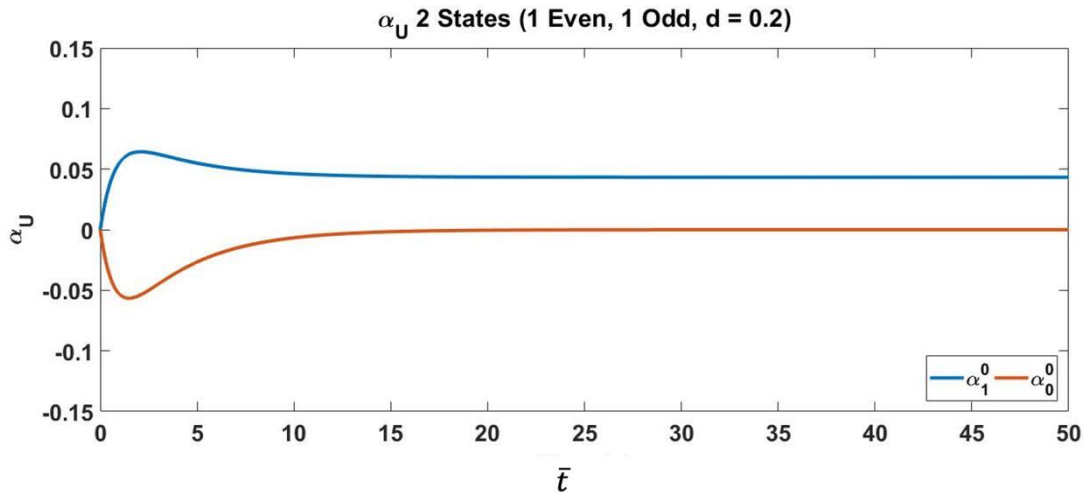
Figure 4-2: $\{\alpha_n^0\}_U$ state variable for 2 inflow states (1 even and 1 odd) with $d = 0.2$
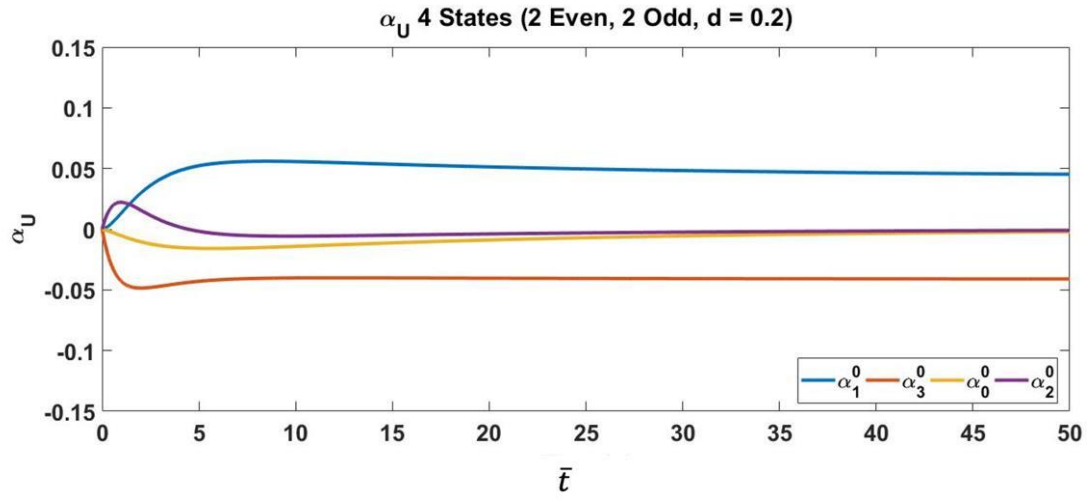
Figure 4-3: $\{\alpha_n^0\}_U$ state variable for 4 inflow states (2 even and 2 odd) with $d = 0.2$
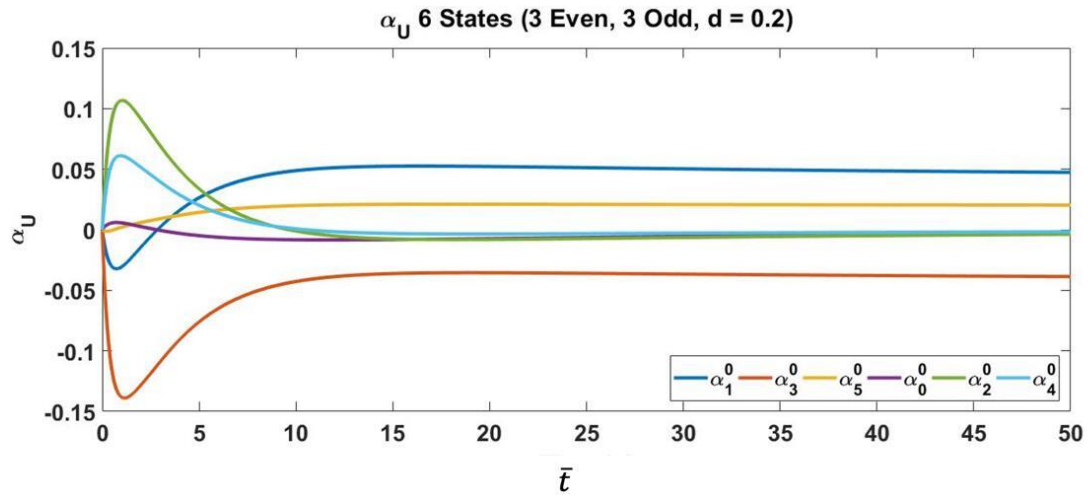
Figure 4-4: $\{\alpha_n^0\}_U$ state variable for 6 inflow states (3 even and 3 odd) with $d = 0.2$
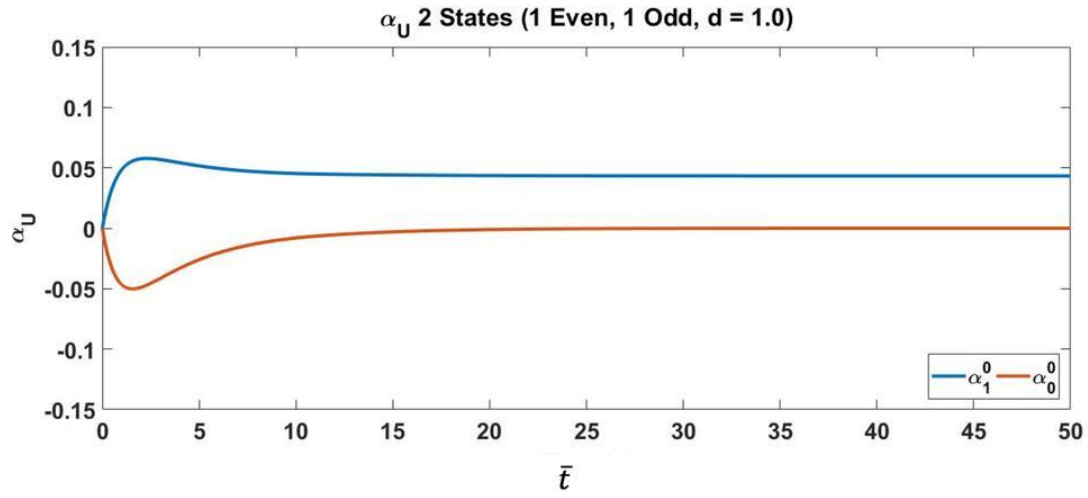
Figure 4-5: $\{\alpha_n^0\}_U$ state variable for 2 inflow states (1 even and 1 odd) with $d = 1.0$
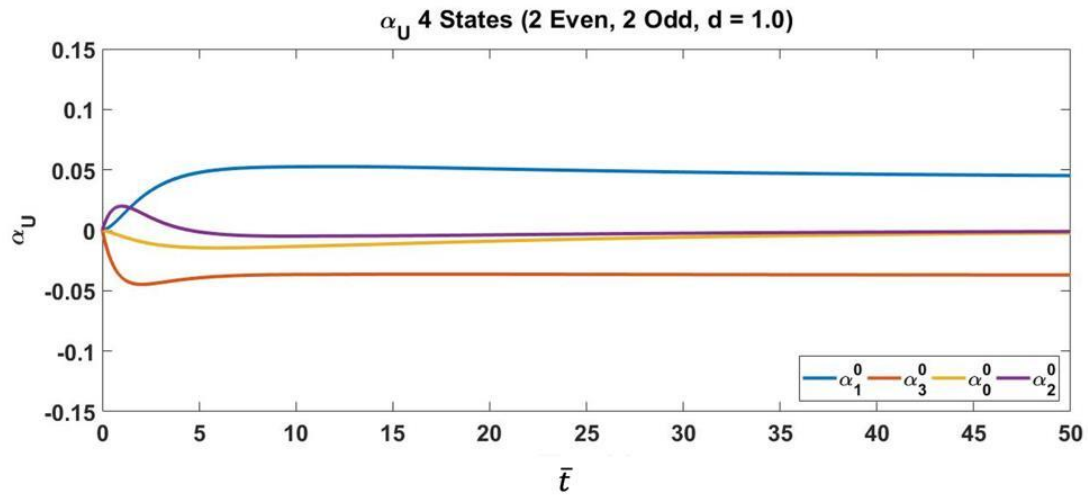
Figure 4-6: $\{\alpha_n^0\}_U$ state variable for 4 inflow states (2 even and 2 odd) with $d = 1.0$
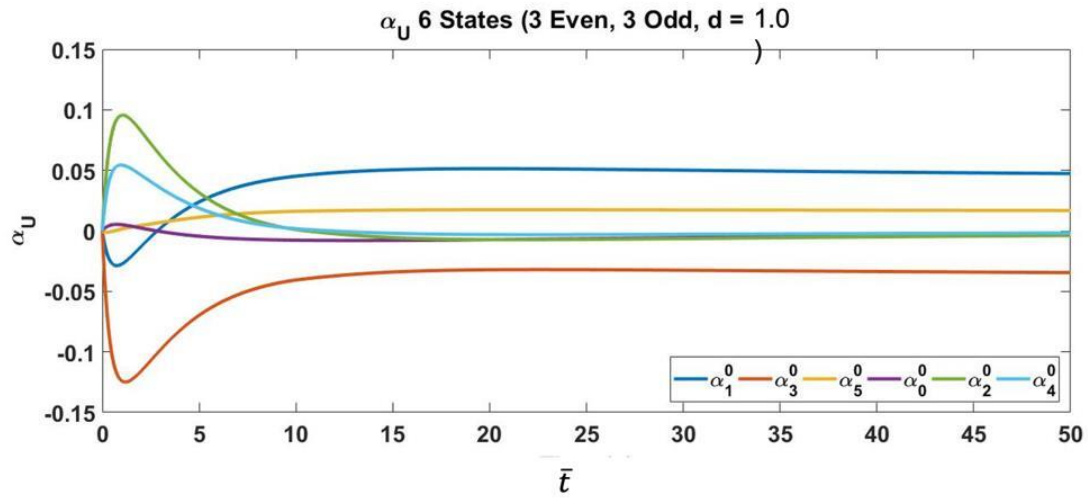
Figure 4-7: $\{\alpha_n^0\}_U$ state variable for 6 inflow states (3 even and 3 odd) with $d = 1.0$
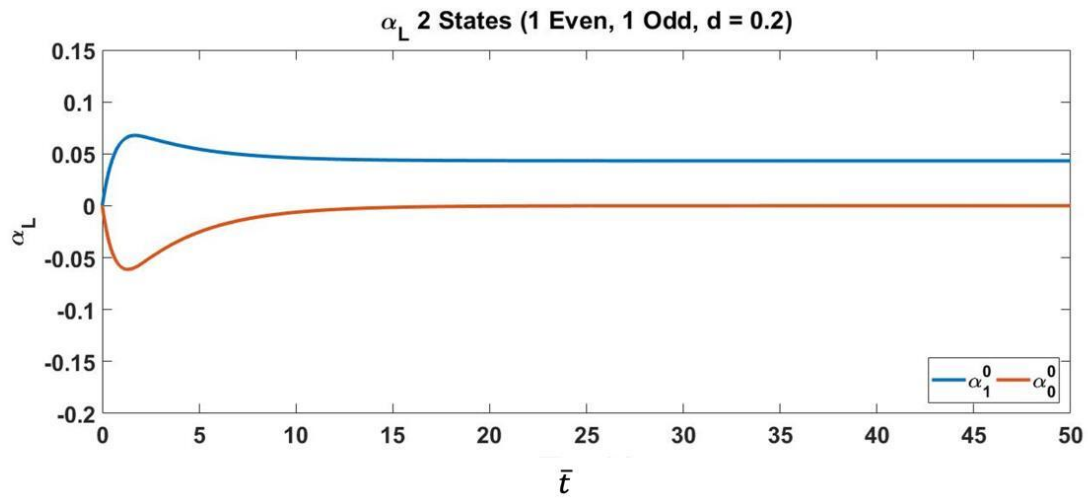
Figure 4-8: $\{\alpha_n^0\}_L$ state variable for 2 inflow states (1 even and 1 odd) with $d = 0.2$
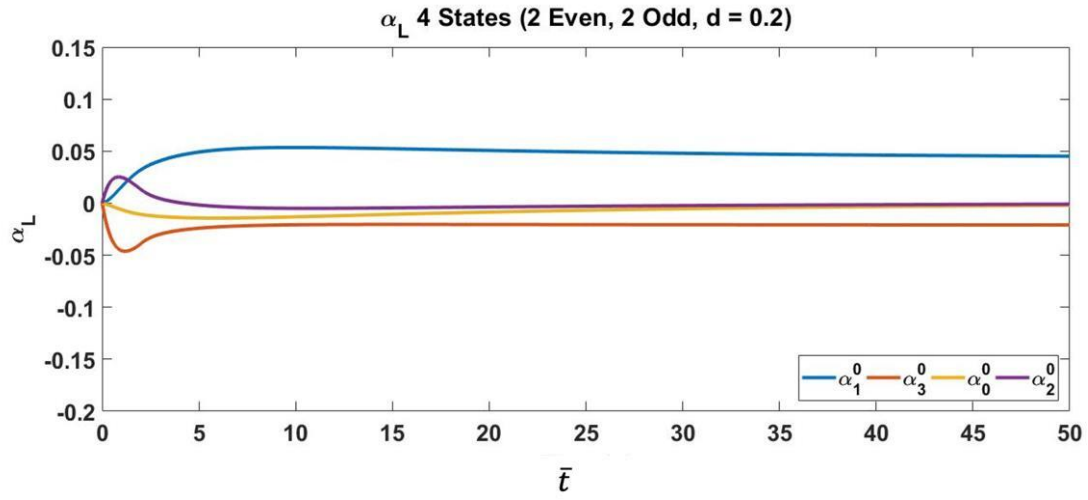
Figure 4-9: $\{\alpha_n^0\}_L$ state variable for 4 inflow states (2 even and 2 odd) with $d = 0.2$
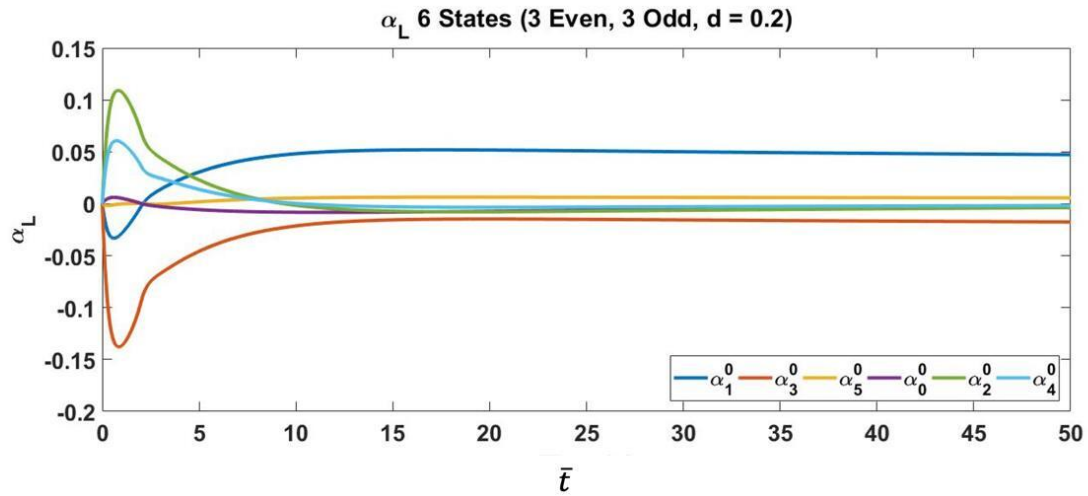
Figure 4-10: $\{\alpha_n^0\}_L$ state variable for 6 inflow states (3 even and 3 odd) with $d = 0.2$
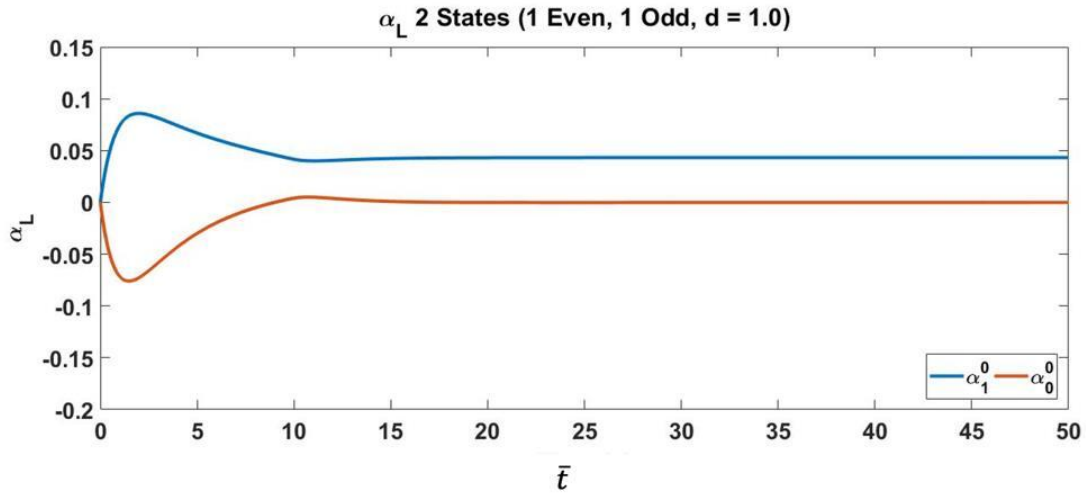
Figure 4-11: $\{\alpha_n^0\}_L$ state variable for 2 inflow states (1 even and 1 odd) with $d = 1.0$
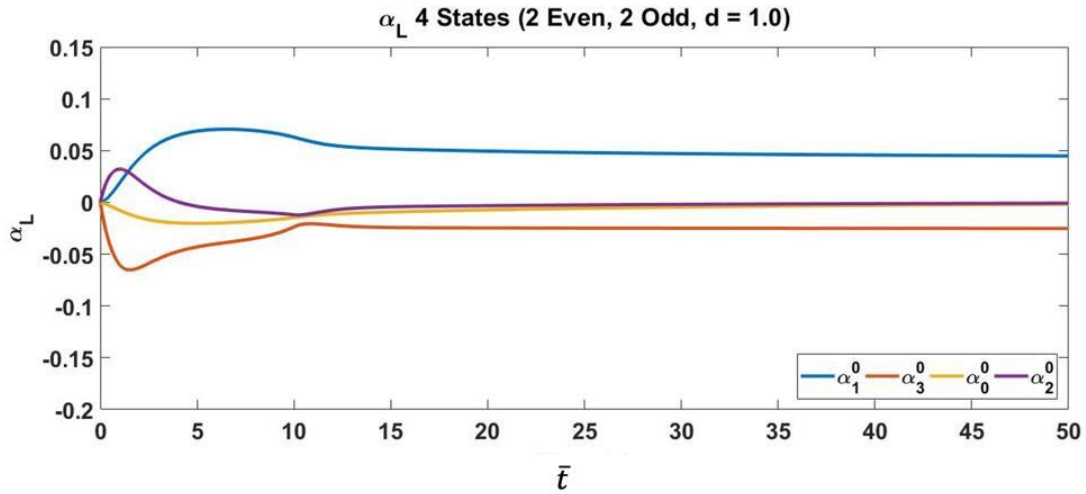
Figure 4-12: $\{\alpha_n^0\}_L$ state variable for 4 inflow states (2 even and 2 odd) with $d = 1.0$
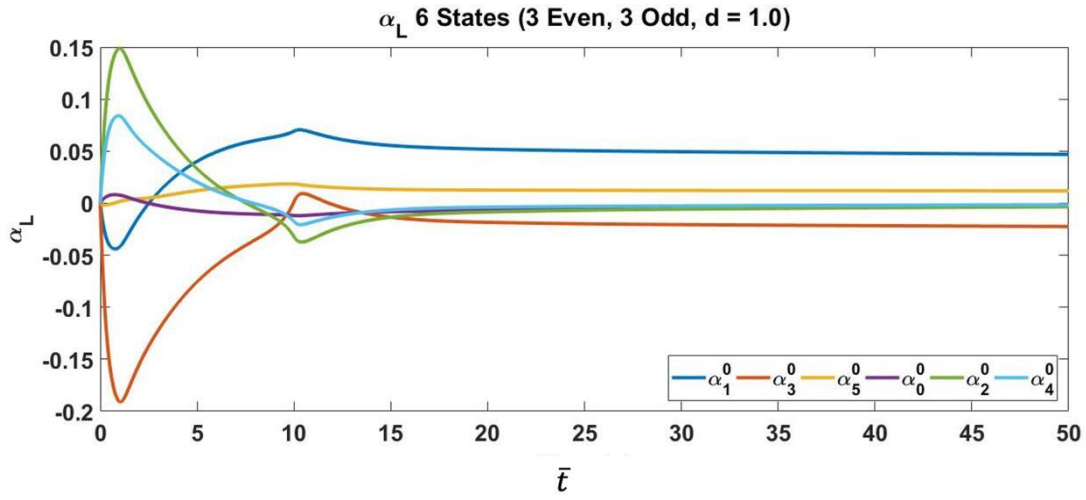
Figure 4-13: $\{\alpha_n^0\}_L$ state variable for 6 inflow states (3 even and 3 odd) with $d = 1.0$
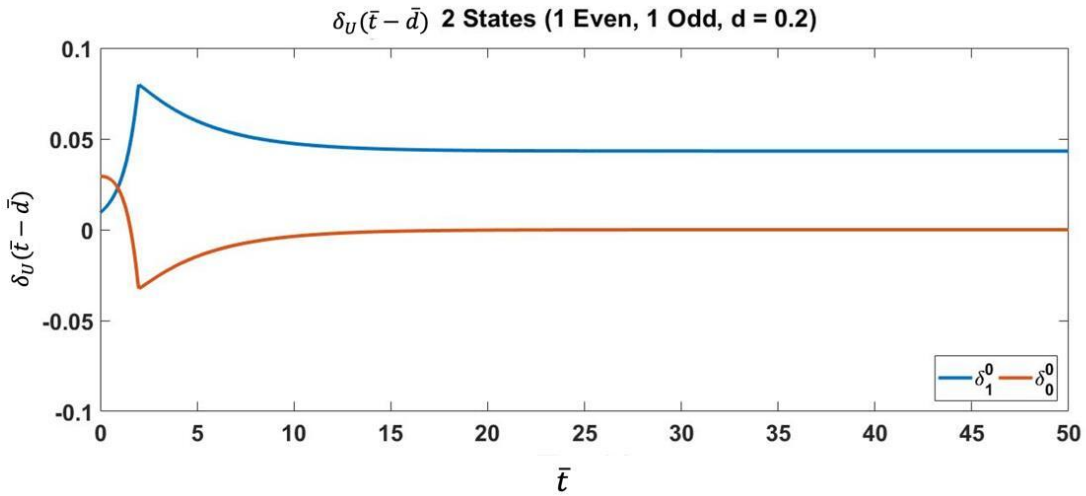
Figure 4-14: $\{\delta_n^0(\bar{t}-\bar{d})\}_U$ co-state variable for 2 inflow states (1 even and 1 odd) with $d = 0.2$
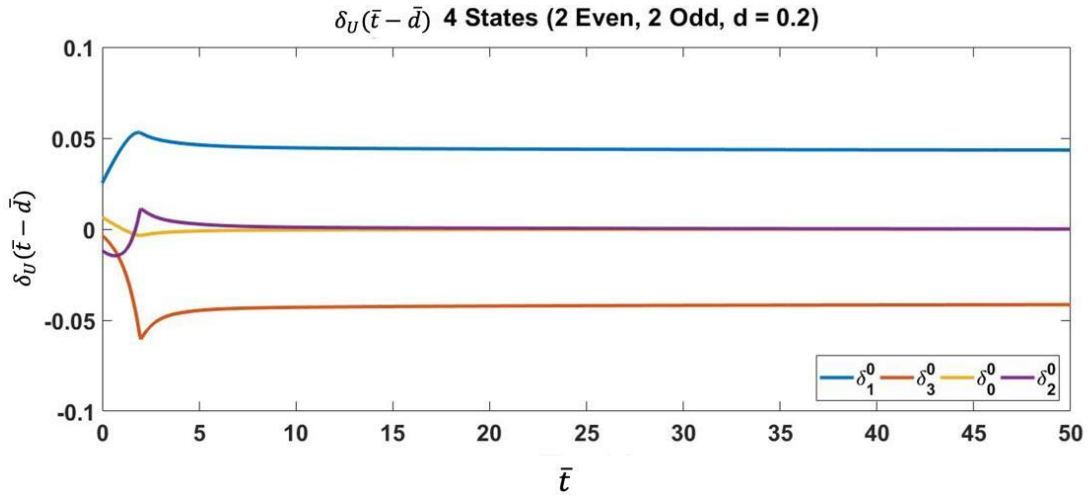
Figure 4-15: $\{\delta_n^0(\bar{t}-\bar{d})\}_U$ co-state variable for 4 inflow states (2 even and 2 odd) with $d = 0.2$
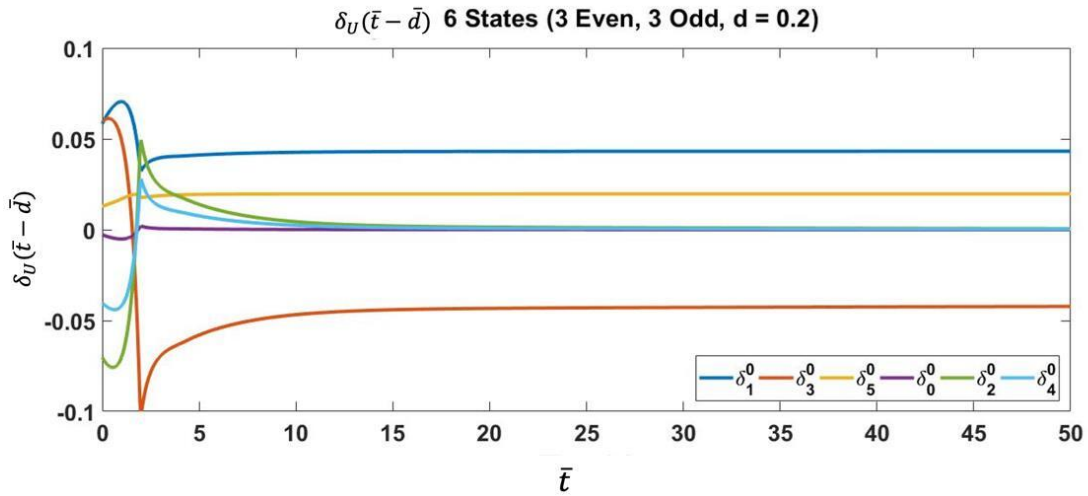
Figure 4-16: $\{\delta_n^0(\bar{t}-\bar{d})\}_U$ co-state variable for 6 inflow states (3 even and 3 odd) with $d = 0.2$
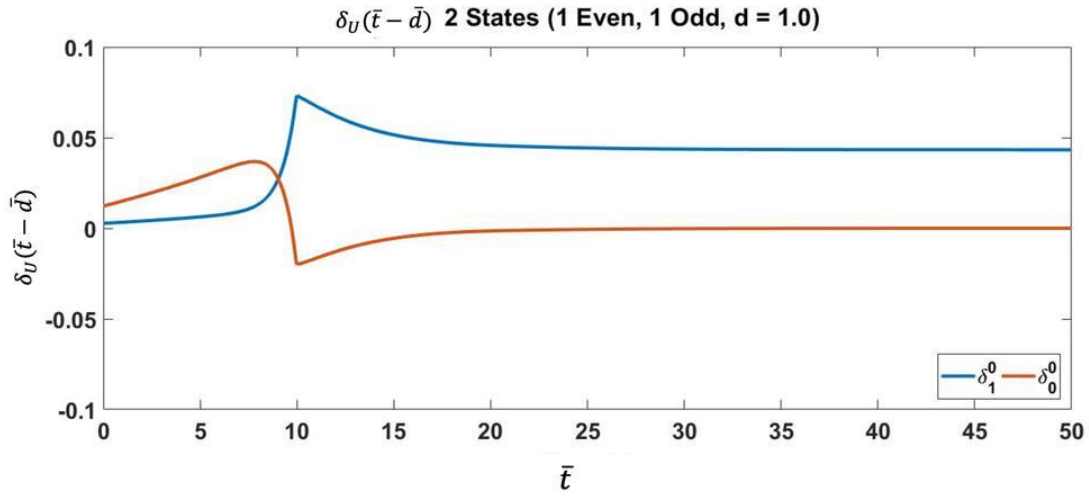
Figure 4-17: $\{\delta_n^0(\bar{t}-\bar{d})\}_U$ co-state variable for 2 inflow states (1 even and 1 odd) with $d = 1.0$
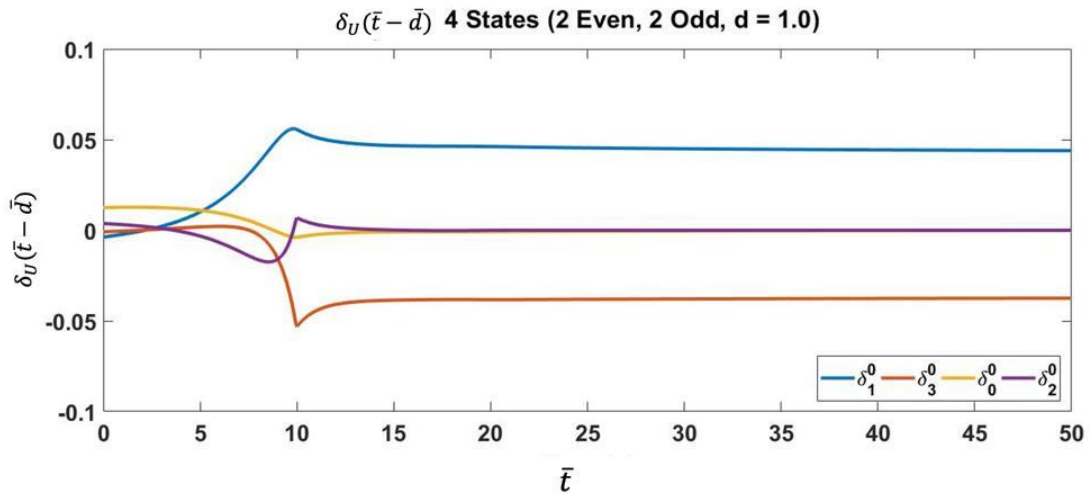
Figure 4-18: $\{\delta_n^0(\bar{t}-\bar{d})\}_U$ co-state variable for 4 inflow states (2 even and 2 odd) with $d = 1.0$
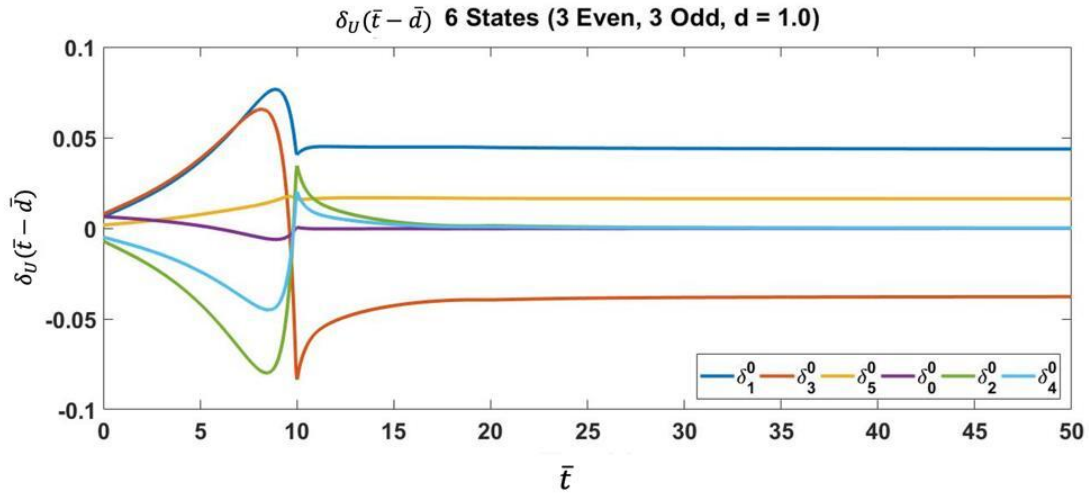
Figure 4-19: $\{\delta_n^0(\bar{t}-\bar{d})\}_U$ co-state variable for 6 inflow states (3 even and 3 odd) with $d = 1.0$
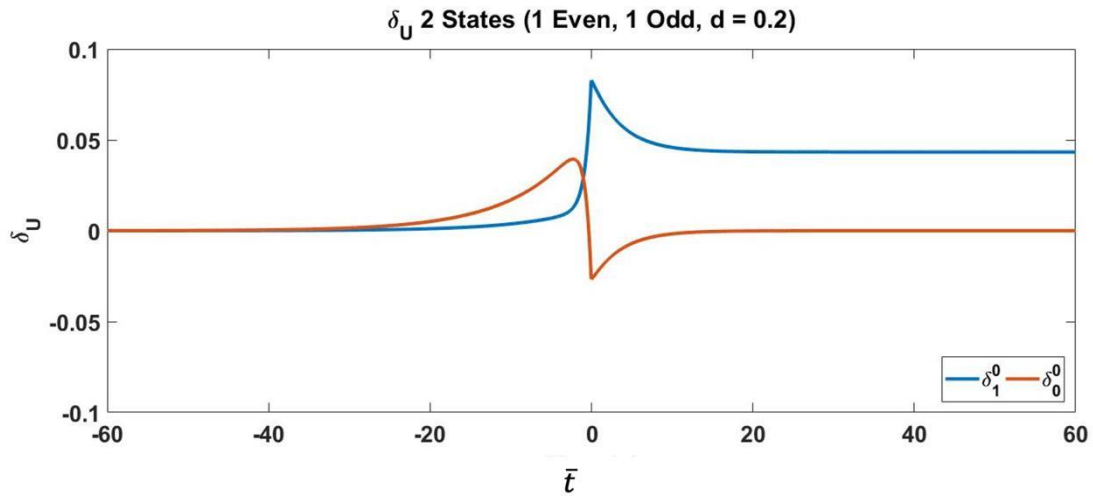
Figure 4-20: $\{\delta_n^0\}_U$ co-state variable for 2 inflow states (1 even and 1 odd) with $d = 0.2$
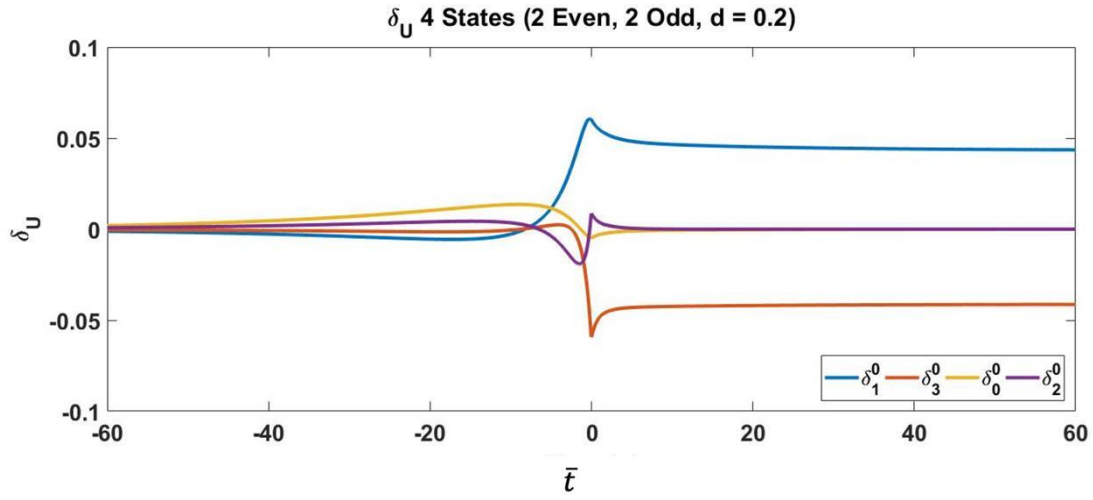
Figure 4-21: $\{\delta_n^0\}_U$ co-state variable for 4 inflow states (2 even and 2 odd) with $d = 0.2$
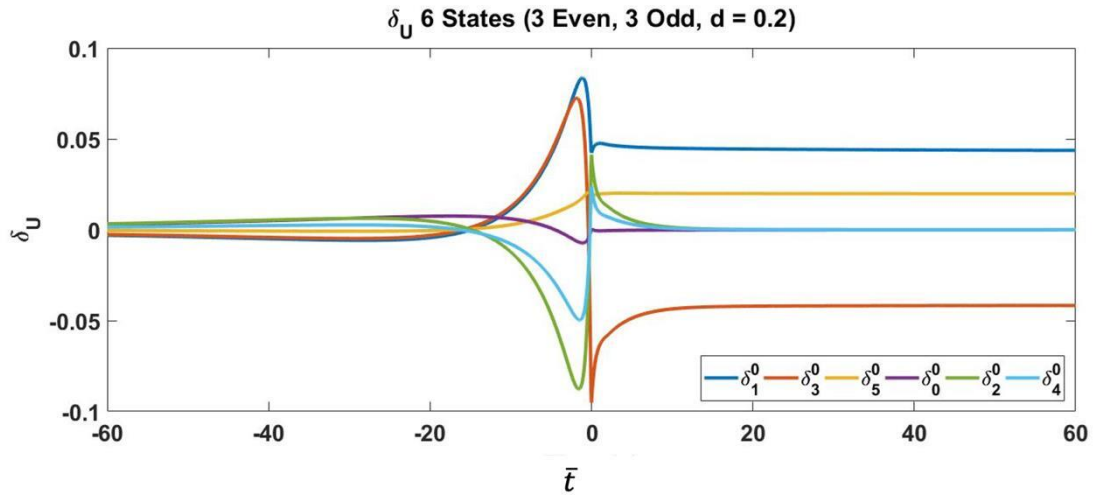
Figure 4-22: $\{\delta_n^0\}_U$ co-state variable for 6 inflow states (3 even and 3 odd) with $d = 0.2$

81
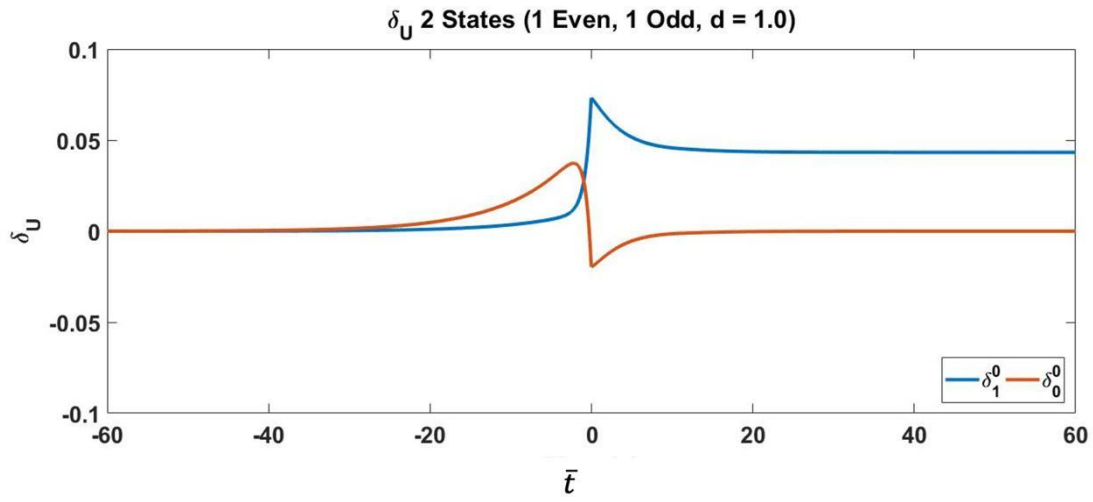
Figure 4-23: $\{\delta_n^0\}_U$ co-state variable for 2 inflow states (1 even and 1 odd) with $d = 1.0$
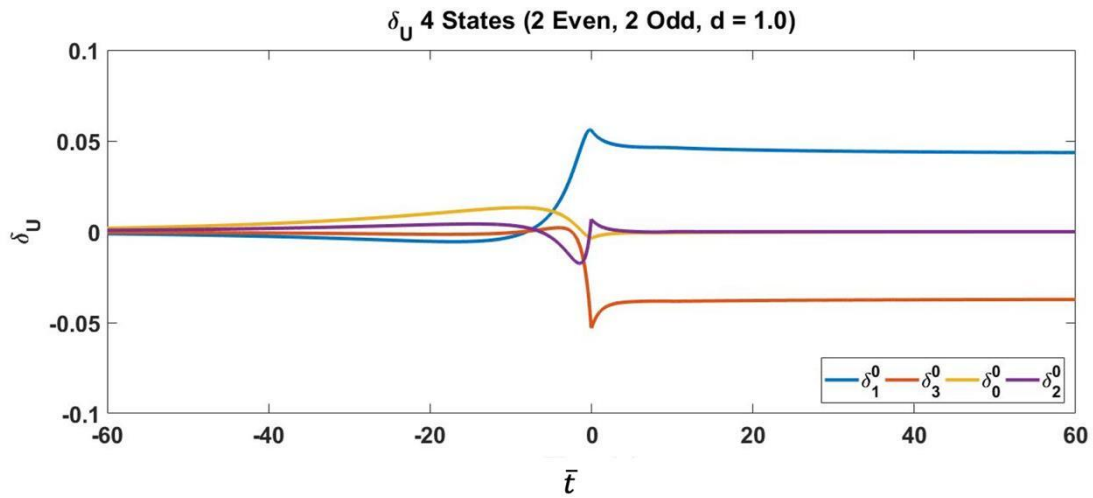
Figure 4-24: $\{\delta_n^0\}_U$ co-state variable for 4 inflow states (2 even and 2 odd) with $d = 1.0$
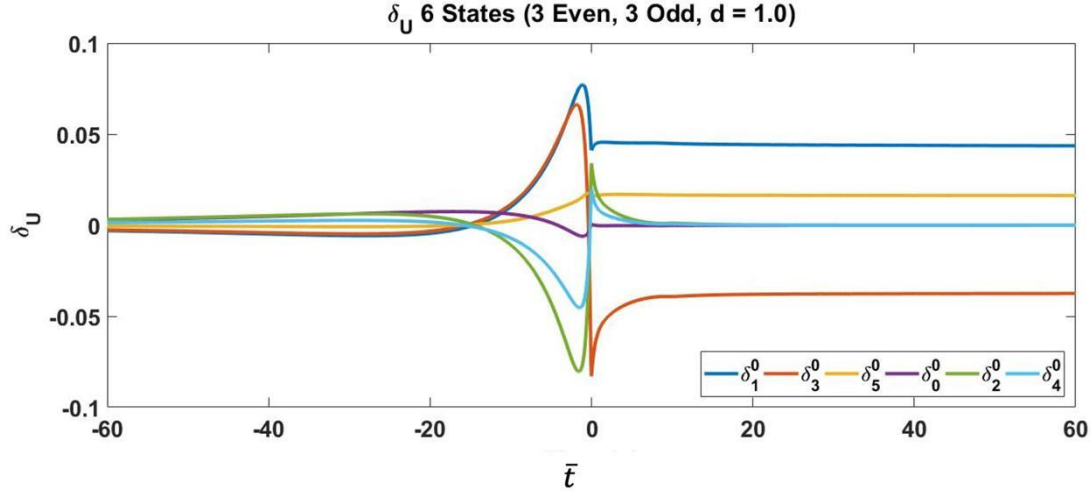
Figure 4-25: $\{\delta_n^0\}_U$ co-state variable for 6 inflow states (3 even and 3 odd) with $d = 1.0$

4.2.2 Velocity Profiles Across the Upper and Lower Rotor Disks

The velocity profiles in this section are total velocity on the rotor disks and can mathematically be expressed as:

$$\overline{V}_U = \overline{V}_{UU} + \overline{V}_{UL} \tag{4.67}$$

$$\overline{V}_L = \overline{V}_{LL} + \overline{V}_{LU} \tag{4.68}$$

The velocity profile is given over $\bar{r}$. As can be seen in Figs. 4-26 through 4-29, the velocity profiles vary drastically with differing numbers of states but begin to form a uniform trend as the number of states increases. As $\bar{r} \to 1$, the velocity on the rotor disk drops of to zero, which is due to the fact that the odd Legendre functions of the first kind all are zero at the tip. In addition, there is a notable difference in the magnitude of the velocity profiles for different rotor spacings. $\overline{V}_U$ increases when the rotor spacing decreases. Meanwhile $\overline{V}_L$ increases as rotor spacing increases. A deeper correlation of this trend is discussed in the next section. From this work it was discovered that somewhere in the range of 10 inflow states provide good results, but the use 16-20 states are more ideal, if it can be supported

83

computationally. For most of this work 10 inflow states are used because of limitations with required computational resources for extremely small rotor spacings. Ten states are enough to demonstrate the dynamics of the system.
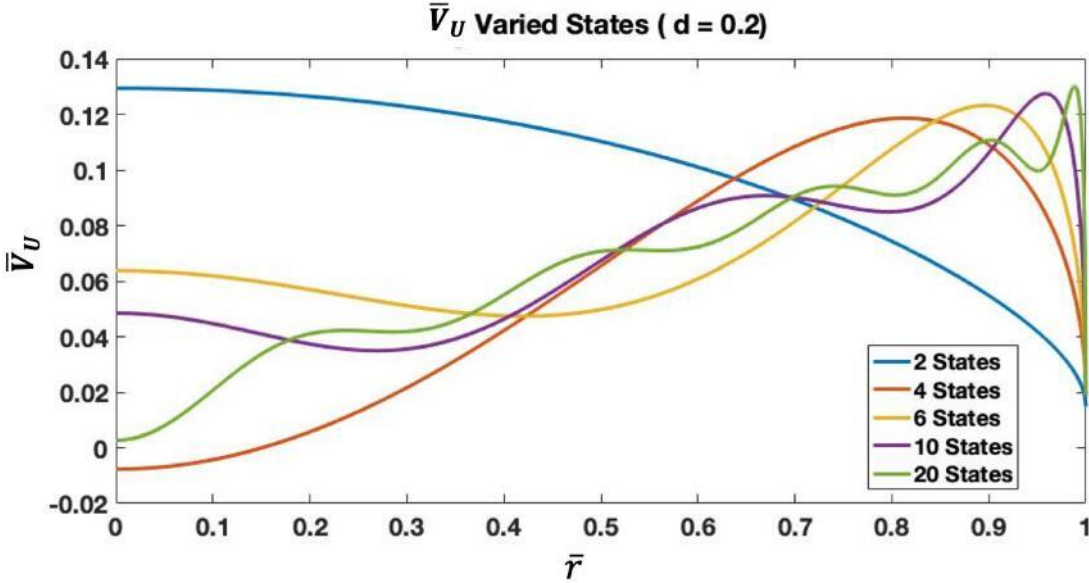
Figure 4-26: $\overline{V}_U$ for varied number of inflow states with rotor spacing $d = 0.2$
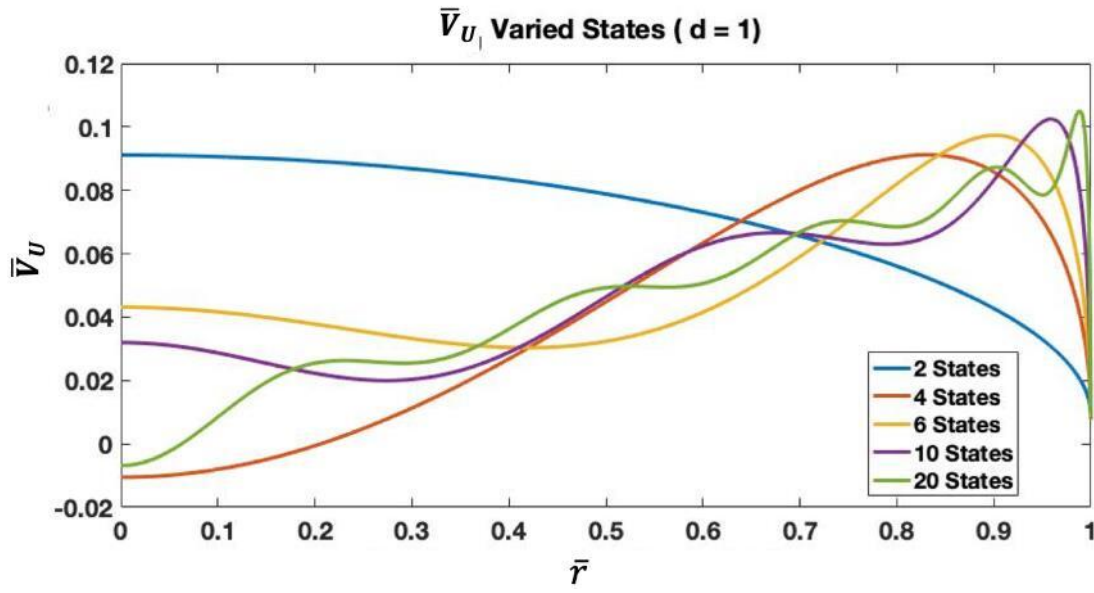
Figure 4-27: $\overline{V}_U$ for varied inflow states with rotor spacing $d = 1.0$
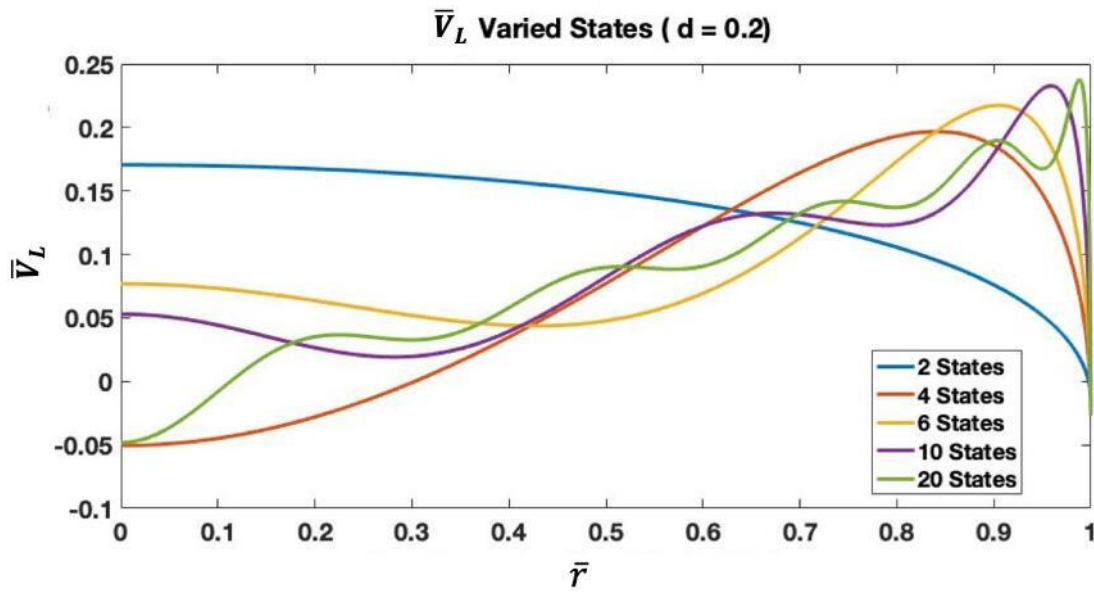
Figure 4-28: $\overline{V}_L$ for varied inflow states with rotor spacing $d = 0.2$
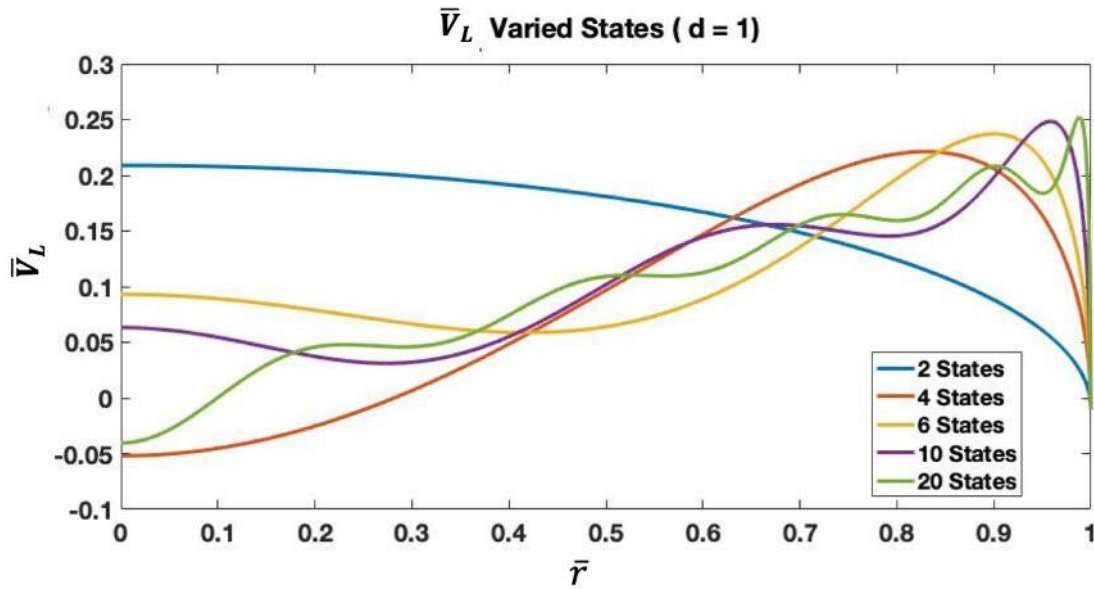
Figure 4-29: $\overline{V}_L$ for varied inflow states with rotor spacing $d = 1.0$

4.2.3 Velocity Profiles with 10 States with Varied Rotor Spacing

This section discusses the impact of rotor spacing on the dynamics of the system with ten inflow states. Theory suggests that at a rotor spacing of $d = 0$, the velocity profiles for $\overline{V}_U$ and $\overline{V}_L$ would be identical for both rotors. As has previously been demonstrated, the total velocity on the lower rotor disk ($\overline{V}_L$) is larger than that of the upper rotor ($\overline{V}_U$). However, this is more noticeable with larger rotor spacings. Momentum theory proves that at a large distance downstream from a rotor, the magnitude of velocity doubles. It is important to understand that this theory is for a single lifting rotor system; and, thus, for a coaxial rotor system, the theory implies that (for large d) the velocity on the upper rotor caused by the upper rotor ($\overline{V}_{UU}$) is equivalent to one-half the velocity on the lower rotor caused by the upper rotor ($\overline{V}_{LU}$). Demonstration of this concept is done through the comparison of a coaxial system with larger rotor spacing ($d = 10$). The individual components that make up

the velocity on the upper and lower rotor disks are also investigated to demonstrate how the spacing impacts the individual terms.

Rotor spacings of $d = 0.01, 0.2, 1, 2, 10$ were selected to represent the trends at both ends of rotor spacing. A rotor spacing of $d = 0.01$ was utilized to represent the minimal spacing because it was able to represent the trends while remaining a coaxial system. For a larger rotor spacing $d = 10$ was ideal because it represents a large enough rotor spacing without requiring too large of a time domain (*Note: Remember the time delayed terms require a time domain that is at minimum* $-\overline{d} < \overline{t} < \overline{d}$).

To demonstrate the case for identical $\overline{V}_U$ and $\overline{V}_L$ when $d = 0$, we elect to use $d = 0.01$ to illustrate the model performance. In addition, we look at the individual components of velocity and correlate them with the previously derived equations. As can be seen in the velocity profiles in Fig. 30, the velocity components $\overline{V}_{UU}$ and $\overline{V}_{LU}$ are nearly identical, and $\overline{V}_{UL}$ and $\overline{V}_{LL}$ are nearly identical outside of the velocity magnitude near the edge of the rotor disk. One would assume that if the rotor spacing were in fact $d = 0$, the profiles would be identical. As the rotor spacing increases in Figs. 4-31 to 4-34, the component magnitudes gradually become dissimilar and combined velocities on the disk begin to separate.

In Fig. 4-35, the ratio of $\overline{V}_{LU}$ to $\overline{V}_{UU}$ versus d is shown at distances of $\overline{r} = 0.6,\ 0.7,$ and 0.8 from the center of the rotor. For all three $\overline{r}$, $\overline{V}_{LU}$ begins approaching *twice* the magnitude of $\overline{V}_{UU}$ with a ratio of 1.92 when $d = 2$. At $d = 5$ the ratio climbs to 1.99 and at $d = 10$ the ratio is 2.0.

To better visualize the changes in $\overline{V}_U$ and $\overline{V}_L$ with varied rotor spacing, Figs. 4-36 and 4-37 compare the velocity profiles for $d = 0.01, 0.2, 1, 2, 10$. Figure 4-36 further demonstrates that the $\overline{V}_U$ show very small change in magnitude from $d = 2$ to $d = 10$. Figure 4-37 shows that for $\overline{V}_U$ there are only minor changes in magnitude from $d = 1$ to $d = 10$.

Analysis of the previously-derived equations demonstrates how they incorporate the effect of rotor spacing. The driving force for the variations within the coupled velocity terms Eqs. 4.12-4.15 is the rotor spacing and the impact it has on the shape functions $\overline{P}_n^m(\nu)$ and $\overline{Q}_n^m(i\eta)$. For the case where the rotor spacing is small, we know that, on the disk, where $\eta \to 0$, $\overline{Q}_n^m(i\eta) \to 1$, correlates to a case where $d = 0$. For this explanation we will assume that for $d = 0.01$, $\eta \approx 0$ and $\overline{Q}_n^m(0i) = 1$. Applying this to Eqs. 4.14 and 4.15 in steady state (where $\{\alpha_n^0(\bar{t})\}_U = \{\alpha_n^0(\bar{t} - \bar{d})\}_U$ and $\{\delta_n^0(\bar{t})\}_U = \{\delta_n^0(\bar{t} - \bar{d})\}_U$), we find:

$$\overline{V}_{UL}(t, r_U, \psi_U, d) = \sum \{\alpha_n^0(\bar{t})\}_L \overline{P}_n^0(\nu_L) \tag{4.69}$$

$$\overline{V}_{LU}(t, r_U, \psi_U, d) = \sum \{\alpha_n^0(\bar{t})\}_U \overline{P}_n^0(\nu_U) \tag{4.70}$$

This is due the relationship that when $d = 0$, $[B] = [C]$. Therefore, it can further be observed that:

$$\overline{V}_{UU}(t, r_U, \psi_U, d) = \overline{V}_{LU}(t, r_U, \psi_U, d) \tag{4.71}$$

$$\overline{V}_{LL}(t, r_L, \psi_L, d) = \overline{V}_{UL}(t, r_U, \psi_L, d) \tag{4.72}$$

From this, we can correlate $\overline{V}_U$ and $\overline{V}_L$ through:

$$\overline{V}_U = \overline{V}_{UU} + \overline{V}_{UL} = \overline{V}_{LU} + \overline{V}_{LL} = \overline{V}_L \tag{4.73}$$

Now, for the case for a large rotor spacing, we consider the limit as $d = \infty$. As $z \to -\infty$ (distance far above the rotor disk), $\eta \to \infty$ and $\overline{Q}_n^m(i\eta) \to 0$. In this case $[C] \to 0$. Applying this to Eqs.4.14 and 4.15, we have:

$$\overline{V}_{UL}(t, r_U, \psi_U, -\infty) = 0 \tag{4.74}$$

$$\overline{V}_{LU}(t, r_U, \psi_L, -\infty) = \sum \{\alpha_n^0(\infty)\}_U \overline{P}_n^0(\nu_{on}) + \sum \{\delta_n^0(\infty)\}_U \overline{P}_n^0(\nu_{on}) \tag{4.75}$$

In this case, $\{\alpha_n^m(\infty)\}_U$ and $\{\delta_n^m(\infty)\}_U$ are steady-state values and converge to the same values. Therefore, it can be written that:

$$\overline{V}_{LU}(t, r_U, \psi_L, -\infty) = 2\sum \{\alpha_n^0(\infty)\}_U \overline{P}_n^0(\nu_{on}) = 2\overline{V}_{UU}(t, r_U, \psi_U, -\infty) \qquad (4.76)$$

Finally, Figs. 4-38 and 4-39 illustrate how the velocity profile develops over time for systems with differing numbers of inflow states. Keep in mind that $\bar{r} = 0.8$ in this plot. Therefore, the oscillations in the velocity profile—as a function of r—are not seen. Thus, the magnitude of the steady-state velocity for plots having varying number of harmonics cannot be directly compared. All of the profiles develop in a similar manner for both rotors. Looking at the impact of the rotor spacing on the development of the velocity profiles in Figs. 4-40 and 4-41, the profiles take longer reach steady-state values with increasing rotor spacing. More notably, the $\overline{V}_L$ profiles display noticeable jumps in velocity where $\bar{t} = \bar{d}$, which is when the flow from the upper rotor hits the lower rotor.
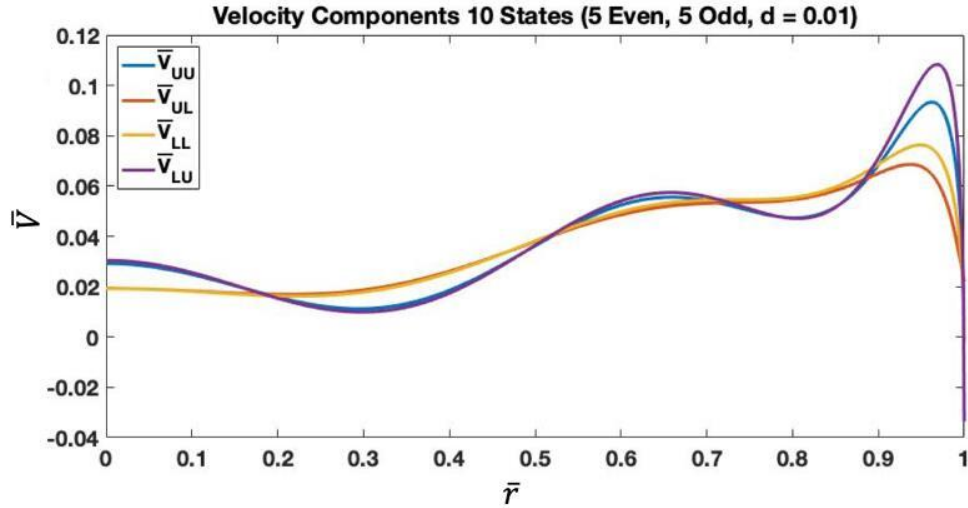
Figure 4-30: Velocity components for 10 inflow states with rotor spacing d $= 0.01$
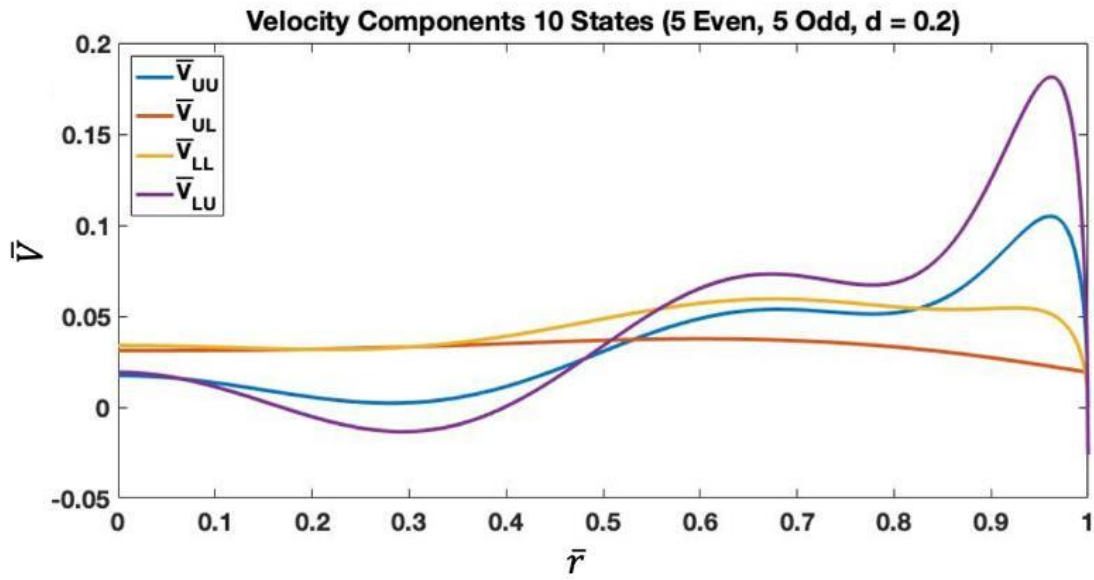
Figure 4-31: Velocity components for 10 inflow states with rotor spacing $d = 0.2$
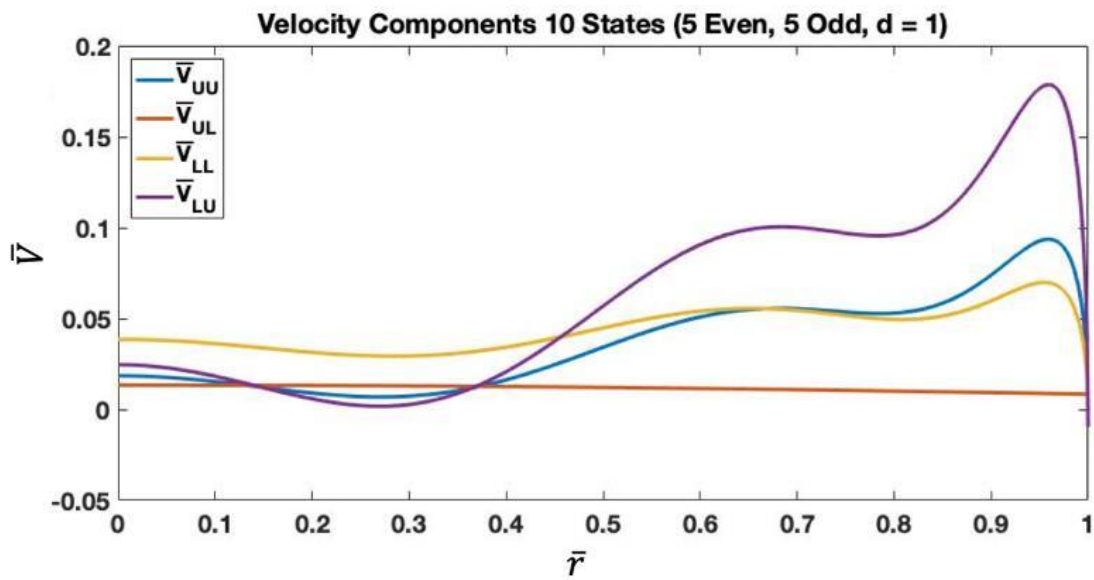
Figure 4-32: Velocity components for 10 inflow states with rotor spacing $d = 1.0$
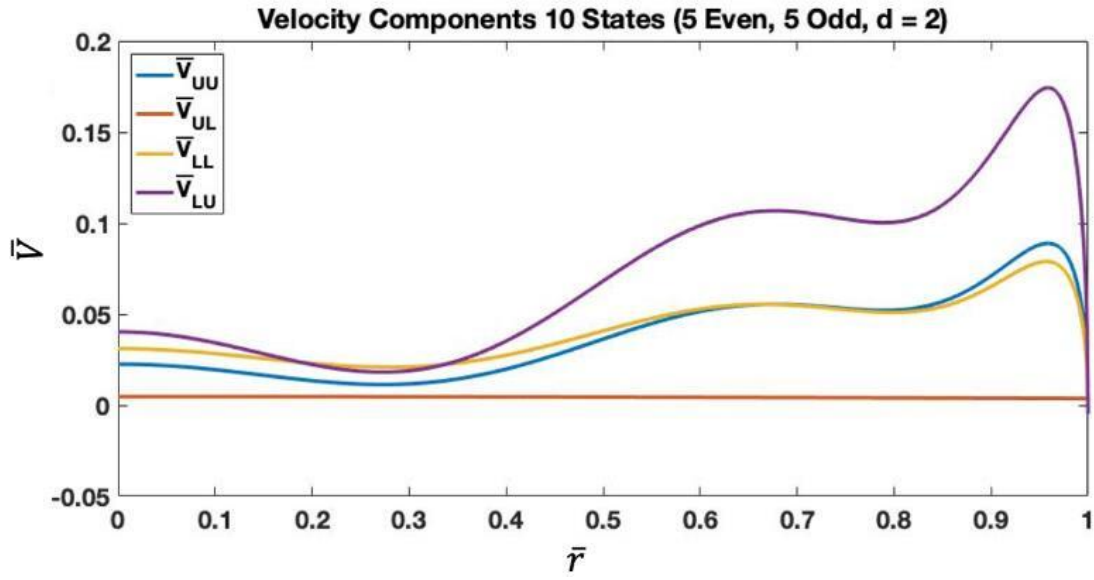
Figure 4-33: Velocity components for 10 inflow states with rotor spacing $d = 2.0$
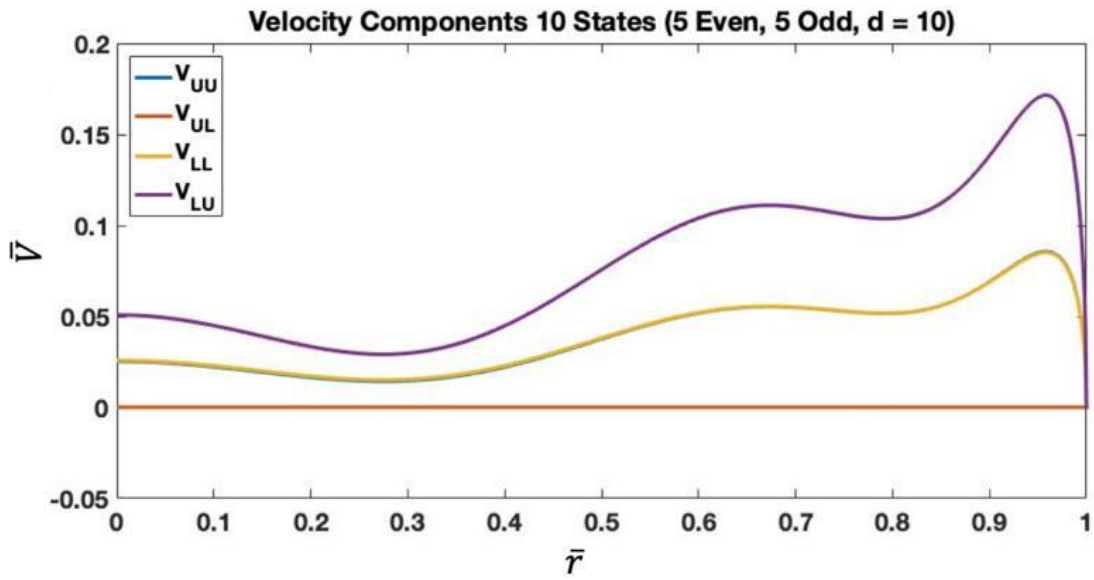
Figure 4-34: Velocity components for 10 inflow states with rotor spacing $d = 10$
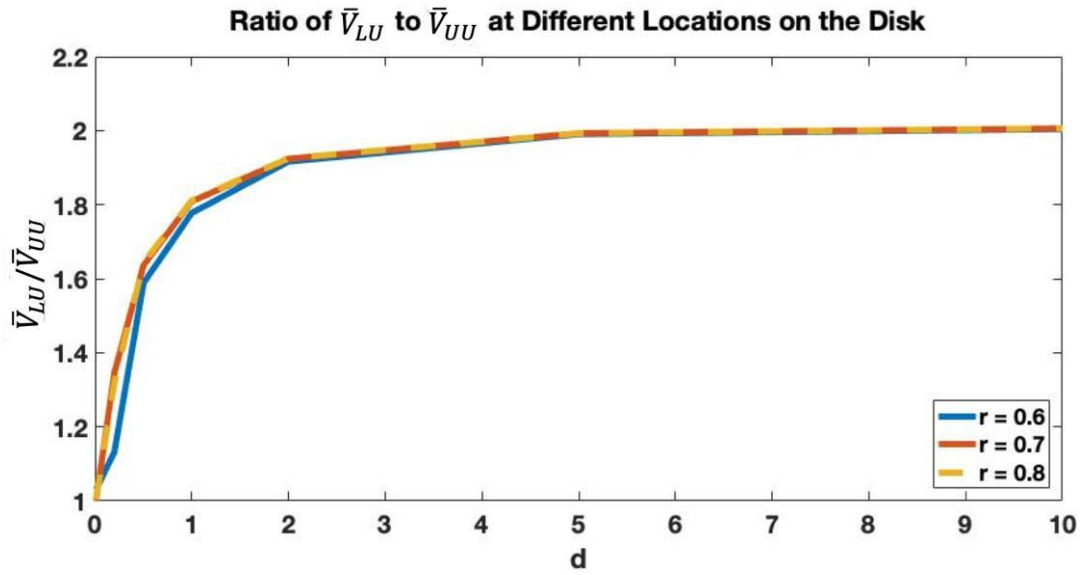
Figure 4-35: Comparison of Ratio of $\overline{V}_{LU}$ to $\overline{V}_{UU}$ for varied rotor spacings
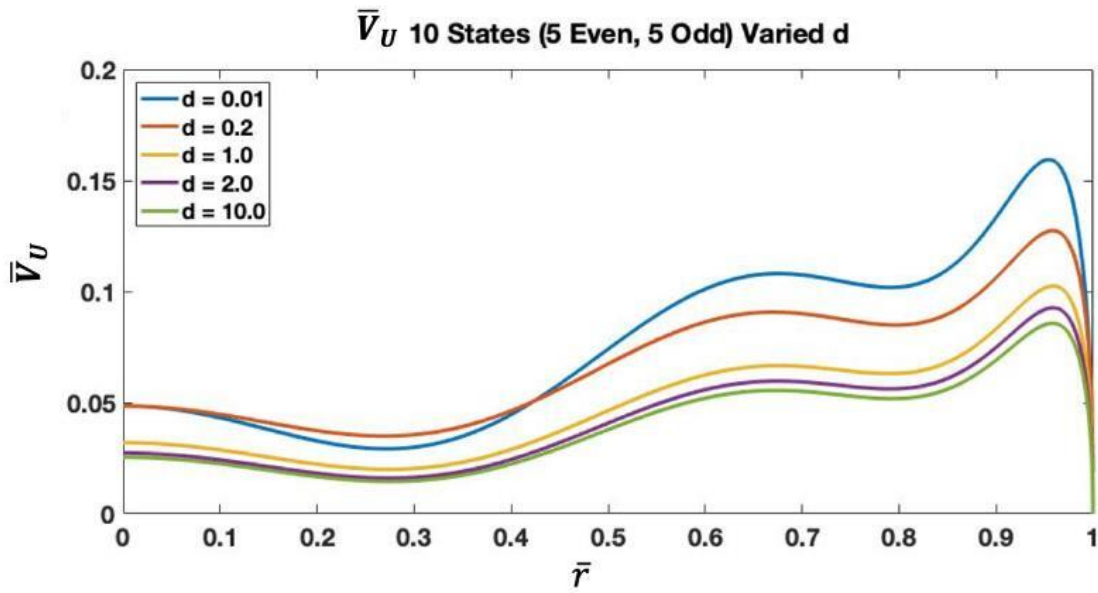
Figure 4-36: $\overline{V}_U$ for 10 inflow states and varied spacing
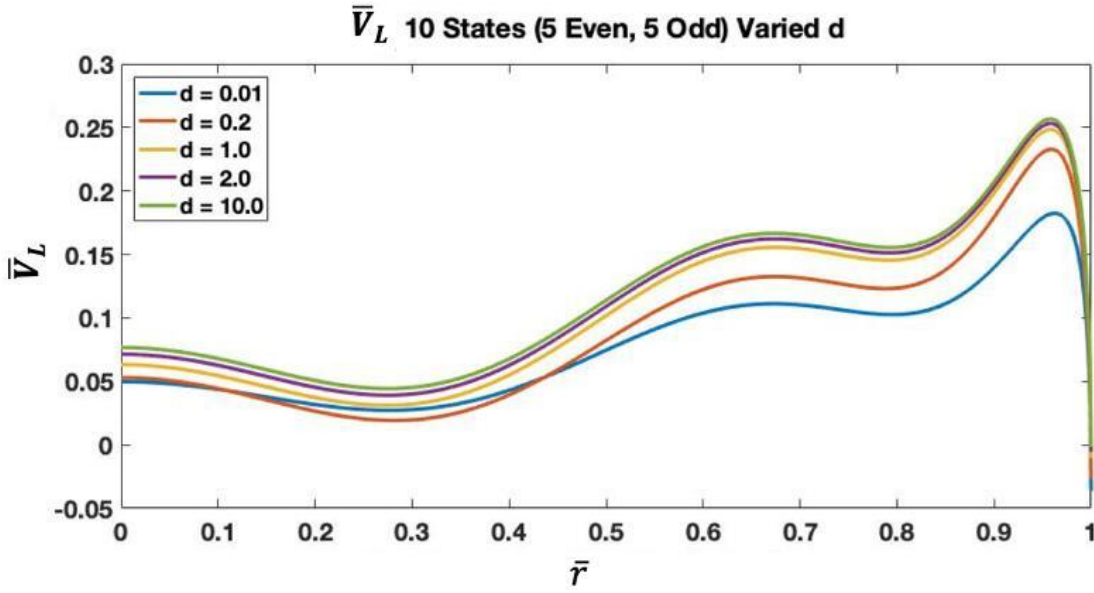
Figure 4-37: $\overline{V}_L$ for 10 inflow states and varied spacing
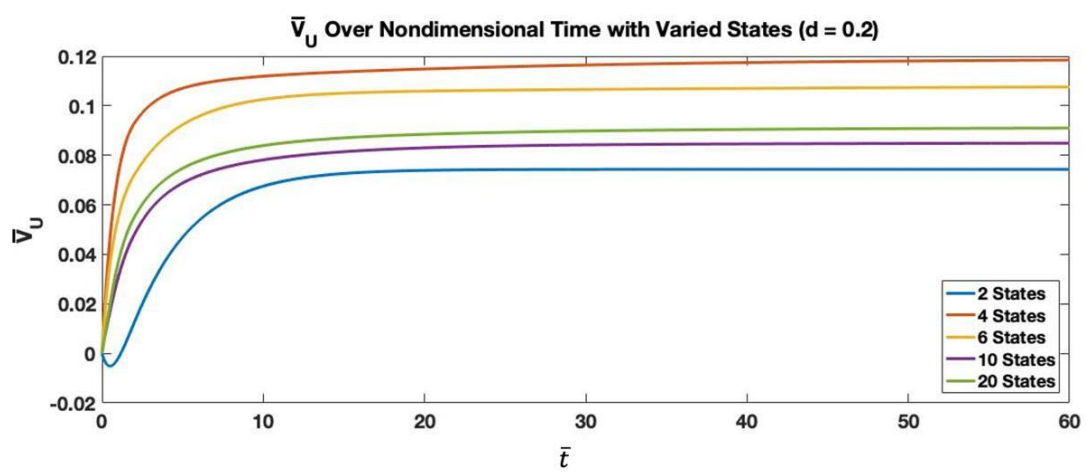
Figure 4-38: $\overline{V}_U$ for varied number of inflow states and $d = 0.2$ spacing
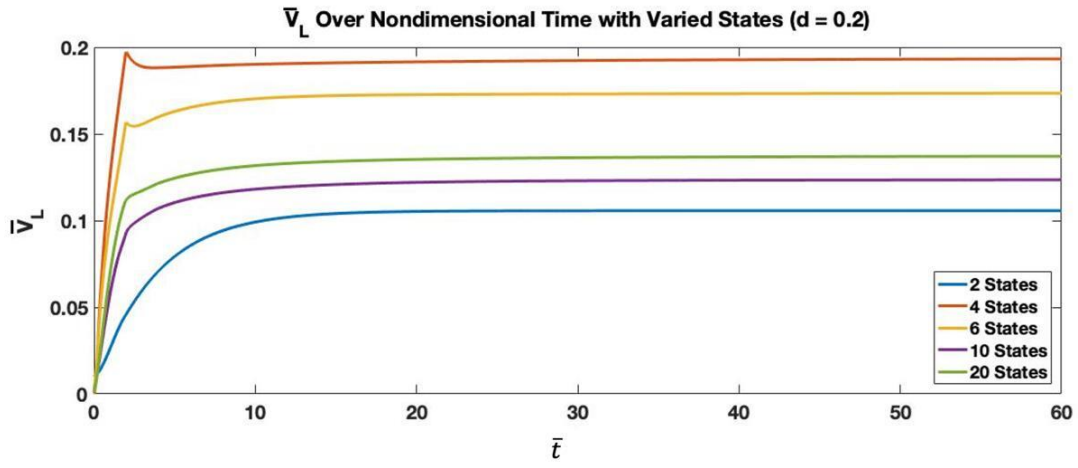
Figure 4-39: $\overline{V}_L$ for varied number of inflow states and $d = 0.2$ spacing
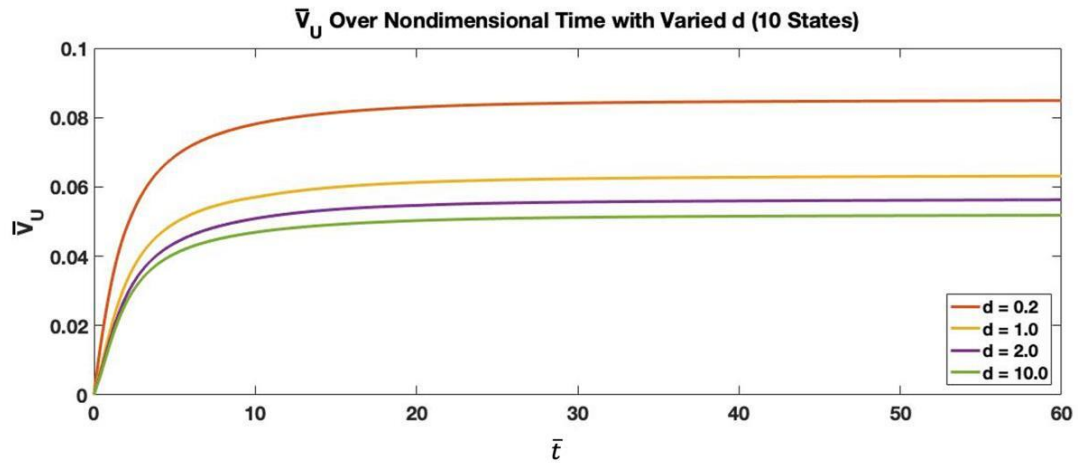
Figure 4-40: $\overline{V}_U$ for 10 inflow states and varied rotor spacing

94
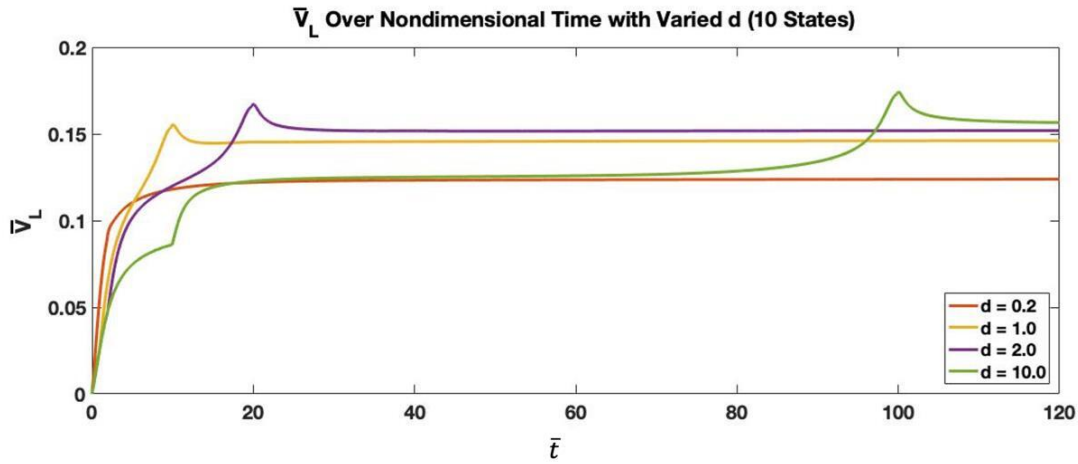
Figure 4-41: $\overline{V}_L$ for 10 inflow states and varied rotor spacing

4.3 Numerical Illustrations of Multiple Inflow States with Blade Flapping

4.3.1 States and Co-states with Blade Flapping

Blade flapping was added to the system to provide a more realistic dynamic interaction between the two rotors. The dynamics of the blade flapping terms die out with time, and eventually the state and co-state profiles reach the same steady-state values as the system without blade flapping. The blade flapping states, b_U and b_L, in Figs. 4-42 through 4-47 reveal how velocity profiles develop for different values of rotor spacing and varying number of inflow states. Figures 4-42 and 4-43 illustrate that a closer rotor spacing results in higher peak magnitudes for the upper rotor; and larger spacings increase the peak magnitudes for the lower rotor. In addition, time-delay dynamics are evident in the b_L profiles, especially when $d = 0.2$ and $d = 10.0$. Figures 4-44 to 4-46 demonstrate that, aside from the case with

95

two inflow states, the number of inflow states has only minor impact on the shape of blade flapping profiles.

Figures 4-47 through 4-70 illustrate $\{\alpha_n^0\}_U$, $\{\alpha_n^0\}_L$, $\{\delta_n^0\}_U$, and $\{\delta_n^0(\bar{t} - \bar{d})\}_U$ with blade flapping in the systems. The biggest take away from these figures is that the addition of blade flapping impacts the profile development. The blade flapping terms, themselves, generally drive an early rise to reach the peaks and then approach the steady-state values with decaying oscillations that are driven by the decay in the blade flapping terms. Overall, the number of states has a similar impact as before where the dynamics occur early in the simulation—but now with the added complexity of blade flapping. The impact of the rotor spacing on state profiles is more evident here than it was for the case without blade flapping. For example, the comparison in profiles for $\{\alpha_n^0\}_L$ in Figs. 4-55 and 4-58 shows different shapes in the peaks and magnitudes in the early dynamics. The development of the time-delay dynamics is more difficult to discern when blade flapping is included, but they still occur when $\bar{t} = \bar{d}$.
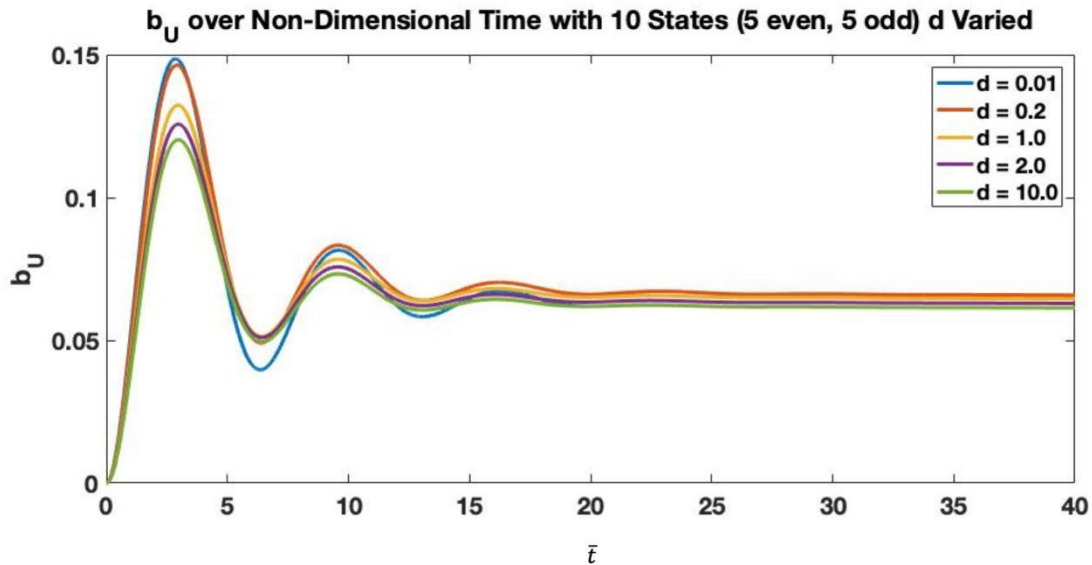
Figure 4-42: b_U profiles for 10 inflow states and varied rotor spacings
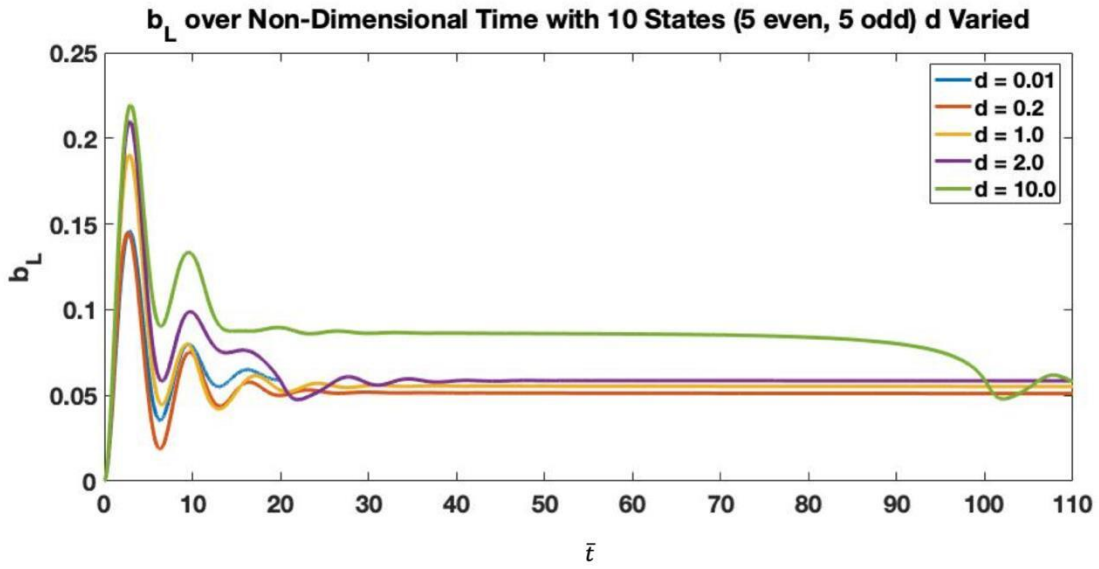
Figure 4-43: b_L profiles for 10 inflow states and varied rotor spacings
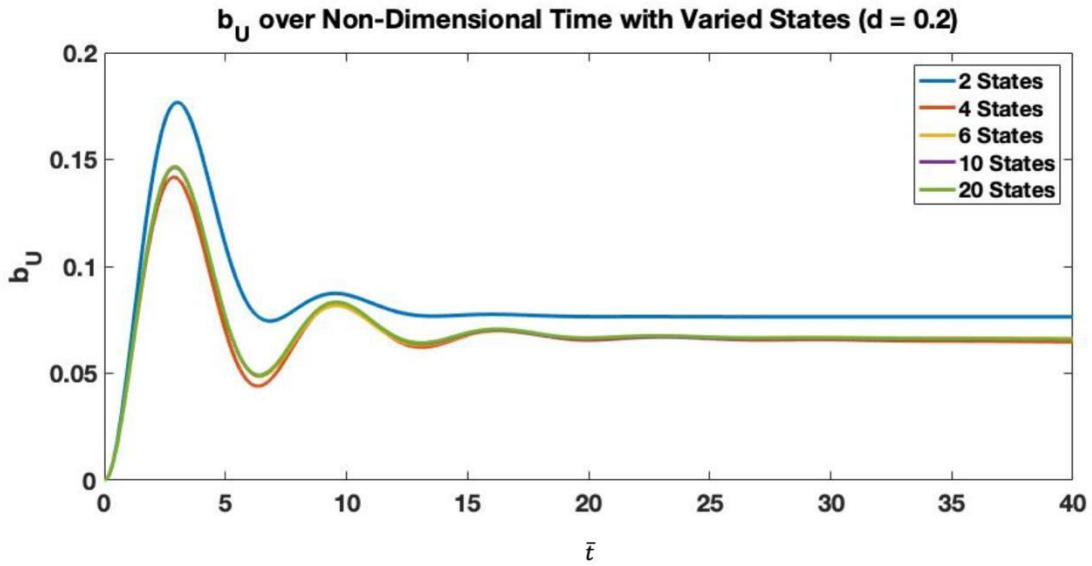
Figure 4-44: b_U profiles for a varied number of inflow states and $d = 0.2$

97
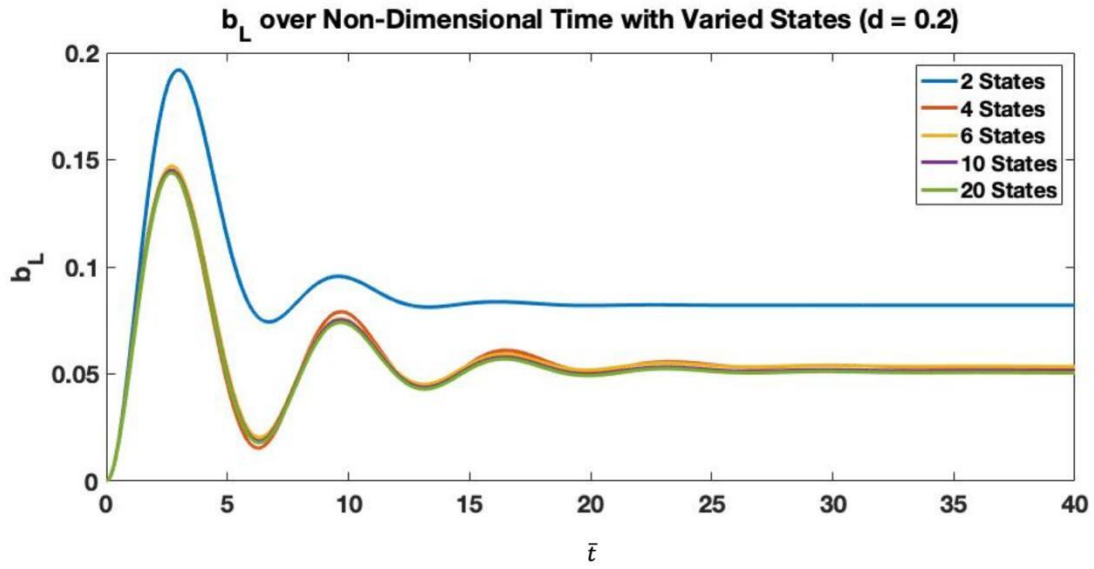
Figure 4-45: b_L profiles for a varied number of inflow states and $d = 0.2$
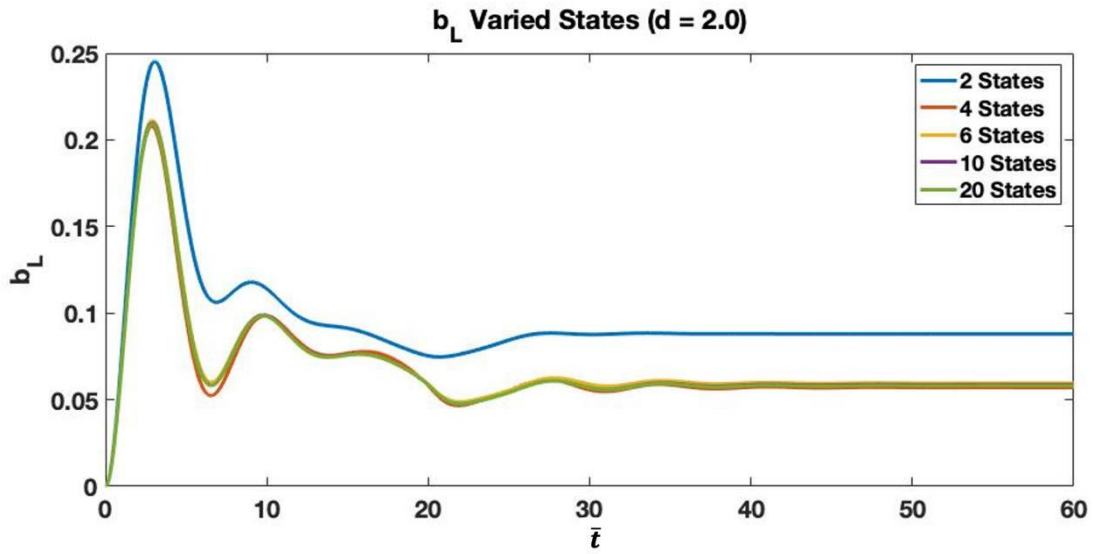
Figure 4-46: b_L profiles for a varied number of inflow states and $d = 2.0$
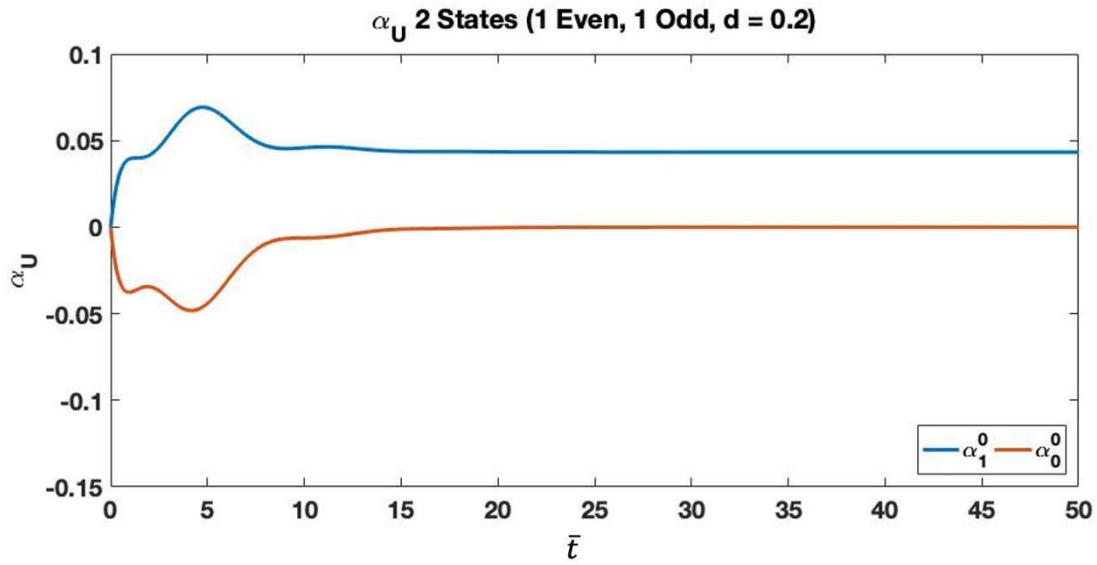
Figure 4-47: $\{\alpha_n^0\}_U$ state variable for 2 inflow states (1 even and 1 odd) with $d = 0.2$ for system with blade flapping
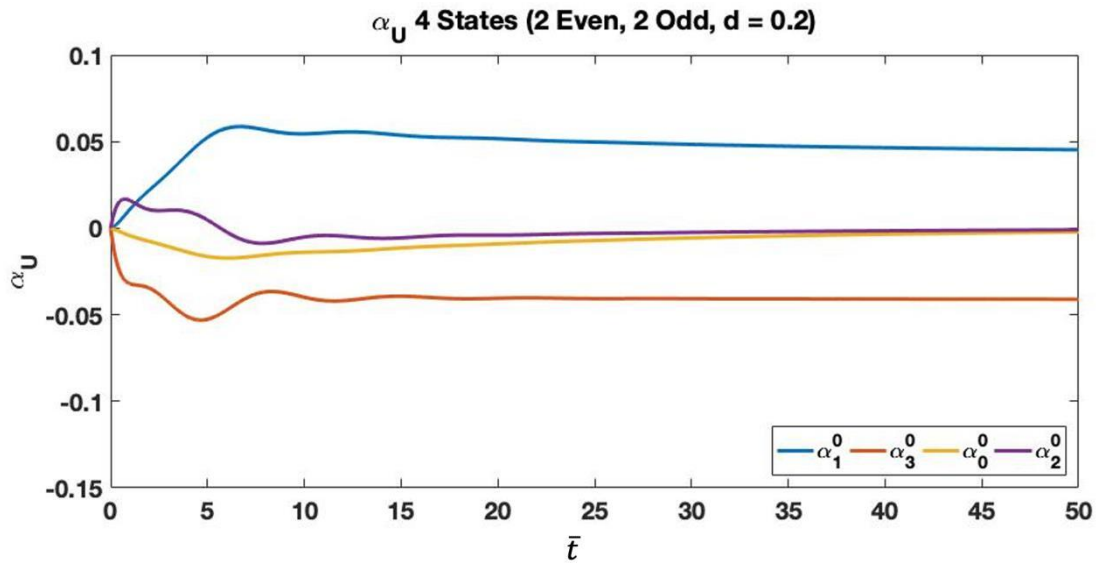
Figure 4-48: $\{\alpha_n^0\}_U$ state variable for 4 inflow states (2 even and 2 odd) with $d = 0.2$ for system with blade flapping
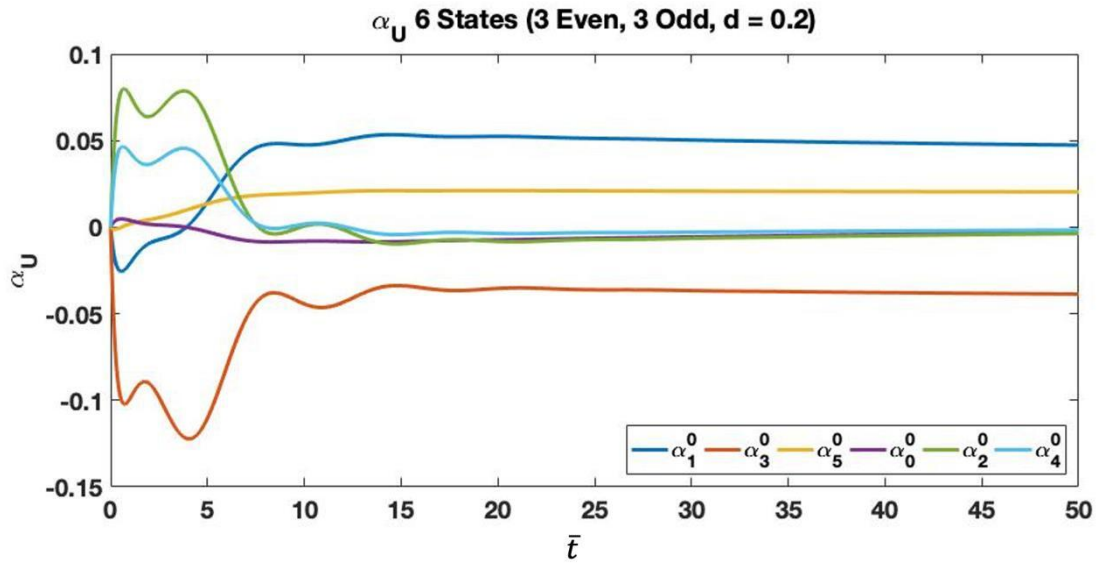
Figure 4-49: $\{\alpha_n^0\}_U$ state variable for 6 inflow states (3 even and 3 odd) with $d = 0.2$ for system with blade flapping
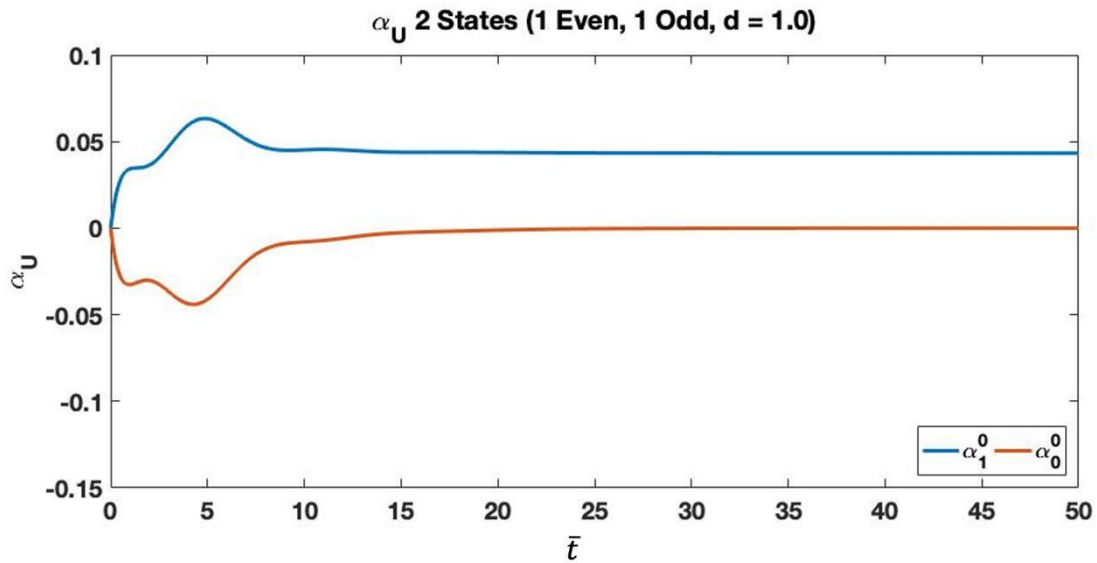
Figure 4-50: $\{\alpha_n^0\}_U$ state variable for 2 inflow states (1 even and 1 odd) with $d = 1.0$ for system with blade flapping
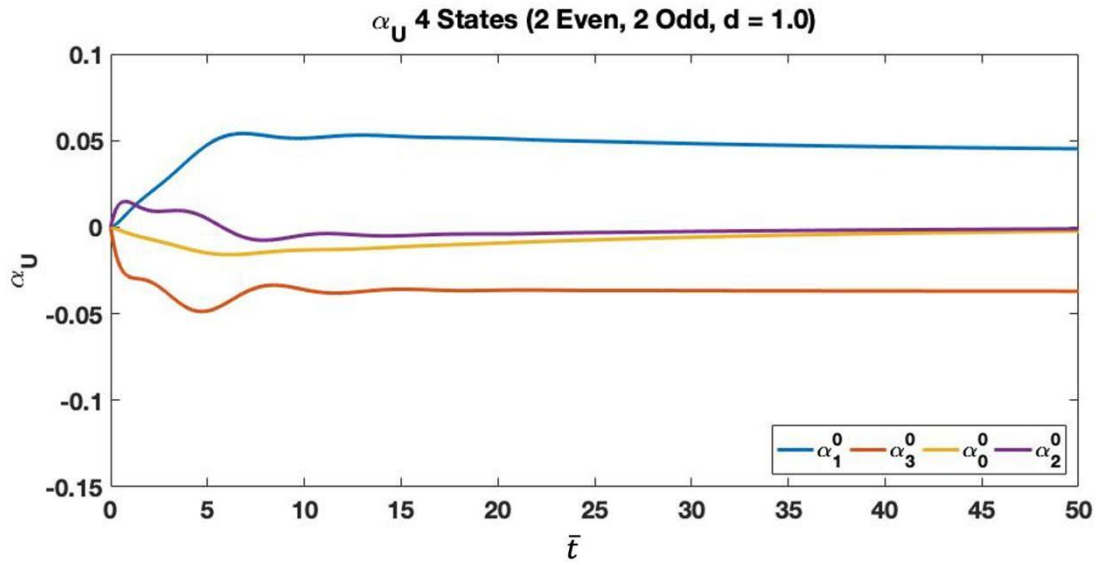
Figure 4-51: $\{\alpha_n^0\}_U$ state variable for 4 inflow states (2 even and 2 odd) with $d = 1.0$ for system with blade flapping
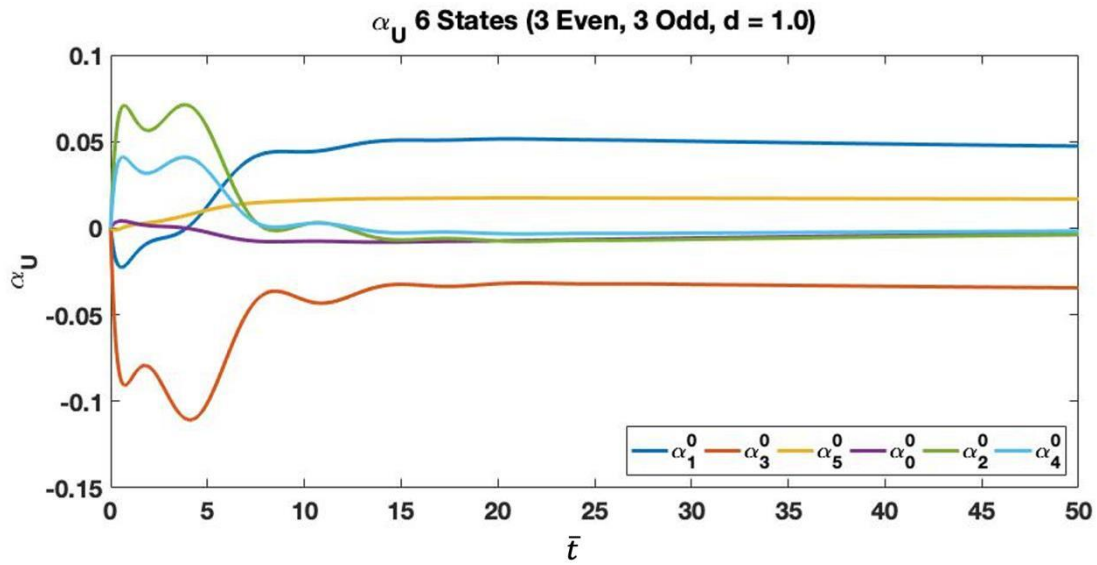
Figure 4-52: $\{\alpha_n^0\}_U$ state variable for 6 inflow states (3 even and 3 odd) with $d = 0.2$ for system with blade flapping
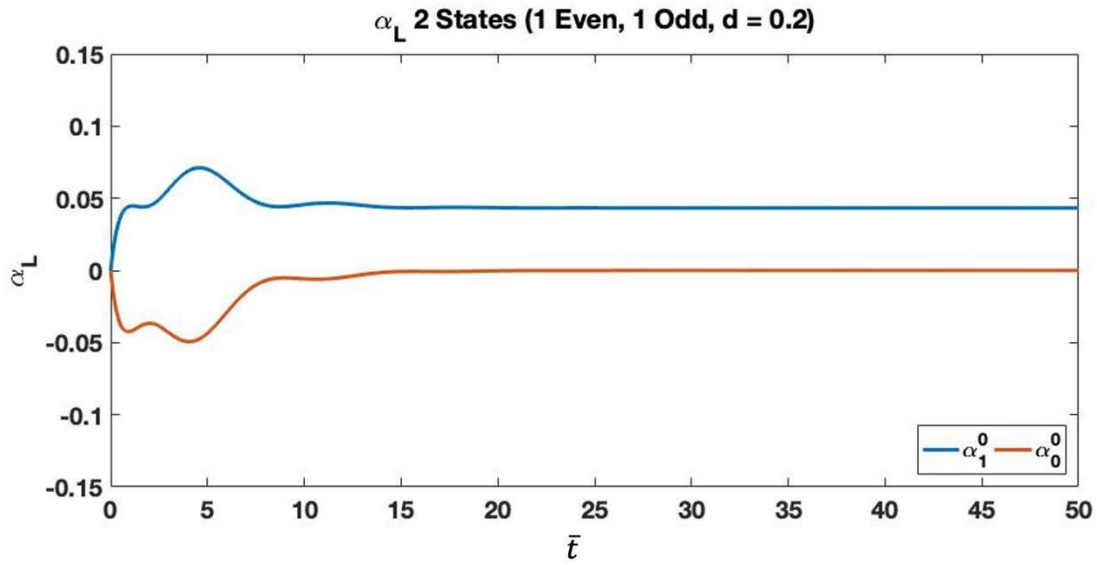
Figure 4-53: $\{\alpha_n^0\}_L$ state variable for 2 inflow states (1 even and 1 odd) with $d = 0.2$ for system with blade flapping
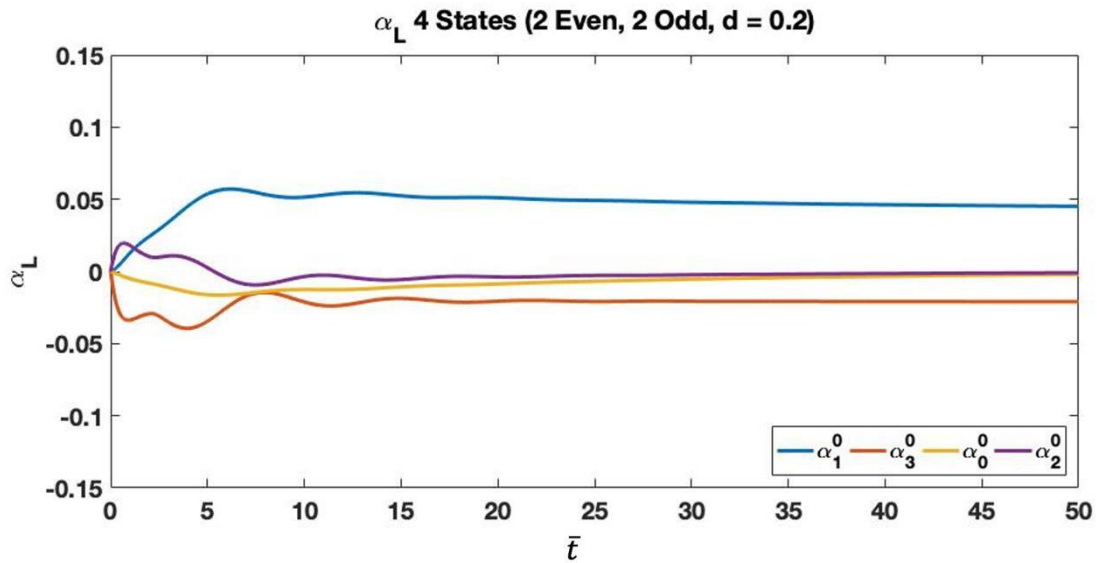
Figure 4-54: $\{\alpha_n^0\}_L$ state variable for 4 inflow states (2 even and 2 odd) with $d = 0.2$ for system with blade flapping
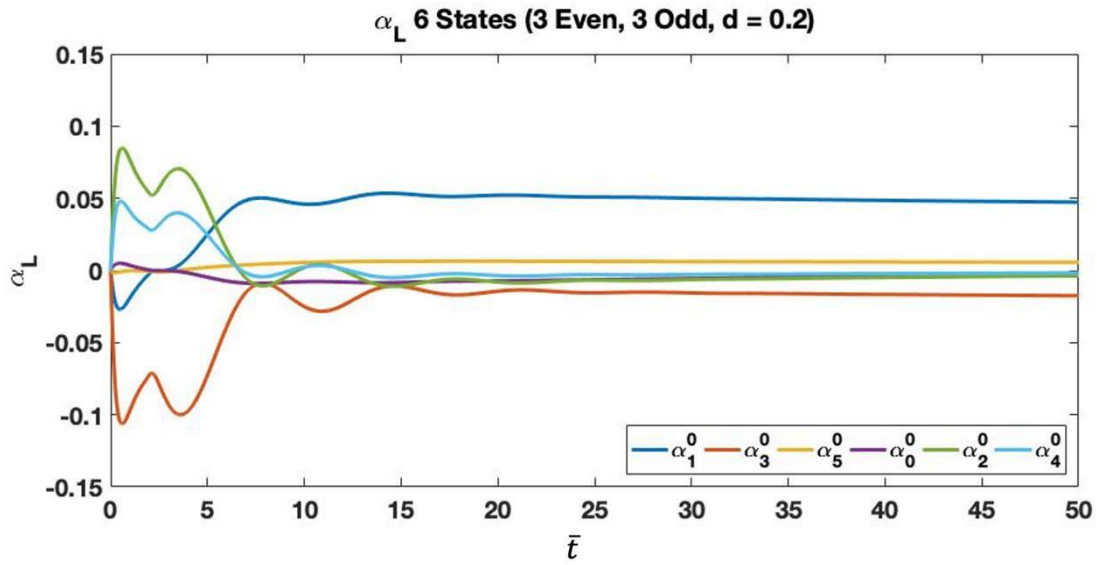
Figure 4-55: $\{\alpha_n^0\}_L$ state variable for 6 inflow states (3 even and 3 odd) with $d = 0.2$ for system with blade flapping
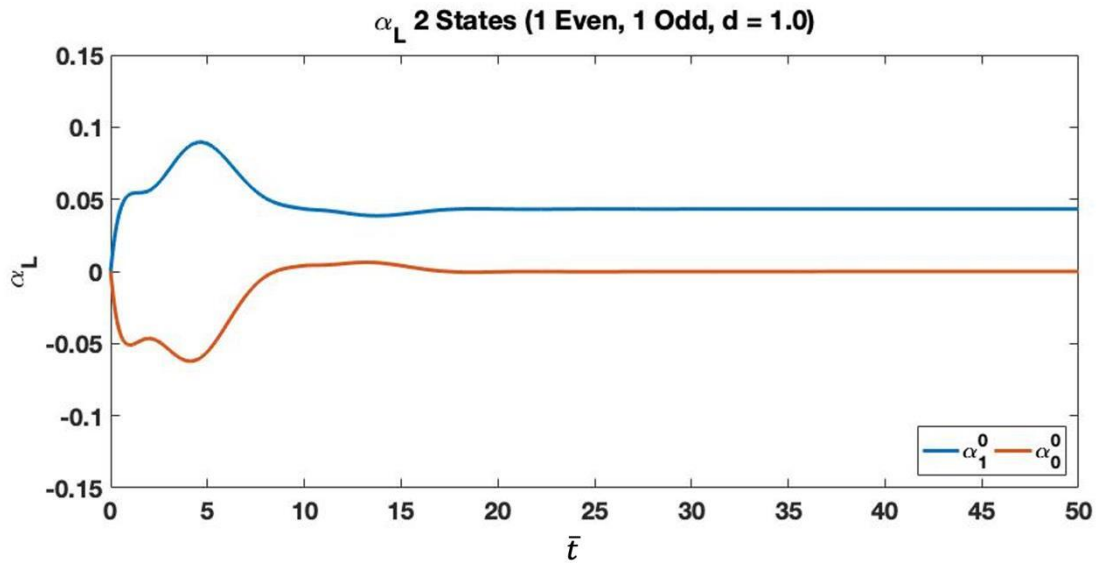
Figure 4-56: $\{\alpha_n^0\}_L$ state variable for 2 inflow states (1 even and 1 odd) with $d = 1.0$ for system with blade flapping
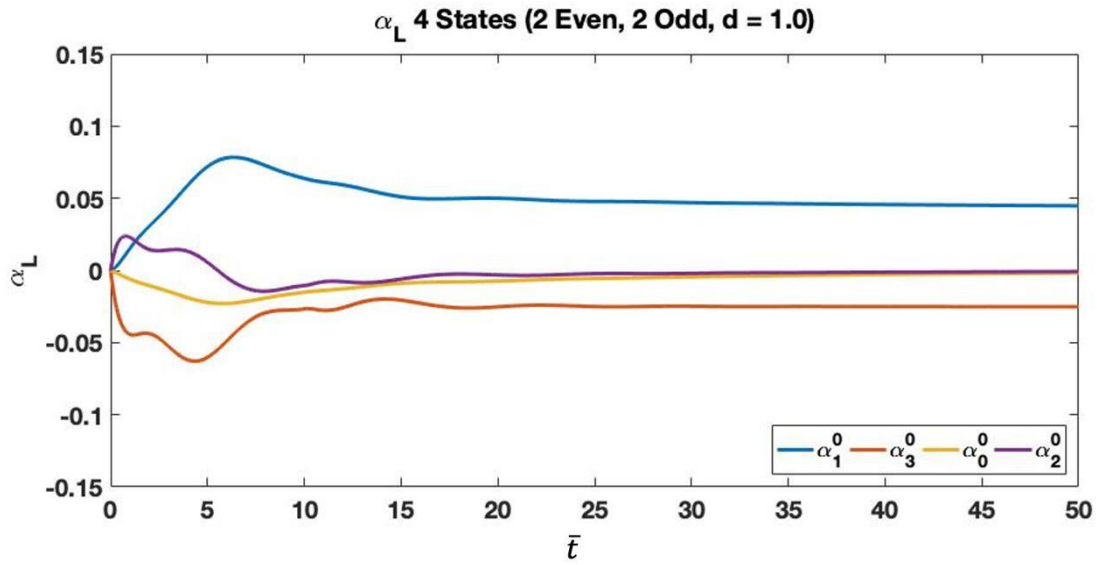
Figure 4-57: $\{\alpha_n^0\}_L$ state variable for 4 inflow states (2 even and 2 odd) with $d = 1.0$ for system with blade flapping
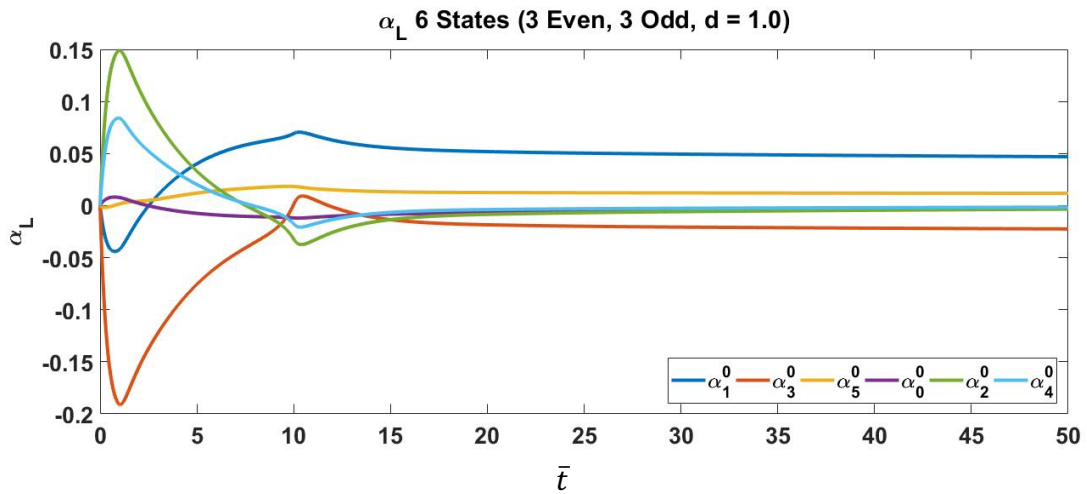
Figure 4-58: $\{\alpha_n^0\}_L$ state variable for 6 inflow states (3 even and 3 odd) with $d = 1.0$ for system with blade flapping
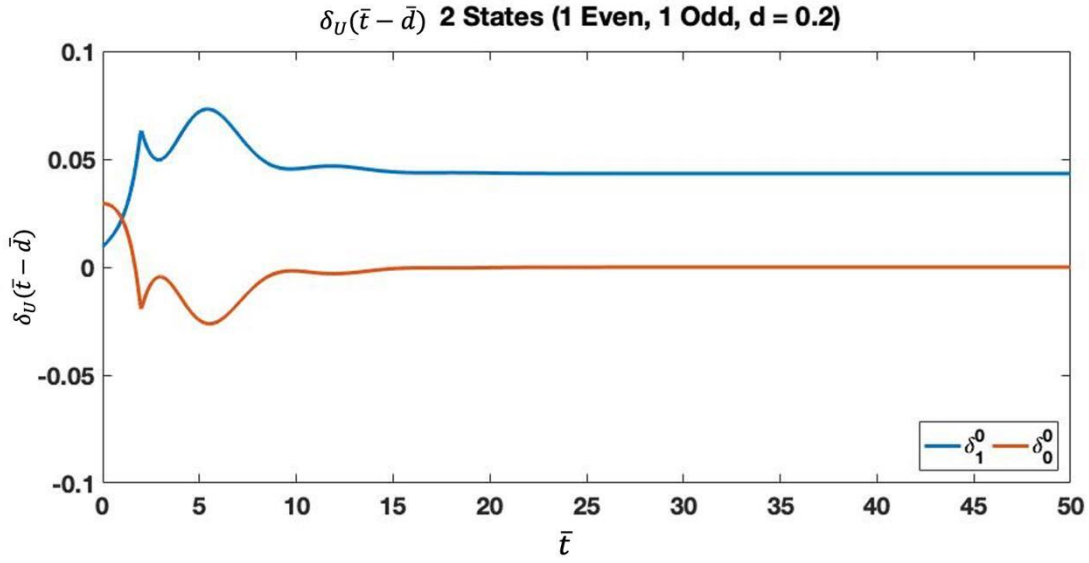
Figure 4-59: $\{\delta_n^0(\bar{t} - \bar{d})\}_U$ state variable for with 2 inflow states (1 even and 1 odd) with $d = 0.2$ with blade flapping
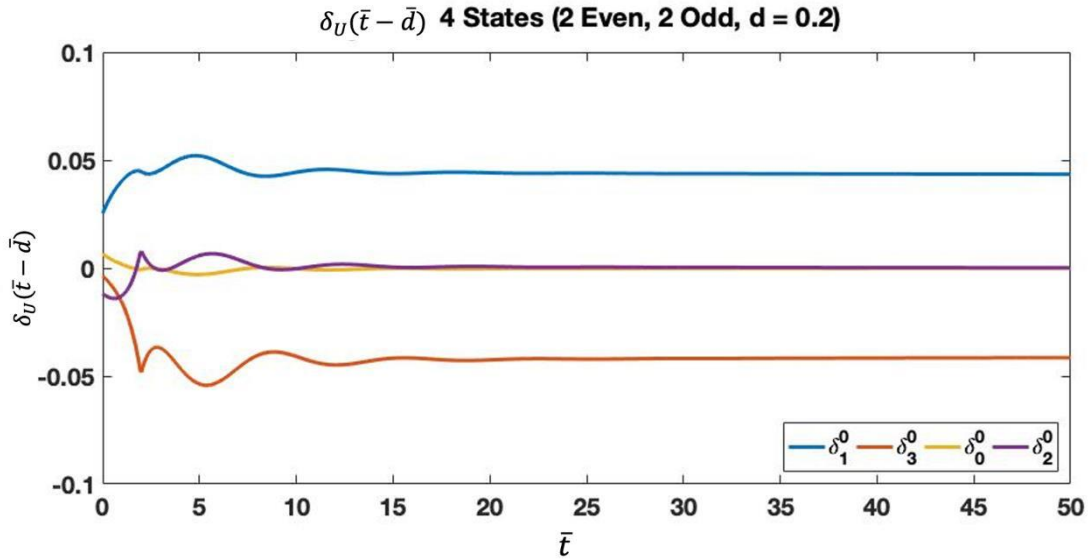
Figure 4-60: $\{\delta_n^0(\bar{t} - \bar{d})\}_U$ state variable for 4 inflow states (2 even and 2 odd) with $d = 0.2$ with blade flapping
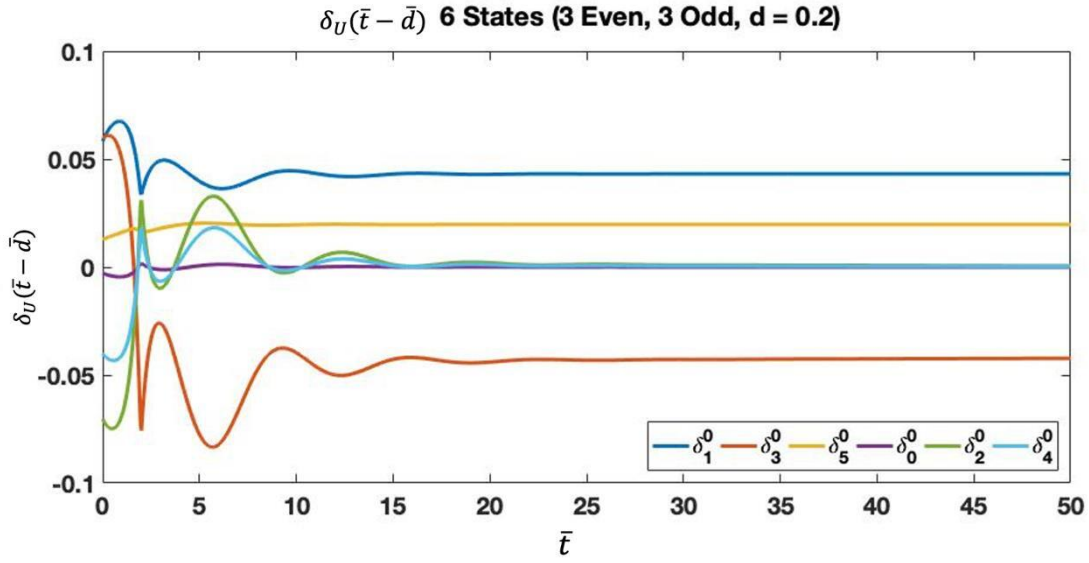
Figure 4-61: $\{\delta_n^0(\bar{t}-\bar{d})\}_U$ state variable for 6 inflow states (3 even and 3 odd) with $d = 0.2$ with blade flapping
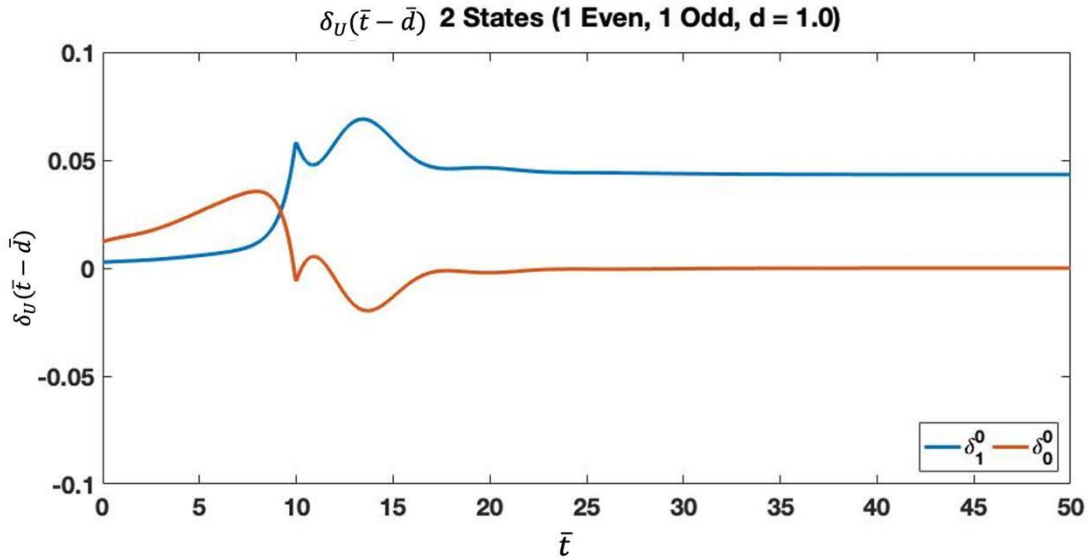
Figure 4-62: $\{\delta_n^0(\bar{t}-\bar{d})\}_U$ state variable for 2 inflow states (1 even and 1 odd) with $d = 1.0$ with blade flapping
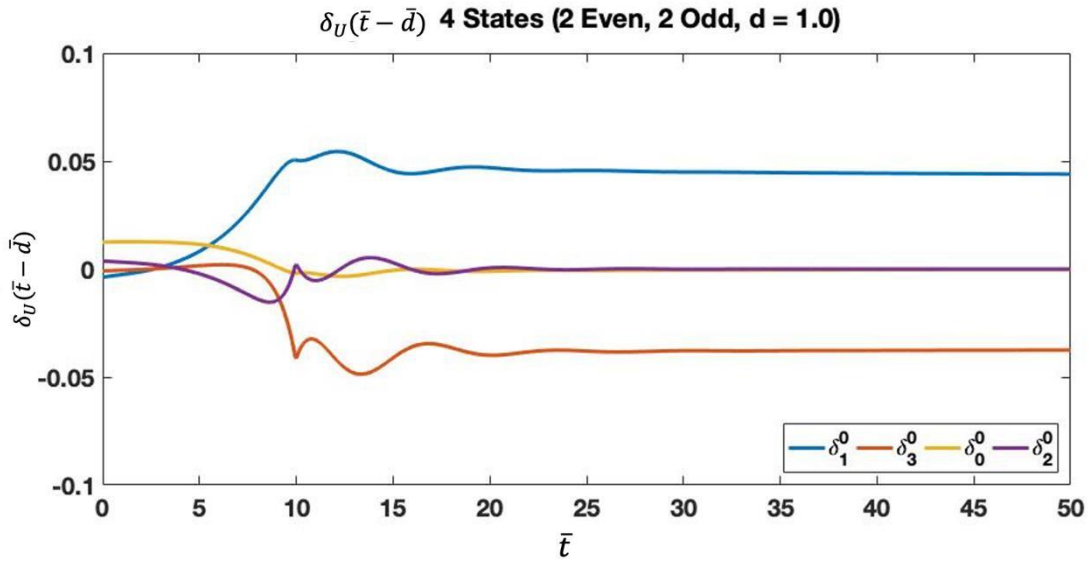
Figure 4-63: $\{\delta_n^0(\bar{t}-\bar{d})\}_U$ state variable for with 4 inflow states (2 even and 2 odd) with $d = 1.0$ with blade flapping
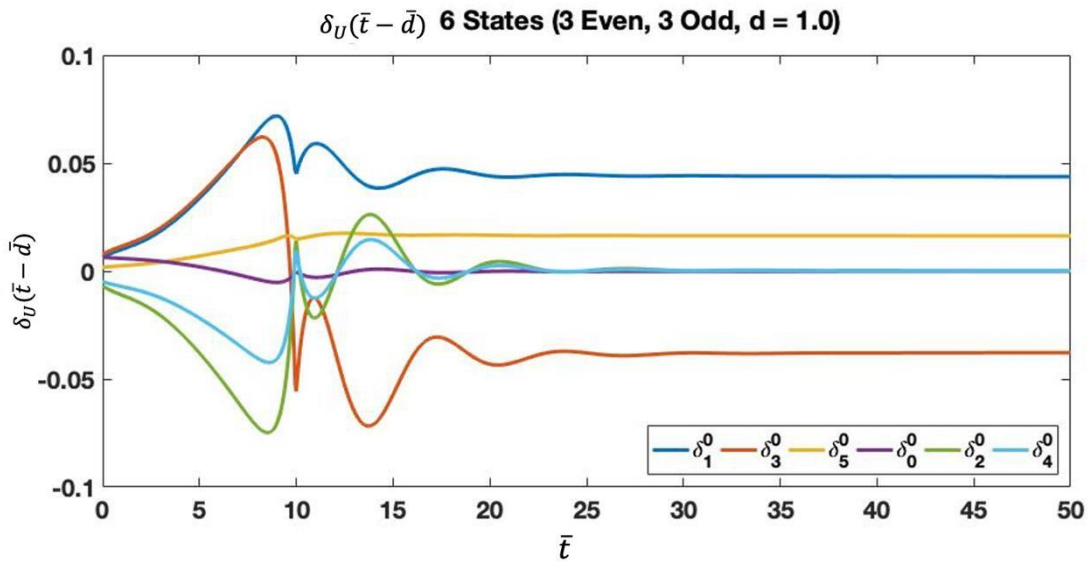
Figure 4-64: $\{\delta_n^0(\bar{t}-\bar{d})\}_U$ state variable for 6 inflow states (3 even and 3 odd) with $d = 1.0$ with blade flapping
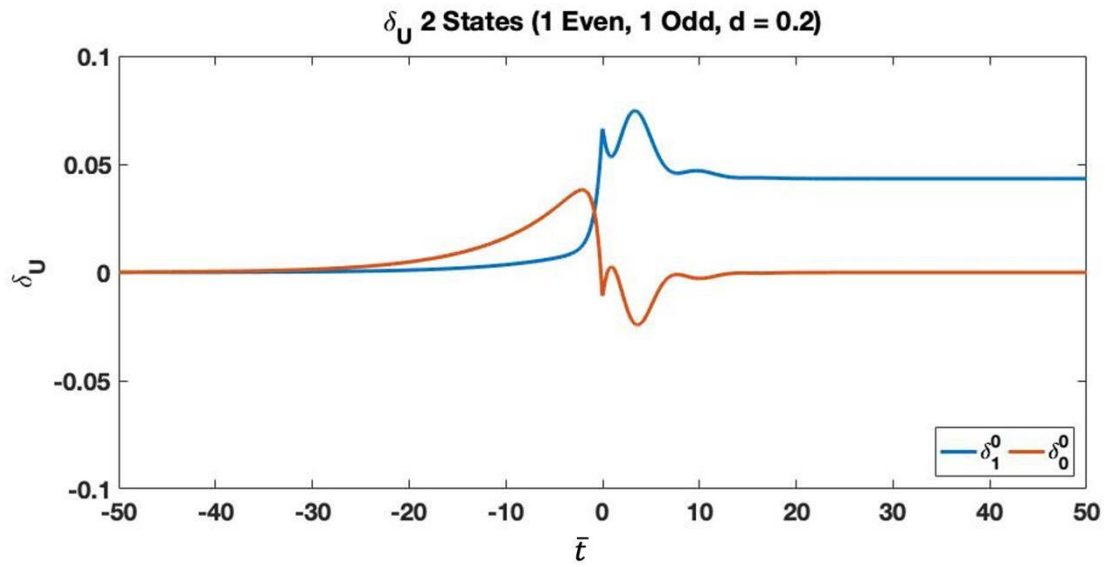
Figure 4-65: $\{\delta_n^0\}_U$ state variable for 2 inflow states (1 even and 1 odd) with $d = 0.2$ with blade flapping
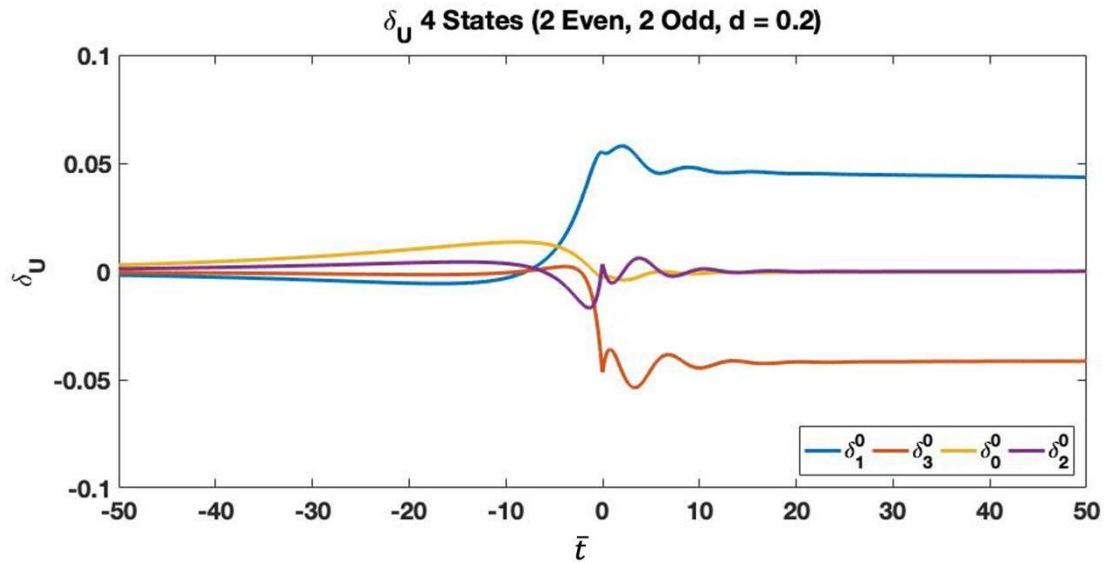
Figure 4-66: $\{\delta_n^0\}_U$ state variable for 4 inflow states (2 even and 2 odd) with $d = 0.2$ with blade flapping

108
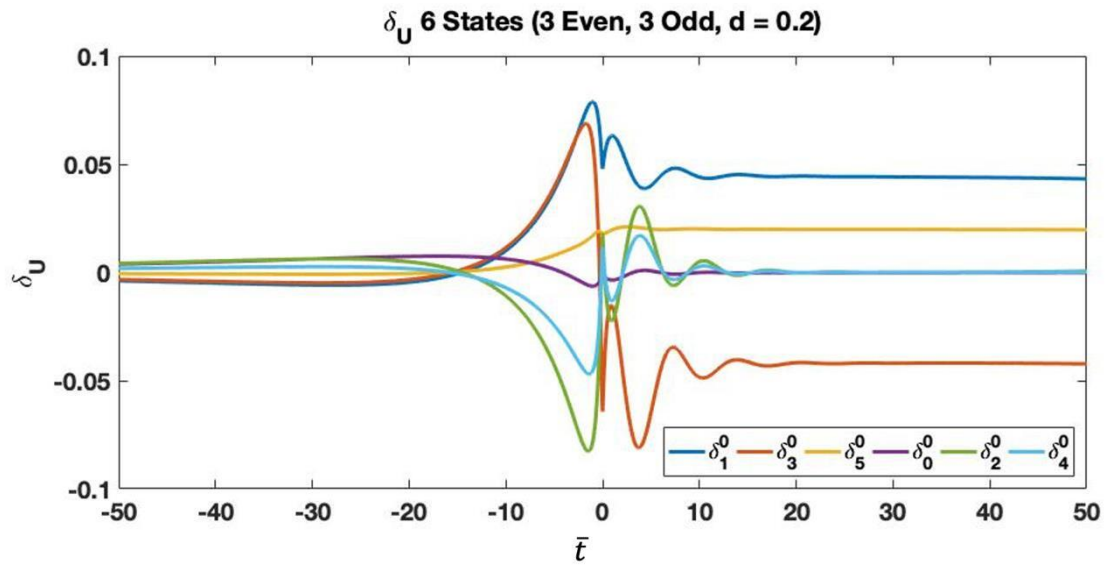
Figure 4-67: $\{\delta_n^0\}_U$ state variable for 6 inflow states (3 even and 3 odd) with $d = 0.2$ with blade flapping
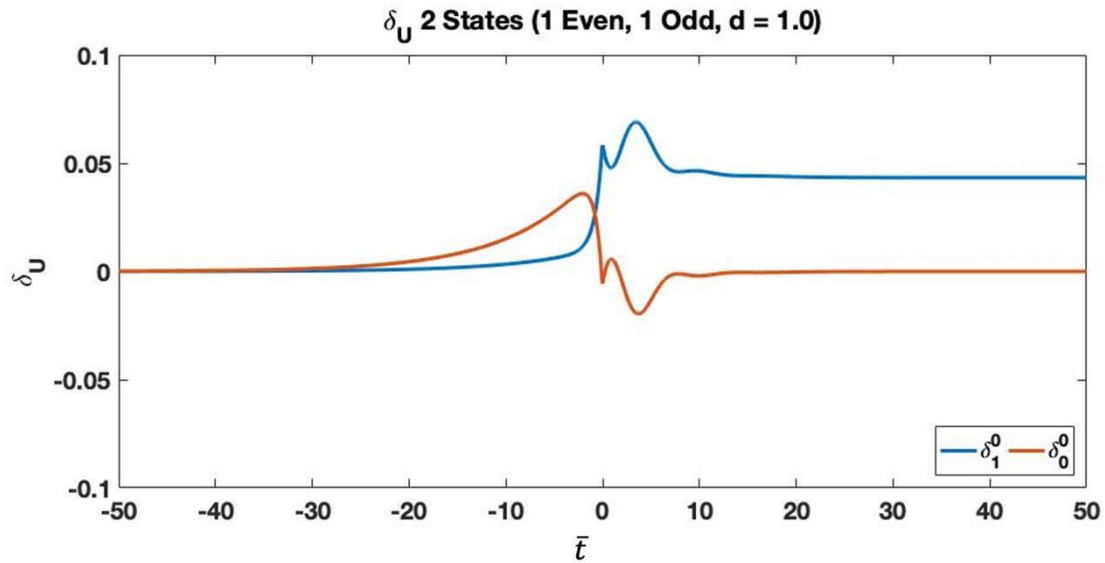
Figure 4-68: $\{\delta_n^0\}_U$ state variable for 2 inflow states (1 even and 1 odd) with $d = 1.0$ with blade flapping

109
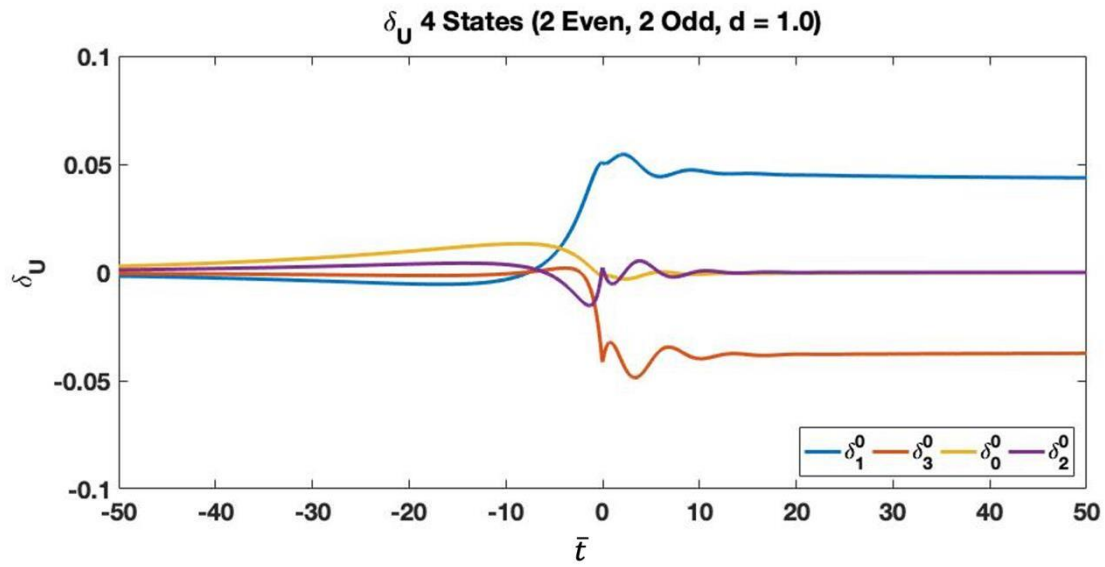
Figure 4-69: $\{\delta_n^0\}_U$ state variable for 4 inflow states (2 even and 2 odd) with $d = 1.0$ with blade flapping
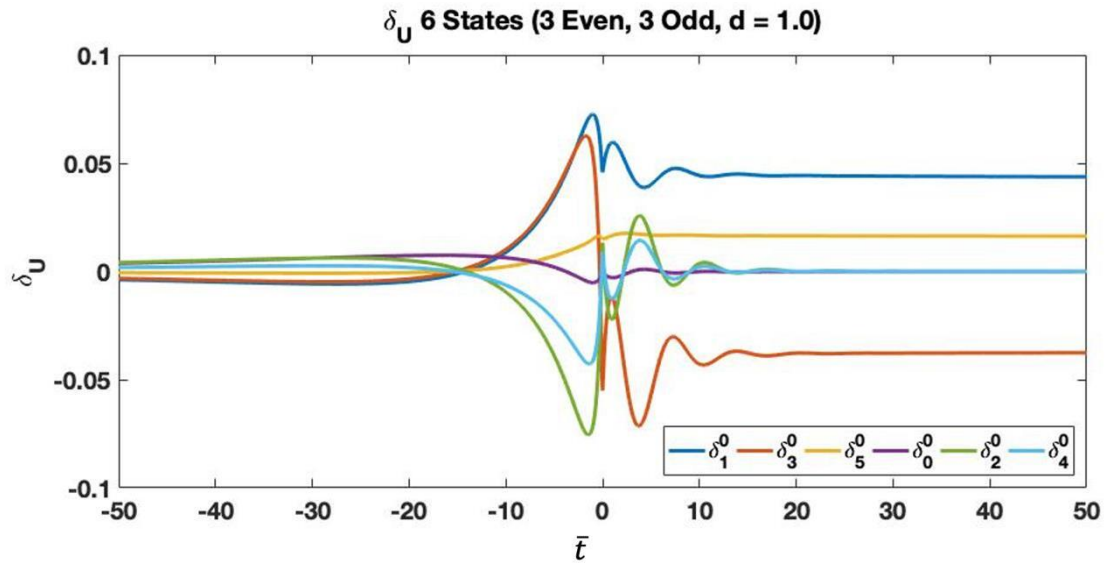
Figure 4-70: $\{\delta_n^0\}_U$ state variable for 6 inflow states (3 even and 3 odd) with $d = 1.0$ with blade flapping

110

4.3.2   Velocity Profiles with Blade Flapping

Recreating the previous velocity profiles with blade flapping we find that, for both rotors in Figs. 4-71 and 4-72, the case with 4 inflow states sees the largest dynamic oscillations from blade flapping. This is largely a result of the location on the disk and the development of the velocity profiles across the rotor (Figs. 4-26 to 4-29). The 4 inflow state profile has the highest magnitude of the profiles at $\bar{r} = 0.8$ and therefore the largest max velocity in Figs. 4-71 and 4-72. It can be said, however, that the profile shape differs significantly between the 2 state and 4 state simulation cases. The profiles with 4, 6, 10, and 20 states illustrated in Figs. 4-71 and 4-72 appear to have similar shapes and illustrate similar dynamics.

The velocity profiles with respect to $\bar{t}$ in Figs. 4-73 and 4-74 illustrate that blade flapping causes very shallow oscillations, but the previous trends of magnitudes and location of time-delay dynamics remain the same. For the rotor spacings of $d = 1.0, 2.0, 10.0$, the shape and size of the time-delay dynamics are different due to the blade flapping dynamics. For the smaller rotor spacings, the changes are more subtle and blend with the early blade flapping dynamics.
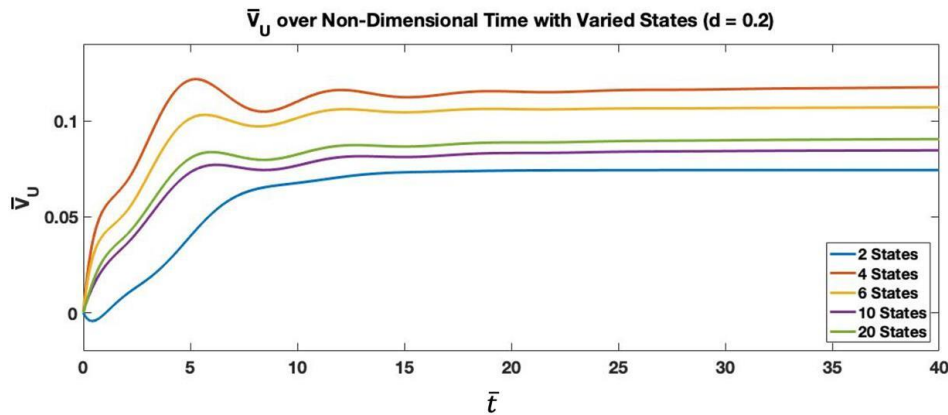
Figure 4-71: $\overline{V}_U$ for varied number of inflow states and $d = 0.2$ for system with blade flapping
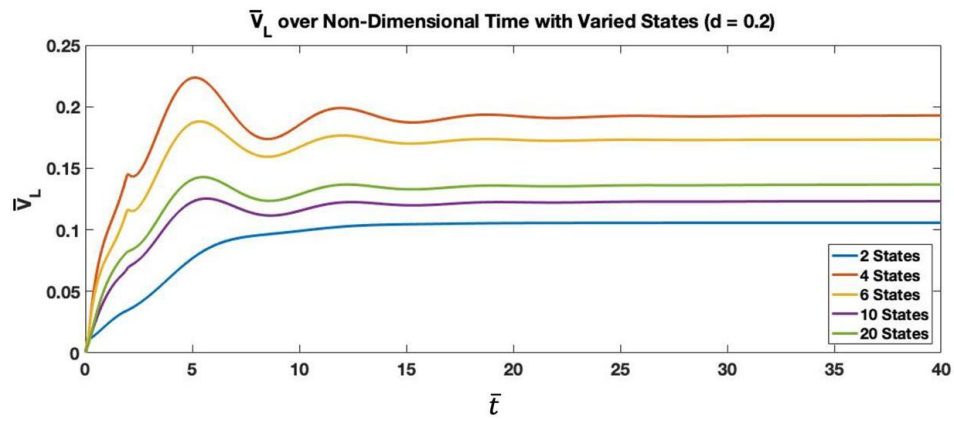
Figure 4-72: $\overline{V}_L$ for varied number of inflow states and $d = 0.2$ for system with blade flapping
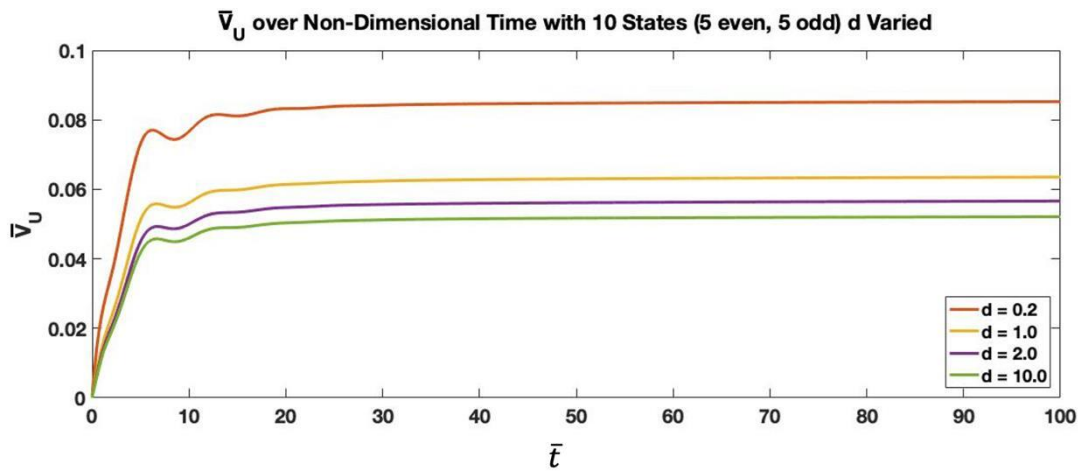
Figure 4-73: $\overline{V}_U$ for system with blade flapping and 10 inflow states and varied rotor spacing
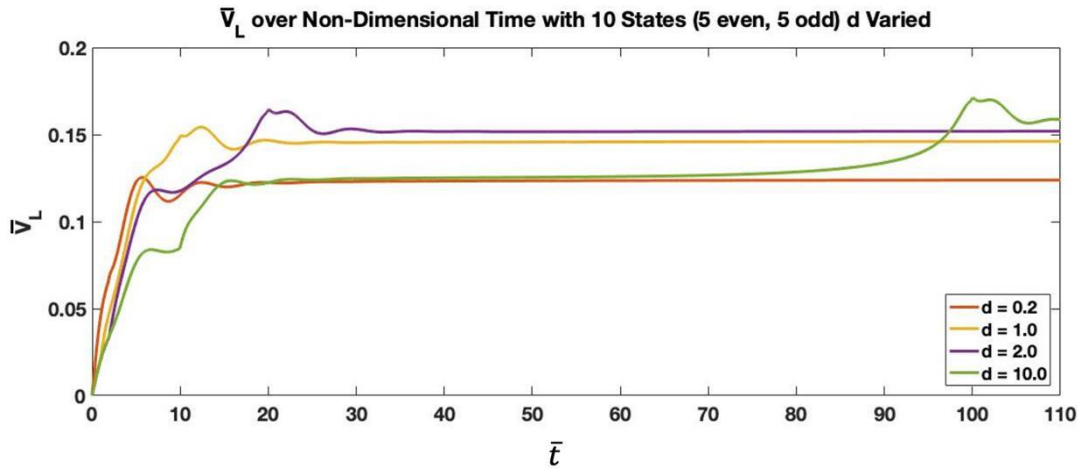
Figure 4-74: $\overline{V}_L$ for system with blade flapping and 10 inflow states and varied rotor spacing

Chapter 5

Chapter 5: Finite Number of Blades

In Chapter 4, a solution for a coaxial rotor system with an infinite number of blades was developed as a broader proof of concept with the intent of being expanded for a system with a finite number of blades. The transition to a system with a finite number of blades primarily requires summations over the number of blades to develop the state and co-state equations and the inclusion of higher harmonic solutions. In addition, climb rate (η) and advance ratio (μ) terms were added to this model. This system also provides more unique dynamics that better illustrate the rotor coupling in the system.

5.1   Model Development for Finite Number of Blades

The basis of the finite number of blades model is an extension of the work in Chapter 4. The solution of the state and co-state variables now involve sine and cosine portions of the solution. The solution approach is that used by Morillo [11] and Fei [3]. The cosine forms of the state and co-state variables are represented by α_n^m and δ_n^m, respectively, while the sine form of the state variables are β_n^m and co-state variables are ε_n^m. The state and co-state variable equations for the cosine and sine forms are:

$$[M]\left\{\overset{*}{\alpha}{}_n^m\right\}_U + \upsilon\,[D]\left[\tilde{L}^c\right]^{-1}[M]\{\alpha_n^m\}_U = [D]\{\tau_n^{mc}\}_U \tag{5.1}$$

$$[M]\left\{\overset{*}{\alpha}{}_n^m\right\}_L + \upsilon\,[D]\left[\tilde{L}^c\right]^{-1}[M]\{\alpha_n^m\}_L = [D]\{\tau_n^{mc}\}_L \tag{5.2}$$

$$-[M]\left\{\overset{*}{\delta}{}_n^m\right\}_U + \upsilon\,[D]\left[\tilde{L}^c\right]^{-1}[M]\{\delta_n^m\}_U = [D]\begin{bmatrix} \ddots & & \\ & (-1)^{n+1} & \\ & & \ddots \end{bmatrix}\{\tau_n^{mc}\}_U \tag{5.3}$$

$$[M]\left\{\overset{*}{\beta}{}_n^m\right\}_U + \upsilon\,[D]\left[\tilde{L}^s\right]^{-1}[M]\{\beta_n^m\}_U = [D]\{\tau_n^{ms}\}_U \tag{5.4}$$

$$[M]\left\{\overset{*}{\beta}{}_n^m\right\}_L + \upsilon\,[D]\left[\tilde{L}^s\right]^{-1}[M]\{\beta_n^m\}_L = [D]\{\tau_n^{ms}\}_L \tag{5.5}$$

$$-[M]\left\{\overset{*}{\varepsilon}{}_n^m\right\}_U + \upsilon\,[D]\left[\tilde{L}^s\right]^{-1}[M]\{\varepsilon_n^m\}_U = [D]\begin{bmatrix} \ddots & & \\ & (-1)^{n+1} & \\ & & \ddots \end{bmatrix}\{\tau_n^{ms}\}_U \tag{5.6}$$

The solution of the differential equations for the state and co-state variables assume zero initial conditions for all states. The co-states, on the other hand must be given defined terminal conditions, due to the backward time-marching. Here, the terminal conditions for the co-state variables are also set to zero. Although the velocity does not depend on the terminal conditions in the limit of many states, there can be some residual effect, especially for a lower number of states; but zero terminal conditions is the simplest to manipulate numerically.

Developing the finite number of blades model primarily focuses on reworking $\{\tau_n^{mc}\}_k$ and $\{\tau_n^{ms}\}_k$ terms by enhancing the lift equations and keeping the summation over the finite number of blades. In this model the U_P and U_T terms in the lift equations include the perpendicular and in plane components of flow. In Chapter 4, the summation over the finite

number of blades was manipulated to accommodate the infinite number of blades. We begin with the same $\{\tau_n^{mc}\}_k$ and $\{\tau_n^{ms}\}_k$ in Chapter 4, which are:

$$\left\{\tau_n^{0c}\right\}_k = \frac{1}{4\pi}\sum_{q=1}^{Q}\left[\int_0^1 \frac{L_{q,k}}{\rho\Omega^2 R^3}\phi_n^0\left(\bar{r}\right)d\bar{r}\right] \tag{5.7}$$

$$\left\{\tau_n^{mc}\right\}_k = \frac{1}{2\pi}\sum_{q=1}^{Q}\left[\int_0^1 \frac{L_{q,k}}{\rho\Omega^2 R^3}\phi_n^m\left(\bar{r}\right)d\bar{r}\right]\cos\left(m\psi_{q,k}\right) \tag{5.8}$$

$$\left\{\tau_n^{ms}\right\}_k = \frac{1}{2\pi}\sum_{q=1}^{Q}\left[\int_0^1 \frac{L_{q,k}}{\rho\Omega^2 R^3}\phi_n^m\left(\bar{r}\right)d\bar{r}\right]\sin\left(m\psi_{q,k}\right) \tag{5.9}$$

For the upper and lower rotors, the azimuth location of each blade is found by:

$$\psi_{q,U} = \bar{t} + 2\pi\left(\frac{q-1}{Q}\right) \tag{5.10}$$

$$\psi_{q,L} = -\bar{t} - 2\pi\left(\frac{q-1}{Q}\right) \tag{5.11}$$

In this work we will only derive the cosine form of the pressure potential ($\{\tau_n^{mc}\}_k$) in Eq. 5.8, but the axisymmetric and sine form are derived in a similar manner. From blade element theory, the lift on each blade of a rotor is represented as:

$$L_{q,k} = \frac{1}{2}\rho a c \left[U_{T,k}^2\theta_{q,k} - U_{P,k}U_{T,k}\right] \tag{5.12}$$

In this equation, c is the chord length, a is the slope of the lift curve, U_T represents the tangential velocity component, and U_P represents the perpendicular velocity component. U_T is a function of the radius of the rotor (r), the radial velocity (Ω), and the in-plane

component of flow (U) such that:

$$U_{T,k} = \Omega r + \mathrm{U} sin(\psi_{q,k}) \tag{5.13}$$

The perpendicular portion of the velocity with respect to the blade is:

$$U_{P,k} = \vartheta + w_k + \left\{\dot{b}_q\right\}_k r + \{b_q\}_k U cos(\psi_{q,k}) \tag{5.14}$$

In Eq. 5.14 w_k is the induced velocity, ϑ is the flow perpendicular to the disk, and $\{b_q\}_k$ is the blade flapping of blade q on rotor k. The induced velocity for the upper and lower rotors are:

$$w_U = V_{UU} + V_{UL} \tag{5.15}$$

$$w_L = V_{LL} + V_{LU} \tag{5.16}$$

The perpendicular velocity terms for the upper and lower rotors are:

$$U_{P,U} = \vartheta + V_{UU} + V_{UL} + \left\{\dot{b}_q\right\}_U r + \{b_q\}_U U cos(\psi_{q,U}) \tag{5.17}$$

$$U_{P,L} = \vartheta + V_{LL} + V_{LU} + \left\{\dot{b}_q\right\}_L r + \{b_q\}_L U cos(\psi_{q,L}) \tag{5.18}$$

Insertion of Eqs. 5.13, 5.17, and 5.18 into Eq. 5.12 gives the lift equations for each blade on the upper and lower rotors:

$$
\begin{aligned}
L_{q,U} = \frac{1}{2}\rho ac \bigg[&(\Omega x + U \sin{(\psi_{q,U})})^2\, \theta_{q,U} \\
&- \left(\nu + V_{UU} + V_{UL} + \left\{\dot{b}_q\right\}_U x + \{b_q\}_U\, U \cos{(\psi_{q,U})}\right) (\Omega x + U \sin{(\psi_{q,U})}) \bigg]
\end{aligned}
\tag{5.19}
$$

$$
\begin{aligned}
L_{q,L} = \frac{1}{2}\rho ac \bigg[&(\Omega x + U sin{(\psi_{q,L})})^2 \theta_{q,U} \\
&- \left(\nu + V_{LL} + V_{LU} + \left\{\dot{b}_q\right\}_L x + \{b_q\}_L U cos{(\psi_{q,L})}\right) (\Omega x + U sin{(\psi_{q,L})}) \bigg]
\end{aligned}
\tag{5.20}
$$

117

At this point, we revisit the updated axisymmetric, cosine, and sine Φ terms from Chapter 4 and further enhance them for multi-blade, coaxial rotor systems by adding the subscripts q and k to ψ to obtain:

$$\Phi_n^{0c} = \overline{P}_n^m(\nu)\overline{Q}_n^m(i\eta) \tag{5.21}$$

$$\Phi_n^{mc} = \overline{P}_n^m(\nu)\overline{Q}_n^m(i\eta)\cos(m\psi_{q,k}) \tag{5.22}$$

$$\Phi_n^{ms} = \overline{P}_n^m(\nu)\overline{Q}_n^m(i\eta)\sin(m\psi_{q,k}) \tag{5.23}$$

The shape functions are a factor of the location in space in ellipsoidal coordinates $(\overline{\nu}, \overline{\eta}, \overline{\psi})$. On the rotor disk, $\eta = 0$ and $\overline{Q}_n^m(0i) = 1$, which simplifies the above shape functions to:

$$\Phi_n^{0c} = \overline{P}_n^m(\nu) \tag{5.24}$$

$$\Phi_n^{mc} = \overline{P}_n^m(\nu)\cos(m\psi_{q,k}) \tag{5.25}$$

$$\Phi_n^{ms} = \overline{P}_n^m(\nu)\sin(m\psi_{q,k}) \tag{5.26}$$

At this point, the coupled velocity terms in are updated with the new Φ_n^m in Eqs. 5.24-5.26 and summations accounting for multiple inflow states. Finally, nondimensionalizing the coupled velocity terms ($\overline{V}_{xx} = V_{xx}/\Omega R$), we obtain:

$$
\begin{aligned}
\overline{V}_{UU}(\overline{t}, \nu, \eta, \psi_{q,U}) = &\sum \{\alpha_n^m(\overline{t})\}_U \overline{P}_n^m(\nu_{on})\cos(m\psi_{q,U}) \\
&+ \sum \{\beta_n^m(\overline{t})\}_U \overline{P}_n^m(\nu_{on})\sin(m\psi_{q,U})
\end{aligned}
\tag{5.27}
$$

$$
\begin{aligned}
\overline{V}_{LL}(\overline{t}, \nu, \eta, \psi_{q,L}) = &\sum \{\alpha_n^m(\overline{t})\}_L \overline{P}_n^m(\nu_{on})\cos(m\psi_{q,L}) \\
&+ \sum \{\beta_n^m(\overline{t})\}_L \overline{P}_n^m(\nu_{on})\sin(m\psi al_{q,L})
\end{aligned}
\tag{5.28}
$$

118

$$\overline{V}_{UL}\left(\bar{t}, \nu, \eta, \psi_{q,U}\right) = \sum \left\{\alpha_n^m(\bar{t})\right\}_L \overline{P}_n^m\left(\nu_{off}\right) \overline{Q}_n^m\left(i\eta_{off}\right) \cos\left(m\psi_{q,U}\right)$$
$$+ \sum \left\{\beta_n^m(\bar{t})\right\}_L \overline{P}_n^m\left(\nu_{off}\right) \overline{Q}_n^m\left(i\eta_{off}\right) \sin(m\psi_{q,U}) \tag{5.29}$$

$$\overline{V}_{LU}\left(\bar{t}, \nu, \eta, \psi_{q,L}\right) = \sum \left\{\alpha_n^m(\bar{t}-\bar{d})\right\}_U \overline{P}_n^m\left(\nu_{on}\right) \cos\left(m\psi_{q,L}\right)$$
$$+ \sum \left\{\beta_n^m\left(\bar{t}-\bar{d}\right)\right\}_L \overline{P}_n^m\left(\nu_{on}\right) \sin\left(m\psi_{q,L}\right)$$
$$+ \sum \left\{\delta_n^m(\bar{t}-\bar{d})\right\}_L \overline{P}_n^m\left(\nu_{on}\right) \cos\left(m\psi_{q,L}^*\right)$$
$$+ \sum \left\{\varepsilon_n^m(\bar{t}-\bar{d})\right\}_L \overline{P}_n^m\left(\nu_{on}\right) \sin(m\psi_{q,L}^*) \tag{5.30}$$
$$+ \sum \left\{\delta_n^m(\bar{t})\right\}_L \overline{P}_n^m\left(\nu_{off}\right) \overline{Q}_n^m\left(i\eta_{off}\right) \cos\left(m\psi_{q,L}^*\right)$$
$$+ \sum \left\{\varepsilon_n^m(\bar{t})\right\}_L \overline{P}_n^m\left(\nu_{off}\right) \overline{Q}_n^m\left(i\eta_{off}\right) \sin(m\psi_{q,L}^*)$$

We next combine Eqs. 5.27-5.30 with Eqs. 5.19-5.20 and plug them into Eq. 5.8 and nondimensionalize the terms with the relations $\mu = U/\Omega R, \eta = \vartheta/\Omega R, \bar{r} = x/R$, and $b^* = \dot{b}/\Omega$. Thus, the new $\{\tau_n^{mc}\}_U$ and $\{\tau_n^{mc}\}_L$ terms are represented as:

$$\{\tau_n^{mc}\}_U = \frac{\sigma a}{4Q} \sum_{q=1}^{Q} \begin{bmatrix} \ddots & & \\ & \cos{(m\psi_{q,U})} & \\ & & \ddots \end{bmatrix}$$

$$\left(\left(\{A_n^m\} + 2\mu\sin{(\psi_{q,U})}\{A_n^m\}_2 + \mu^2\sin^2{(\psi_{q,U})}\{A_n^m\}_3 \right)\theta_{q,U} - \eta\{A_n^m\}_2 - \mu\eta\sin{(\psi_{q,U})}\{A_n^m\}_3 \right.$$

$$- \left([B_{nj}^{mr}] + \mu\sin{(\psi_{q,U})}[B_{nj}^{mr}]_2\right)\left(\begin{bmatrix} \ddots & & \\ & \cos{(r\psi_{q,U})} & \\ & & \ddots \end{bmatrix}\{\alpha_j^r(\bar{t})\}_U + \begin{bmatrix} \ddots & & \\ & \sin{(r\psi_{q,U})} & \\ & & \ddots \end{bmatrix}\{\beta_j^r(\bar{t})\}_U\right)$$

$$- \left([C_{nj}^{mr}] + \mu\sin{(\psi_{q,U})}[C_{nj}^{mr}]_2\right)\left(\begin{bmatrix} \ddots & & \\ & \cos{(r\psi_{q,U})} & \\ & & \ddots \end{bmatrix}\{\alpha_j^r(\bar{t})\}_L + \begin{bmatrix} \ddots & & \\ & \sin{(r\psi_{q,U})} & \\ & & \ddots \end{bmatrix}\{\beta_j^r(\bar{t})\}_L\right)$$

$$\left. - \{A_n^m\}\overset{*}{b}_{q,U} - \mu\sin{(\psi_{q,U})}\{A_n^m\}_2\overset{*}{b}_{q,U} - \mu\cos{(\psi_{q,U})}\{A_n^m\}_2 b_{q,U} - \mu^2\cos{(\psi_{q,U})}\sin{(\psi_{q,U})}\{A_n^m\}_3 b_{q,U}\right)$$

$$(5.31)$$

$$\{\tau_n^{mc}\}_L = \frac{\sigma a}{4Q} \sum_{q=1}^{Q} \begin{bmatrix} \ddots & & \\ & \cos{(m\psi_{q,L})} & \\ & & \ddots \end{bmatrix}$$

$$\left(\left(\{A_n^m\} + 2\mu\sin{(\psi_{q,L})}\{A_n^m\}_2 + \mu^2\sin^2{(\psi_{q,L})}\{A_n^m\}_3 \right)\theta_{q,L} - \eta\{A_n^m\}_2 - \mu\eta\sin{(\psi_{q,L})}\{A_n^m\}_3 \right.$$

$$- \left([B_{nj}^{mr}] + \mu\sin{(\psi_{q,L})}[B_{nj}^{mr}]_2\right)\left(\begin{bmatrix} \ddots & & \\ & \cos{(r\psi_{q,L})} & \\ & & \ddots \end{bmatrix}\left(\{\alpha_j^r(\bar{t})\}_L + \{\alpha_j^r(\bar{t}-\bar{d})\}_U + \{\delta_j^r(\bar{t}-\bar{d})\}_U\right)\right.$$

$$\left. + \begin{bmatrix} \ddots & & \\ & \sin{(r\psi_{q,L})} & \\ & & \ddots \end{bmatrix}\left(\{\beta_j^r(\bar{t})\}_L + \{\beta_j^r(\bar{t}-\bar{d})\}_U + \{\varepsilon_j^r(\bar{t}-\bar{d})\}_U\right)\right)$$

$$+ \left([C_{nj}^{mr}] + \mu\sin{(\psi_{q,L})}[C_{nj}^{mr}]_2\right)\left(\begin{bmatrix} \ddots & & \\ & \cos{(r\psi_{q,L})} & \\ & & \ddots \end{bmatrix}\{\delta_j^r(\bar{t})\}_U + \begin{bmatrix} \ddots & & \\ & \sin{(r\psi_{q,L})} & \\ & & \ddots \end{bmatrix}\{\varepsilon_j^r(\bar{t})\}_U\right)$$

$$\left. - \{A_n^m\}\overset{*}{b}_{q,L} - \mu\sin{(\psi_{q,L})}\{A_n^m\}_2\overset{*}{b}_{q,L} - \mu\cos{(L)}\{A_n^m\}_2 b_{q,L} - \mu^2\cos{(\psi_{q,L})}\sin{(\psi_{q,L})}\{A_n^m\}_3 b_{q,L}\right)$$

$$(5.32)$$

where $\{A\}$, $\{A_2\}$, and $\{A_3\}$ are pitch coupling terms, $[B]$ and $[B_2]$ are the on-disk inflow coupling terms, and $[C]$ and $[C_2]$ are the off-disk inflow coupling terms. These terms can be precalculated prior to simulation because they are not a function of time. The coupling

terms are defined as follows:

$$\{A_n^m\} = \int_0^1 \sqrt{1 - \nu_{on}^2} \, \overline{P}_n^m \left(\nu_{on} \right) d\nu \tag{5.33}$$

$$\{A_n^m\}_2 = \int_0^1 \overline{P}_n^m \left(\nu_{on} \right) d\nu \tag{5.34}$$

$$\{A_n^m\}_3 = \int_0^1 \frac{1}{\sqrt{1 - \nu_{on}^2}} \overline{P}_n^m \left(\nu_{on} \right) d\nu \tag{5.35}$$

$$[B_{nj}^{mr}] = \int_0^1 \overline{P}_n^m \left(\nu_{on} \right) \overline{P}_j^r \left(\nu_{on} \right) d\nu \tag{5.36}$$

$$[B_{nj}^{mr}]_2 = \int_0^1 \frac{1}{\sqrt{1 - \nu_{on}^2}} \overline{P}_n^m \left(\nu_{on}^2 \right) \overline{P}_j^r \left(\nu_{on}^2 \right) d\nu \tag{5.37}$$

$$[C_{nj}^{mr}] = \int_0^1 \overline{P}_n^m \left(\nu_{off} \right) \overline{Q}_n^m \left(i\eta_{off} \right) \overline{P}_j^r \left(\nu_{on} \right) d\nu \tag{5.38}$$

$$[C_{nj}^{mr}]_2 = \int_0^1 \frac{1}{\sqrt{1 - \nu_{off}^2}} \overline{P}_n^m \left(\nu_{off} \right) \overline{Q}_n^m \left(i\eta_{off} \right) \overline{P}_j^r \left(\nu_{on} \right) d\nu \tag{5.39}$$

In this dissertation, numerical results include only the case of axial flow (climb); and, therefore, the nondimensional in-plane component of flow, μ, is zero. This reduces the impact of some of the coupling matrices in Eqs. 5.31-5.32. This will also impact the blade flapping terms below in Eqs. 5.47-5.48.

5.2 Development of Blade Flapping Terms

The final portion of the derivation of equations is developing the blade flapping terms. The equations for the blade flapping terms have many similarities to the equations for the state and co-state variables but differ slightly in format. The governing equation for the blade flapping terms is:

$$I_y \ddot{b}_{q,k} + \left(I_y \Omega^2 + \kappa_\beta\right) b_{q,k} = \int_0^L L_{q,k} r dr \tag{5.40}$$

where I_y is the flapping inertia of the blade and κ_β is the root spring. The coupling terms in this case only consist of on-disk and off-disk terms and work out to be:

$$\left\{\widetilde{B}_n^m\right\} = \int_0^1 \nu_{on} \sqrt{1 - \nu_{on}^2} \overline{P}_n^m (\nu_{on}) \, d\nu \tag{5.41}$$

$$\left\{\widetilde{B}_n^m\right\}_2 = \int_0^1 \nu_{on} \, \overline{P}_n^m (\nu_{on}) \, d\nu \tag{5.42}$$

$$\left\{\widetilde{C}_n^m\right\} = \int_0^1 \nu_{off} \sqrt{1 - \nu_{off}^2} \overline{P}_n^m (\nu_{off}) \overline{Q}_n^m (i\eta_{off}) \, d\nu \tag{5.43}$$

$$\left\{\widetilde{C}_n^m\right\}_2 = \int_0^1 \nu \, \overline{P}_n^m (\nu_{off}) \overline{Q}_n^m (i\eta_{off}) \, d\nu \tag{5.44}$$

We further simplify the blade flapping solution with the following relationships:

$$p^2 = \left(1 + \frac{\kappa_\beta}{I_y \Omega^2}\right) \tag{5.45}$$

$$\gamma = \frac{\rho a c R^4}{I_y} \tag{5.46}$$

Applying these relationships along with the blade flapping coupling terms and nondimensionalizing the equation, we obtain:

$$
\overset{**}{b}_{q,U} + p^2 b_{q,U} =
$$

$$
\frac{\gamma}{2}\left(\left(\frac{1}{4} + \frac{2}{3}\mu\sin\left(\psi_{q,U}\right) + \frac{1}{2}\mu^2\sin^2\left(\psi_{q,U}\right)\right)\theta_{q,U} - \frac{1}{3}\eta - \frac{1}{2}\eta\mu\sin\left(\psi_{q,U}\right)\right.
$$

$$
- \left(\{\tilde{B}_n^m\}^T + \mu\sin\left(\psi_{q,U}\right)\{\tilde{B}_n^m\}_2^T\right)\left(\begin{bmatrix} \ddots & & \\ & \cos\left(m\psi_{q,U}\right) & \\ & & \ddots \end{bmatrix}\{\alpha_n^m\left(\bar{t}\right)\}_U\right.
$$

$$
+ \begin{bmatrix} \ddots & & \\ & \sin\left(m\psi_{q,U}\right) & \\ & & \ddots \end{bmatrix}\{\beta_n^m\left(\bar{t}\right)\}_U\Bigg)
$$

$$
- \left(\{\tilde{C}_n^m\}^T + \mu\sin\left(\psi_{q,U}\right)\{\tilde{C}_n^m\}_2^T\right)\left(\begin{bmatrix} \ddots & & \\ & \cos\left(m\psi_{q,U}\right) & \\ & & \ddots \end{bmatrix}\{\alpha_n^m\left(\bar{t}\right)\}_L\right.
$$

$$
+ \begin{bmatrix} \ddots & & \\ & \sin\left(m\psi_{q,U}\right) & \\ & & \ddots \end{bmatrix}\{\beta_n^m\left(\bar{t}\right)\}_L\Bigg)
$$

$$
\left. - \frac{1}{4}\overset{*}{b}_{q,U} - \frac{1}{3}\mu\sin\left(\psi_{q,U}\right)\overset{*}{b}_{q,U} - \frac{1}{3}\mu\cos\left(\psi_{q,U}\right)b_{q,U} - \frac{1}{2}\mu^2\cos\left(\psi_{q,U}\right)\sin\left(\psi_{q,U}\right)b_{q,U}\right)
$$

$$(5.47)$$

$$\overset{**}{b}_{q,L} + p^2 b_{q,L} =$$

$$\frac{\gamma}{2}\Bigg(\Big(\Big(\frac{1}{4} + \frac{2}{3}\mu\sin\left(\psi_{q,U}\right) + \frac{1}{2}\mu^2\sin^2\left(\psi_{q,U}\right)\Big)\Big)\theta_{q,L} - \frac{1}{3}\eta - \frac{1}{2}\eta\mu\sin\left(\psi_{q,L}\right)$$

$$- \Big(\{\widetilde{B}_n^m\}^T + \mu\sin\left(\psi_{q,L}\right)\{\widetilde{B}_n^m\}_2^T\Big)\Bigg(\begin{bmatrix} \ddots & & \\ & \cos\left(m\psi_{q,L}\right) & \\ & & \ddots \end{bmatrix}\Big(\{\alpha_n^m\left(\bar{t}\right)\}_L + \{\alpha_n^m\left(\bar{t}-\bar{d}\right)\}_U + \{\delta_n^m\left(\bar{t}-\bar{d}\right)\}_U\Big)$$

$$+ \begin{bmatrix} \ddots & & \\ & \sin\left(m\psi_{q,L}\right) & \\ & & \ddots \end{bmatrix}\Big(\{\beta_n^m\left(\bar{t}\right)\}_L + \{\beta_n^m\left(\bar{t}-\bar{d}\right)\}_U + \{\varepsilon_n^m\left(\bar{t}-\bar{d}\right)\}_U\Big)\Bigg)$$

$$+ \Big(\{\widetilde{C}_n^m\}^T + \mu\sin\left(\psi_{q,L}\right)\{\widetilde{C}_n^m\}_2^T\Big)\Bigg(\begin{bmatrix} \ddots & & \\ & \cos\left(m\psi_{q,L}\right) & \\ & & \ddots \end{bmatrix}\{\delta_n^m\left(\bar{t}\right)\}_U$$

$$+ \begin{bmatrix} \ddots & & \\ & \sin\left(m\psi_{q,L}\right) & \\ & & \ddots \end{bmatrix}\{\varepsilon_n^m\left(\bar{t}\right)\}_U\Bigg)$$

$$- \frac{1}{4}\overset{*}{b}_{q,L} - \frac{1}{3}\mu\sin\left(\psi_{q,L}\right)\overset{*}{b}_{q,L} - \frac{1}{3}\mu\cos\left(\psi_{q,L}\right)b_{q,L} - \frac{1}{2}\mu^2\cos\left(\psi_{q,L}\right)\sin\left(\psi_{q,L}\right)b_{q,L}\Bigg)$$

$$(5.48)$$

5.3 Numerical Illustrations of Coaxial Rotor with a Finite Number of Blades

With the model developed in this chapter, we investigate how variations in d, N, and Q impact the dynamics in velocity profiles, the steady-state region in the velocity profiles, and the blade flapping dynamics. In addition, velocity contour plots of each rotor disk plane will be discussed to illustrate velocity across the entire disk at a given time. All of the results in this section are presented for the case of axial flow ($\chi = 0$, $\mu = 0$) and, aside from the contour plots, are at a nondimensional radial distance $\bar{r} = 0.8$ and azimuth angle $\psi_{q,k} = 0$. The fixed system parameters for the coaxial rotor system in this work are as follows: $\theta_U = \theta_L = 0.1605$, $\gamma = 5$, $p^2 = 1.08$, $\sigma = 0.1$, and $C_T = 0.001$. It is acknowledged that a coaxial rotor system would not actually have a rotor spacing equal to and exceeding

the length of the rotor radius, but the focus of this work is to explore the boundaries of the system to determine how the finite-state model behaves in a wide range of scenarios. The time delays presented here are realistic because v could be realistically adjusted to create the same $\overline{d}$ relationships. The profiles presented here would not be entirely the same because v appears several times throughout the model, but it is important to understand how the time delay would behave in many scenarios should a system require a larger time delay.

5.3.1 Impact of Rotor Spacing on Velocity Profile Dynamics

The total velocity on the upper rotor $\overline{V}_U$ for varied d is outlined in Figs. 5-1 to 5-4. In Fig. 5-1, for a system that contains three-bladed rotors with $M = 3$ harmonics, the velocity profiles decrease in amplitude and magnitude as the rotor spacing increases. This is due to the decreasing impact of the lower rotor on the upper rotor. Overall, the dynamics of the profile are uniform with no unique variation due to the rotor spacing. In Fig. 5-2, the same three-bladed system is analyzed with $M = 6$ harmonics and shows the similar trend of decreasing magnitudes and amplitudes with increased rotor spacing. Figures 5-3 and 5-4 illustrate $\overline{V}_U$ for a system of four-bladed rotors with $M = 4$ and $M = 8$ harmonics, respectively. The major difference in the trends for the four-bladed system is that the addition of an extra blade to each rotor (with the same solidity as the three-bladed system) results in a reduction in the magnitudes of the velocity peaks because the load in the system is now distributed between more blades. In addition, there is an extra oscillation per full revolution because of the extra blade. However, the average velocity remains the same in the system. After a rotor spacing of $d = 0.4$ there is very little change in the $\overline{V}_U$ profile as the effect of the lower rotor on the upper approaches zero. It is important to note that blade passage does not actually occur at the peak, but instead it occurs right before the peak. For an $M = Q$ harmonic case, the blade passing occurs midway between the minima and maxima. For the

125

lower rotor case this is not entirely true after $\bar{t} = \bar{d}$ because the vortices from the upper rotor impact the peak occurrence in the lower rotor velocity profile.

The impact of rotor spacing on the total velocity on the lower rotor $\overline{V}_L$ is outlined in Figs. 5-5 to 5-8. For a three-bladed system with $M = 3$ harmonics in Figs. 5-5 and 5-6, it is illustrated that the rotor spacing impacts the development of the velocity profile due to the variability in how long it takes the flow from the upper rotor to hit the lower rotor. The early dynamics of the velocity profiles are similar. This is especially evident for the larger rotor spacings, $d = 1.1 - 1.9$. However, the more interesting dynamics on the lower rotor occur when the flow from the upper rotor hits the lower rotor. This happens when the $\bar{t} = \bar{d}$ and thus we will refer to the dynamics in this region as the time-delay dynamics. The time-delay dynamics are denoted by black vertical lines and rotor spacing descriptors throughout this chapter. In Figs. 5-5 and 5-6 the time-delay dynamics cause sudden jumps before the profile begins to oscillate around a higher magnitude. For a four-bladed system with $M = 4$ harmonics, Figs. 5-7 and 5-8 illustrate that the time-delay dynamics in the $\overline{V}_L$ profiles can vary significantly. For $d = 0.1$ in Fig. 5-7, there is a sudden drop off, whereas for $d = 0.3$ the change very slight. For $d = 0.9$ the dynamics span a larger region in the area where the effect of the time delay takes place. For all of these plots, as the rotor spacing increases, the magnitude and amplitude of the $\overline{V}_L$ profiles increase. In addition, it should be noted that the dynamics are not constant for different azimuth angles around the disk and the dynamics shown here are simply a representation of how the time-delay dynamics at a set point change with d and Q. The variations in dynamics in relation to different locations on the disk, specifically azimuth, will be discussed later in this chapter.

The velocity components $\overline{V}_{UU}$, $\overline{V}_{UL}$, $\overline{V}_{LL}$, and $\overline{V}_{LU}$ for a system with $Q = 3$ and $M = 3$ are outlined in Figs. 5-9 and 5-10 and for a system with $Q = 4$ and $M = 4$ are outlined in

Figs. 5-11 and 5-12. The rotor spacings for these systems are $d = 0.1$ and $d = 0.5$. As the rotor spacing is increased $\overline{V}_{UL}$ approaches zero and $\overline{V}_{LU}$ increases significantly. There are only minor changes to $\overline{V}_{UU}$ and $\overline{V}_{LL}$ illustrates a slight drop off in average velocity for the larger rotor spacing. The fact that $\overline{V}_{UL}$ approaches zero and $\overline{V}_{UU}$ shows little change with increasing rotor spacing validates the above trend that $\overline{V}_{U}$ does not vary much with larger rotor spacing. In addition, because $\overline{V}_{UL}$ approaches zero and $\overline{V}_{UU}$ experiences minor change, only a deeper analysis of the impact of rotor spacing on $\overline{V}_{LL}$ and $\overline{V}_{LU}$ will be discussed.

The $\overline{V}_{LL}$ profiles in Figs. 5-13 to 5-16 reveal that there is an initial overall increase followed by a decrease. This is a result of the time-delay and the rotor adjusting to the initial startup of the system. The later portion of the overall decrease is a result of the flow from the upper rotor hitting the lower rotor. The number of blades on each rotor does not impact the overall trends but does impact the shape of the peaks. This is due to spreading the total load between a different number of blades and the location on the disk.

The $\overline{V}_{LU}$ profiles in Figs. 5-17 through 5-20 show two distinct regions that are divided at $\overline{t} = \overline{d}$. The region before the flow from the upper rotor hits the lower rotor is highlighted by a smooth increase without oscillations. The region after $\overline{t} = \overline{d}$ also includes an overall gradual increase with oscillations. These oscillations represent the vortices shed from the blades on the upper rotor hitting the lower rotor. At $\overline{t} = \overline{d}$, there is either a jump (three-bladed rotors) or a slight drop (four-bladed rotors) that marks the flow from the upper rotor reaching the lower rotor.
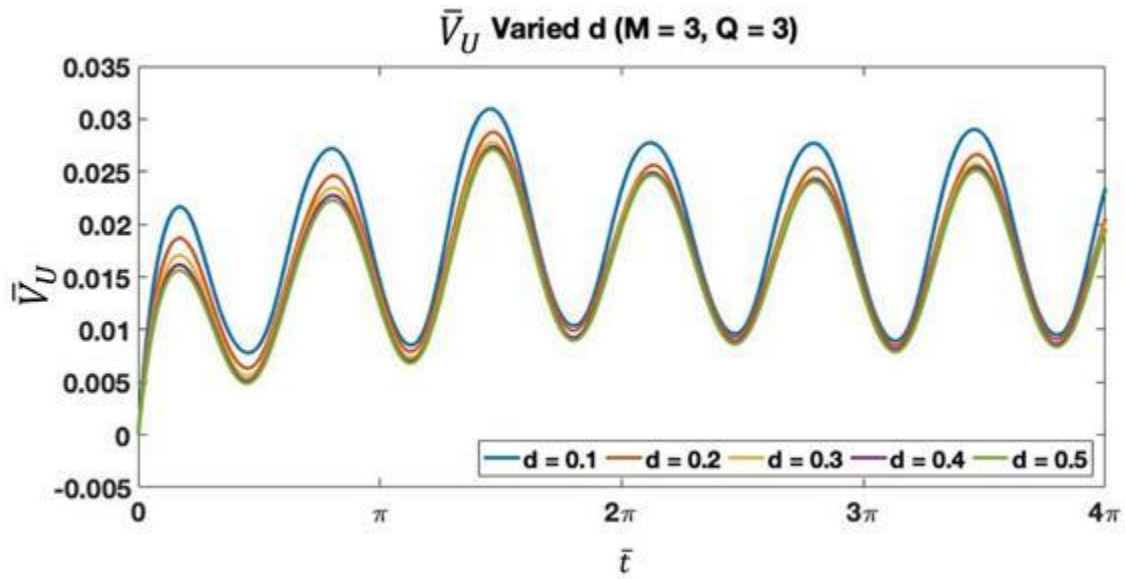
Figure 5-1: Velocity on upper rotor with 3 blades and 3 harmonics at varied rotor spacings ($d = 0.1$-0.5)
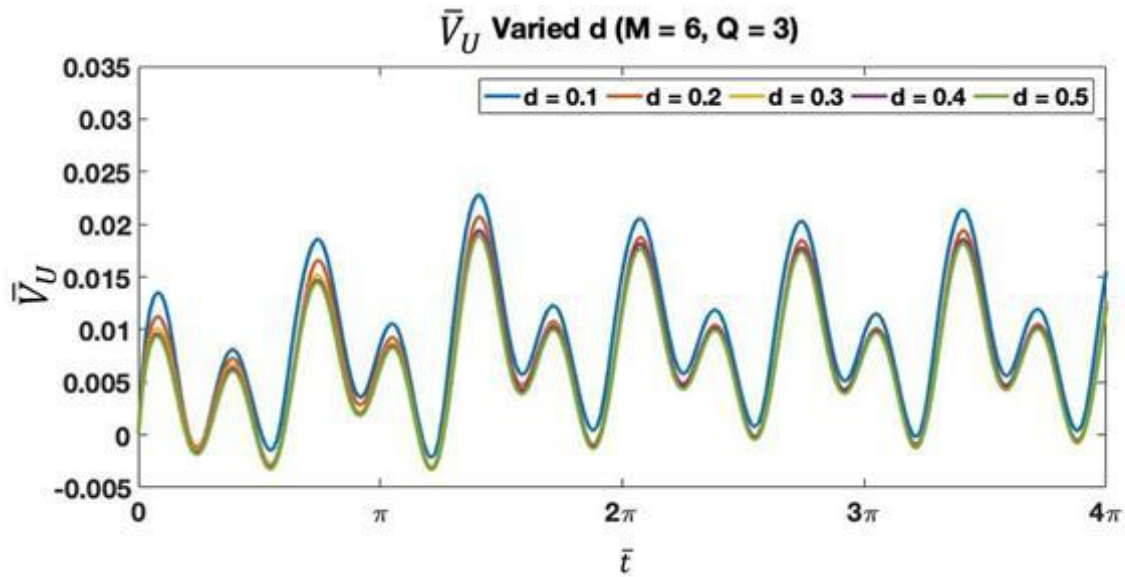
Figure 5-2: Velocity on upper rotor with 3 blades and 6 harmonics at varied rotor spacings ($d = 0.1$-0.5)
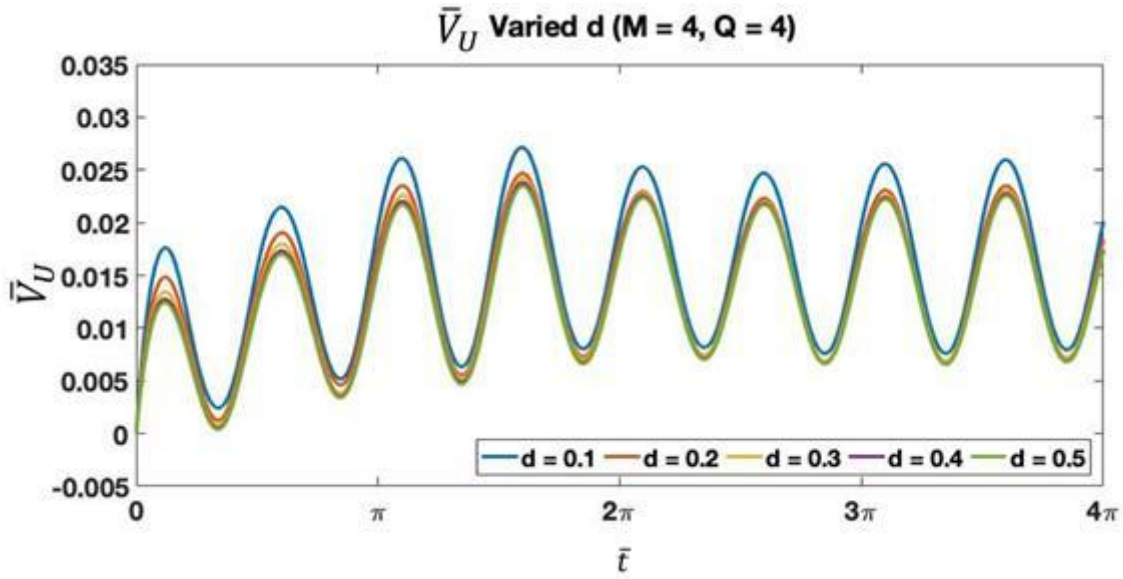
Figure 5-3: Velocity on upper rotor with 4 blades and 4 harmonics at varied rotor spacings ($d = 0.1$-0.5)
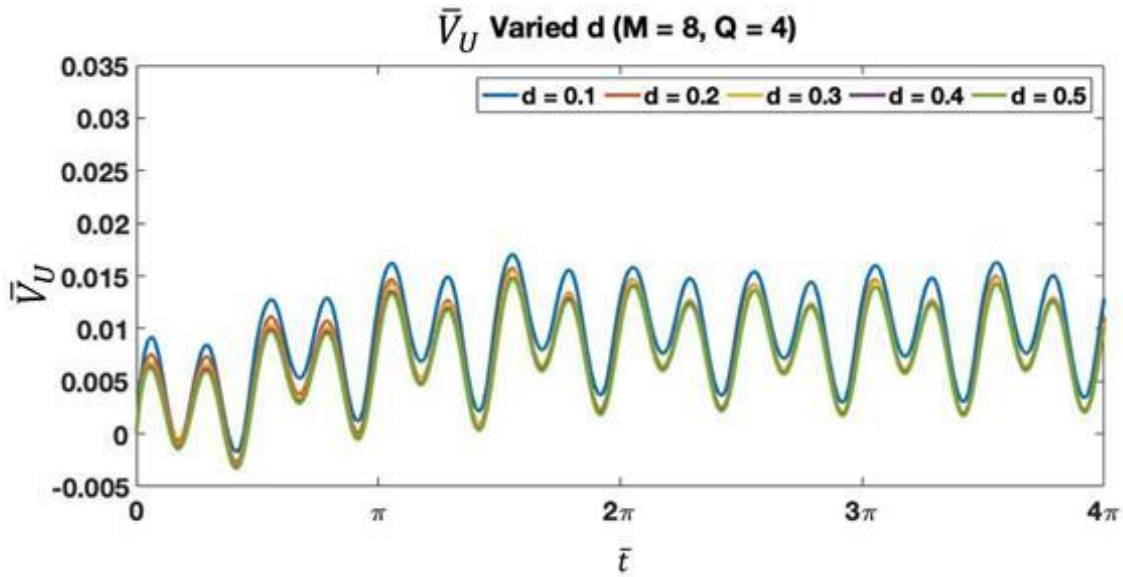
Figure 5-4: Velocity on upper rotor with 4 blades and 8 harmonics at varied rotor spacings ($d = 0.1$-0.5)
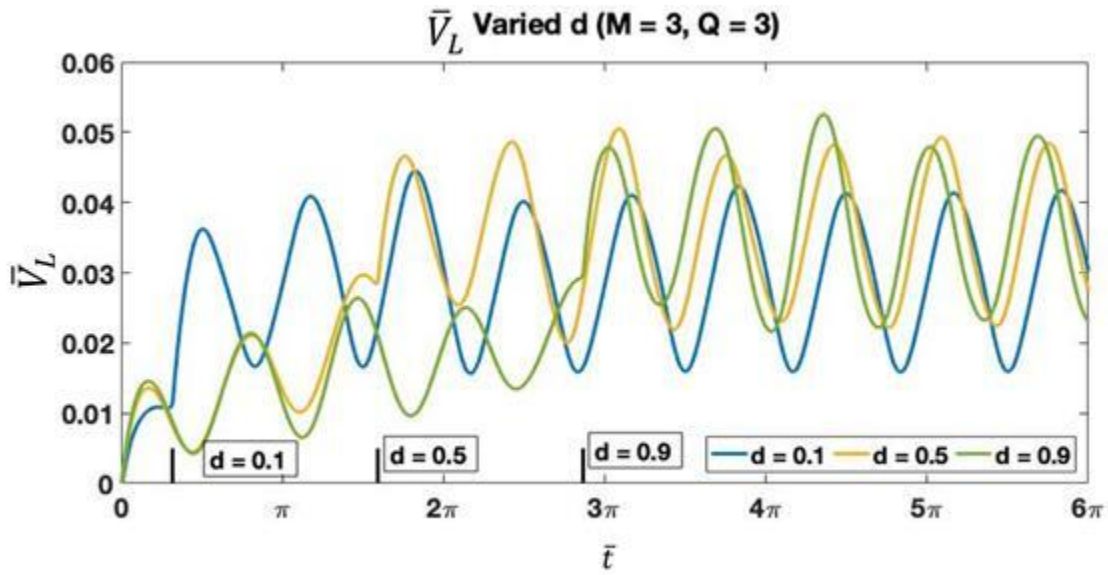
Figure 5-5: Velocity on lower rotor with 3 blades and 3 harmonics at varied rotor spacings ($d = 0.1$-0.9)
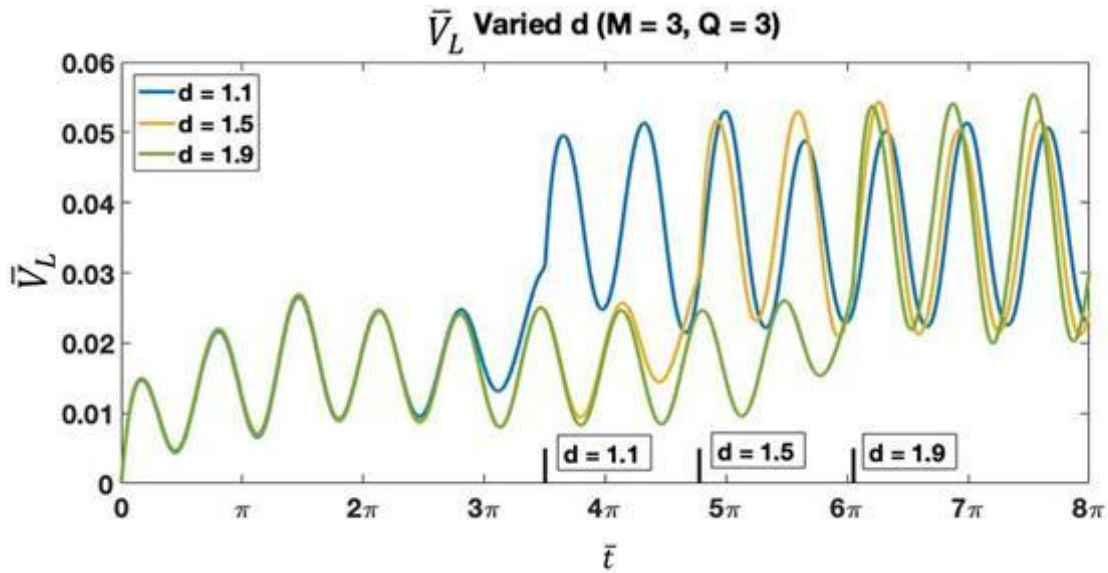
Figure 5-6: Velocity on lower rotor with 3 blades and 3 harmonics at varied rotor spacings ($d = 1.1$-1.9)
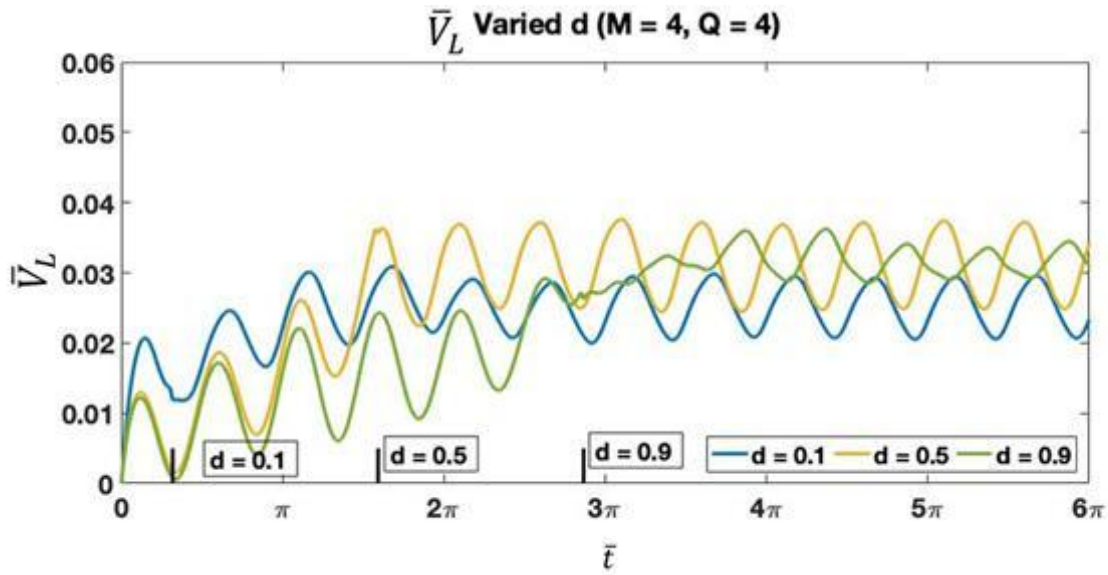
Figure 5-7: Velocity on lower rotor with 4 blades and 4 harmonics at varied rotor spacings ($d = 0.1$-0.9)
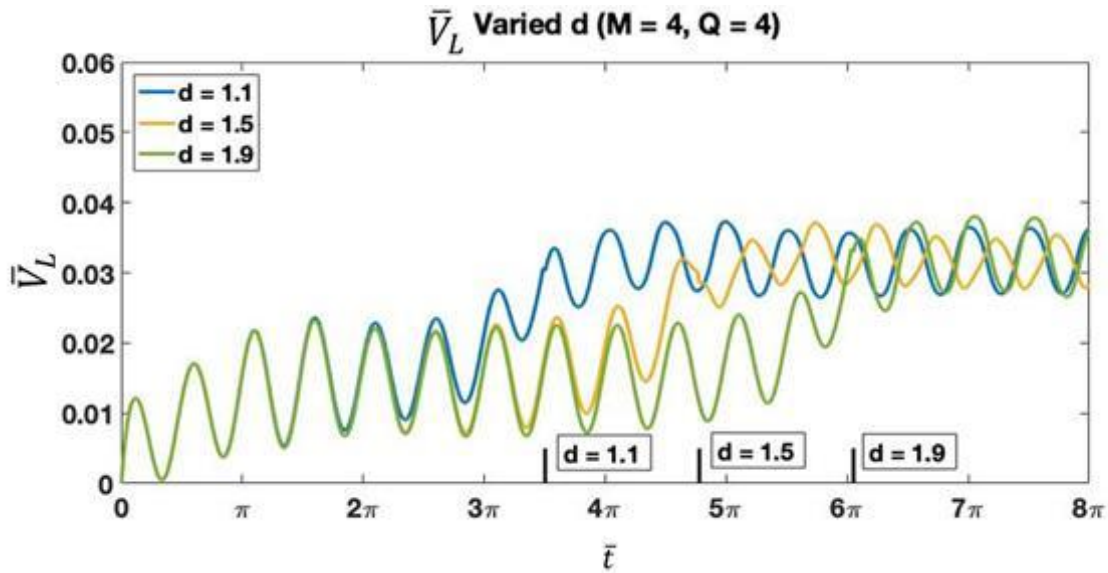
Figure 5-8: Velocity on lower rotor with 4 blades and 4 harmonics at varied rotor spacings ($d = 1.1$-1.9)
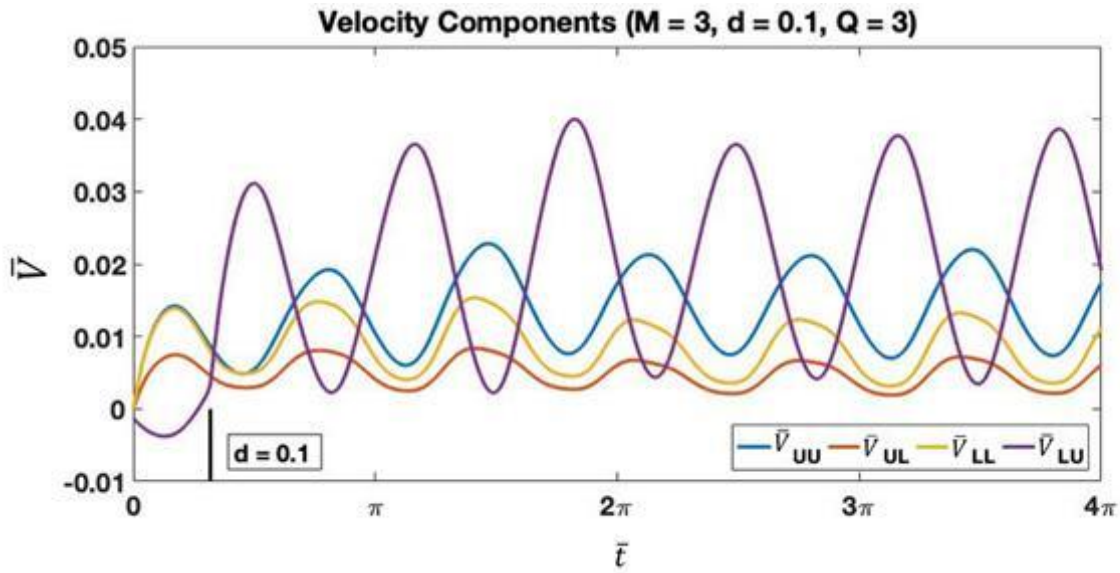
Figure 5-9: Velocity components for system with 3 blades per rotor and 3 harmonics at rotor spacing $d = 0.1$.
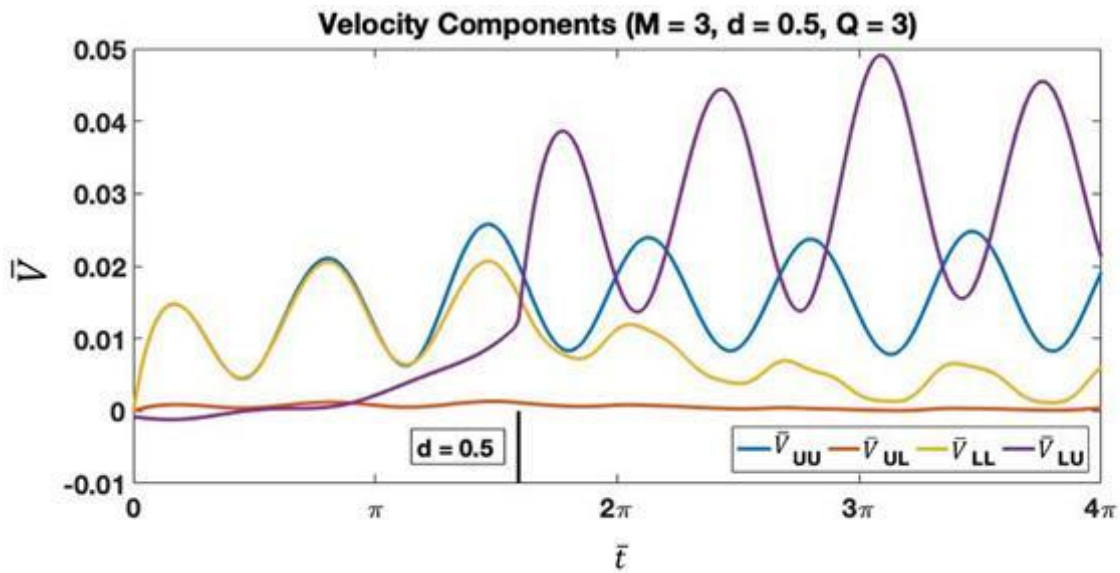
Figure 5-10: Velocity components for system with 3 blades per rotor and 3 harmonics at rotor spacing $d = 0.5$
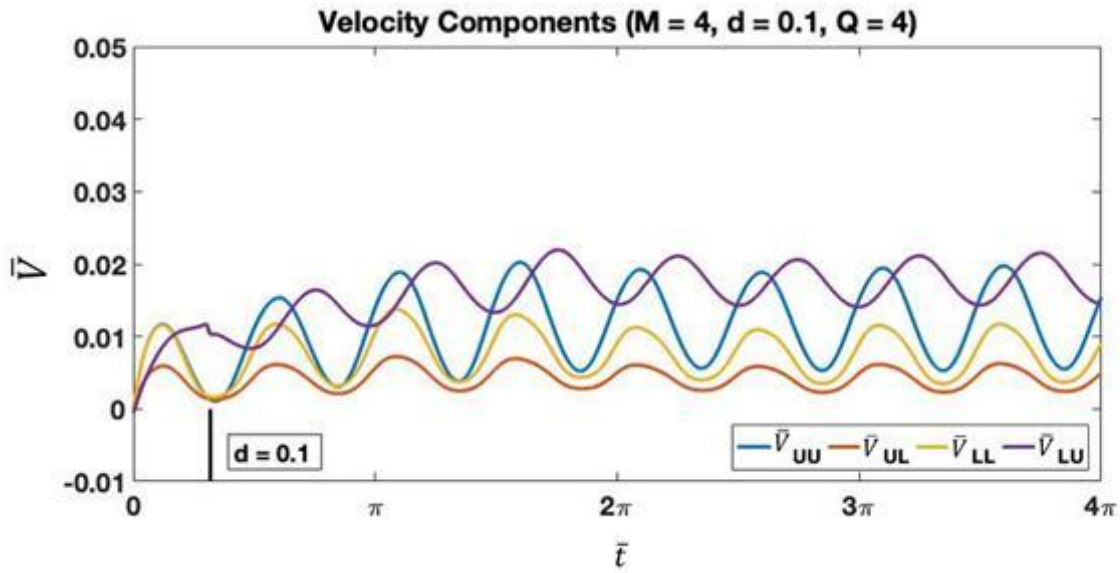
Figure 5-11: Velocity components for system with 4 blades per rotor and 4 harmonics at rotor spacing $d = 0.1$.
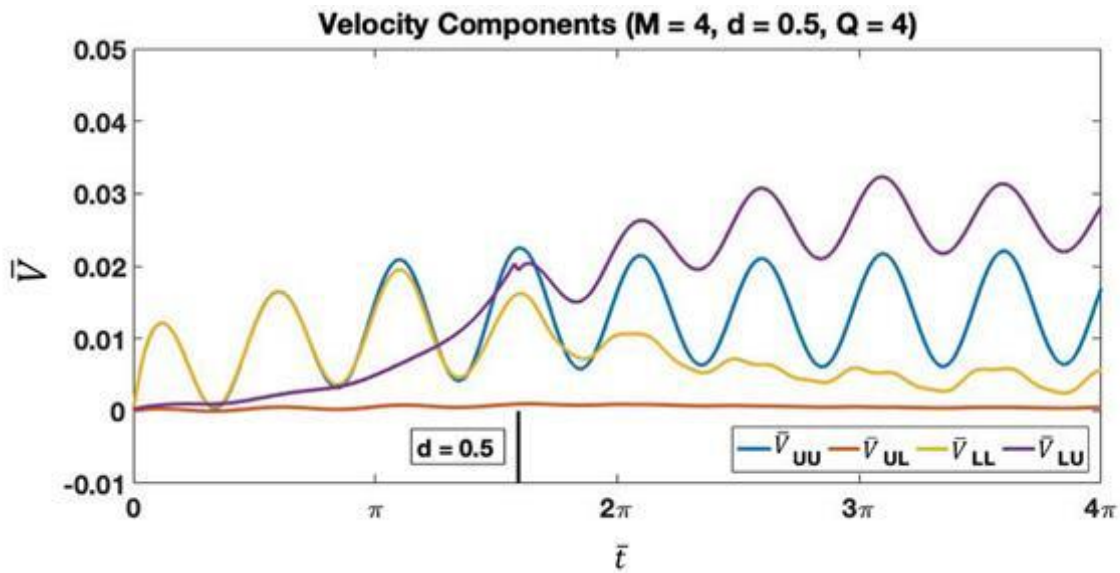
Figure 5-12: Velocity components for system with 4 blades per rotor and 4 harmonics at rotor spacing $d = 0.5$.

133
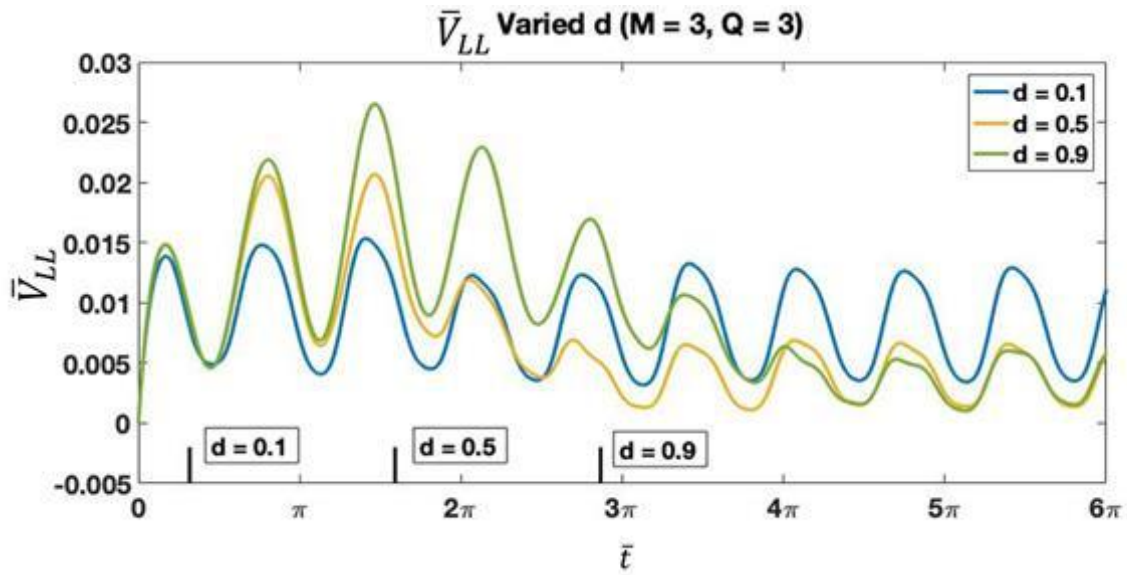
Figure 5-13: $\overline{V}_{LL}$ for system with 3 blades and 3 harmonics at varied rotor spacings $(d = 0.1 - 0.9)$
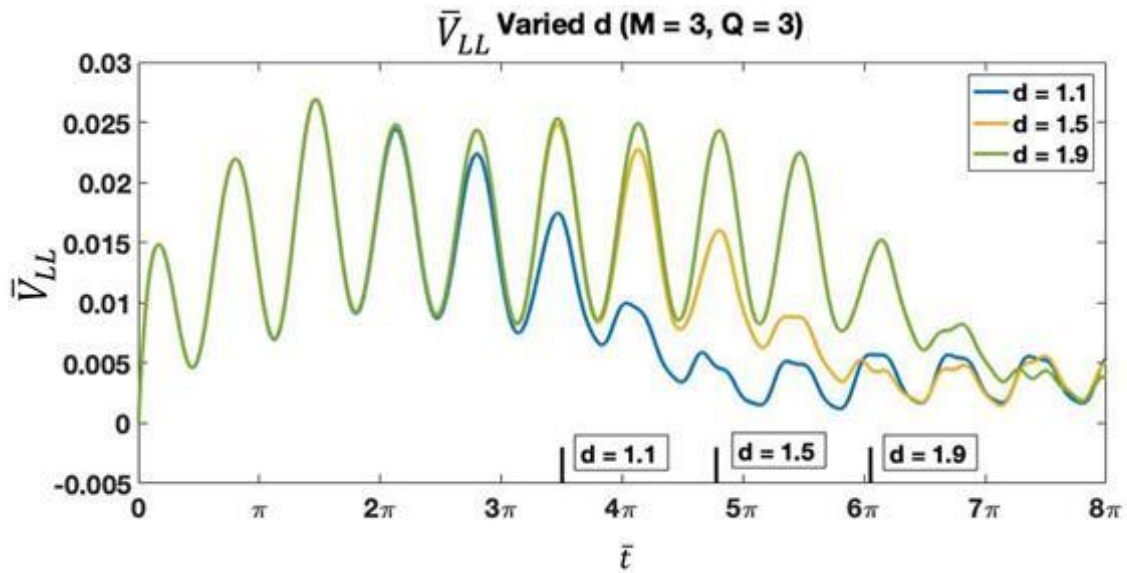
Figure 5-14: $\overline{V}_{LL}$ for system with 3 blades and 3 harmonics at varied rotor spacings $(d = 1.1\text{-}1.9)$
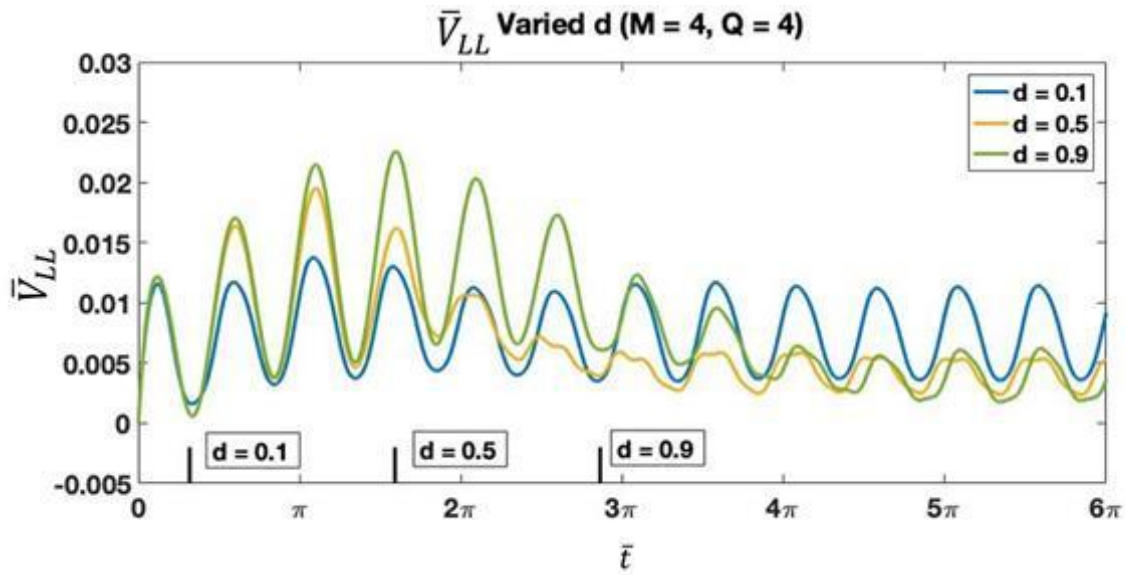
Figure 5-15: $\overline{V}_{LL}$ for system with 4 blades and 4 harmonics at varied rotor spacings ($d = 0.1\text{-}0.9$)
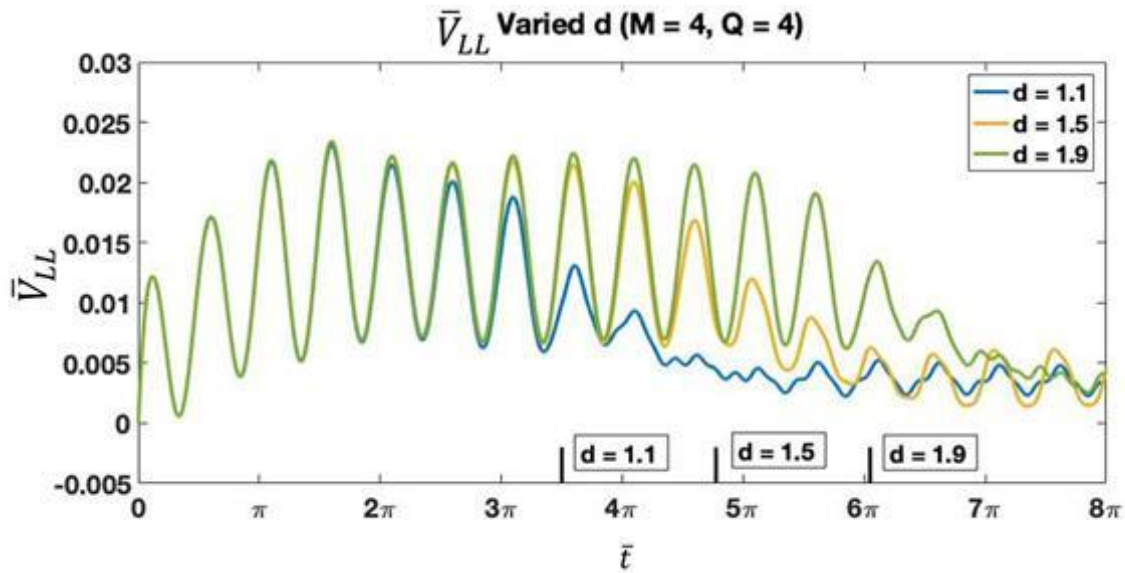
Figure 5-16: $\overline{V}_{LL}$ for system with 4 blades and 4 harmonics at varied rotor spacings ($d = 1.1\text{-}1.9$)
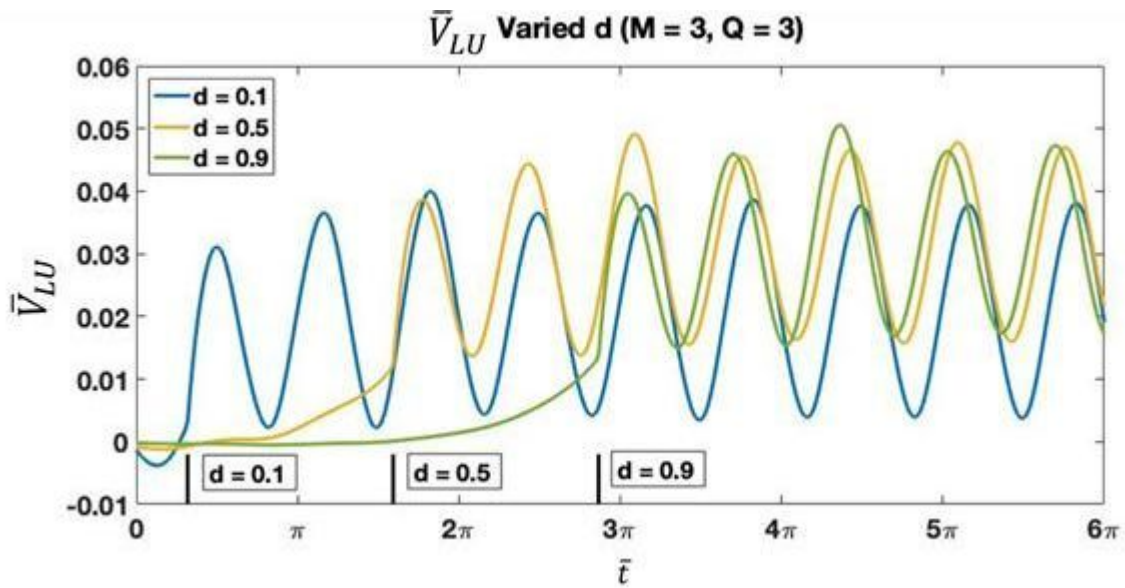
Figure 5-17: $\overline{V}_{LU}$ for system with 3 blades and 3 harmonics at varied rotor spacings (d = 0.1-0.9)
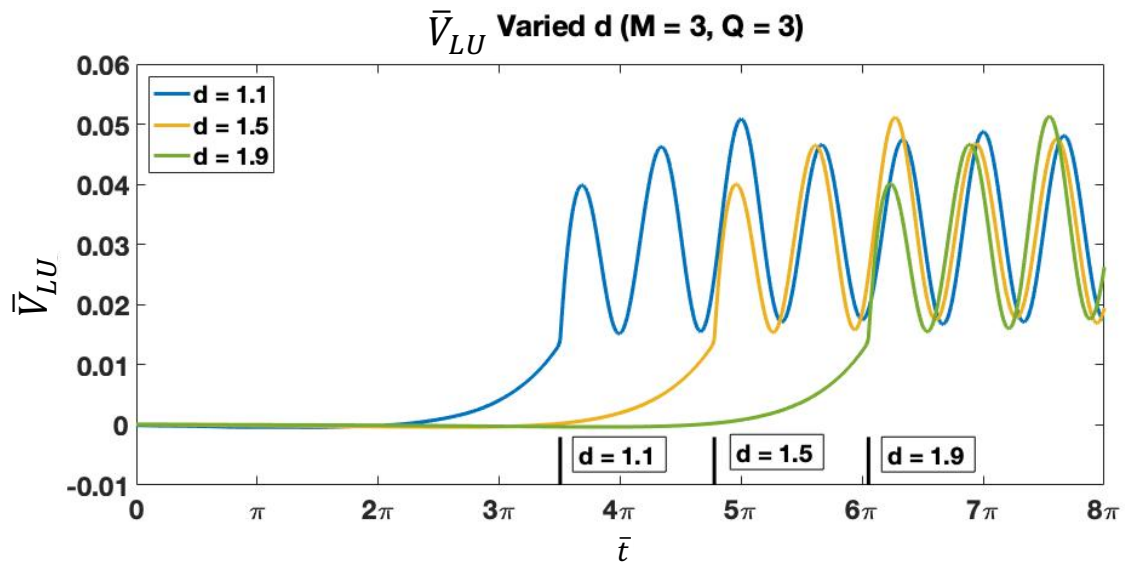
Figure 5-18: $\overline{V}_{LU}$ for system with 3 blades and 3 harmonics at varied rotor spacings (d = 1.1-1.9)
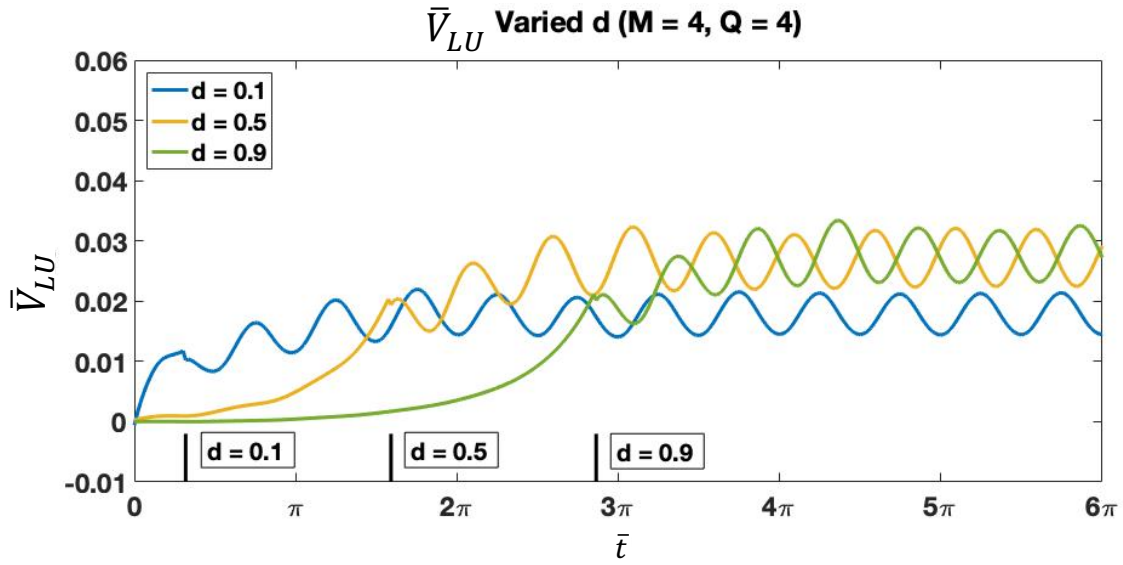
Figure 5-19: $\overline{V}_{LU}$ for system with 4 blades and 4 harmonics at varied rotor spacings ($d = 0.1\text{-}0.9$)
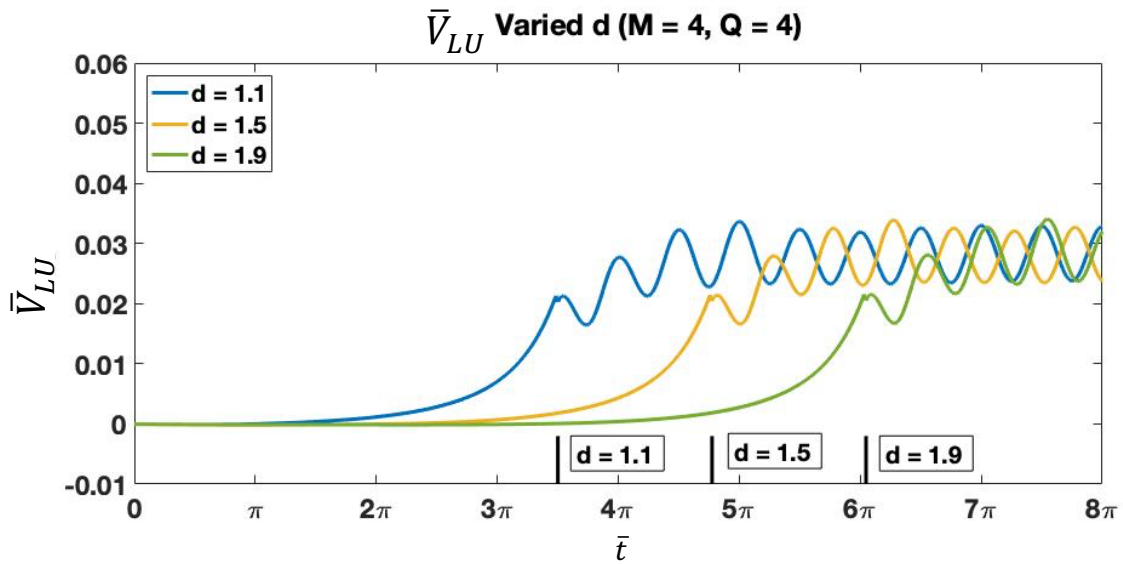
Figure 5-20: $\overline{V}_{LU}$ for system with 4 blades and 4 harmonics at varied rotor spacings ($d = 1.1\text{-}1.9$)

5.3.2 Impact of Harmonics on Velocity Profile Dynamics

The next phase of analyses investigates how the number of harmonics impacts the velocity profile, starting with $\overline{V}_U$ in Figs. 5-21 to 5-24. For the three-blades per rotor system in Figs 5-21 and 5-22 it is noticeable that as the number of harmonics increases, we obtain a more defined time of when the blade passes over the point being investigated ($\overline{r} = 0.8$, $\psi = 0$). In addition, the region between blade passages trends closer to the average velocity in the higher harmonic cases. It is again illustrated that the rotor spacing has little impact on the rotor dynamics and primarily just impacts the magnitude and amplitude. For the four-blade per rotor system in Figs. 5-23 and 5-24, the region between blade passages trends even closer to the average for $M = 16$ harmonics. Overall, the number of blades impacts the early dynamics, but this is not unique to a coupled, coaxial rotor system.

The $\overline{V}_L$ profiles in Figs. 5-25 through 5-32 illustrate the impact of the number of harmonics on the dynamics in the lower rotor velocity profile and steady-state velocity. There is a clear illustration of the time-delay dynamics, however it can be difficult to see in the higher harmonic cases because the profiles are more dynamic. The locations of blades passing over are marked with red lines and the nondimensional times when shed vortices are hitting the lower rotor marked by purple lines. It should be noted that shed vortices are always hitting at this location when $\overline{t} = \overline{d}$ because we selected an azimuth angle ($\psi_{q,k} = 0$) where a blade on the upper rotor starts from rest. The transition to steady-state is highlighted by a general increase in magnitude of the major peaks. Also, in the transition to steady-state the shapes of the peaks change slightly. The dynamics on the lower rotor are unique in the steady-state region because at higher harmonics ($M \geq 2Q$) they better illustrate blade passage and where the vortices shed by the upper rotor hit the lower rotor. For the lower harmonic case, the blade passage and shed vortices hitting the rotor are rolled into a single peak.

When the rotor spacing is increased from $d = 0.1$ to $d = 2.0$ in Figs. 5-25 to 5-28, the early dynamics develop slightly different depending on the rotor spacing, with the variations in development occurring slightly before the point when $\bar{t} = \bar{d}$. A prime example of the development process starting out similar is the comparison of Fig. 5-27 and Fig. 5-28 with rotor spacings of $d = 1$ and $d = 2$, respectively. Up to the nondimensional time $\bar{t} = 8p/3$, the profiles are approximately the same, but then the dynamics begin to change for the $d = 1$ case in Fig. 5-27. The early region is composed of on-disk terms ($\overline{V}_{LL}$) and therefore the regions are initially similar.

For $\bar{t} > \bar{d}$, additional peaks begin to develop representing the shed vortices from the upper rotor; but they occur in different shapes and at varying locations for the various rotor spacings. This is due to the difference in time delays and how close together a blade passage and shed vortices intersection are to the point under investigation. In addition, the residuals of solutions also impact the shape and are the reason why the profiles often have more than two peaks between blades passing. Comparing the proximity of shed vortices to blades passing, it can be further understood how the profile shapes differ. Typically, a blade passing is easy to recognize, occurring midway between the minima and maxima on a large oscillation, but the addition of shed vortices changes the trend. In Fig. 5-25, the blade passing is generally occurring near the decline to the minima and the shed vortices are hitting near the maxima of the oscillation pattern. In Fig. 5-27, the blade passing occurs slightly after the maxima of the oscillation pattern and the shed vortices are hitting slightly before. The patterns are dependent on the proximity of blades passing to shed vortices hitting the rotor.

The addition of an extra blade to each rotor in Figs. 5-29 to 5-32 demonstrates different trends in the dynamics near the where the time-delay effect occurs and in the steady-state profiles. The extra blade has a large impact on the early dynamics and the time-delay

dynamics because it changes the blade passage and vortex shedding pattern and where the shed vortices from the upper rotor hit the lower rotor for a given rotor spacing. It can be concluded that the time-delay dynamics are a factor of $d, Q, M, \overline{r}$,and ψ. The time-delay dynamics are often easier to locate in lower harmonic cases because they are less complex, but the blade passage and steady-state regions are more accurate and easier to analyze with a higher number of harmonics.

In order to better understand how the varied M cases for $\overline{V}_L$ is impacted by each rotor, the $\overline{V}_{LL}$ and $\overline{V}_{LU}$ components are analyzed here in Figs. 5-33 to 5-40. The $\overline{V}_{LL}$ profiles in Figs. 5-33 to 5-36 provide a good amount of detail for when a blade on the lower rotor passes by the location being observed and the average velocity. $\overline{V}_{LL}$ does not contain any time-delayed terms and therefore only sees minor secondary impacts around $\overline{t} = \overline{d}$.

The $\overline{V}_{LU}$ profiles,in Figs. 5-37 to 5-40 the time-delay dynamics are evident given the drastic change in the profile. There is some variation in the time-delay dynamics with number of harmonics, but the general trend tends to be an overall drop off before increasing and oscillating. For a blade passage, the general trend is for the velocity profile to go from minima to maxima with the blade passage occurring in the middle. For vortices, the lower rotor feels bound vortices from the upper rotor for small rotor spacings. Therefore, the profile for the vortices in this case would behave similar to the blade passage. However, for a larger rotor spacing when the shed vortices hit the lower rotor, the behavior is different. The peak due to the vortex sheet is smooth and diminishes as the rotor spacing increases. The shed vortices are at the peak instead of midway between the maxima and minima. In Fig. 5-37, due to the close rotor spacing the impact due to the vortices is on the increasing slope towards the maxima. In Fig. 5-38 the rotor spacing increases to $d = 1.0$ and the vortex effects are closer to the peak. This is also illustrated for a four bladed system in Figs. 5-39 and 5-40.
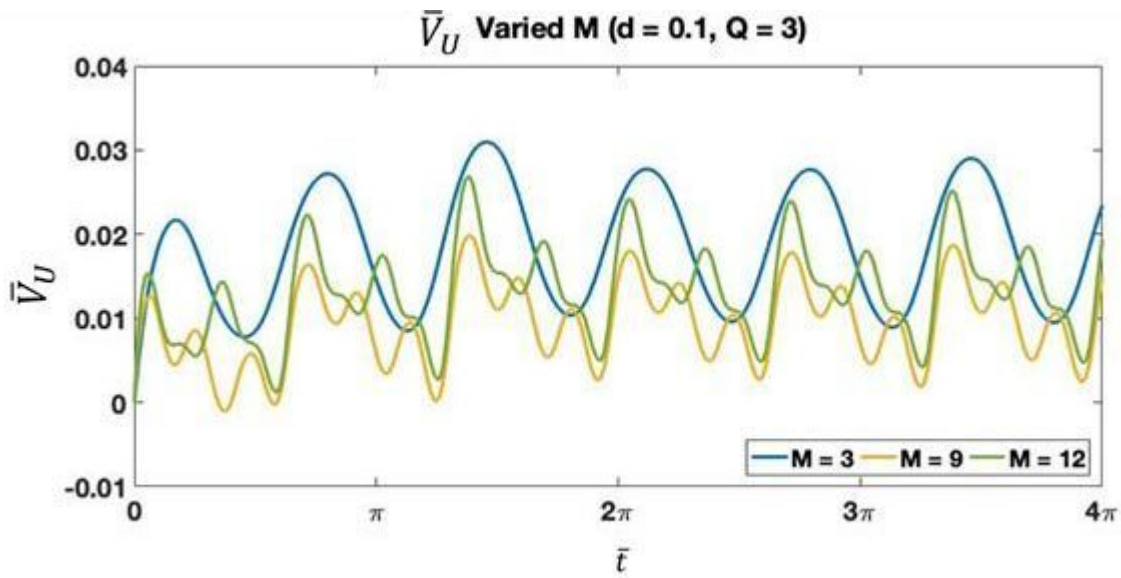
Figure 5-21: Velocity on upper rotor with 3 blades and $d = 0.1$ and varied harmonics
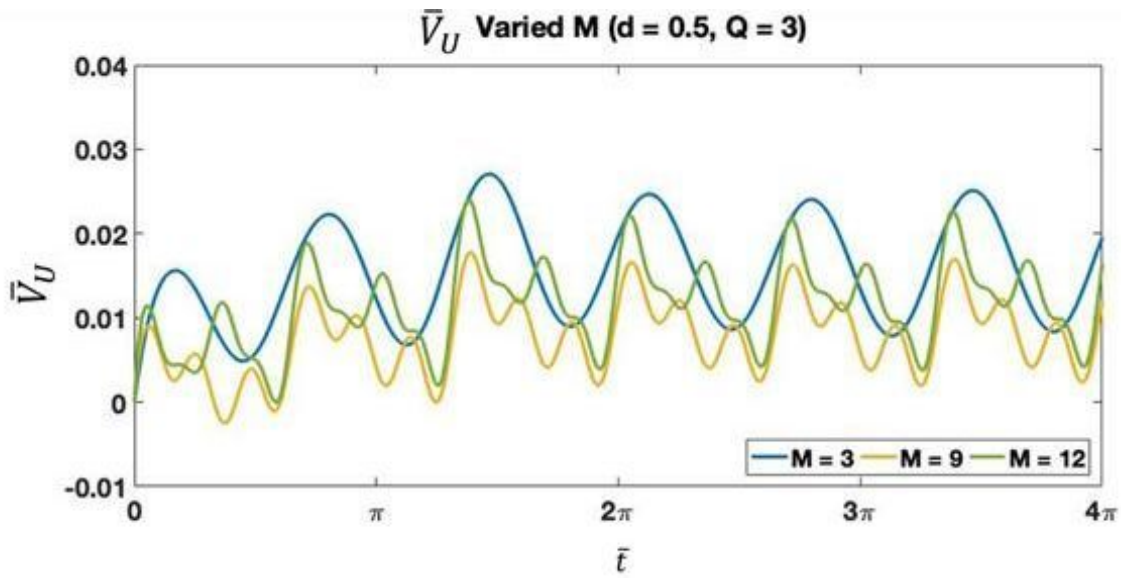
Figure 5-22: Velocity on upper rotor with 3 blades and $d = 0.1$ and varied harmonics

141
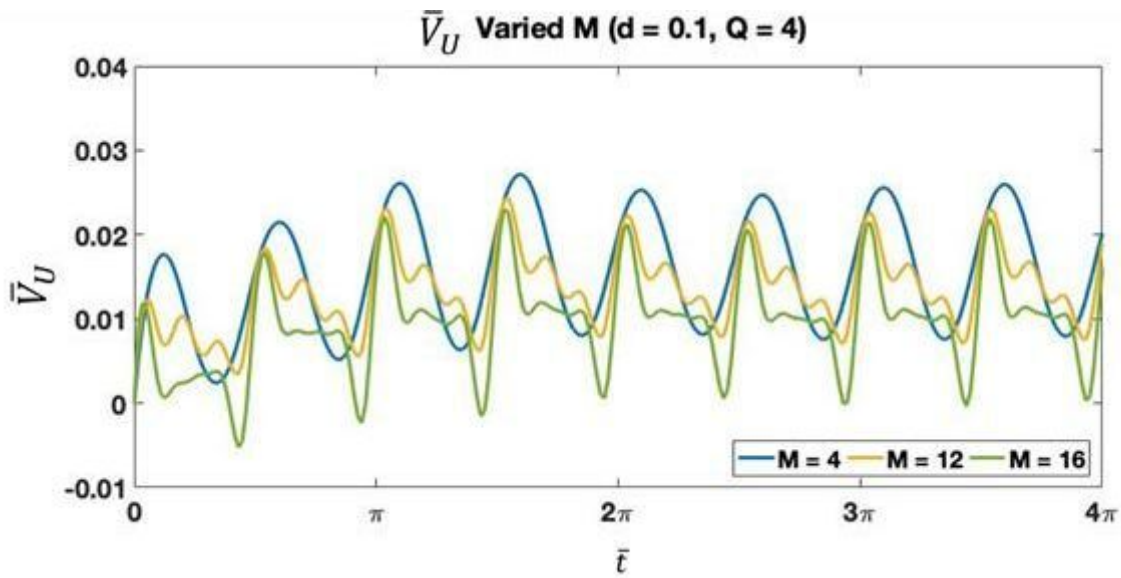
Figure 5-23: Velocity on upper rotor with 4 blades and $d = 0.1$ and varied harmonics
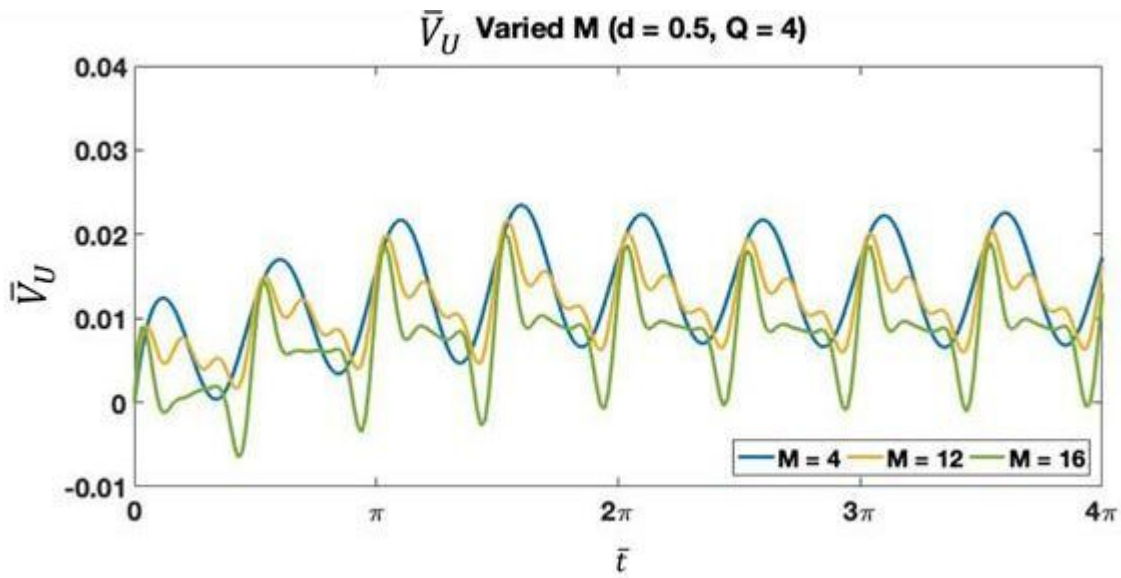
Figure 5-24: Velocity on upper rotor with 4 blades and $d = 0.1$ and varied harmonics
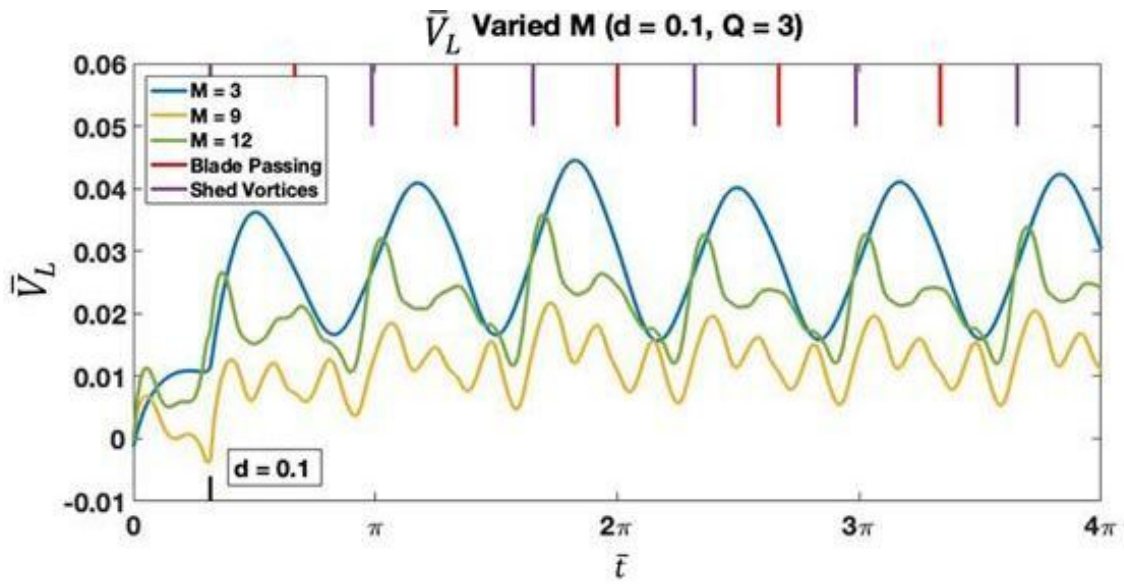
Figure 5-25: Velocity on lower rotor with 3 blades and $d = 0.1$ and varied harmonics
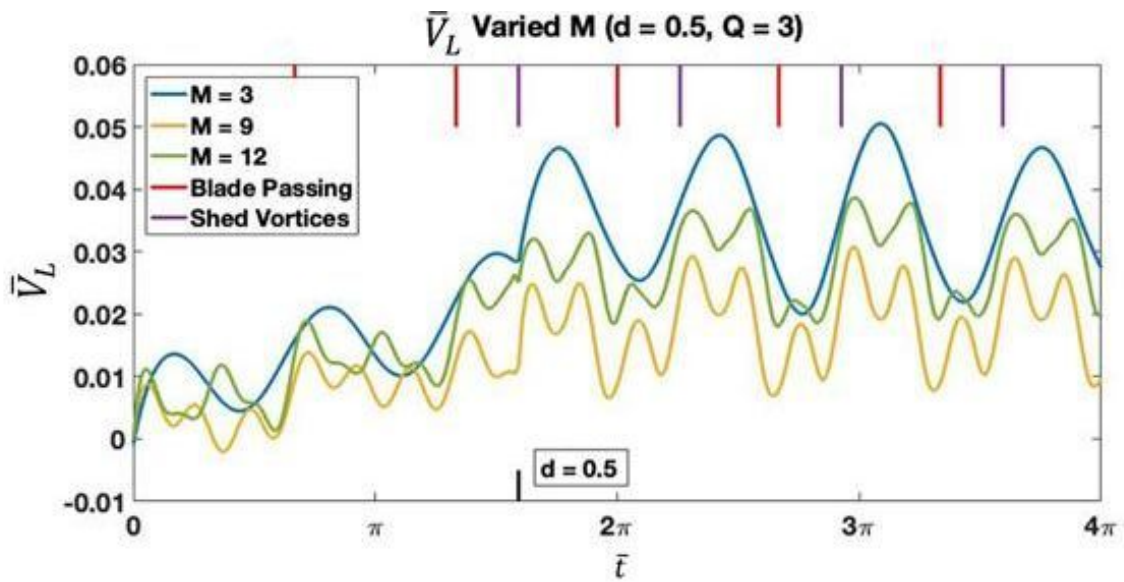
Figure 5-26: Velocity on lower rotor with 3 blades and $d = 0.1$ and varied harmonics
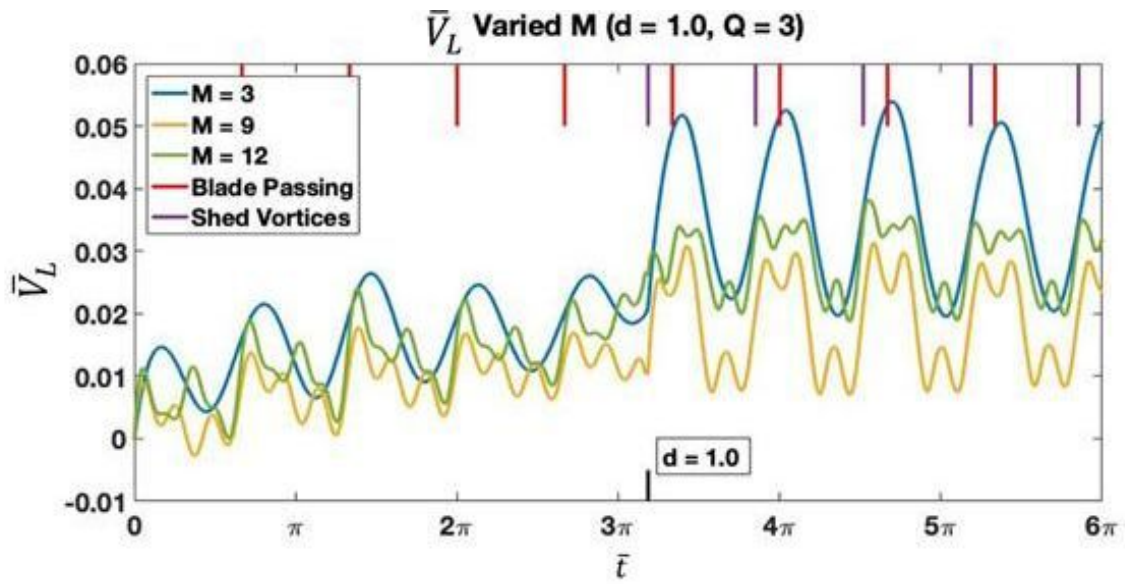
Figure 5-27: Velocity on lower rotor with 3 blades and $d = 0.1$ and varied harmonics
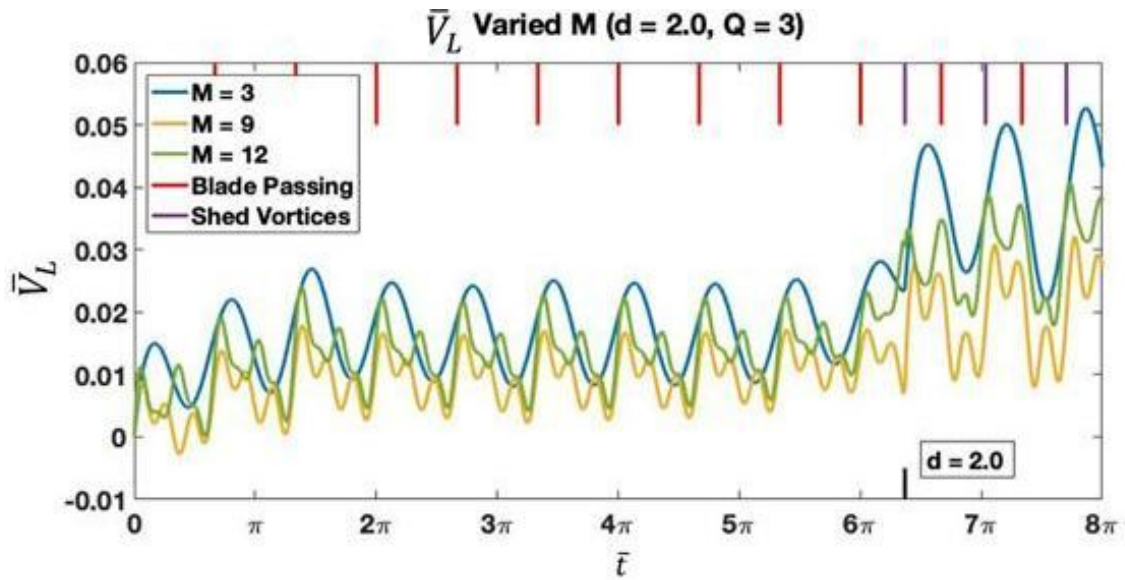
Figure 5-28: Velocity on lower rotor with 3 blades and $d = 0.1$ and varied harmonics

144
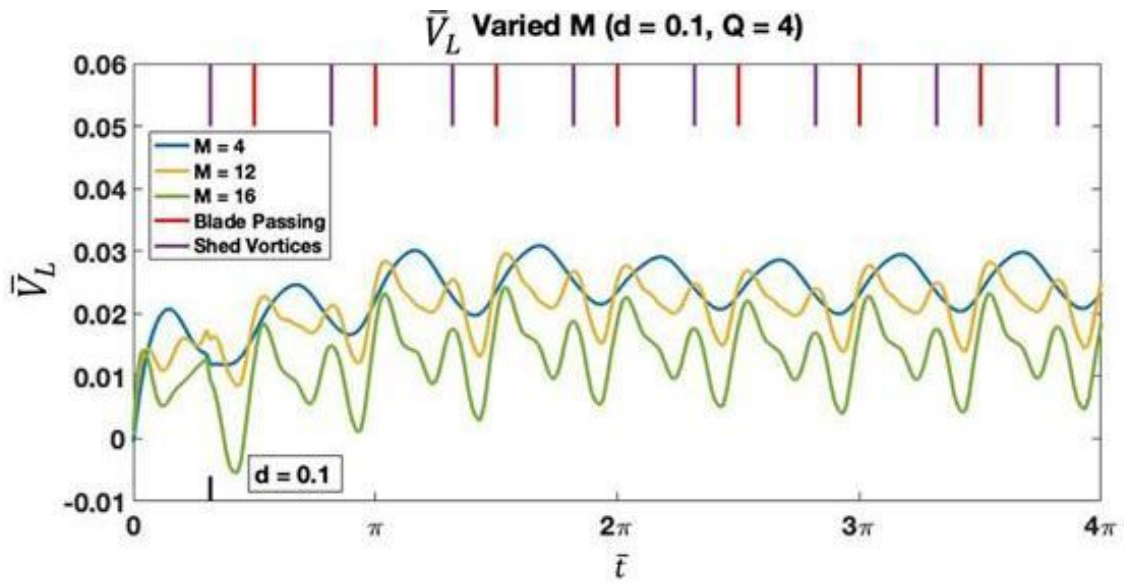
Figure 5-29: Velocity on lower rotor with 4 blades and $d = 0.1$ and varied harmonics
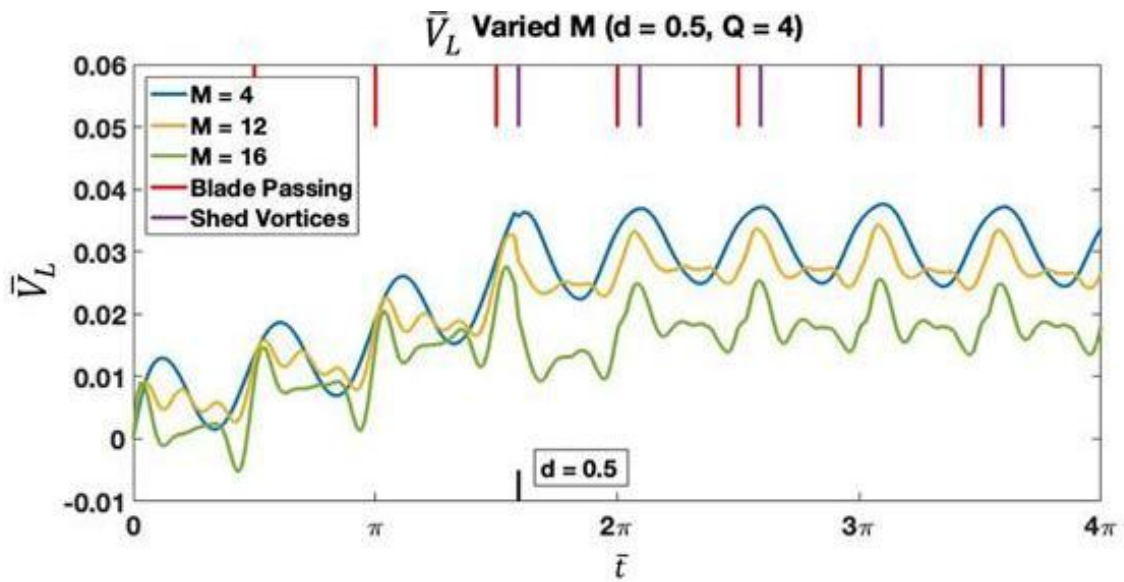
Figure 5-30: Velocity on lower rotor with 4 blades and $d = 0.1$ and varied harmonics
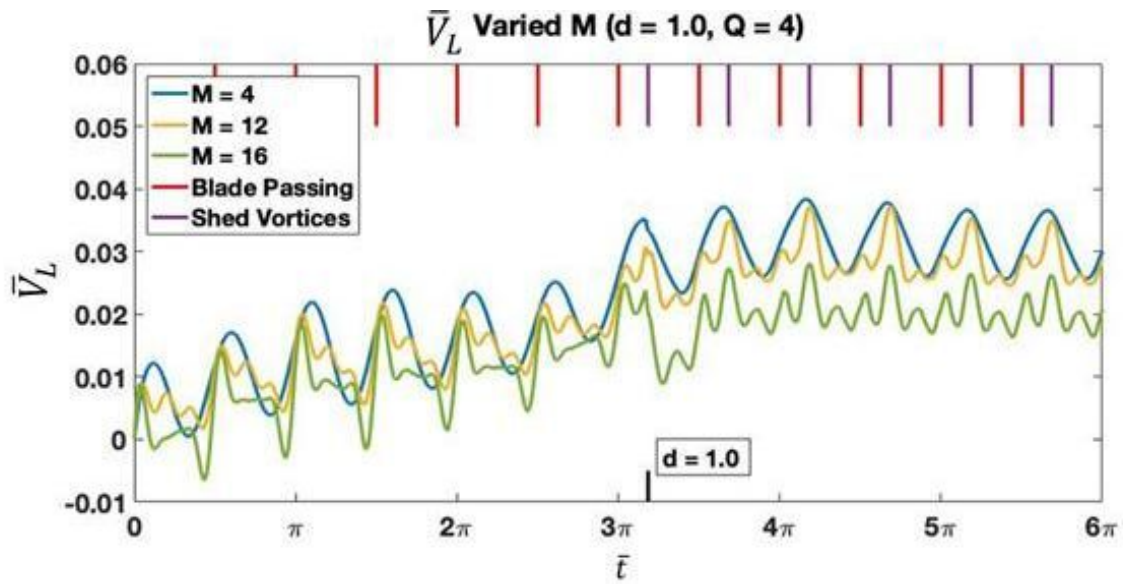
Figure 5-31: Velocity on lower rotor with 4 blades and $d = 0.1$ and varied harmonics
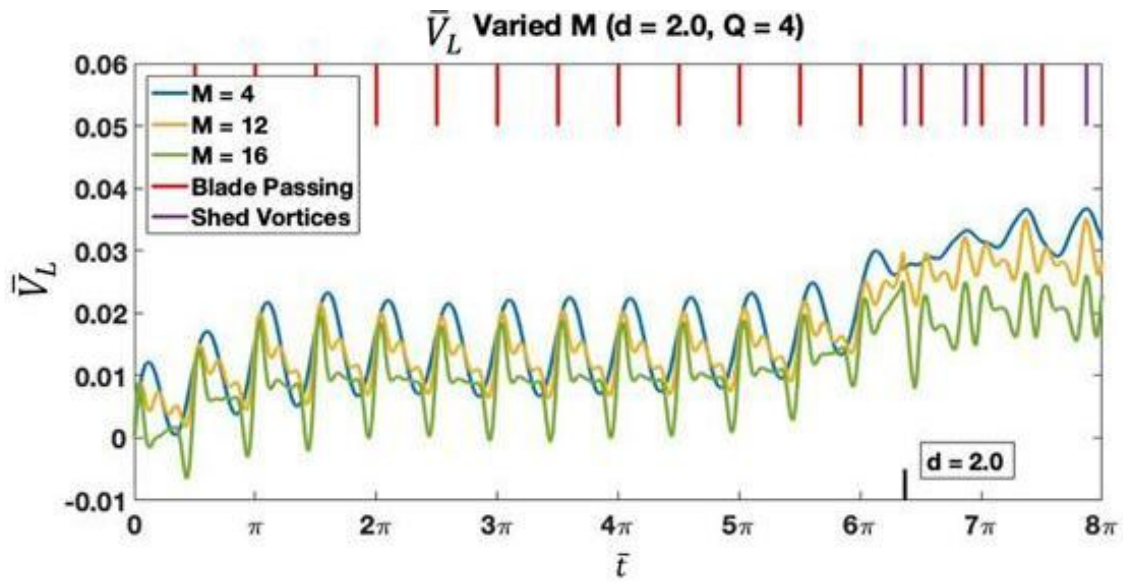
Figure 5-32: Velocity on lower rotor with 4 blades and $d = 0.1$ and varied harmonics

146
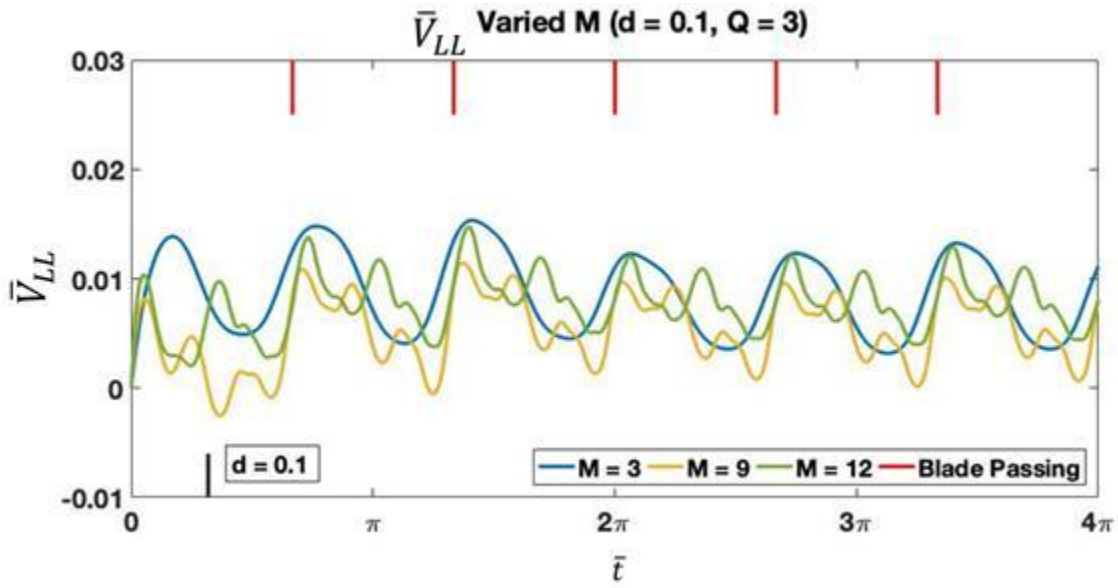
Figure 5-33: $\overline{V}_{LL}$ for system with 3 blades and $d = 0.1$ and varied harmonics
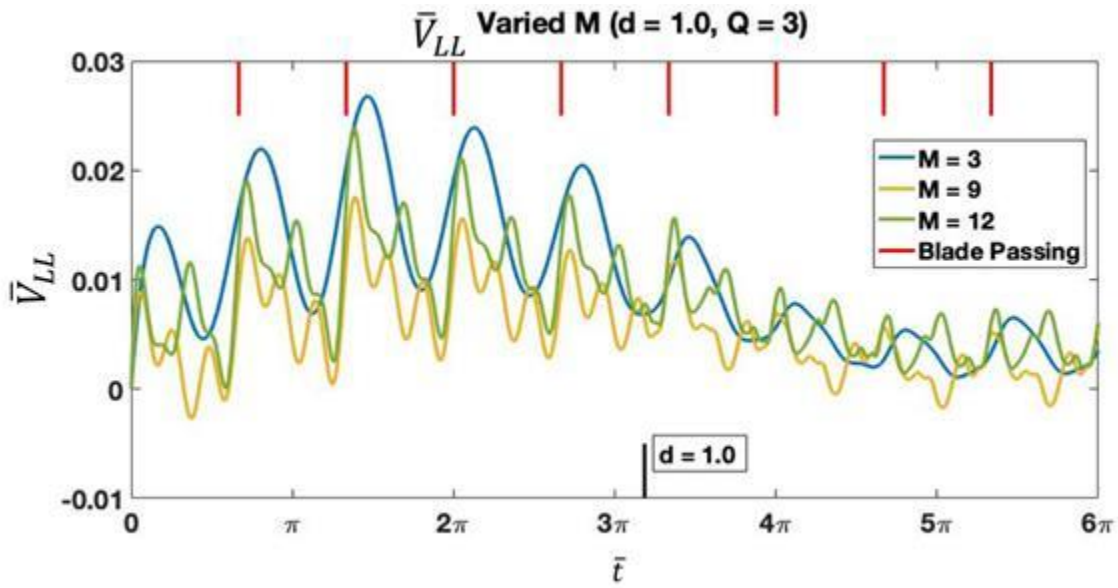
Figure 5-34: $\overline{V}_{LL}$ for system with 3 blades and $d = 0.1$ and varied harmonics
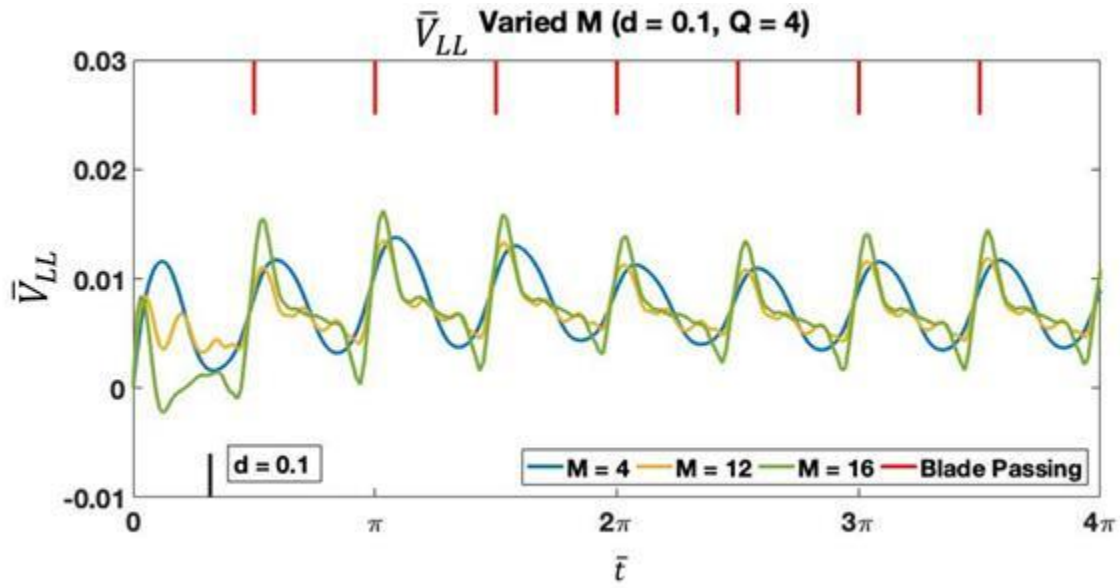
Figure 5-35: $\overline{V}_{LL}$ for system with 4 blades and $d = 0.1$ and varied harmonics
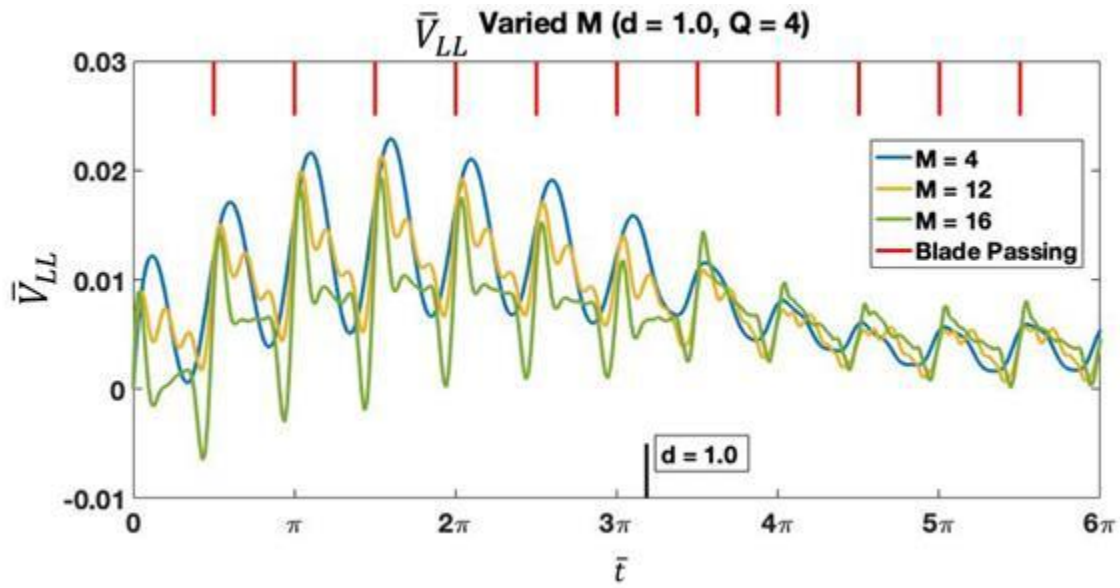
Figure 5-36: $\overline{V}_{LL}$ for system with 3 blades and $d = 0.1$ and varied harmonics
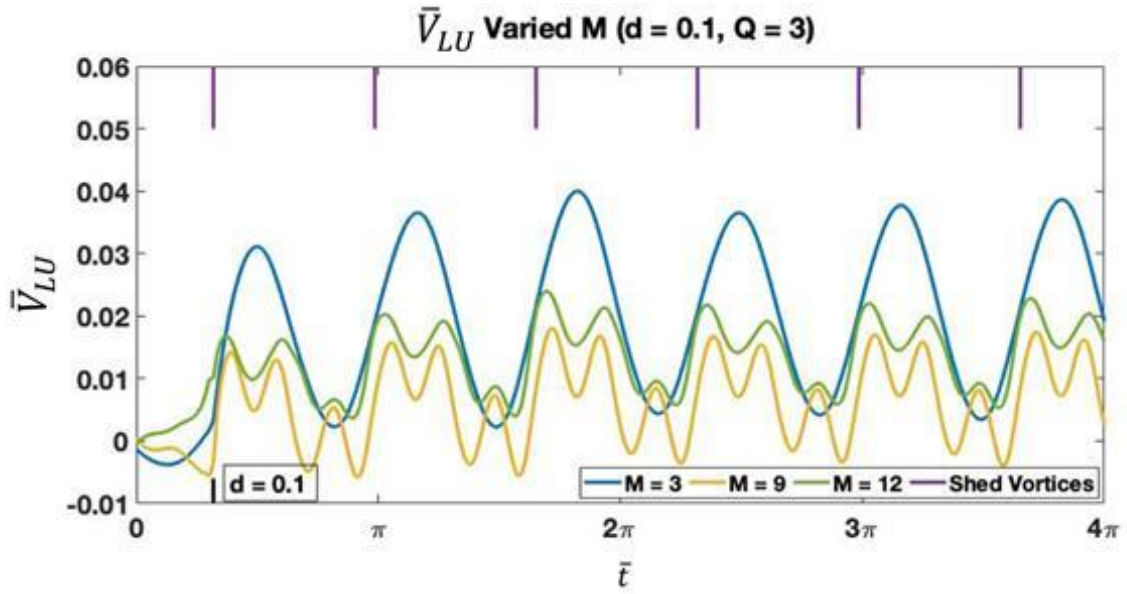
Figure 5-37: $\overline{V}_{LU}$ for system with 3 blades and $d = 0.1$ and varied harmonics
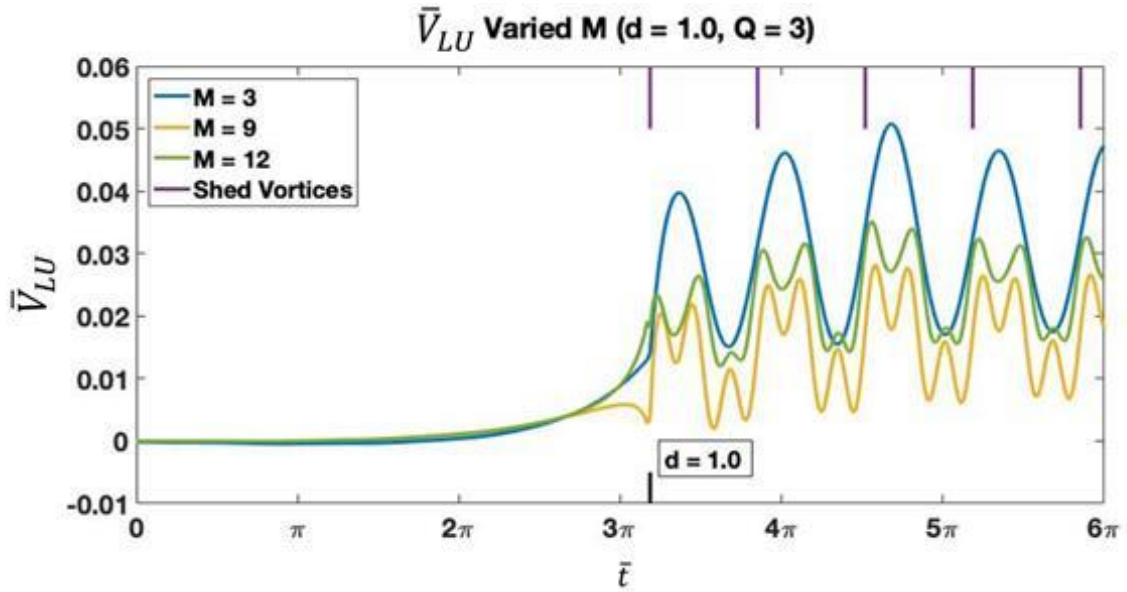
Figure 5-38: $\overline{V}_{LU}$ for system with 3 blades and $d = 0.1$ and varied harmonics

149
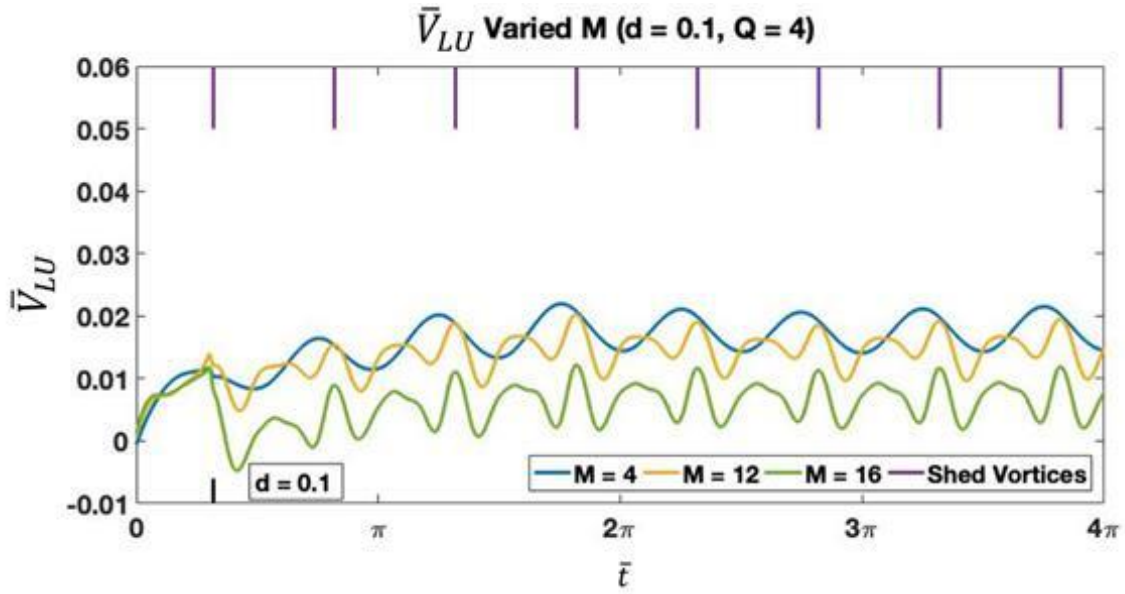
Figure 5-39: $\overline{V}_{LU}$ for system with 4 blades and $d = 0.1$ and varied harmonics
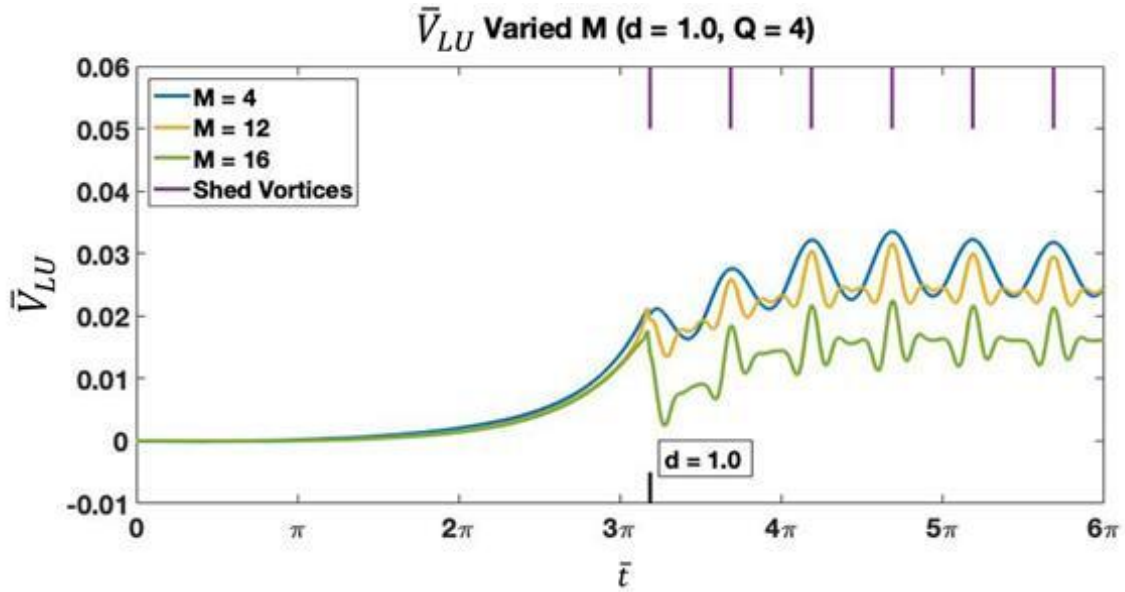
Figure 5-40: $\overline{V}_{LU}$ for system with 4 blades and $d = 0.1$ and varied harmonics

5.3.3 Blade Flapping Dynamics

Looking at the blade flapping dynamics in Figs. 5-41 through 5-48, we compare how d and M impact the upper and lower rotors of three and four blade per rotor systems. In Figs. 5-41 and 5-42 b_U profiles for $Q = 3$ and $Q = 4$ are compared for different d. Dynamically the only variation with respect to d is the small oscillations when $d = 0.1$. These oscillations occur at a rate of $2Q$ per revolution and are a result of the interactions of the rotors with each containing Q blades. The profiles for b_L with variations in d are shown in Figs. 5-43 and 5-44. In these figures, the impact of d on the dynamics and the delay to reach steady-state is clearly illustrated. d impacts the time-delay dynamics differently for each rotor spacing. When the flow from the upper rotor hits the lower rotor the b_L profile drops off and hits its minimum before oscillating to reach a steady-state. For $d = 0.1$, the initial peak does not reach as high of an amplitude because flow from the upper rotor hits the lower rotor during its initial increase and suppresses the oscillation. For $d = 0.5$, the oscillation is already trending down when the flow from the upper rotor hits the lower rotor. For the other three cases the system is in the process reaching a steady state (as it would in a single rotor system) when the flow from the upper rotor hits the lower rotor and causes b_L to drop. In both the upper and lower rotor, the number of blades impacts the magnitude of the blade flapping profiles and the $2Q$ per revolution oscillations but has little impact on the larger dynamics of the blades.

The impact of harmonics on the blade flapping profiles is shown in Figs. 5-45 to 5-48. Here it is noticeable that the number of harmonics impacts the magnitudes of blade flapping for the upper and lower rotors. The blade flapping profile for the upper rotor in Fig. 5-45 does not illustrate any notable dynamic differences other than the $2Q$ per rev oscillations become shallower as the number of harmonics increases. For the b_L in Figs. 5-46 to 5-48, the cases

with $M = 6, 9$, and 12 are all very similar dynamically. The dynamic differences between the $M = 3$ case and the higher harmonic cases appear slightly after $\bar{t} = \bar{d}$. If blade dynamics are of the primary interest of a simulation, no more than $M = 2Q$ harmonics would be needed.
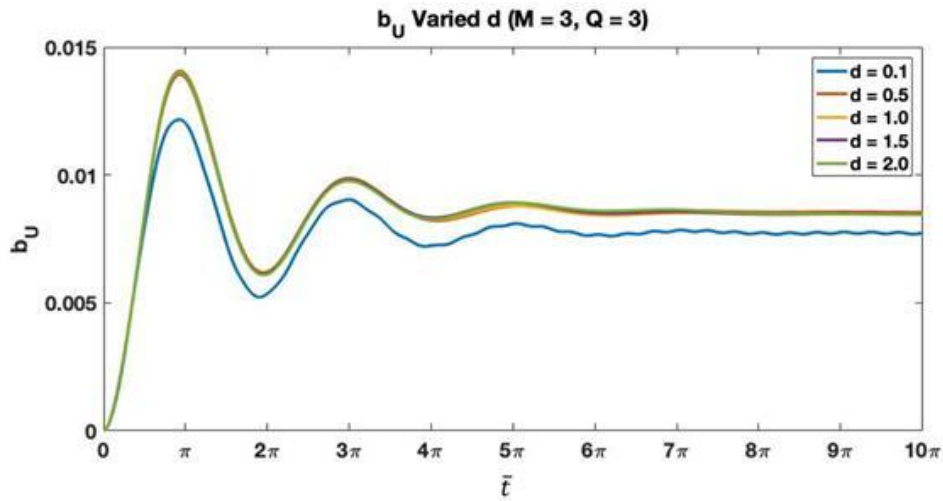
Figure 5-41: Upper rotor blade flapping for system with 3 blade and 3 harmonics and varied rotor spacings (d = 0.1-2.0)
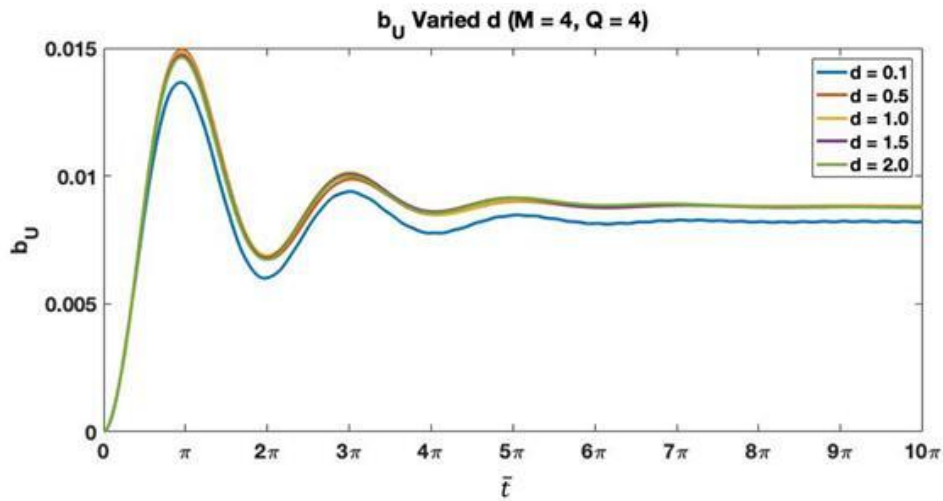
Figure 5-42: Upper rotor blade flapping for system with 4 blade and 4 harmonics and varied rotor spacings (d = 0.1-2.0).
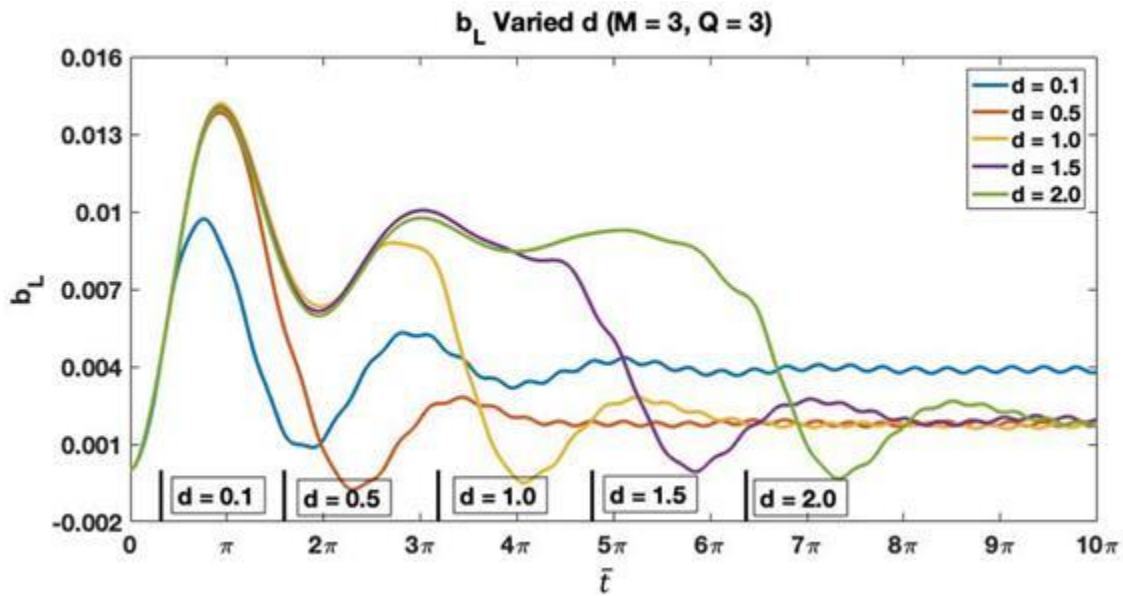
Figure 5-43: Lower rotor blade flapping for system with 3 blade and 3 harmonics and varied rotor spacings ($d = 0.1$-2.0).
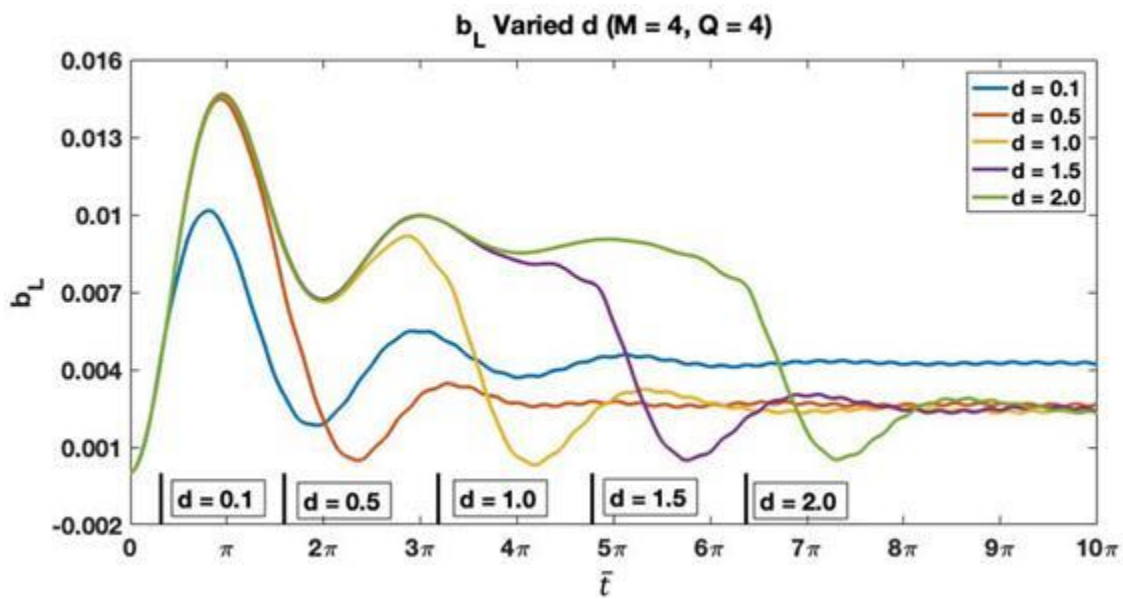
Figure 5-44: Lower rotor blade flapping for system with 4 blade and 4 harmonics and varied rotor spacings ($d = 0.1$-2.0).

153
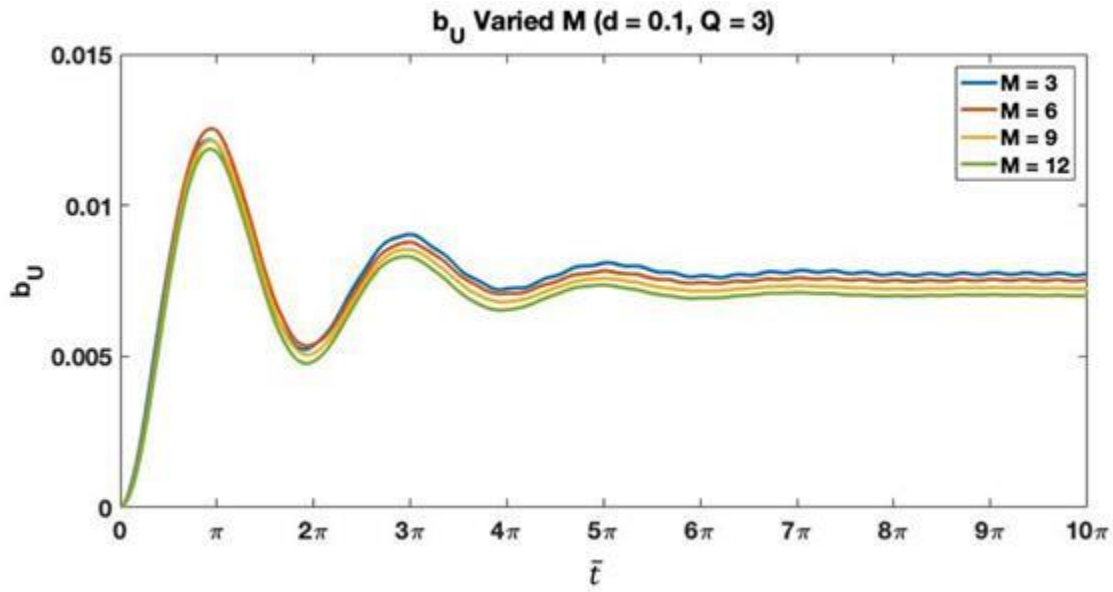
Figure 5-45: Upper rotor blade flapping for system with 3 blades and $d = 0.1$ and varied number of harmonics.
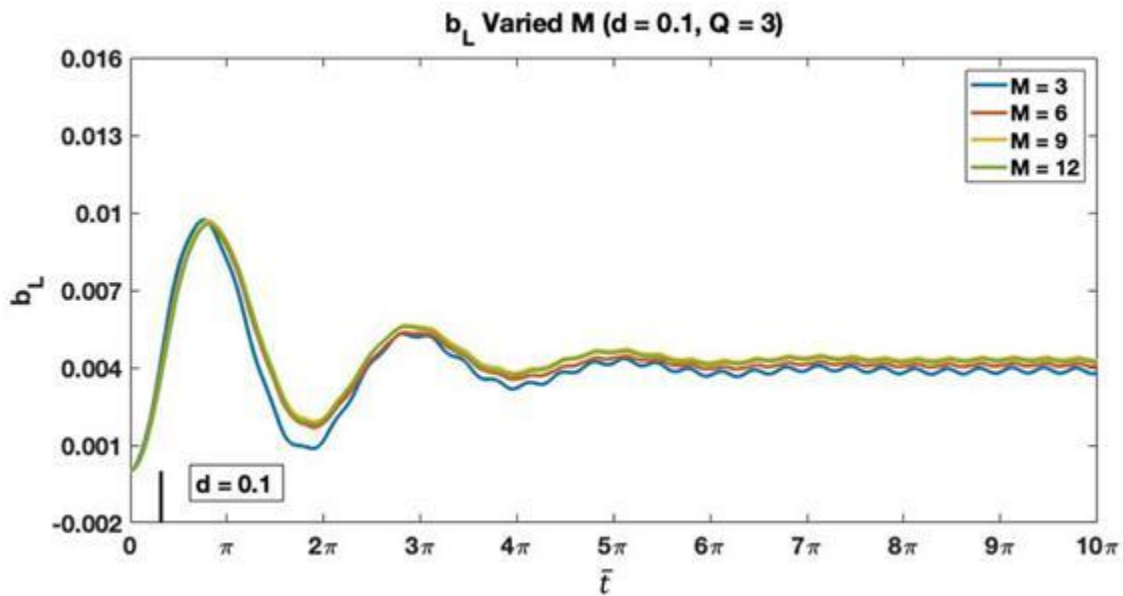
Figure 5-46: Lower rotor blade flapping for system with 3 blades and $d = 0.1$ and varied number of harmonics
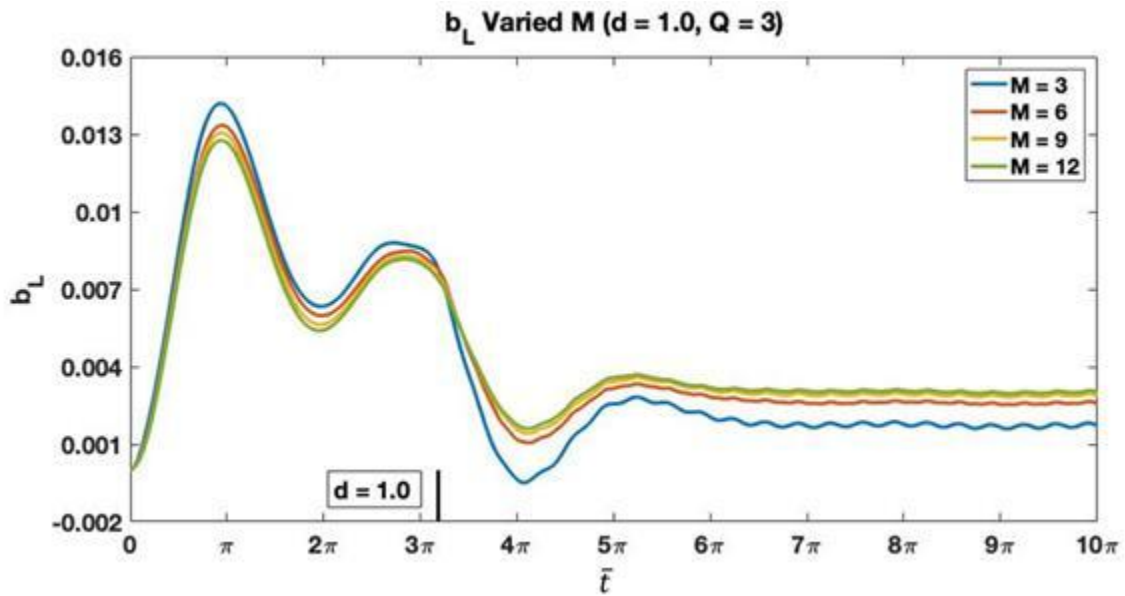
Figure 5-47: Lower rotor blade flapping for system with 3 blades and $d = 1.0$ and varied number of harmonics
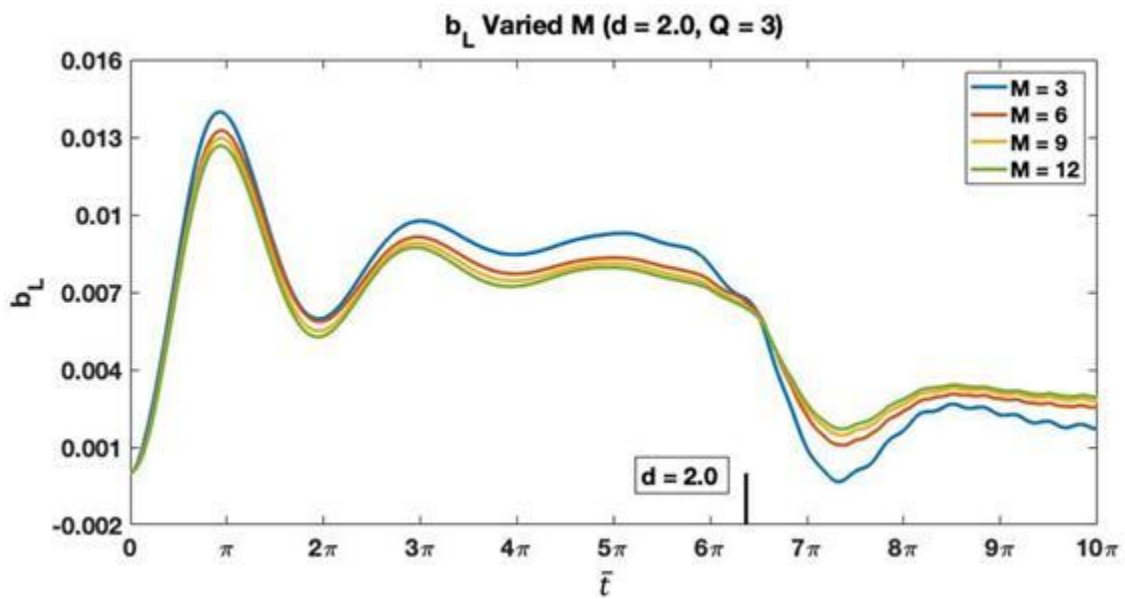
Figure 5-48: Lower rotor blade flapping for system with 3 blades and $d = 2.0$ and varied number of harmonics

155

5.3.4 Velocity Dynamics Variation by Location on the Rotor

In addition to d and Q, the location on the rotor disk, in terms of ψ and $\bar{r}$, impacts the time-delay dynamics on the lower rotor. In this section, we only outline the variations with ψ and use the same $\bar{r} = 0.8$. The three-bladed, $M = 3$ system with a rotor-spacing of $d = 0.5$ in Fig. 5-49 illustrates that at $\bar{t} = \bar{d}$ different azimuth angles have different time-delay dynamics. The dynamics in this region are impacted by two major components, the location of the blade relative to the location being observed and where the shed vortices from the upper rotor are hitting on the lower rotor when. In this case, the blade on the lower rotor is at about $\psi = 74°$, which is why the effect of the time-delay is smoother at $\psi = 80°$.

Now, looking at Figs. 5-50 and 5-51 for a four-bladed system ($M = 4$) with $d = 0.9$ and $d = 2.0$, the time-delay dynamics illustrate a flatter transition to steady-state for $\psi = 0°$ than the other azimuth angles. The flow from the vortex sheets are hitting in similar proximity to the blade for both cases. The exact correlation between shed vortices and blade location when the flow from the upper rotor hits the lower rotor should be further studied in the future to understand what relationship causes the large variation in dynamic differences.
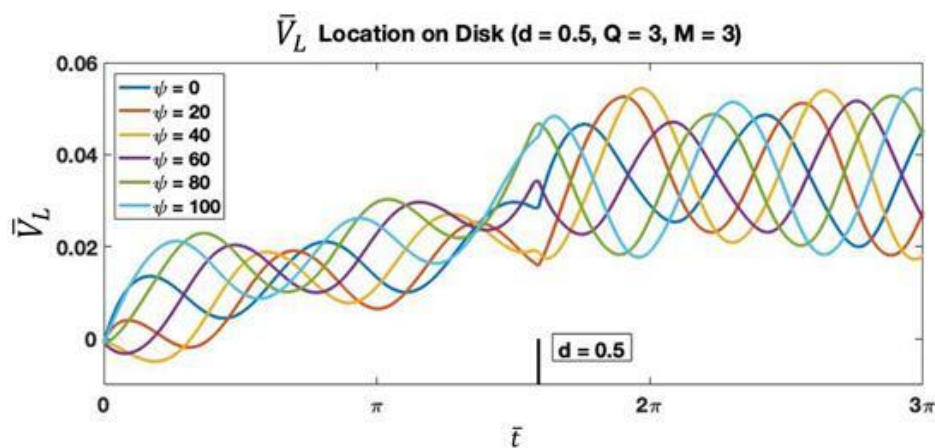
Figure 5-49: Variation in time-delay dynamics on lower rotor velocity with location on disk for a system $d = 0.5$, $Q = 3$, $M = 3$.
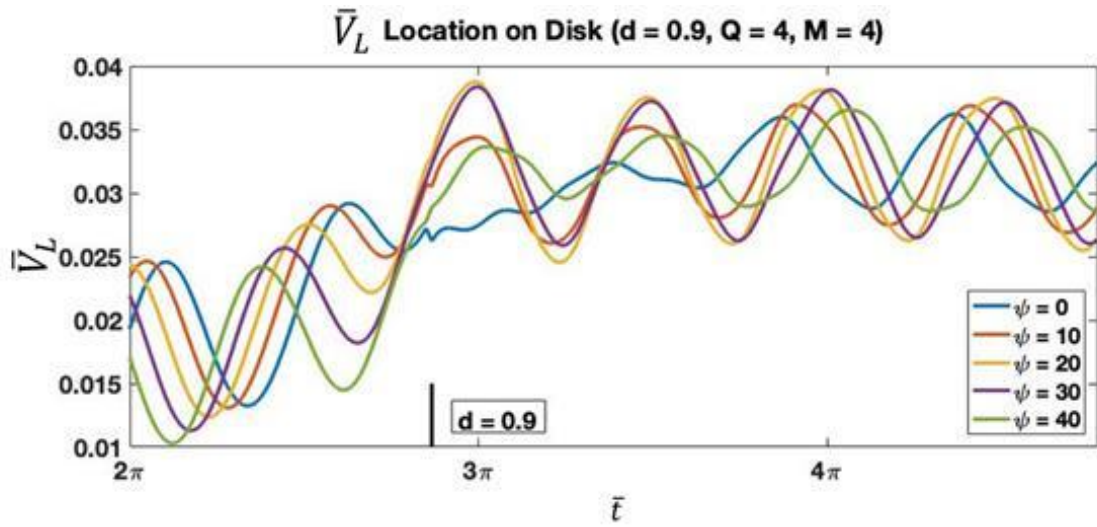
Figure 5-50: Variation in time-delay dynamics on lower rotor velocity with location on disk for a system $d = 0.9$, $Q = 4$, $M = 4$.
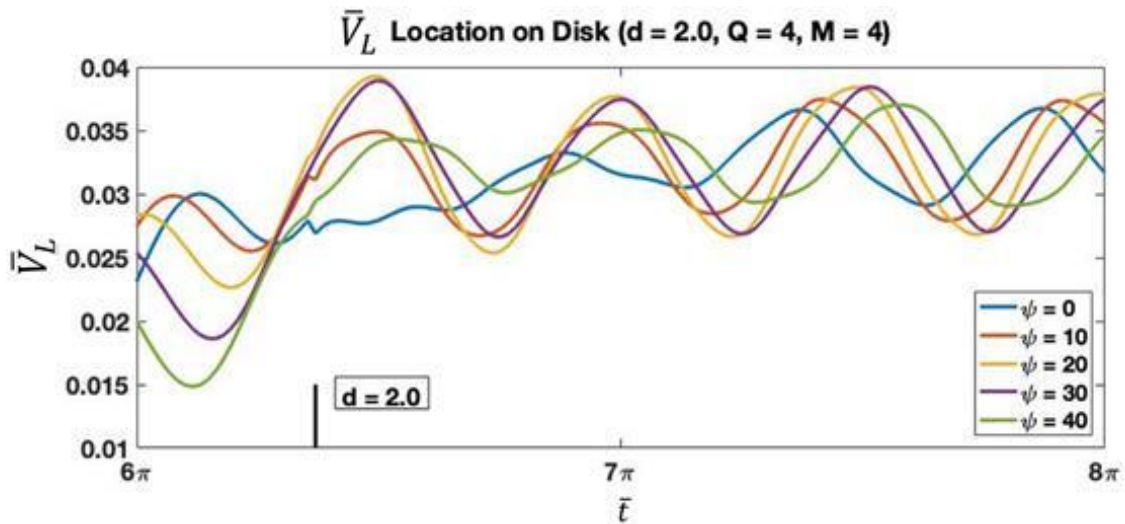
Figure 5-51: Variation in time-delay dynamics on lower rotor velocity with location on disk for a system $d = 2.0$, $Q = 4$, $M = 4$.

5.3.5 Velocity Contours

The development of the velocity contour profiles provides a visual of the flow across the entire disk at a moment in time. The velocity contours help better visualize where the rotor blades are at in the system and where the vortex sheets from the upper rotor hit the lower rotor. Some of the variables that are evaluated with the contour profiles are Q, M, d, and $\bar{t}$. To keep the profiles cleaner and provide a better visualization of the flow between the blades and shed vortices that hit the lower rotor, only $Q = 3$ is used. Larger Q values can lead to overlapping in flow regions that do not provide a good representation of the individual impact of each component.

In Fig. 5-52, the total velocity on the upper rotor is analyzed at $\bar{t} = 9\pi$ for $d = 0.1, 0.5, 1.0$ and $M = 3, 6, 9, 12$. Increases in the rotor spacing demonstrate slight increases in the magnitudes of velocities, but the velocities across the rotor for $d = 0.5$ and $d = 1.0$ are almost entirely the same. The increase in the number of harmonics primarily provides a better resolution within the system. The locations of the blade tips are more accurately defined when $M > 3$. Figure 5-53 shows the lower rotor for the same system as Fig. 5-52. As M increases, the location of the blade tips and the shed vortices again become more well defined. We can differentiate the lower rotor blades from the locations where the shed vortices hit with the blade markings in red and vortex sheet markings in black. At the close rotor spacing, the vortices are bound vortices whereas the larger rotor spacing they become shed vortices. As rotor spacing changes, it is also notable that the location of the shed vortices changes due to variations in the time delay.

The contours in Fig. 5-54 compare the total velocity across the three-bladed lower rotor ($M = 12$) for a case where $d = 0.1$ and where $d = 0.5$ at different points in time. Combined these plots show how the variations in rotor spacing and $\bar{t}$ impact the velocity across the

disk. At $\bar{t} = 10\pi$ both systems show 6 distinct regions to account for the three blades and three regions where the shed vortices hit. In the next frame at $\bar{t} = 10.22\pi$ the blades and the shed vortices for the $d = 0.1$ case are separating from overlapping, creating a longer region of higher velocity. Meanwhile the $d = 0.5$ case illustrates that the blade and shed vortices pass over one another. In the final frame the blade and vortices regions in the $d = 0.1$ case are close to overlapping, creating a more elongated region of high velocity. The blade and vortices regions in the $d = 0.5$ case are overlapping, resulting high magnitudes of velocity.
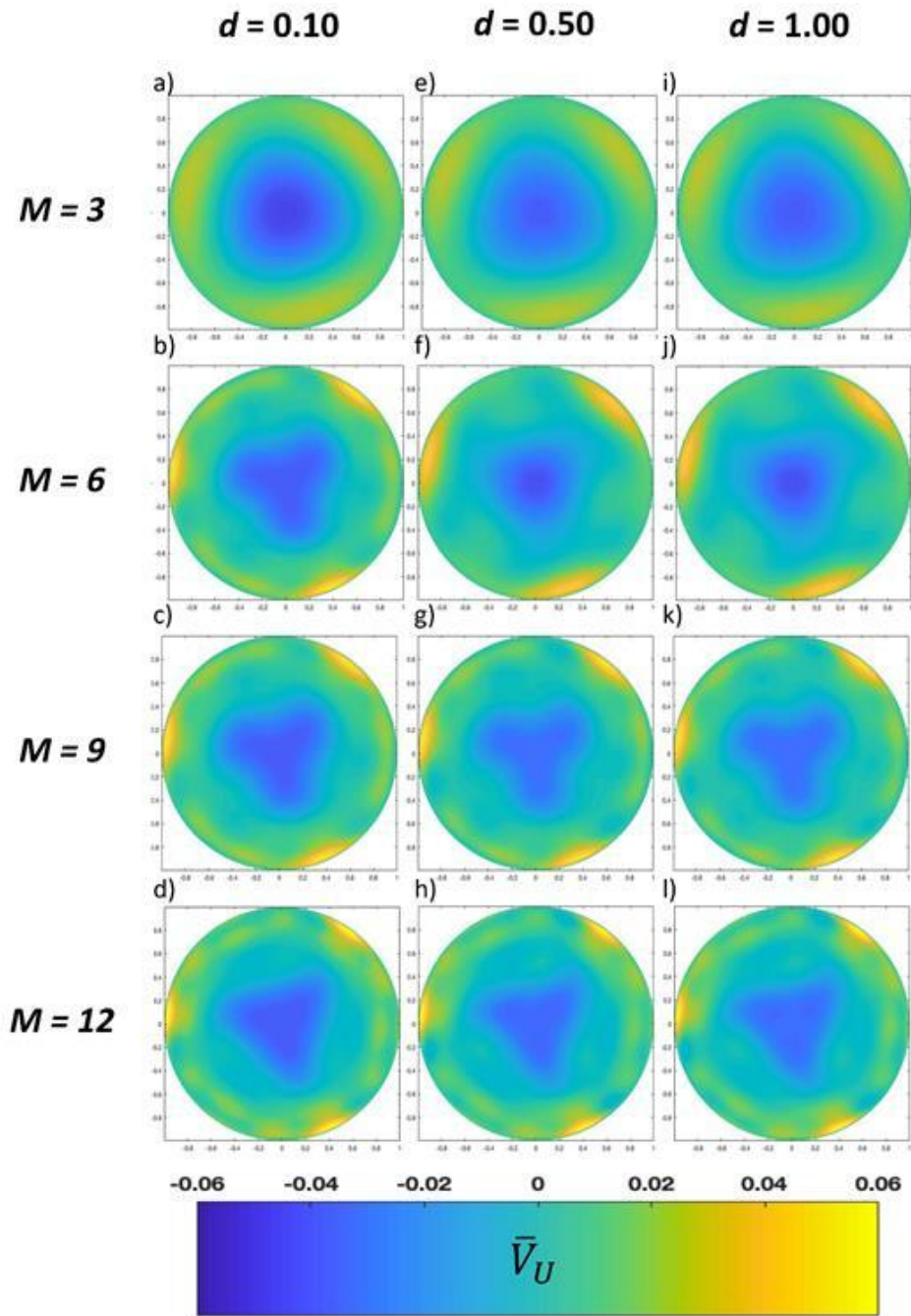
Figure 5-52: Velocity contours for $\overline{V}_U$ across the upper rotor for a three-bladed system at $\bar{t} = 9\pi$ with variables a) $d=0.1$ and $M=3$, b) $d=0.1$ and $M=6$, c) $d=0.1$ and $M=9$, d) $d=0.1$ and $M=12$, e) $d=0.5$ and $M=3$, f) $d=0.5$ and $M=6$, g) $d=0.5$ and $M=9$, h) $d=0.5$ and $M=12$, i) $d=1.0$ and $M=3$, j) $d=1.0$ and $M=6$, k) $d=1.0$ and $M=9$, and l) $d=1.0$ and $M=12$.
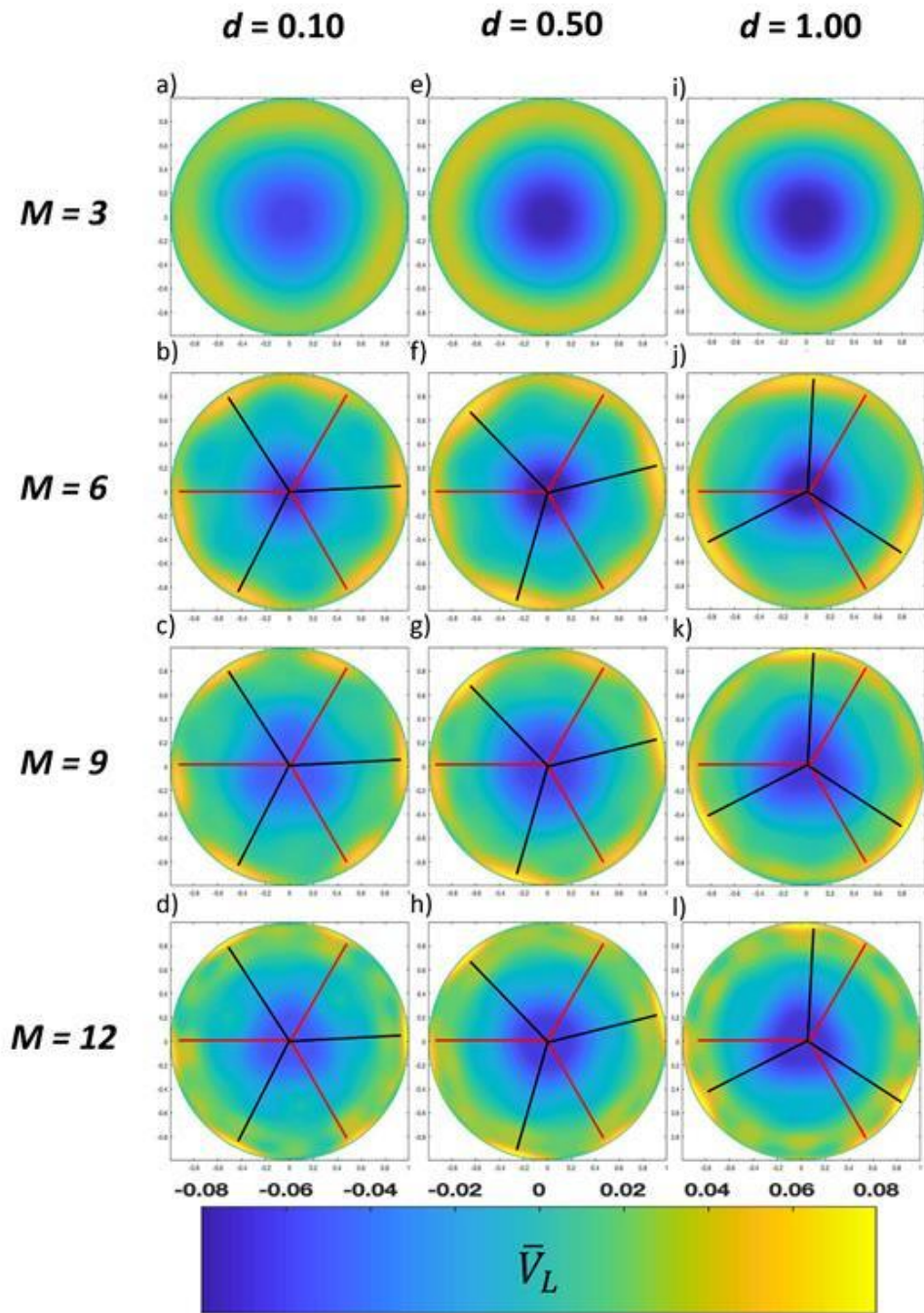
Figure 5-53: Velocity contours for $\overline{V}_L$ across the rotor for a three-bladed system at $\bar{t} = 9\pi$ with variables a) $d=0.1$ and $M=3$, b) $d=0.1$ and $M=6$, c) $d=0.1$ and $M=9$, d) $d=0.1$ and $M=12$, e) $d=0.5$ and $M=3$, f) $d=0.5$ and $M=6$, g) $d=0.5$ and $M=9$, h) $d=0.5$ and $M=12$, i) $d=1.0$ and $M=3$, j) $d=1.0$ and $M=6$, k) $d=1.0$ and $M=9$, and l) $d=1.0$ and $M=12$.
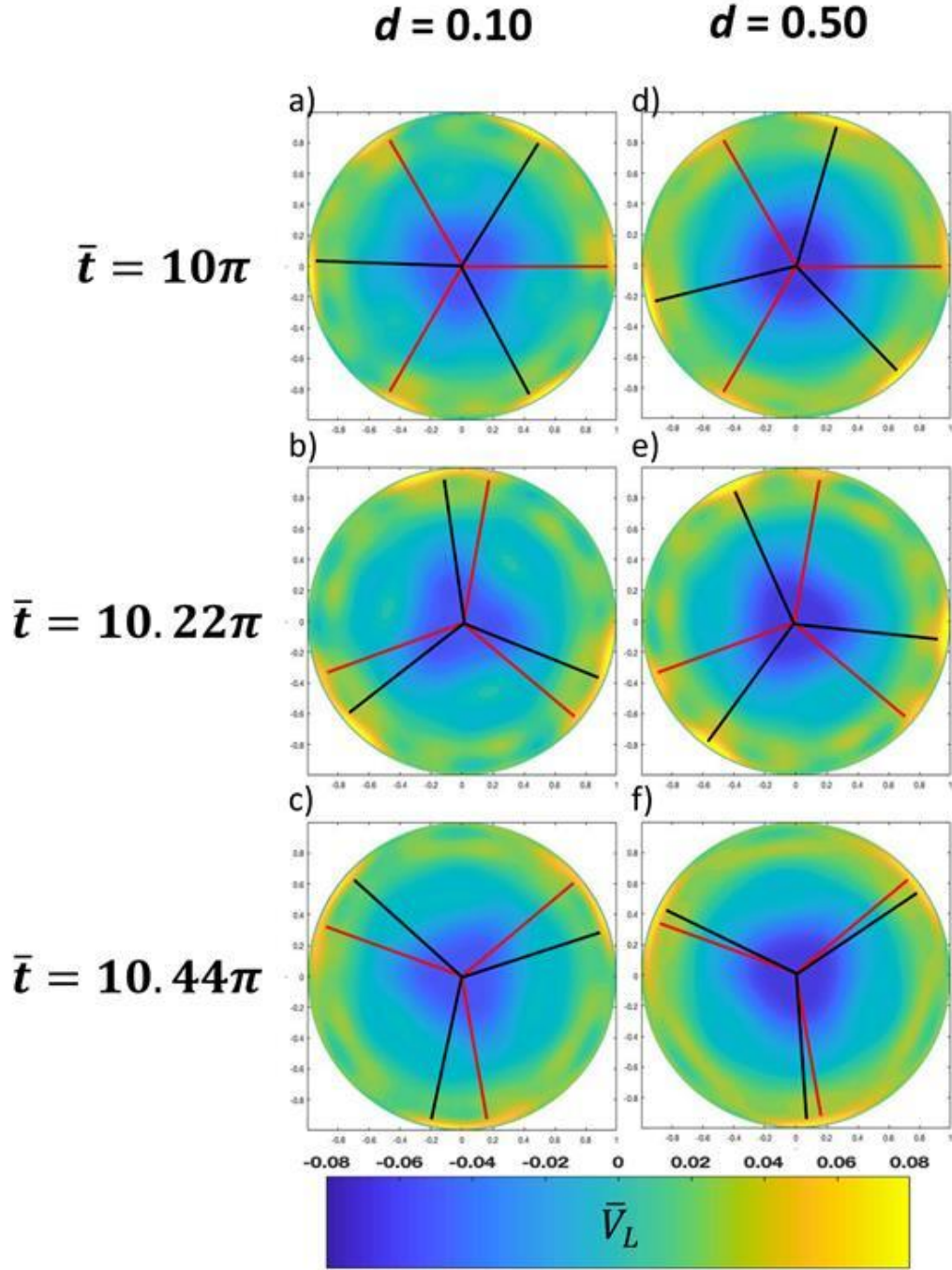
Figure 5-54: Velocity contours for $\overline{V}_U$ across the upper rotor for a three-bladed system with $M=12$ and variables a) $d=0.1$ and at $\bar{t} = 10\pi$, b) $d=0.1$ and $\bar{t} = 10.22\pi$, c) $d=0.1$ and $\bar{t} = 10.4\pi$, d) $d=0.5$ and $\bar{t} = 10\pi$, e) $d=0.5$ and $\bar{t} = 10.22\pi$, and f) $d=0.5$ and $\bar{t} = 10.44\pi$.

Chapter 6

Wind Turbine Applications

6.1   Application of Model to Wind Turbines

The model presented herein is easily adapted to the analysis of wind turbines either for coaxial turbines or two interacting turbines. The maximum distance studied in this work is for a rotor spacing of one diameter. While wind farms generally have turbine spacings of seven rotor diameters or more, some studies suggest spacings of 15 diameters are needed [46]. This work looks at up to one diameter because the model shows no significant changes after that point. The primary adaptation for the model was to change from consuming power to generating power. In addition, the induced flow was adjusted for an ideal scenario. The purpose of this section is to demonstrate the adaptability of the coaxial rotor model for other uses.

For wind-turbine applications, the user defined parameters are $\eta = 1/6$, $\sigma = 0.1$, and $a = 5.73$. η is larger for the wind turbines because the lift to drag ratios of wind turbine airfoils are typically higher. In chapter 5, it is assumed that the coaxial rotor system was lightly loaded and therefore θ was only a function of C_T and η. For the wind turbine simulations, we no longer consider it lightly loaded and therefore η is not $>> \nu$. In the

optimum system for wind energy applications one-third of the wind is stopped such that the ratio of ν to η is:

$$\nu = -\frac{1}{3}\eta \tag{6.1}$$

Here ν is negative because the wind turbine is slowing down the wind. Previously, C_T was a set value in the results for Chapters 4 and 5, but here we calculate it as:

$$C_T = 2\nu(\eta + \nu) \tag{6.2}$$

The pitch angles for the blades on each rotor can be determined with the relationship:

$$\theta = \frac{6C_T}{\sigma a} + \frac{3}{2}(\eta + \nu) \tag{6.3}$$

Applying the defined values above to these equations, ν, C_T, and θ are $\nu = -1/18$, $C_T = -1/81$, and $\theta_F = \theta_T = 0.0432$.

6.2 Numerical Illustrations of Wind Turbine Dynamics

All velocities are presented at the location $\bar{r} = 0.8$ and $\psi = 0$ for the scenario of axial flow ($\chi = 0$, $\mu = 0$). For this work, the rotor spacings vary between $d = 0.1 - 2.0$ rotor radii. The focus of the results in this chapter is to explore the adaptation of the previously developed finite-state model for wind turbine applications.

6.2.1 Impact of Rotor Spacing Variations on Wind Turbine Velocity Profiles

Figures 6-1 to 6-4 illustrate the impact of rotor spacing on the total velocity on the front wind turbine, $\overline{V}_F$. Figure 6-1 gives $\overline{V}_F$ for a three-bladed rotor with three harmonics and

shows that maximum velocities in the oscillations are nearly identical for all rotor spacings, but the minima peaks vary, with the smallest rotor spacings having the largest negative peak. It also illustrates that, for rotor spacing of $d > 0.5$, there is minimal change in the velocity profile. When the number of harmonics is increased to $M = 6$ in Fig. 6-2, it is noticeable that the minimum peak velocities vary; but the maximum peak velocities are similar for all rotor spacings. This is opposite of the helicopter applications, but we are slowing down the wind in this case. Blades passing through the point of interest occurs as the profile approaches the minimum peaks, midway between the maxima and the minima. Figures 6-3 to 6-4 show the velocity profiles for a four-bladed rotor with $M = 4$ and $M = 8$ harmonics, respectively. The main difference between the three-bladed and four-bladed rotors is the magnitudes of the oscillations. The three-blade and four-blade rotors each have the same rotor solidity; but a three-bladed rotor has a larger bound vorticity on each blade which is why the oscillation magnitudes vary, but the average velocity remains the same. The trends for the front turbine rotor are consistent with the patterns illustrated in Chapter 5 for the upper rotor velocity.

The impact of rotor spacing on the total velocity on the trailing rotor, $\overline{V}_T$, is shown in Figs. 6-5 to 6-8. The point in time where the flow from the leading rotor hits the trailing rotor is marked in the images to assist in identifying the time-delay dynamics. In Fig. 6-5, a three-bladed rotor with three harmonics and rotor spacings of $d = 0.1, 0.3, 0.5$ easily depicts the time-delay dynamics with sharp peaks. The nature of the time-delay dynamics and the dynamics—transitioning into the steady-state—is impacted both by the rotor spacing and by the location being observed on the disk. An increase in the rotor spacings to $d = 1.1, 1.5$, and 1.9, respectively, for the three-bladed system in Fig. 6-6 shows that the early dynamics are similar among the cases because the flow from the leading rotor has not reached the trailing rotor, therefore it is driven purely by on-disk terms. This is also the case for the

helicopter dynamics. The trends for the transition dynamics in Fig. 6-6 are similar to those in Fig. 6-5. Figures 6-7 and 6-8 show $\overline{V}_T$ for a four-bladed system and demonstrate that the time-delay dynamics are more difficult to discern without the markings because many of the time-delay dynamics are smooth. It should be noted that the shape of the dynamic oscillations for rotor spacing $d = 1.5$ is more unique and is due to the combination of location on the disk and rotor spacing.

Figures 6-9 to 6-12 show the different components for the velocity on the front rotor ($\overline{V}_{FF}$, $\overline{V}_{FT}$) and trailing rotor ($\overline{V}_{TT}$, $\overline{V}_{TF}$). The main takeaways from these plots are that as rotor spacing increases $\overline{V}_{TF}$ increases and $\overline{V}_{FT}$ decreases. For $d > 0.5$, $\overline{V}_{FT}$ effectively becomes zero. The on-disk components $\overline{V}_{FF}$ and $\overline{V}_{TT}$ only undergo slight variations with rotor spacing. These trends are all similar to those of the helicopter system.

Variations in the velocity profiles of $\overline{V}_{TT}$ with different rotor spacings are highlighted in Figs. 6-13 to 6-16. There are no visible instantaneous changes in the profiles when the flow from the front rotor hits the trailing rotor, which should be expected because $\overline{V}_{TT}$ does not contain any time-delay terms. However, an impact from the flow from the front rotor hitting the trailing rotor can still be noticed in the region between the flow hits and the steady-state oscillations. This is best depicted in Fig. 6-14 in which the early oscillations are identical for all of the rotor spacings. In the range of $2\pi < \bar{t} < 5\pi$, the profiles begin to vary; but ,for $\bar{t} > 5\pi$ they begin to converge again and are similar in shape and magnitude. $\overline{V}_{TT}$ is an on-disk term. Therefore it makes sense that the profiles are relatively similar in the steady-state region.

For $\overline{V}_{TF}$ presented in Figs. 6-17 to 6-20, the time delay causes a smooth increase prior to the flow from the leading rotor hitting the trailing rotor. The peaks in these profiles each represent when the vortex sheets hit the location being investigated on the trailing rotor. It

166

should be noted that for the larger rotor spacings in Fig. 6-18 and Fig. 6-20, the steady-state oscillations have similar magnitudes. The oscillation peaks are also double that of the $\overline{V}_{FF}$ terms shown in Figs. 6-9 to 6-12. For wind turbines, the flow downstream reaches is maximum at a smaller rotor spacing it does for the helicopter. This is due to the differing freestream velocities utilized between the applications. In the wind turbine simulations the vortex sheets are more compact and the time delay is shorter.
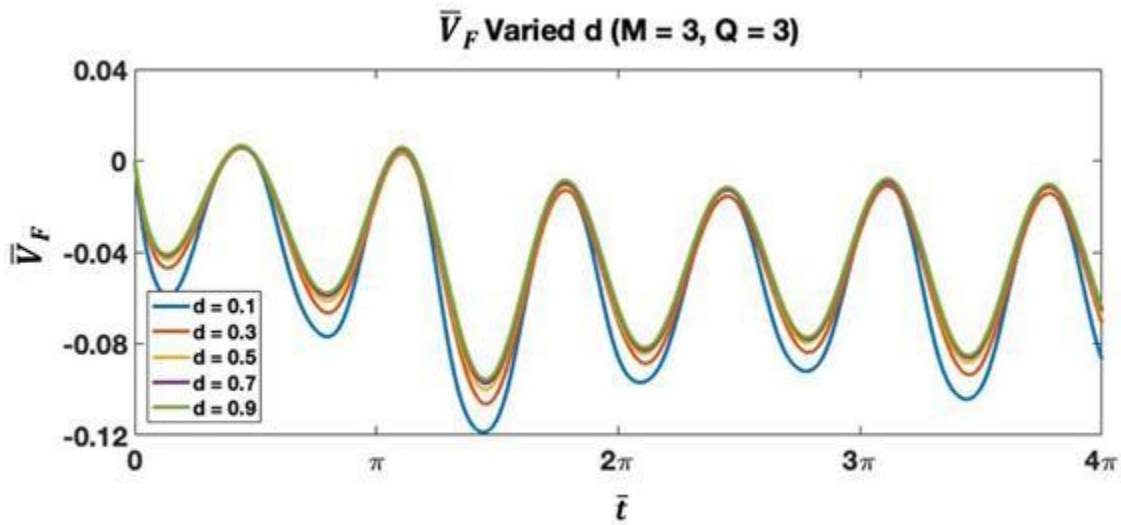
Figure 6-1: Velocity on front turbine rotor with 3 blades and 3 harmonics at varied rotor spacings $(d = 0.1 - 0.9)$
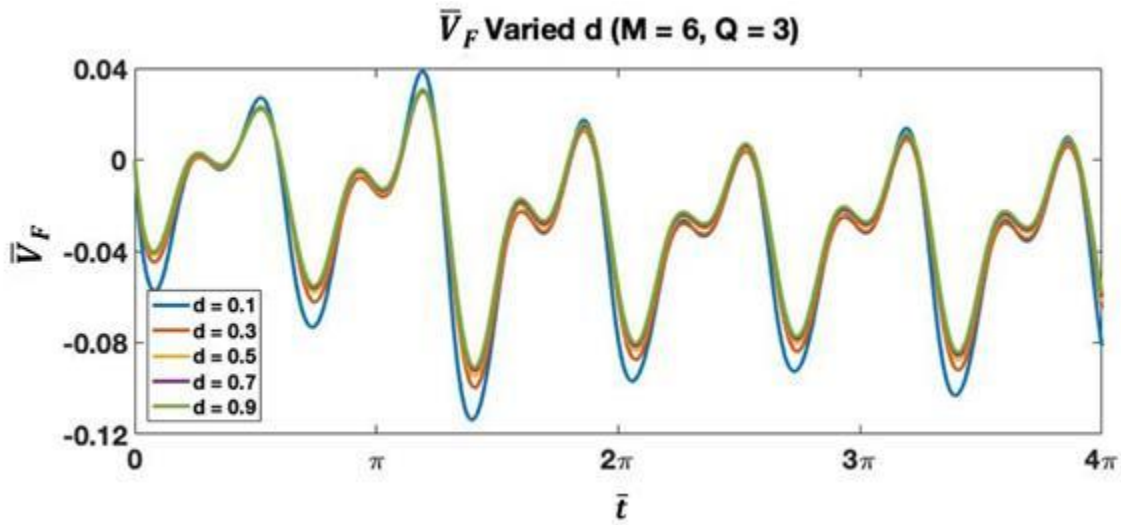
Figure 6-2: Velocity on front turbine rotor with 3 blades and 6 harmonics at varied rotor spacings ($d = 0.1 - 0.9$)
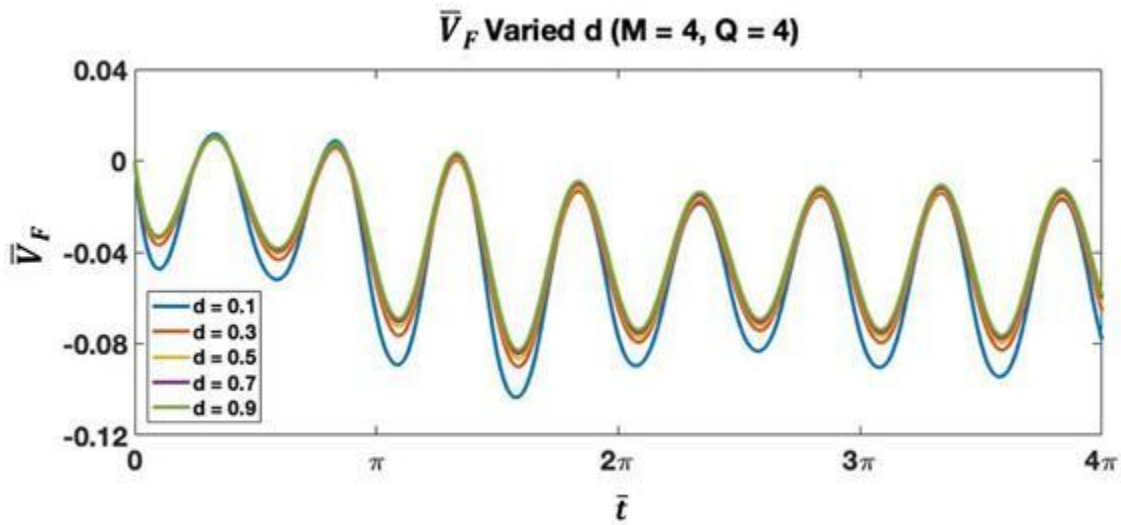
Figure 6-3: Velocity on front turbine rotor with 4 blades and 4 harmonics at varied rotor spacings ($d = 0.1 - 0.9$)
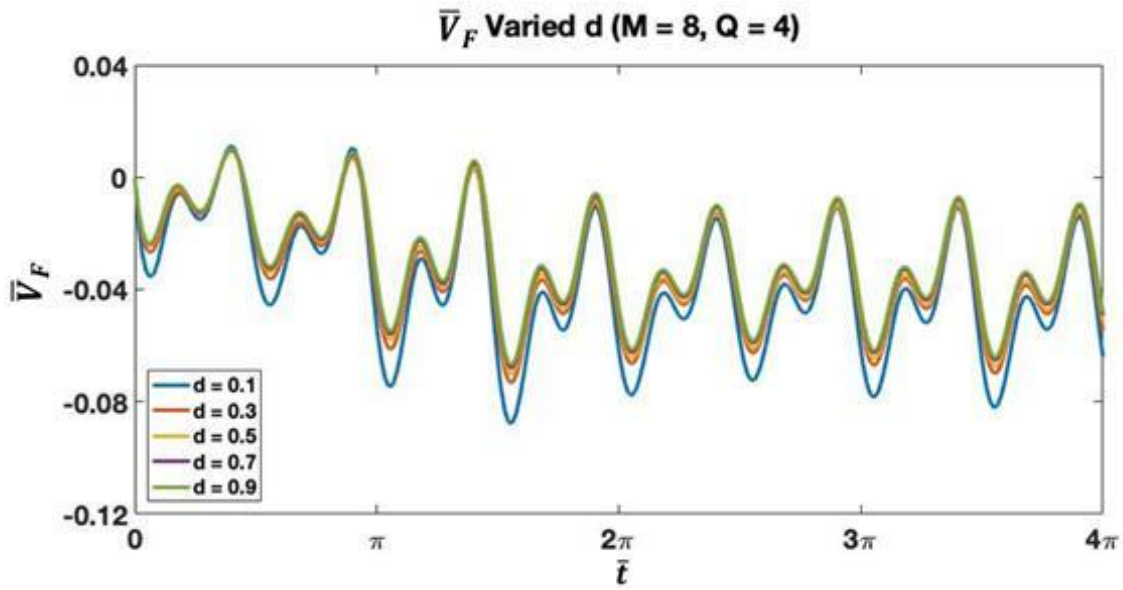
Figure 6-4: Velocity on front turbine rotor with 4 blades and 8 harmonics at varied rotor spacings ($d = 0.1 - 0.9$)
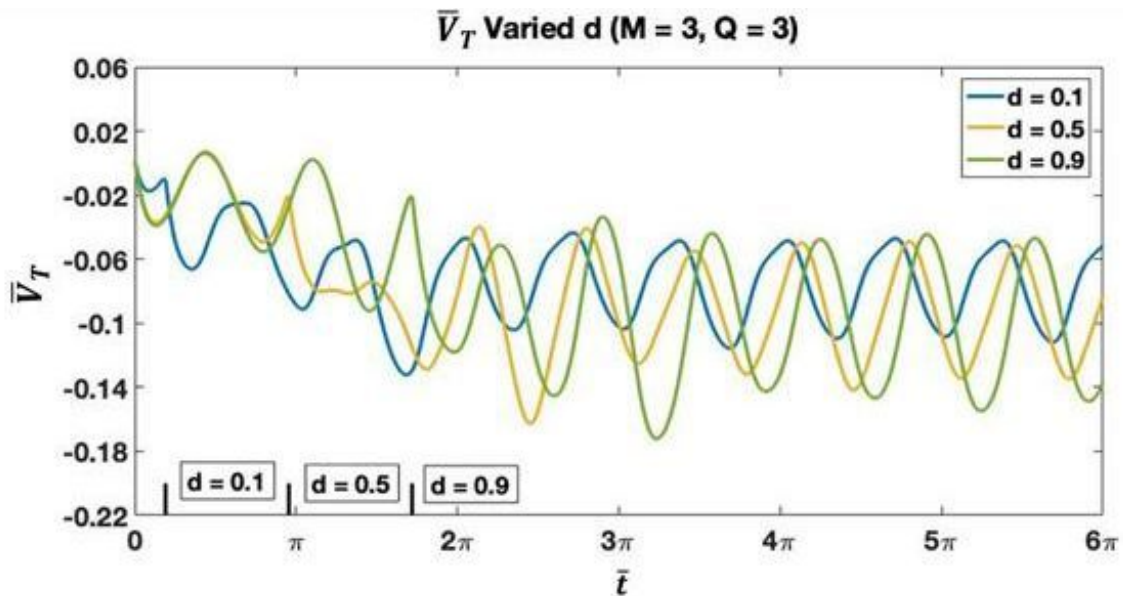
Figure 6-5: Velocity on trailing turbine rotor with 3 blades and 3 harmonics at varied rotor spacings ($d = 0.1 - 0.9$)

169
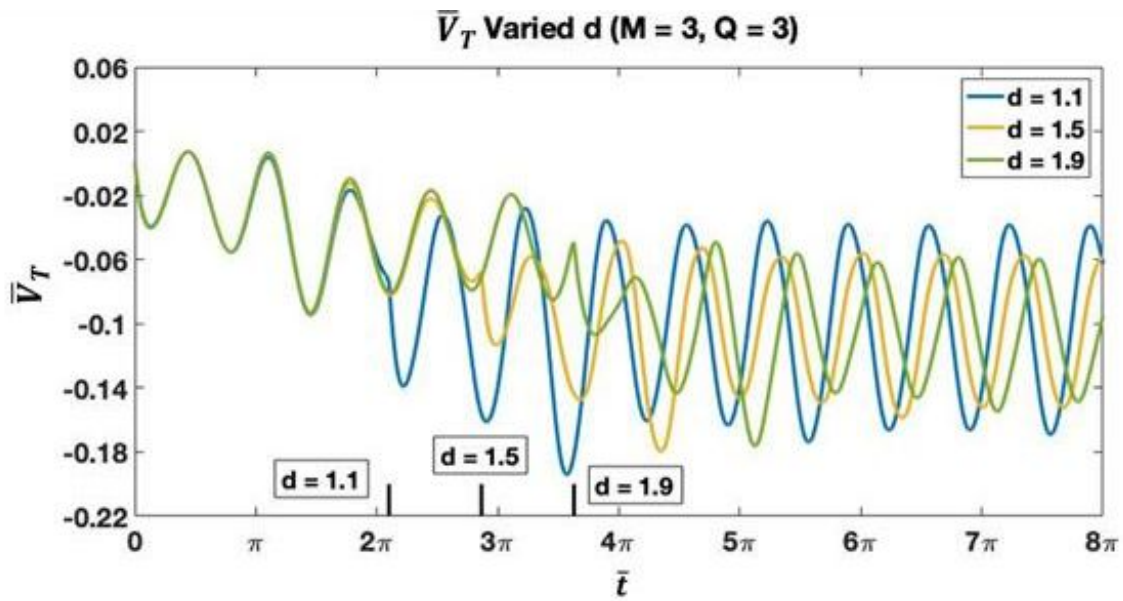
Figure 6-6: Velocity on trailing turbine rotor with 3 blades and 6 harmonics at varied rotor spacings $(d = 1.1 - 1.9)$
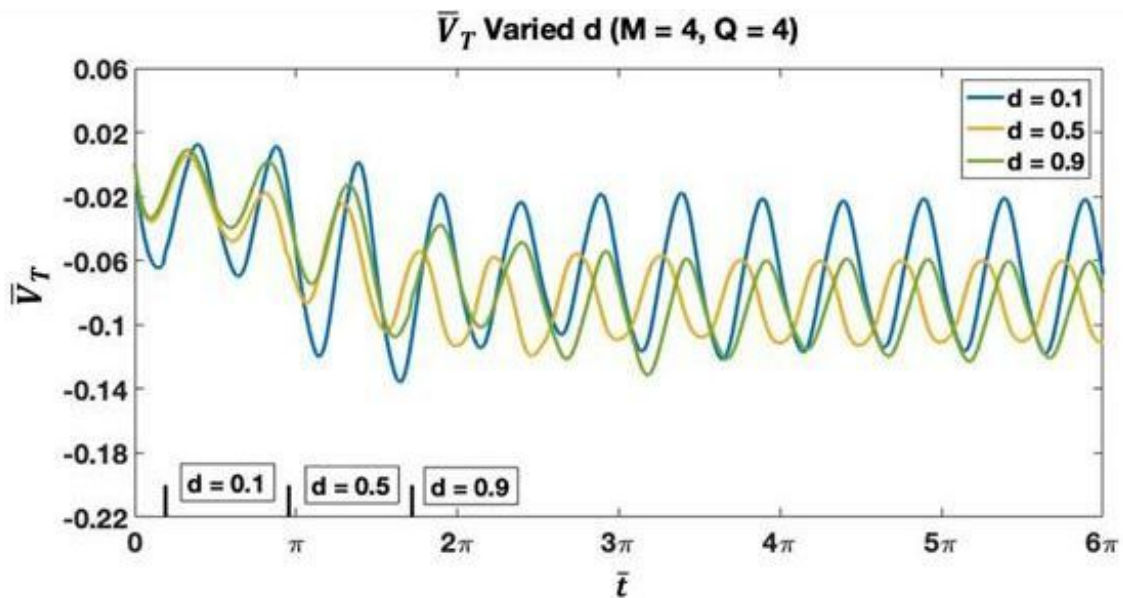
Figure 6-7: Velocity on trailing turbine rotor with 4 blades and 4 harmonics at varied rotor spacings $(d = 1.1 - 1.9)$
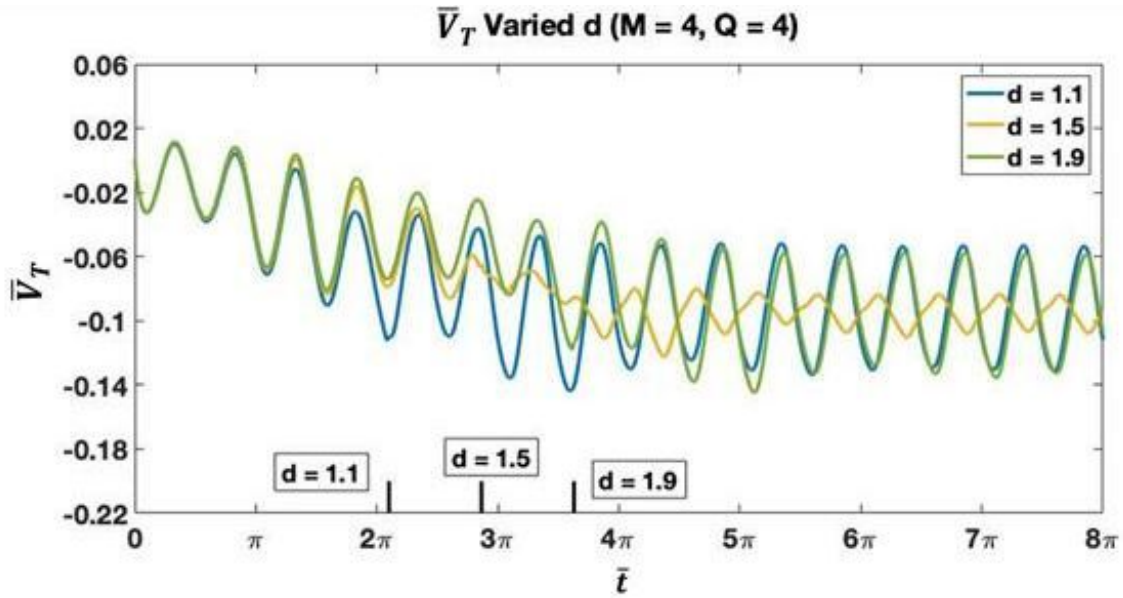
Figure 6-8: Velocity on trailing turbine rotor with 4 blades and 8 harmonics at varied rotor spacings ($d = 1.1 - 1.9$)
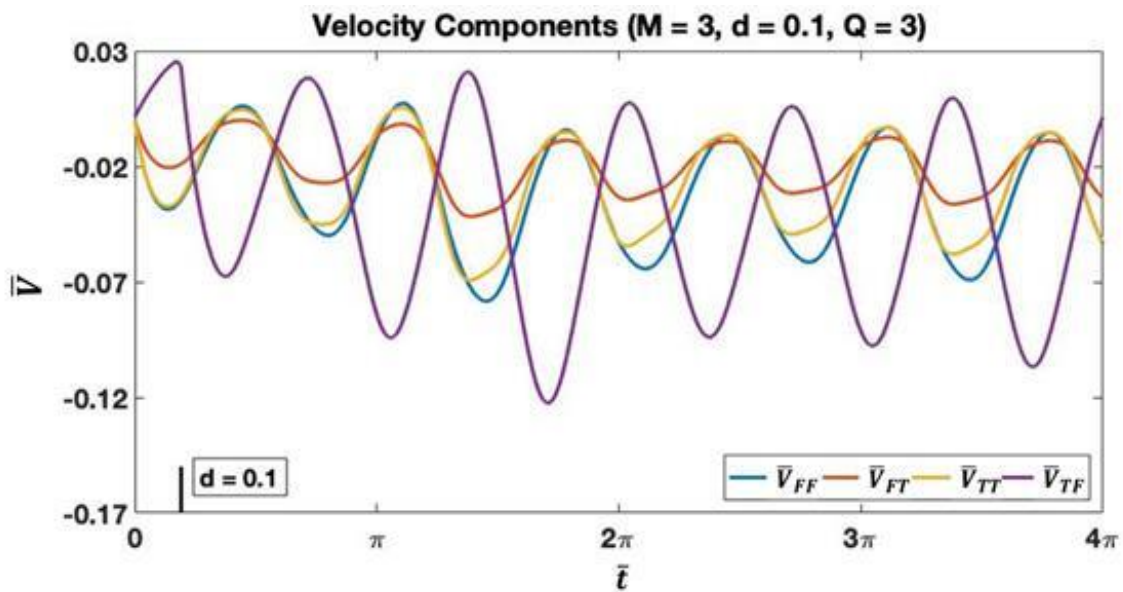
Figure 6-9: Velocity components for system with 3 blades per rotor and 3 harmonics at rotor spacing $d = 0.1$
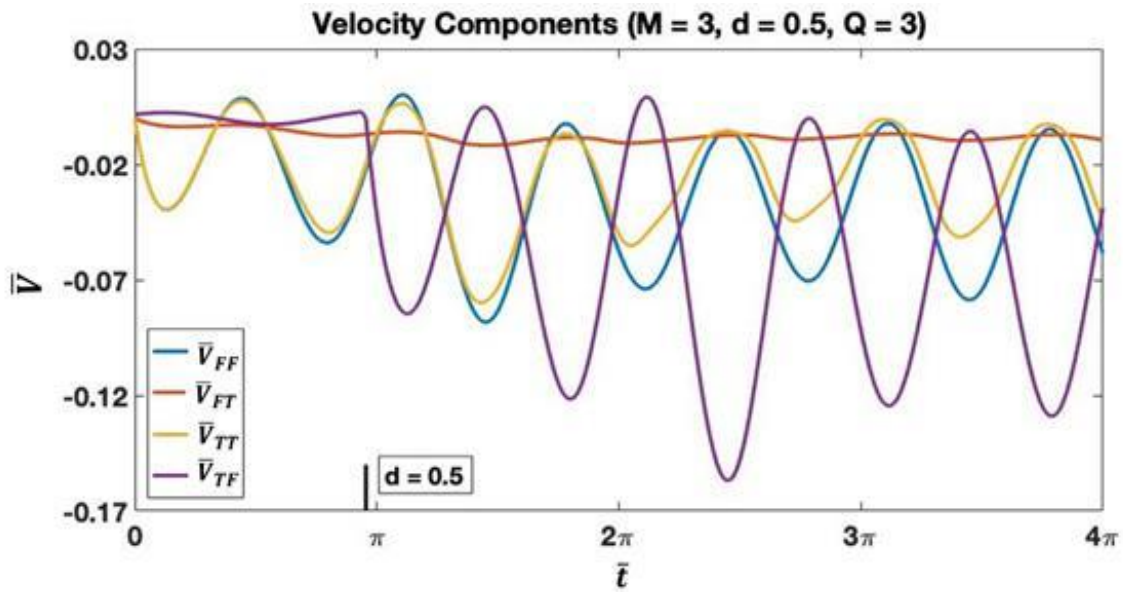
Figure 6-10: Velocity components for system with 3 blades per rotor and 3 harmonics at rotor spacing $d = 0.5$
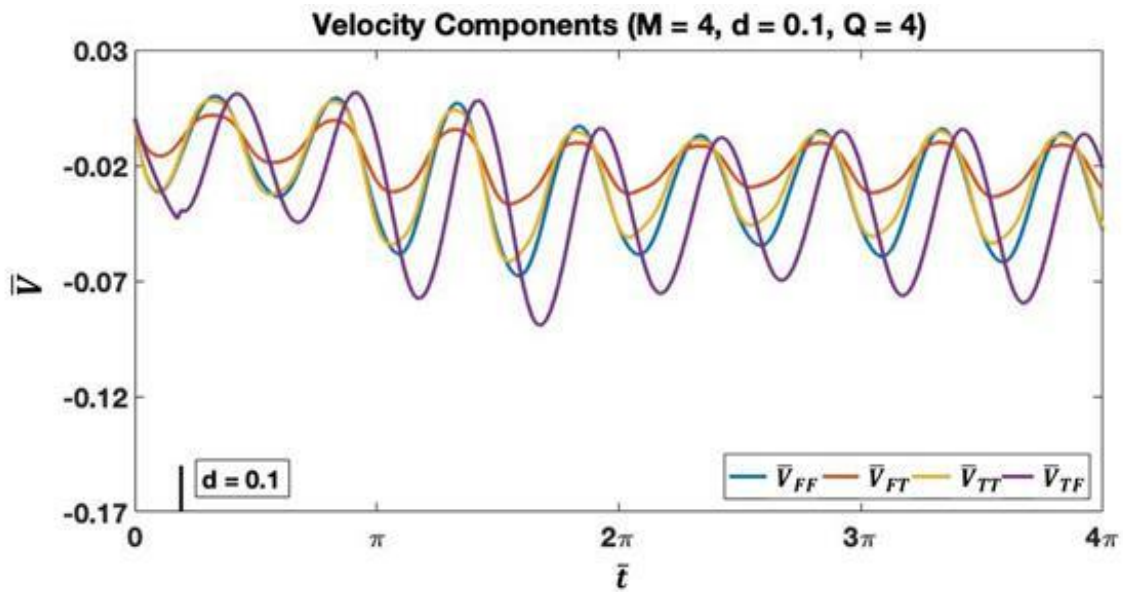
Figure 6-11: Velocity components for system with 4 blades per rotor and 4 harmonics at rotor spacing $d = 0.1$
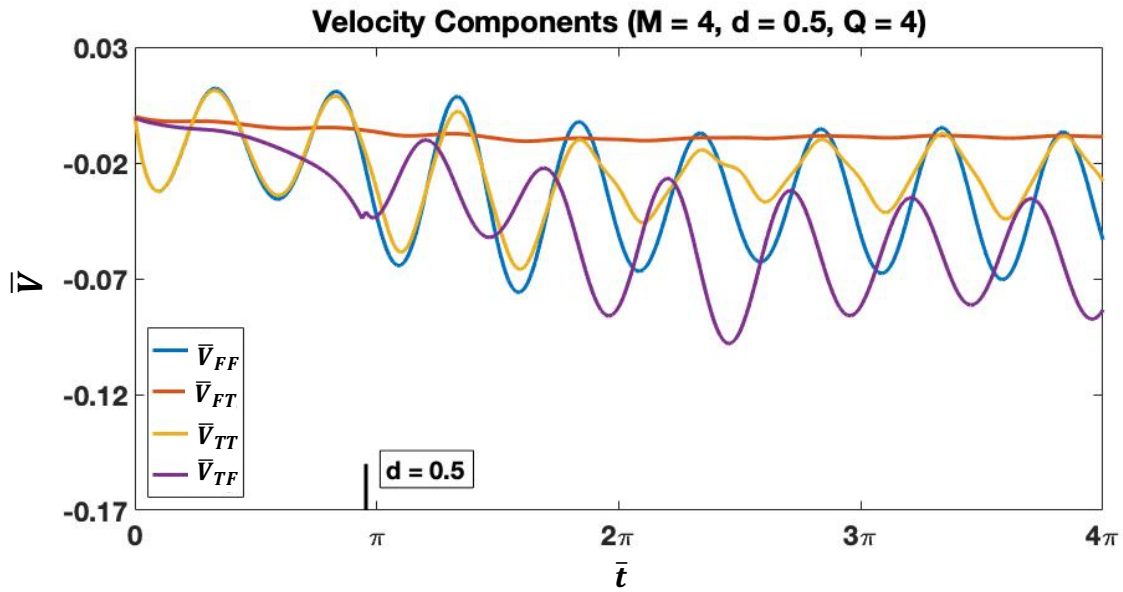
Figure 6-12: Velocity components for system with 4 blades per rotor and 4 harmonics at rotor spacing $d = 0.5$
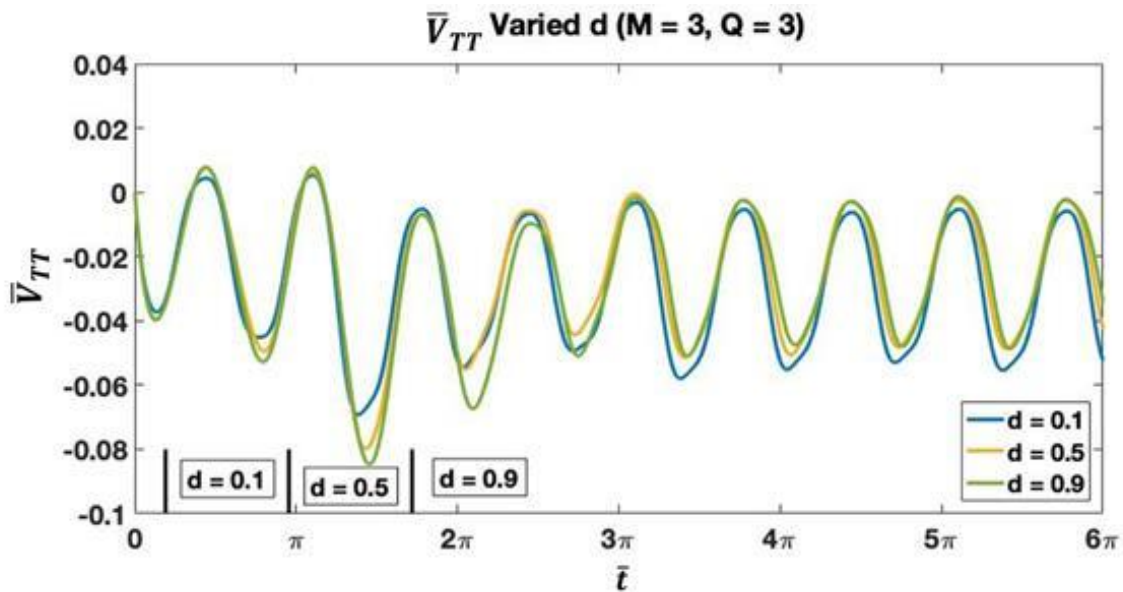
Figure 6-13: $\overline{V}_{TT}$ for system with 3 blades per rotor and 3 harmonics at turbine rotor spacings $(d = 0.1 - 0.9)$
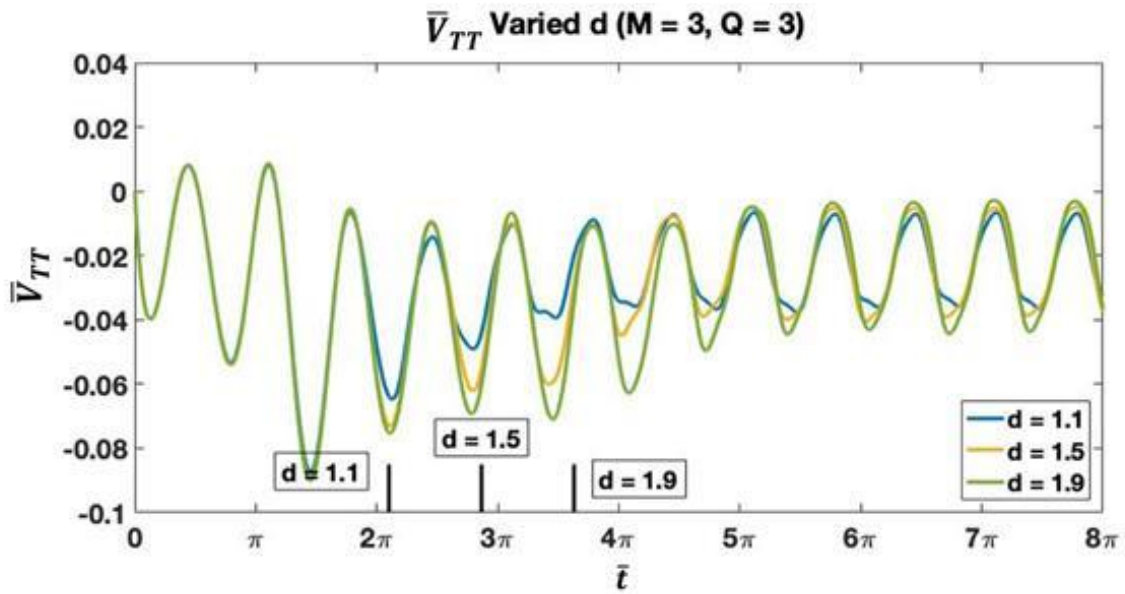
Figure 6-14: $\overline{V}_{TT}$ for system with 3 blades per rotor and 3 harmonics at turbine rotor spacings $(d = 1.1 - 1.9)$
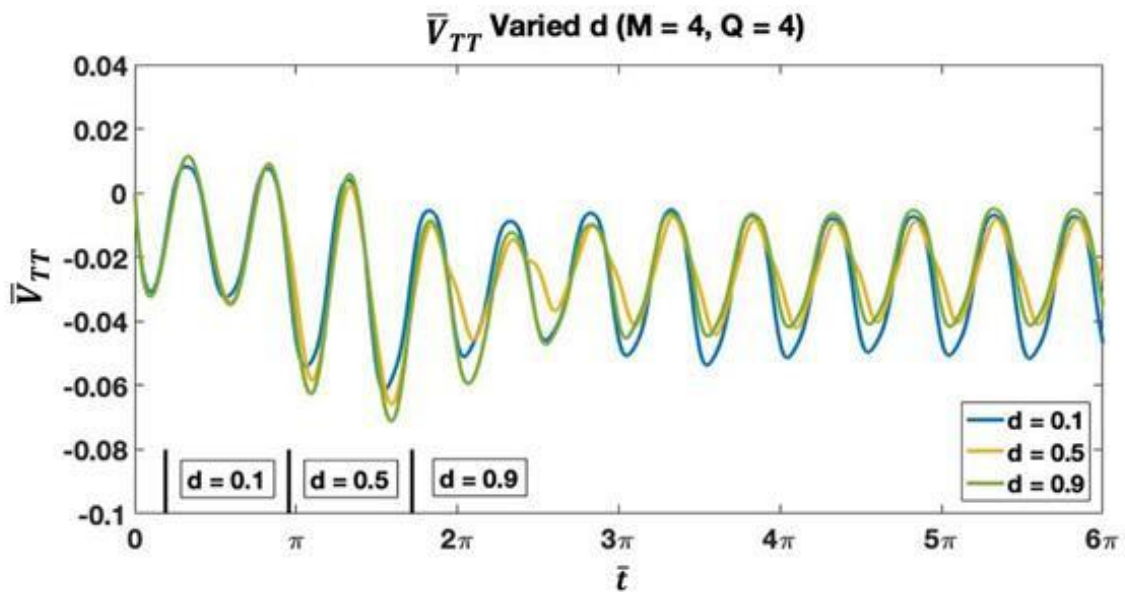
Figure 6-15: $\overline{V}_{TT}$ for system with 4 blades per rotor and 4 harmonics at turbine rotor spacings $(d = 0.1 - 0.9)$
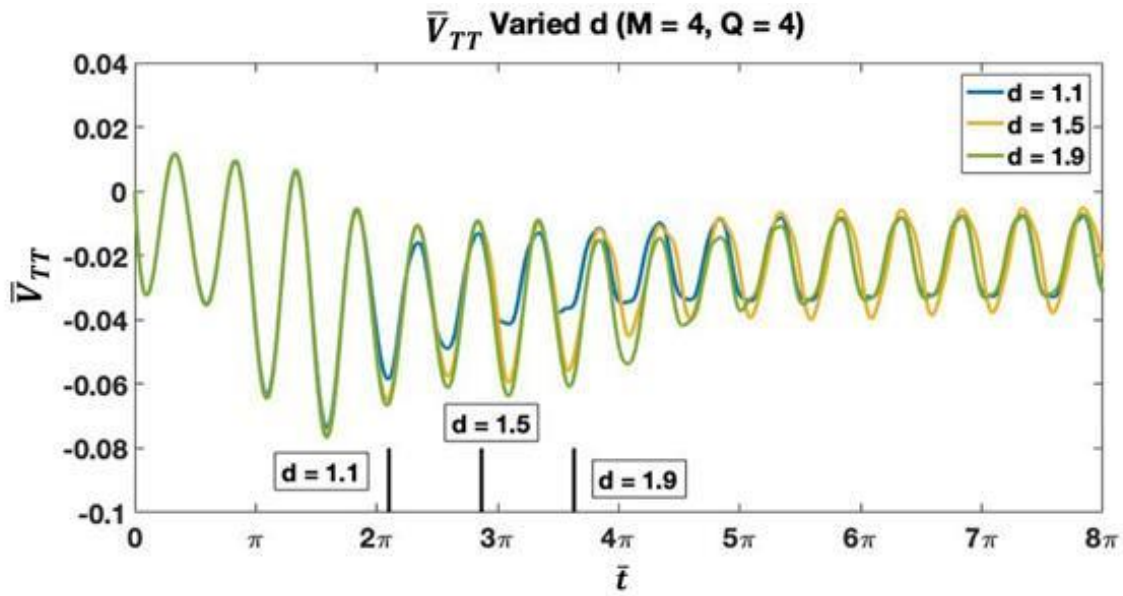
Figure 6-16: $\overline{V}_{TT}$ for system with 4 blades per rotor and 4 harmonics at turbine rotor spacings $(d = 1.1 - 1.9)$
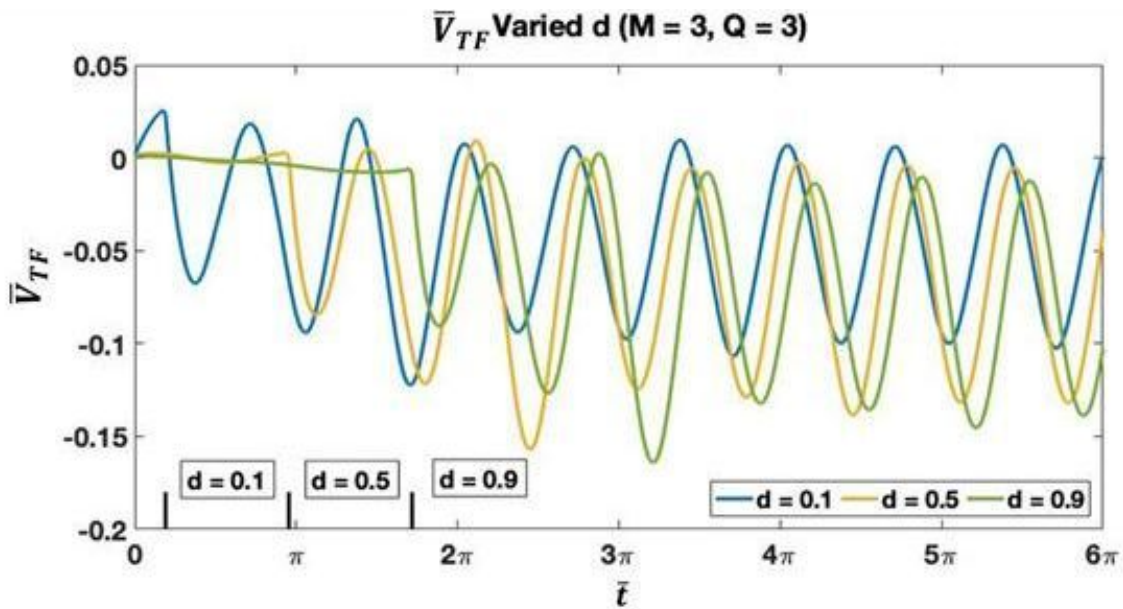
Figure 6-17: $\overline{V}_{TF}$ for system with 3 blades per rotor and 3 harmonics at turbine rotor spacings $(d = 0.1 - 0.9)$
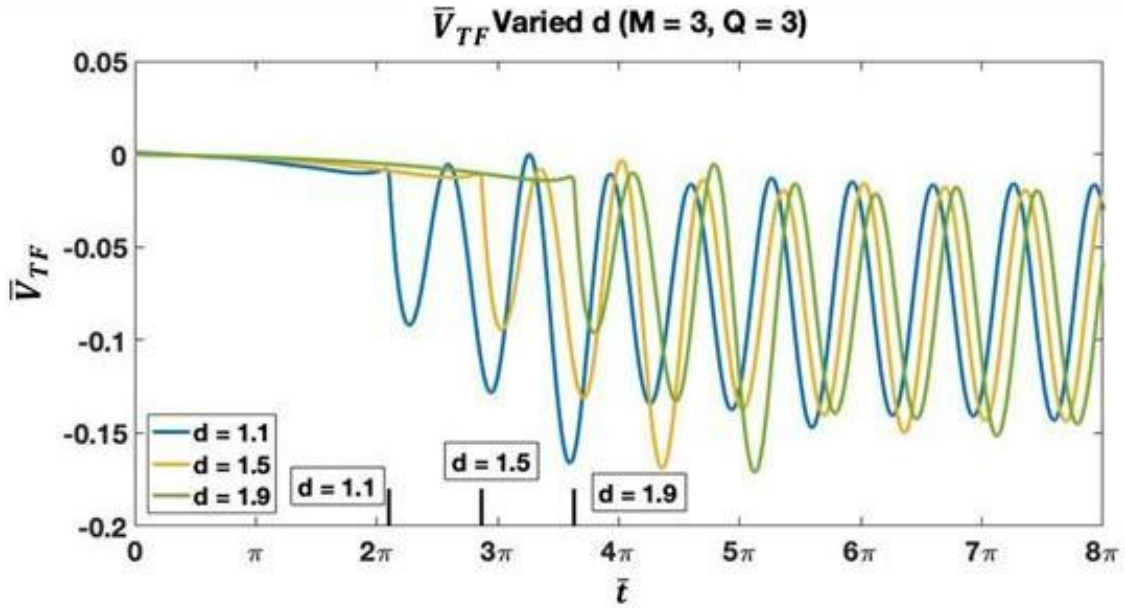
Figure 6-18: $\overline{V}_{TF}$ for system with 3 blades per rotor and 3 harmonics at turbine rotor spacings $(d = 1.1 - 1.9)$
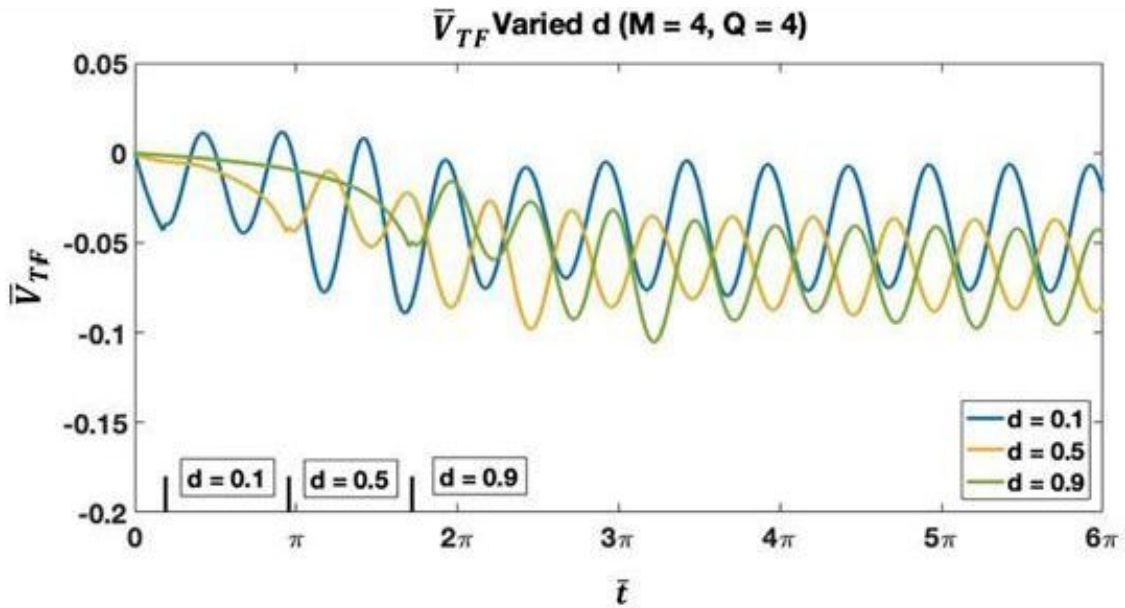
Figure 6-19: $\overline{V}_{TF}$ for system with 4 blades per rotor and 4 harmonics at turbine rotor spacings $(d = 0.1 - 0.9)$

176
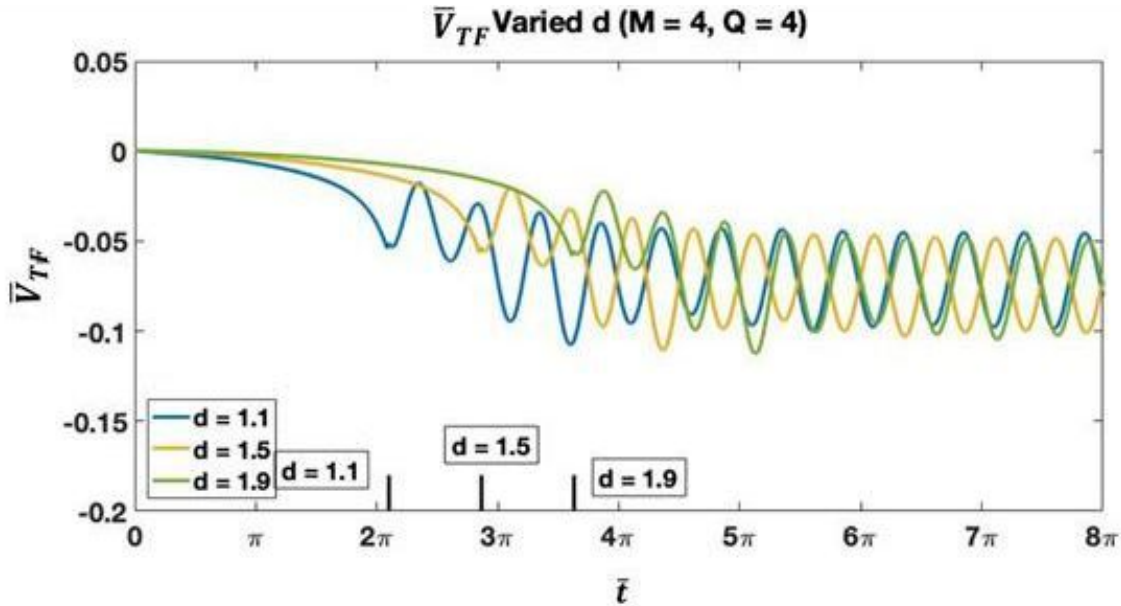
Figure 6-20: $\overline{V}_{TF}$ for system with 4 blades per rotor and 4 harmonics at turbine rotor spacings ($d = 1.1 - 1.9$)

6.2.2 Impact of Harmonic Variations on Wind Turbine Velocity Profiles

Next we study the impact of harmonics on the velocity profiles, starting with $\overline{V}_F$ in Figs. 6-21 to 6-24. An increase in the number of harmonics provides a more focused representation of blade passage over the point of interest—as well as a better representation of the mean velocity between blades passing. The $M = 9$ and $M = 12$ harmonic cases in Figs. 6-21 and 6-22 illustrate the improvement of identify blade passage and mean velocity for a three-bladed rotor. The rotor spacing doesn't have much overall impact on the dynamics of the higher harmonic cases other than in magnitude. The four-bladed rotor case in Figs. 6-23 and 6-24 demonstrates similar trends, but the $M = 12$ harmonic case better models the velocity between blades passing while the $M = 16$ harmonic case better models the blades

passing. If more harmonics are utilized, the representation of both the blades passing and the velocity between blades passing would see further improved representation.

The impact of number of harmonics on $\overline{V}_T$ is illustrated in Figs. 6-25 to 6-32. The oscillations in these figures can be more difficult to decode at times because the profiles illustrate not only the blade passage, but also the shed vortices from the front rotor. The location (in nondimensional time) of the peaks caused by shed vortices are denoted with the purple markers and the blade passage are marked with red lines. The first vortex sheet to hit the point of interest occurs at $\bar{t} = \overline{d}$ because we selected an azimuth that is the same starting azimuth for s a blade from the leading rotor. In Figs. 6-25 through 6-32 it is noticeable that the shape of the profile is dependent on the proximity of the occurrence of blades passing and the shed vortices hitting. In addition, an extra blade changes the dynamics because of the increased frequency of blades passing and vortices hitting the trailing rotor.

The variations in harmonics for the $\overline{V}_{TT}$ profiles in Figs. 6-33 and 6-34 provide a better understanding of how the on-disk terms shape the overall velocity profile on the trailing rotor. The blade passage for all number of harmonics occurs halfway between the maxima and the minima. As the number of harmonics increases the maxima peak to minima peak duration decreases, providing a more precise time of when the blade passes.

The $\overline{V}_{TF}$ profiles in Figs. 6-35 to 6-38 benefit from the increased harmonics and allow one to decipher at what point the vortex sheets hit the rotor. For the smaller rotor spacings, the trailing rotor feels bound vortices from the front rotor which do not occur at the peak. However, as the rotor spacing increases the bound vortices are replaced by shed vortices which occur at a peak and smooth out as rotor spacing increases. The higher harmonic cases in these profiles provide a better illustration of when the vortices hit the rotor. There

are more oscillations in these profiles because the Fourier Series is trying to converge to the sharp peaks of the blade passage.
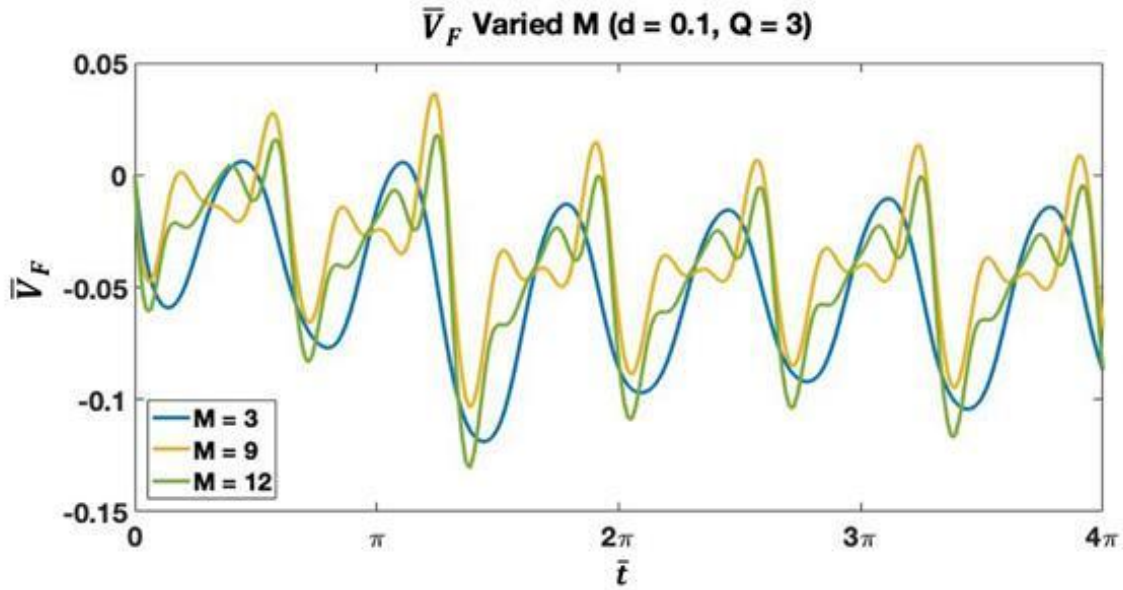
Figure 6-21: Velocity on front turbine rotor with 3 blades and $d = 0.1$ and varied harmonics
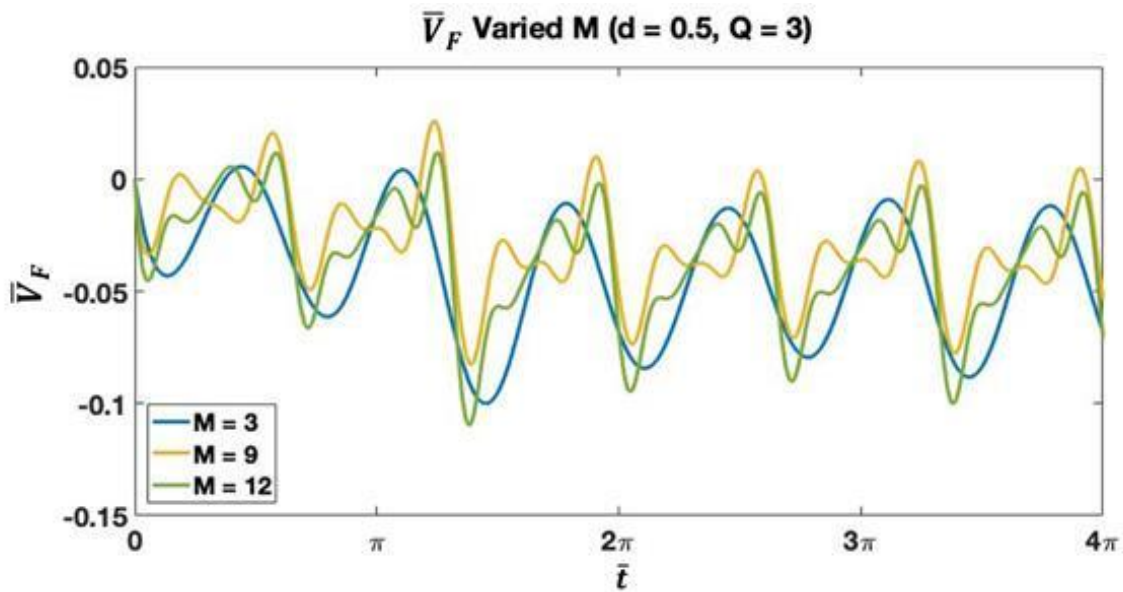
Figure 6-22: Velocity on front turbine rotor with 3 blades and $d = 0.5$ and varied harmonics
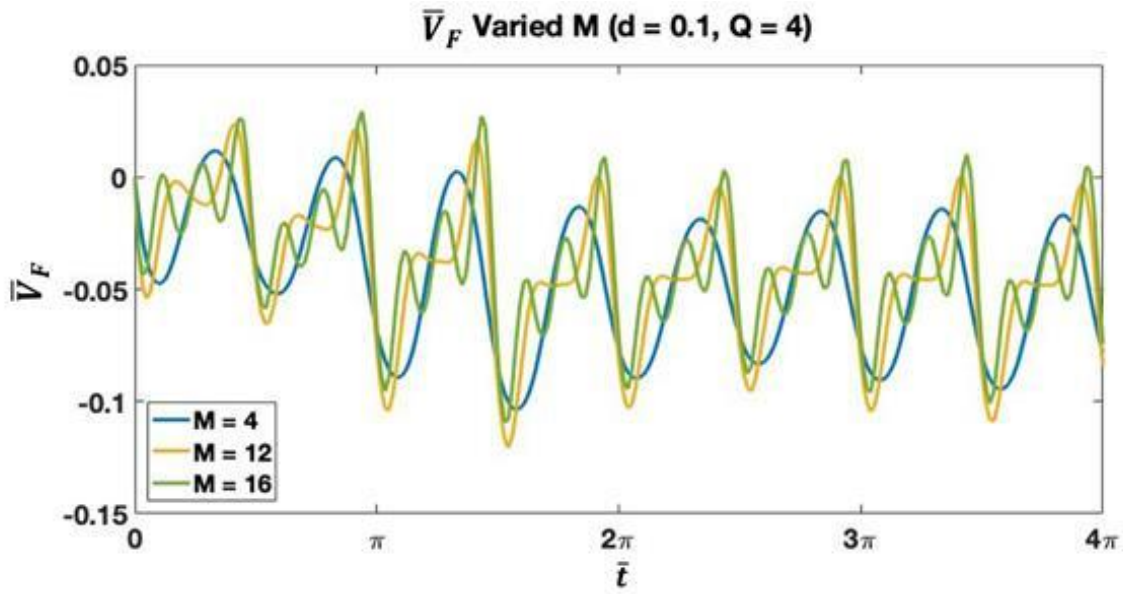
Figure 6-23: Velocity on front turbine rotor with 4 blades and $d = 0.1$ and varied harmonics
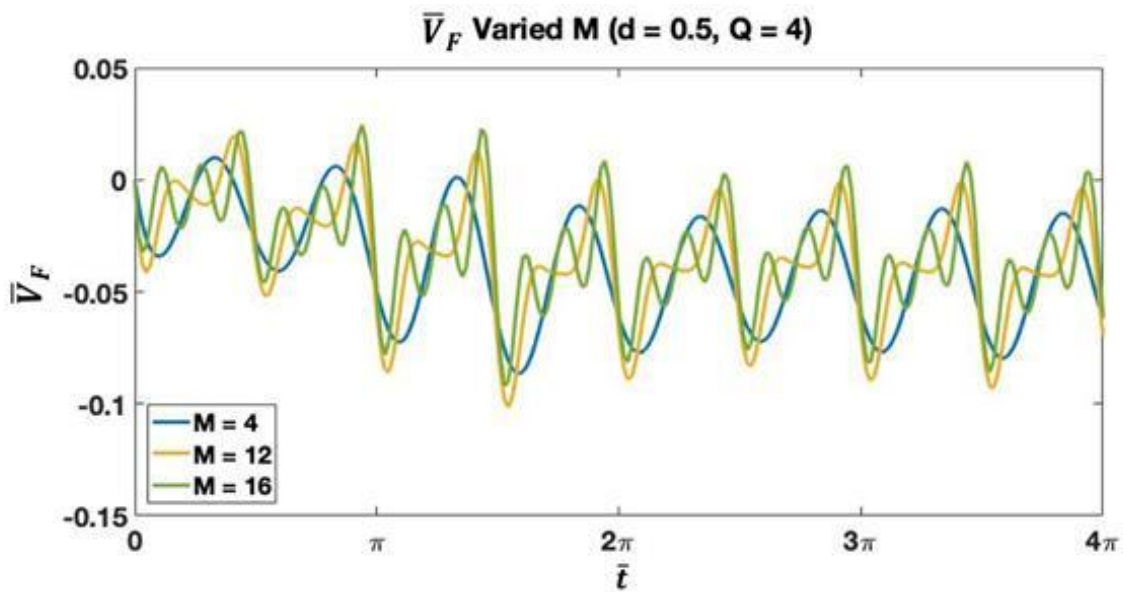
Figure 6-24: Velocity on front turbine rotor with 4 blades and $d = 0.5$ and varied harmonics
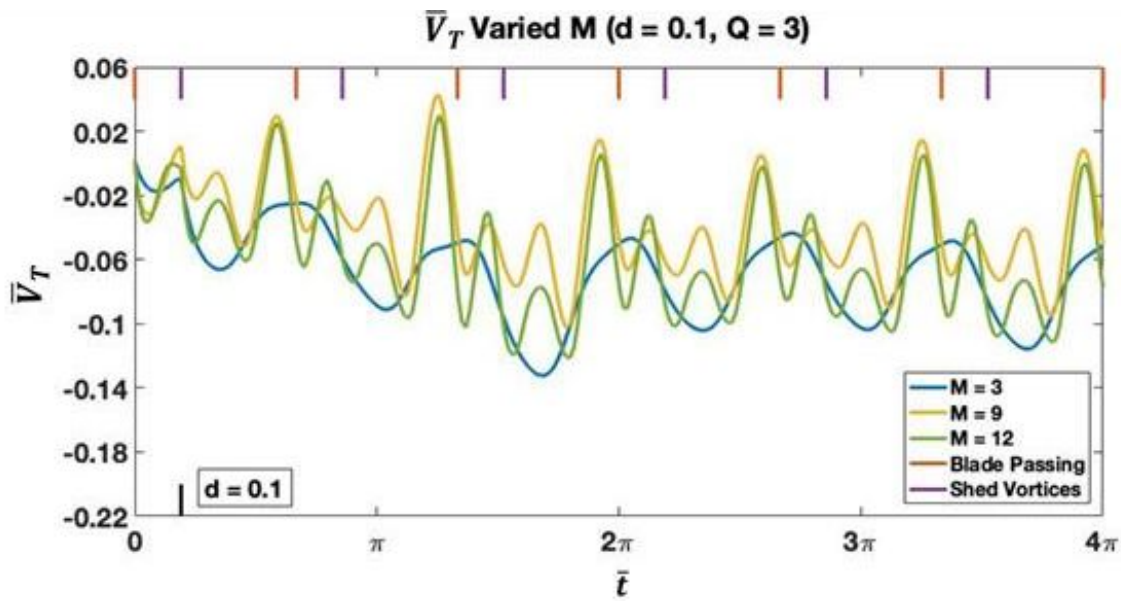
Figure 6-25: Velocity on trailing turbine rotor with 3 blades and $d = 0.1$ and varied harmonics
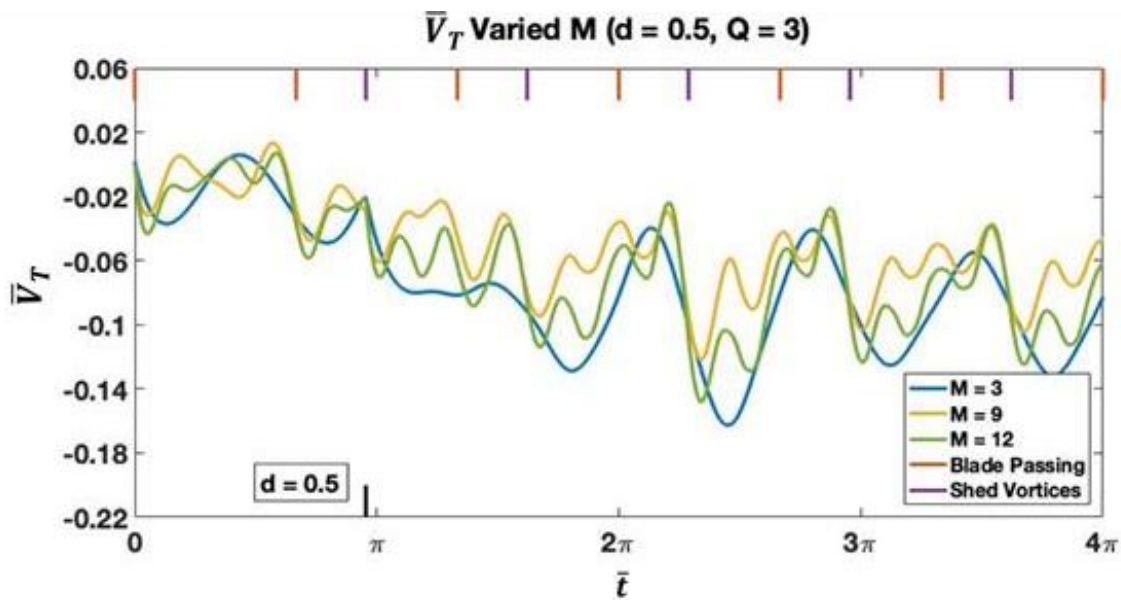
Figure 6-26: Velocity on trailing turbine rotor with 3 blades and $d = 0.5$ and varied harmonics
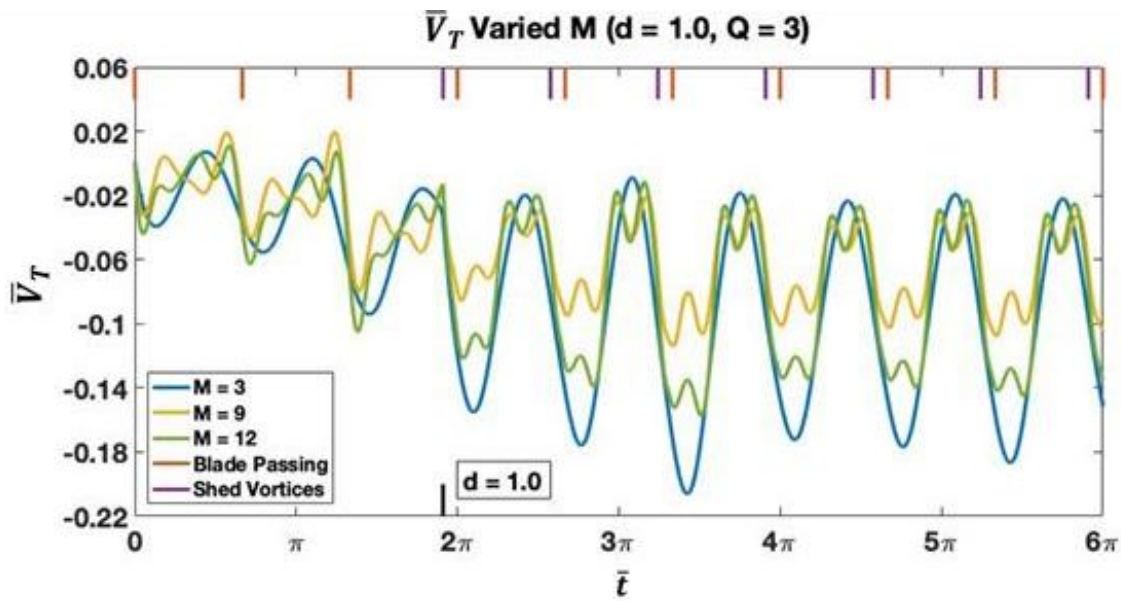
Figure 6-27: Velocity on trailing turbine rotor with 3 blades and $d = 1.0$ and varied harmonics
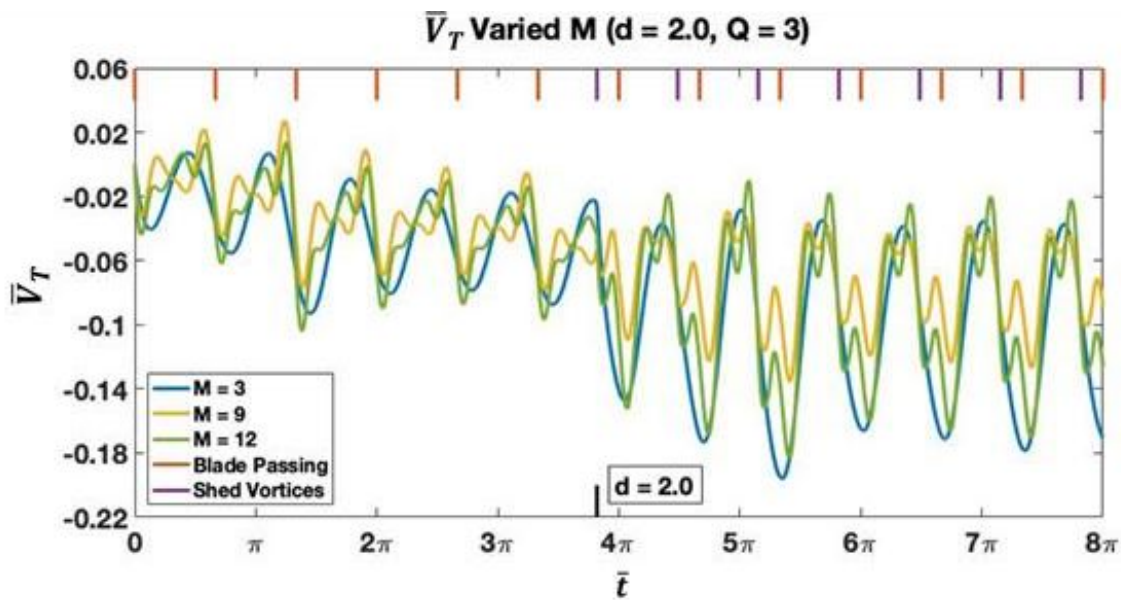
Figure 6-28: Velocity on trailing turbine rotor with 3 blades and $d = 2.0$ and varied harmonics
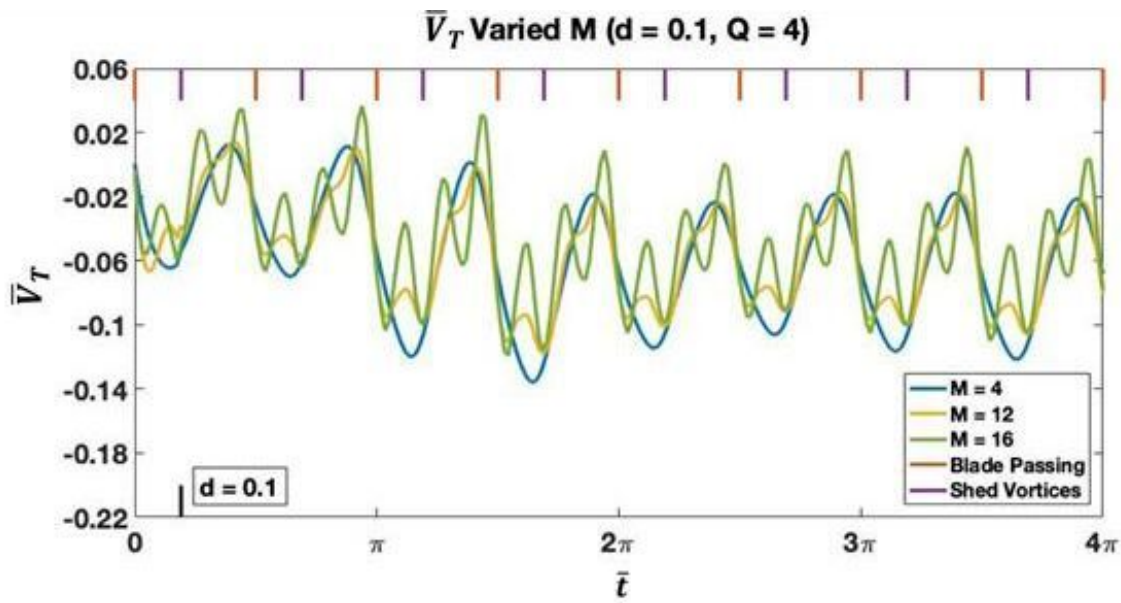
Figure 6-29: Velocity on trailing turbine rotor with 4 blades and $d = 0.1$ and varied harmonics
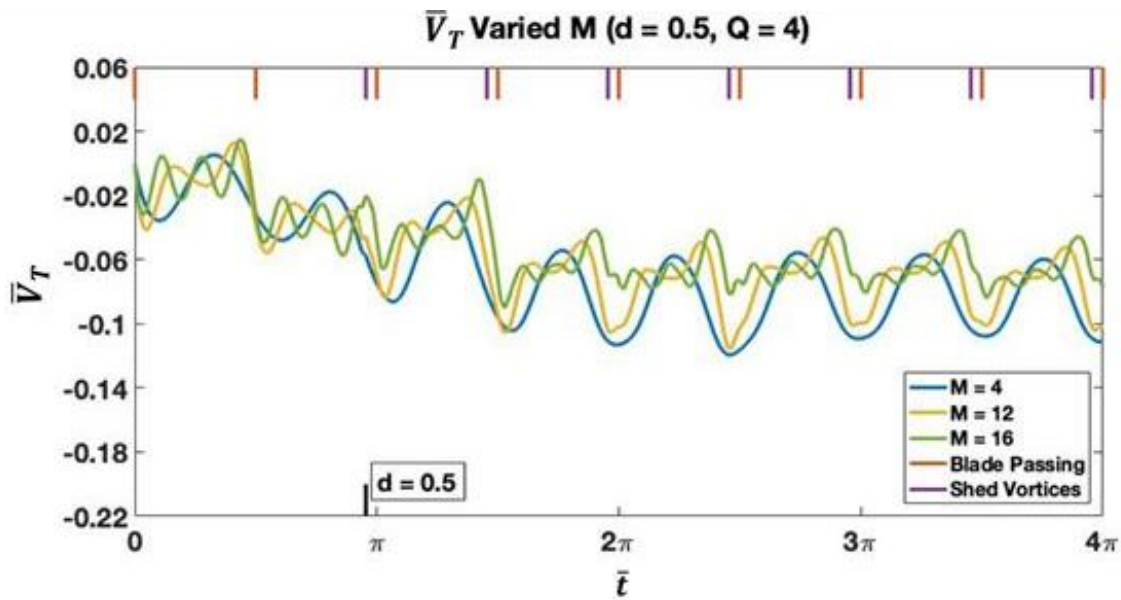
Figure 6-30: Velocity on trailing turbine rotor with 4 blades and $d = 0.5$ and varied harmonics
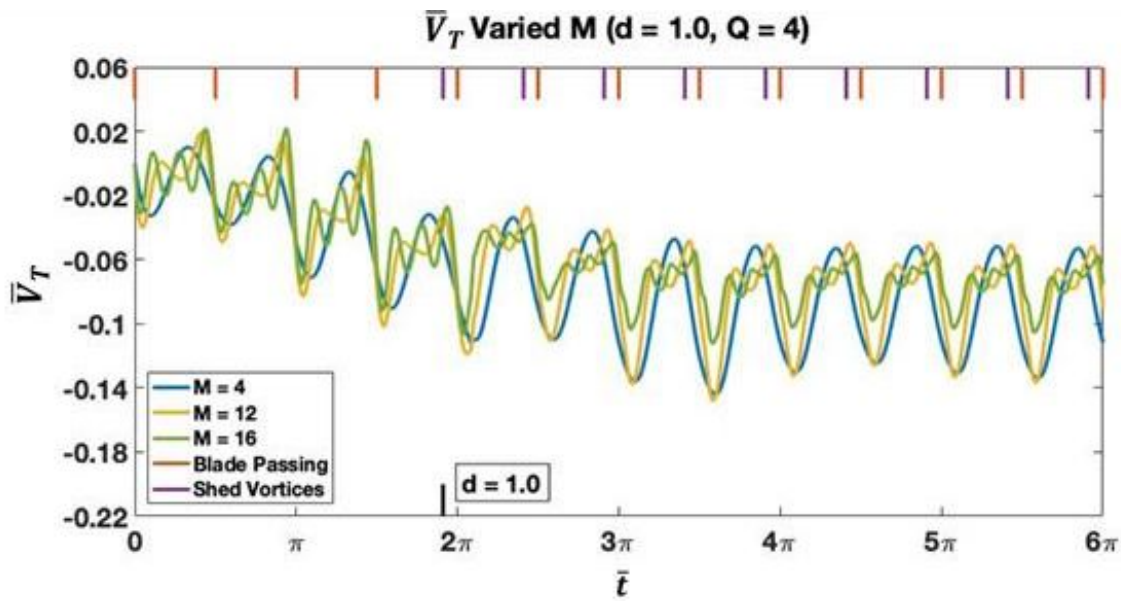
Figure 6-31: Velocity on trailing turbine rotor with 4 blades and $d = 1.0$ and varied harmonics
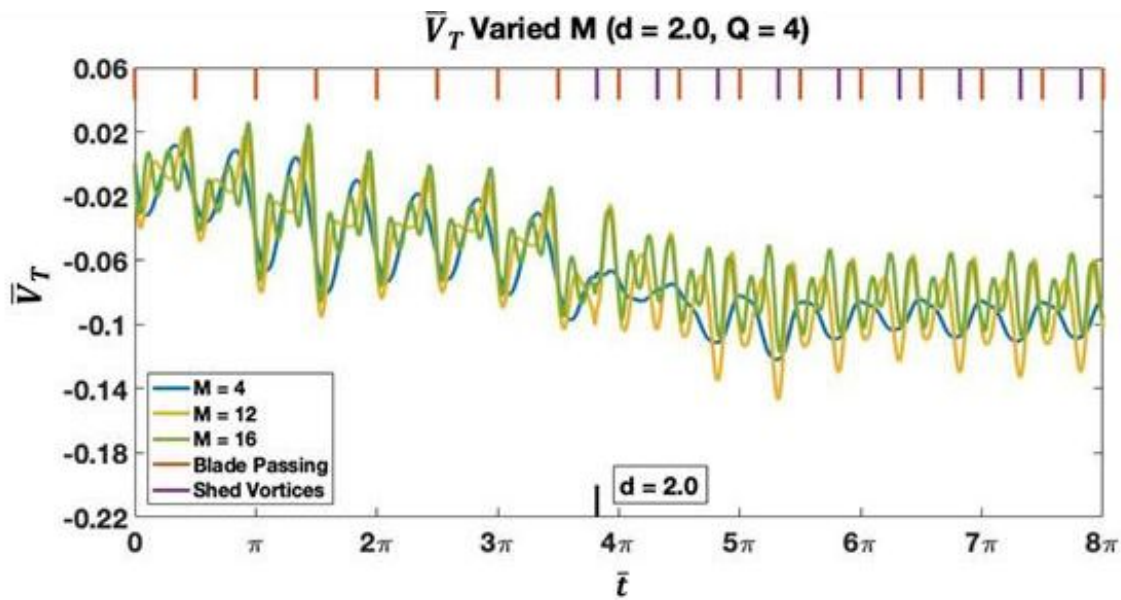
Figure 6-32: Velocity on trailing turbine rotor with 4 blades and $d = 2.0$ and varied harmonics
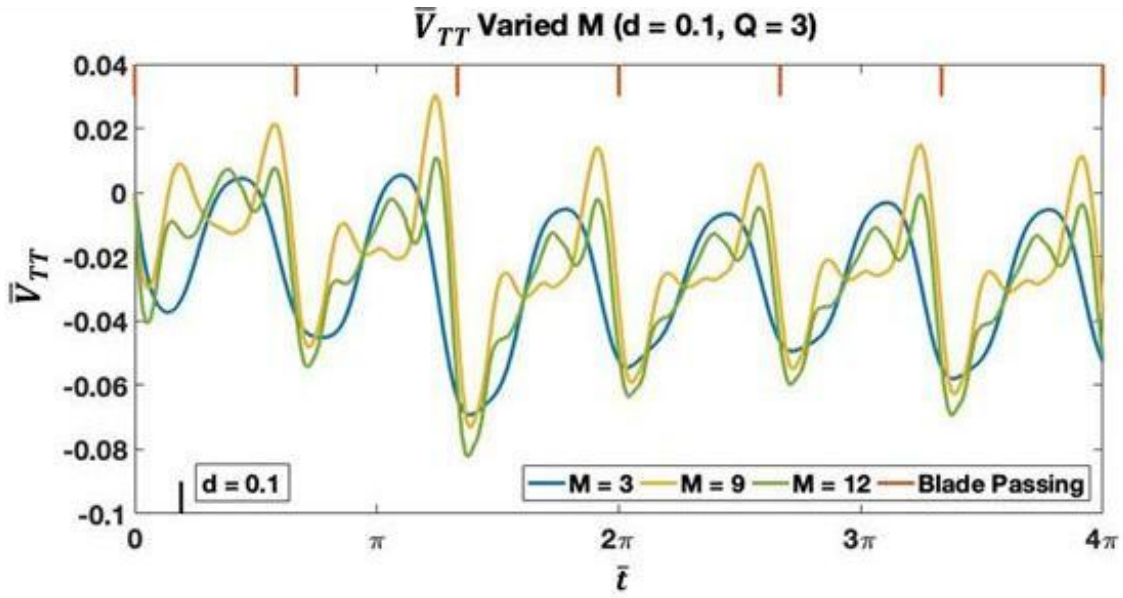
Figure 6-33: $\overline{V}_{TT}$ for system with 3 blades and $d = 0.1$ and varied harmonics
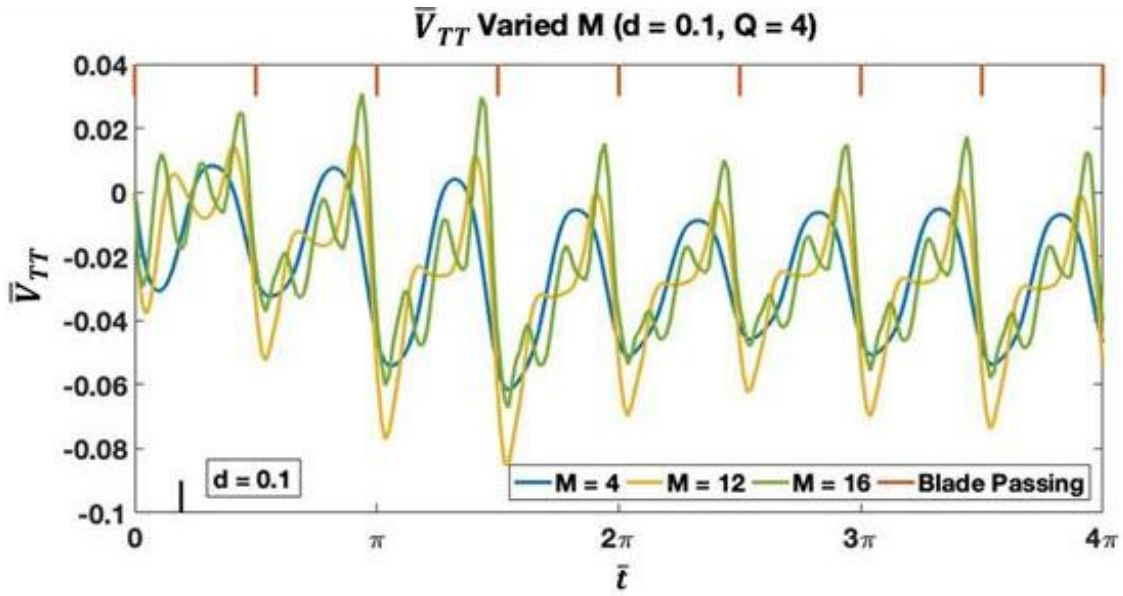
Figure 6-34: $\overline{V}_{TT}$ for system with 4 blades and $d = 0.1$ and varied harmonics .
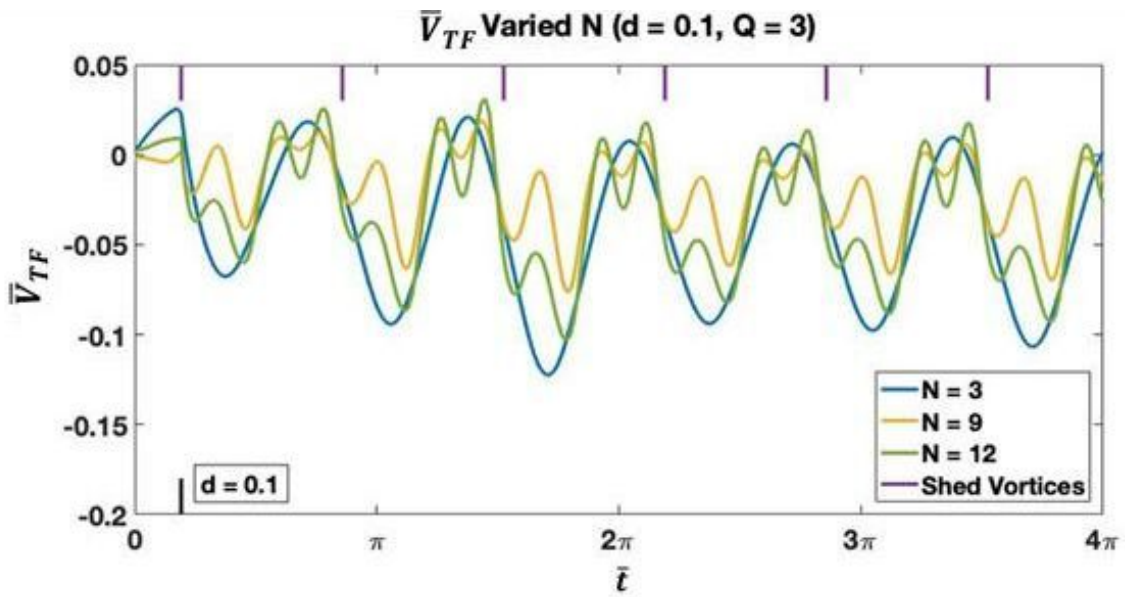
Figure 6-35: $\overline{V}_{TF}$ for system with 3 blades and $d = 0.1$ and varied harmonics
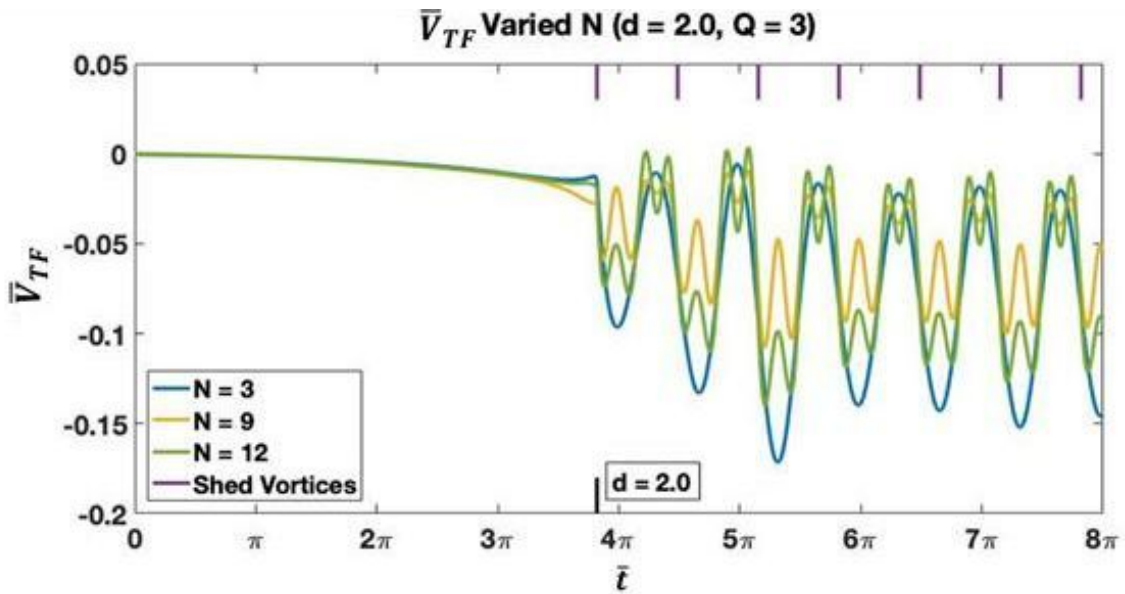
Figure 6-36: $\overline{V}_{TF}$ for system with 3 blades and $d = 2.0$ and varied harmonics
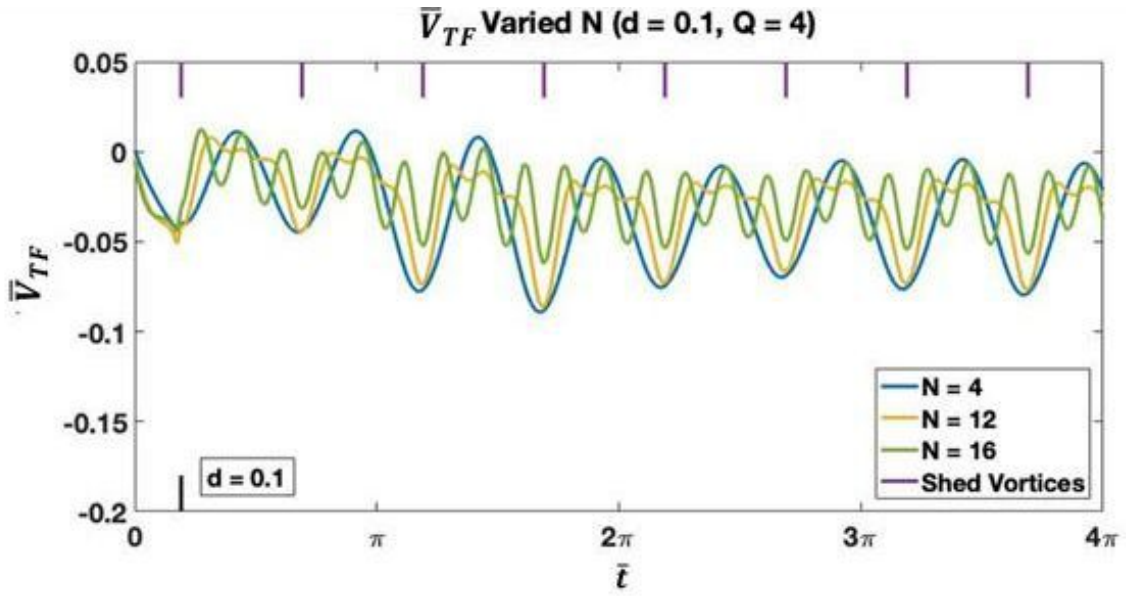
Figure 6-37: $\overline{V}_{TF}$ for system with 4 blades and $d = 0.1$ and varied harmonics
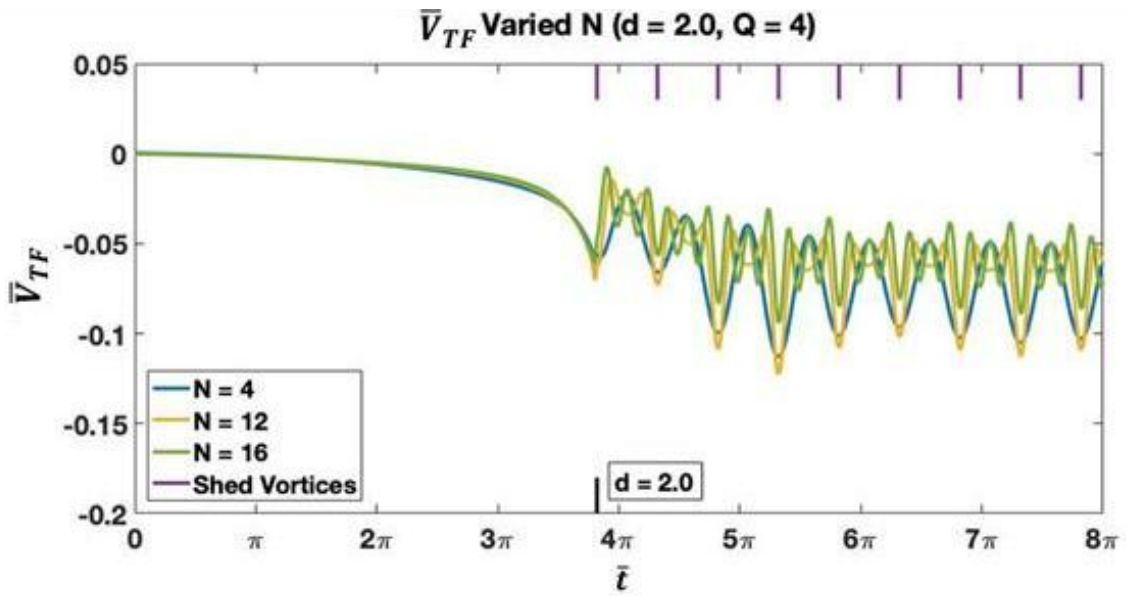
Figure 6-38: $\overline{V}_{TF}$ for system with 4 blades and $d = 2.0$ and varied harmonics

6.2.3   Wind Turbine Blade Flapping Dynamics

The final set of results in Figs. 6-39 through 6-48 illustrates the blade flapping dynamics and how rotor spacing and the number of harmonics impact the blade flapping profiles. Figures 6-39 and 6-40 show the impact of rotor spacing on b_F for for three-bladed and four-bladed rotors, respectively. Rotor spacing has a slight impact on the magnitudes of the oscillations and steady-state values, but no unique variations in dynamics near the time delay. The number of blades has only a slight impact on the magnitudes, and the only dynamic difference is with the 2Q per revolution oscillations. For the trailing rotor, the blade dynamics (b_T) in Figs. 6-41 and 6-42 illustrate the dependence on rotor spacing with unique dynamics occuring near the time delay. The steady-state portion of the profile is similar for larger rotor spacings ($d \geq 0.5$). Figures 6-43 and 6-44 demonstrate that the number of harmonics also has little impact on the b_F profiles. Similar to b_F, b_T does not show significant variations with the number of harmonics. This is illustrated in Figs. 6-45 to 6-48.
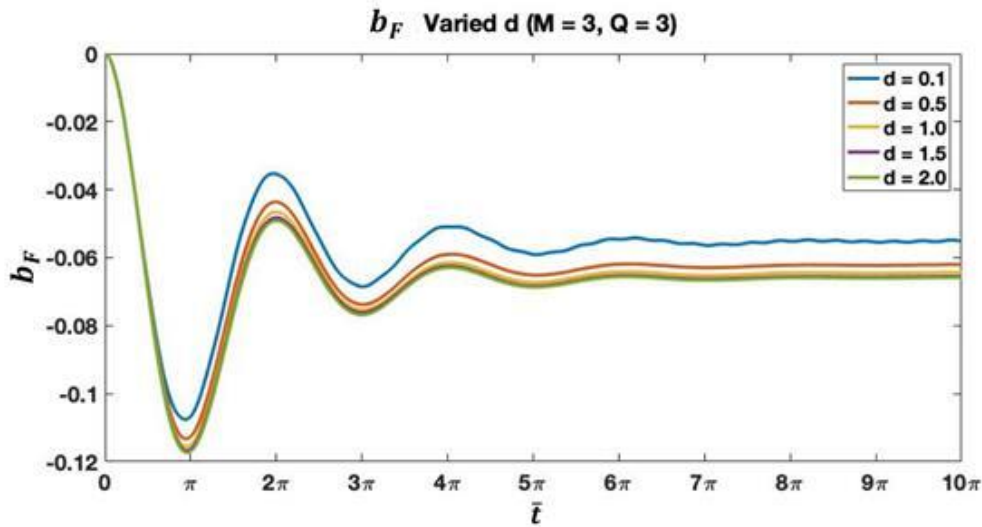
Figure 6-39: Front turbine rotor blade flapping for system with 3 blades and 3 harmonics and varied rotor spacings ($d = 0.1 - 2.0$).
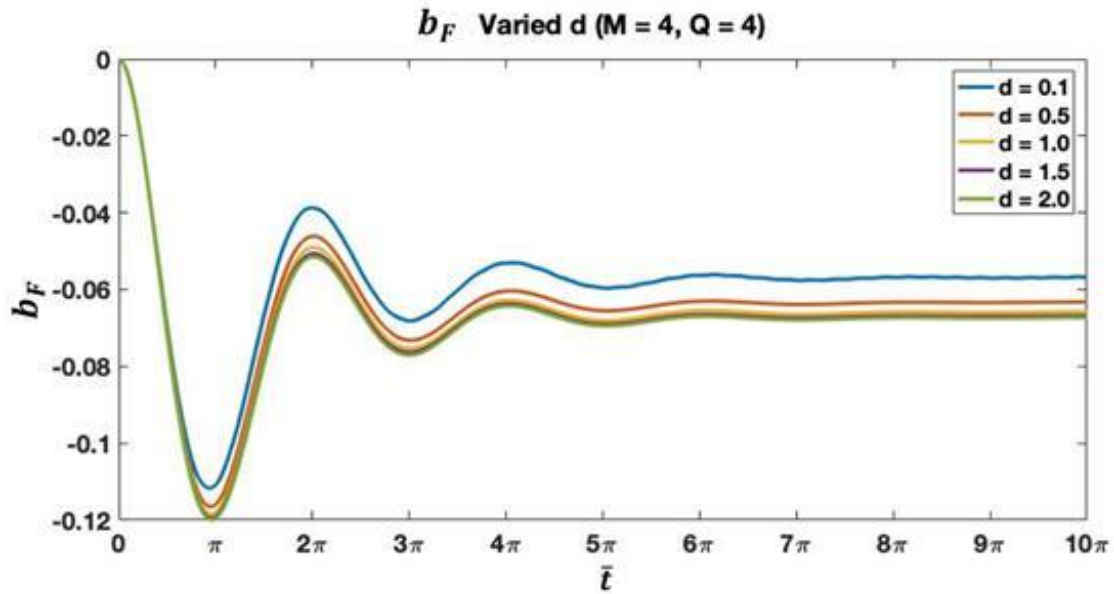
Figure 6-40: Front turbine rotor blade flapping for system with 4 blades and 4 harmonics and varied rotor spacings ($d = 0.1 - 2.0$)
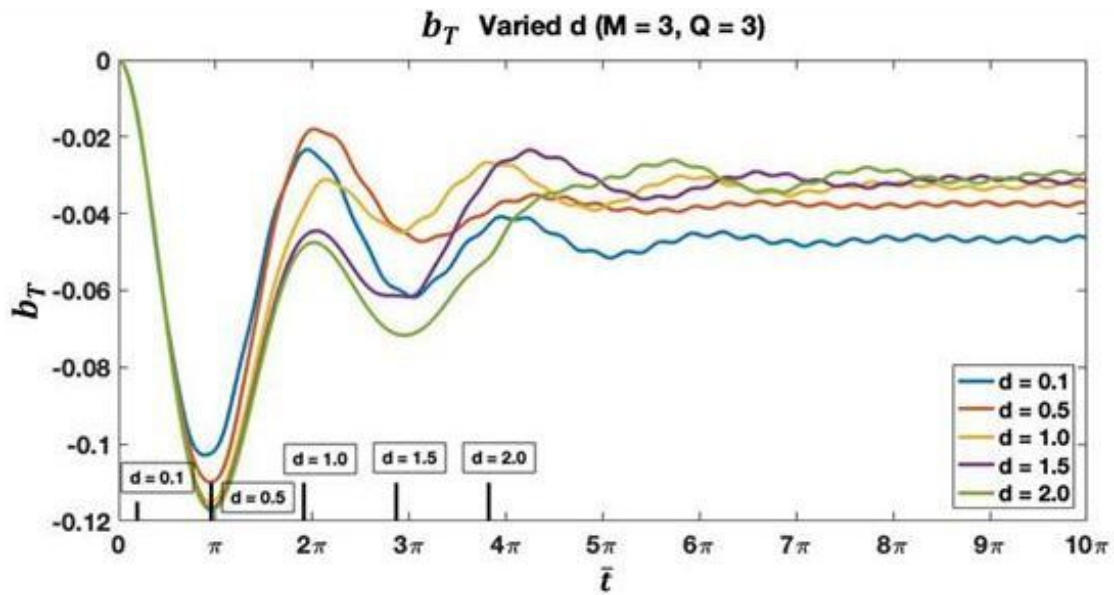
Figure 6-41: Trailing turbine rotor blade flapping for system with 3 blades and 3 harmonics and varied rotor spacings ($d = 0.1 - 2.0$).
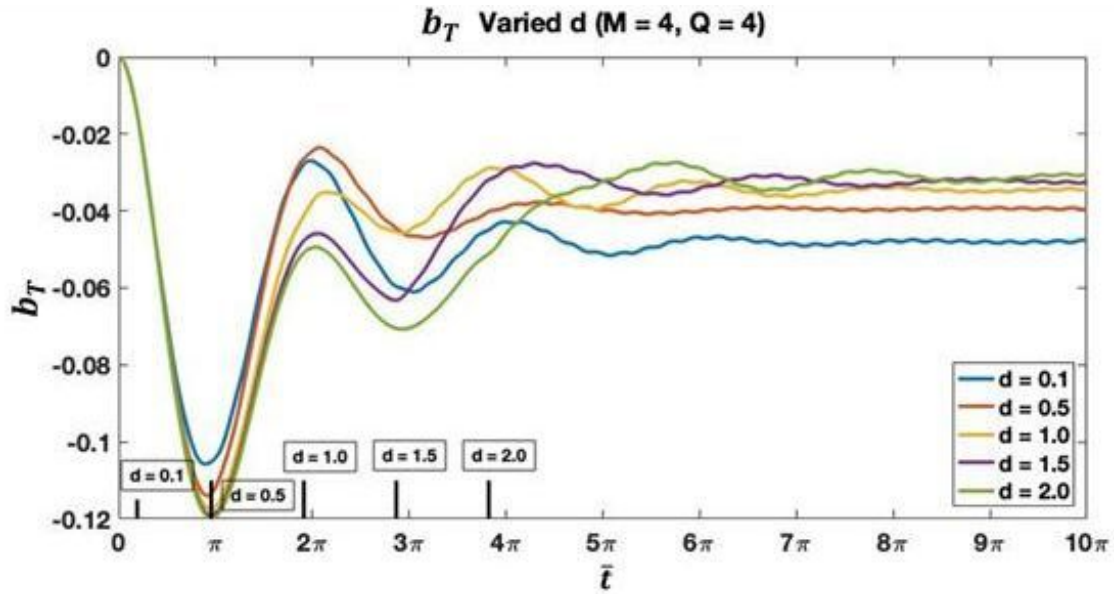
Figure 6-42: Trailing turbine rotor blade flapping for system with 4 blades and 4 harmonics and varied rotor spacings ($d = 0.1 - 2.0$).
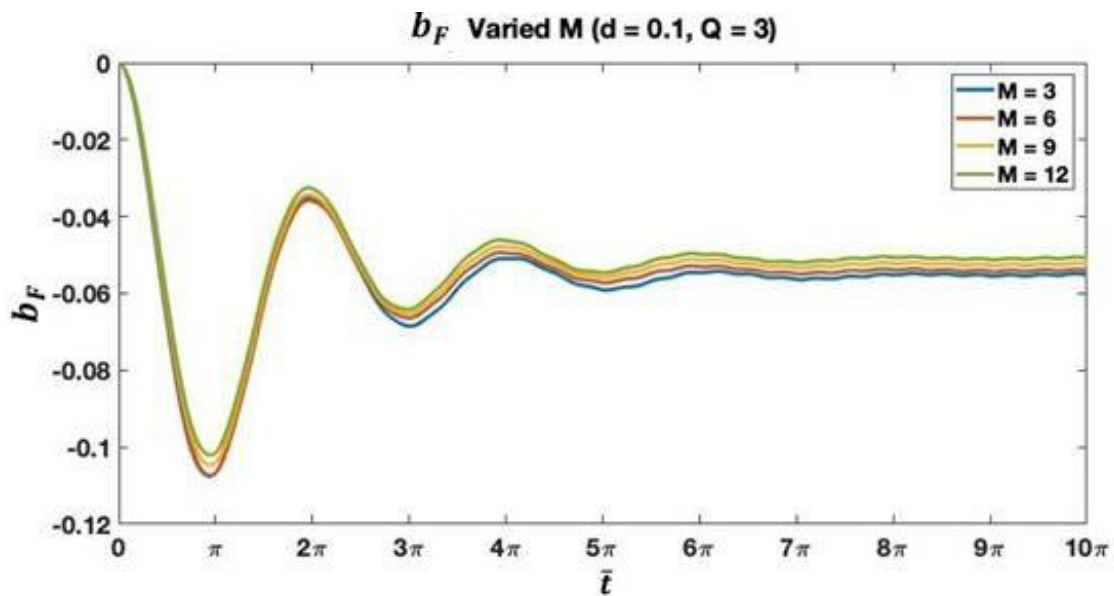
Figure 6-43: Front turbine rotor blade flapping for system with 3 blades at $d = 0.1$ and varied number of harmonics.
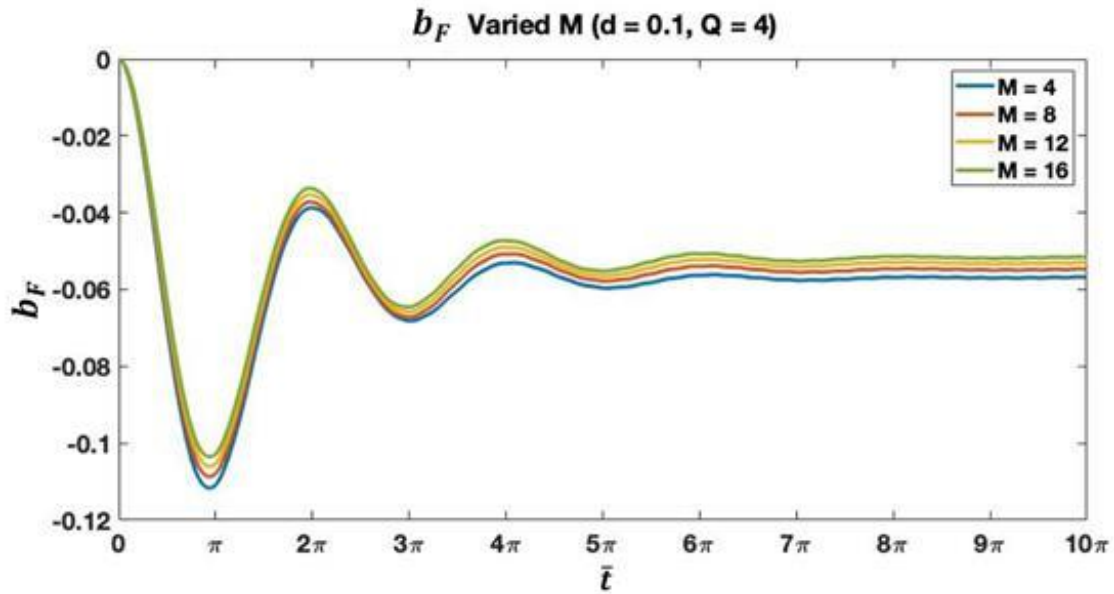
Figure 6-44: Front turbine rotor blade flapping for system with 4 blades at $d = 0.1$ and varied number of harmonics.
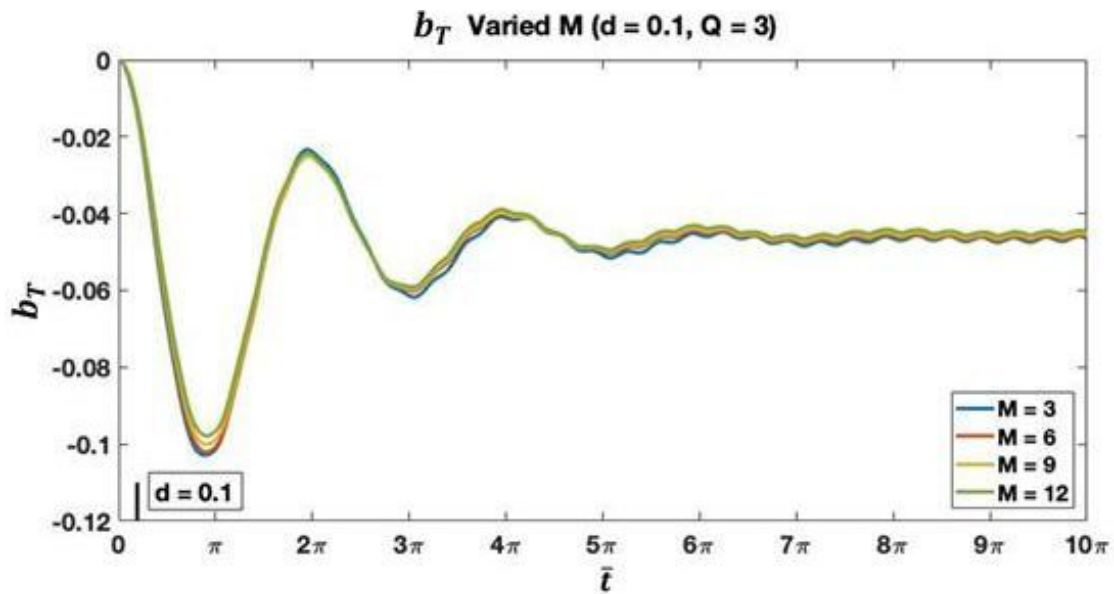
Figure 6-45: Trailing turbine rotor blade flapping for system with 3 blades at $d = 0.1$ and varied number of harmonics.

191
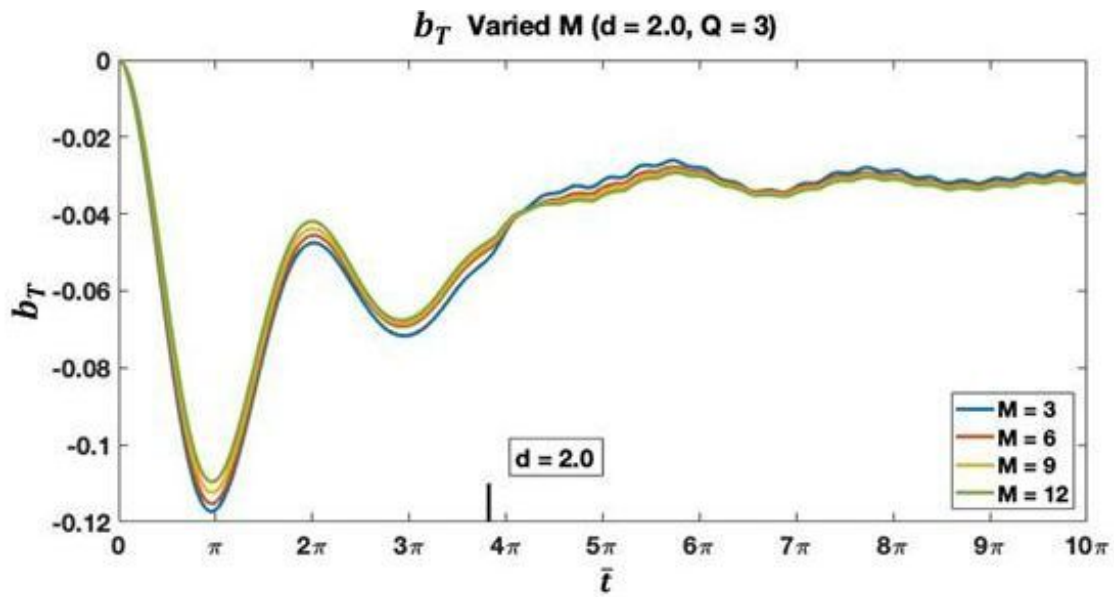
Figure 6-46: Front turbine rotor blade flapping for system with 3 blades at $d = 2.0$ and varied number of harmonics.
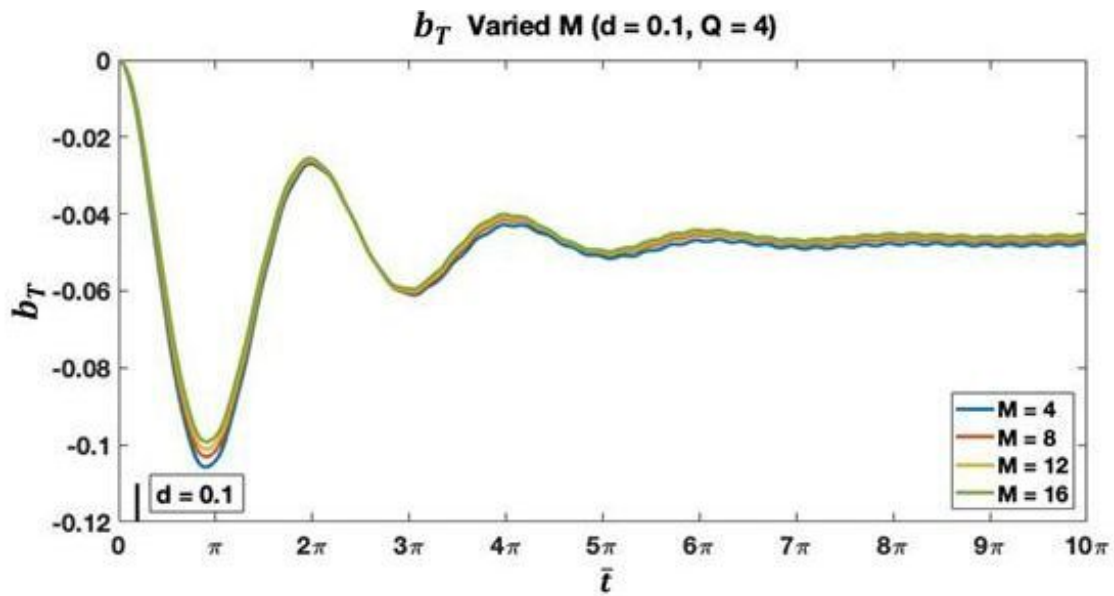
Figure 6-47: Front turbine rotor blade flapping for system with 4 blades at $d = 0.1$ and varied number of harmonics.
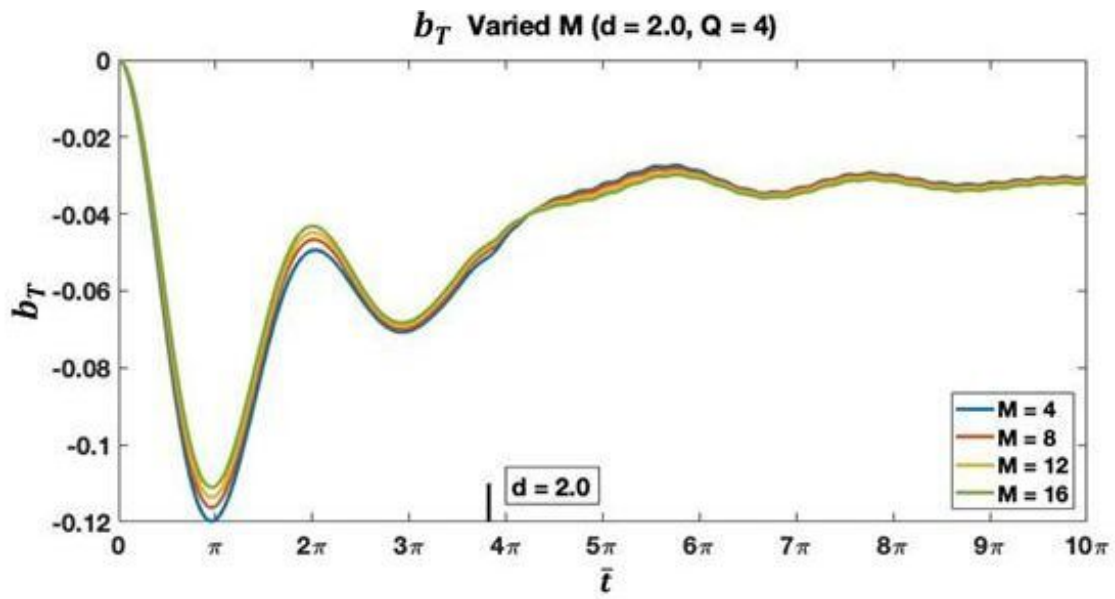
Figure 6-48: Front turbine rotor blade flapping for system with 4 blades at $d = 2.0$ and varied number of harmonics.

Chapter 7

Gradient Boosted Trees

In this chapter, the viability of using gradient boosted trees for estimation of the velocity values on rotor disks is investigated. The finite-state methods developed in previous work by He and Morillo are efficient for single-lifting rotors. In addition, the finite-state methods developed in the previous chapters of this dissertation can also be efficient for coaxial rotor systems with lower harmonic solutions ($M < 6$). However, in higher harmonic solutions, the simulation time for a coaxial rotor system increases significantly, in part due to the reverse time marching requirements of the adjoint variables. The application of gradient boosted trees with XGBoost$^{\text{TM}}$ allows for generation of more densely populated data sets and a greater number of systems by developing data for systems with new parameter combinations.

7.1 Background of Gradient Boosted Trees and XGBoost$^{\text{TM}}$

To better understand XGBoost$^{\text{TM}}$ and gradient boosted trees we will first explain what boosted trees are and then what gradient boosting is. In machine learning the word boosting refers to the process of converting weak learners into strong learners. The trees in boosting are built sequentially. The first tree is fit to the data set and evaluated to determine locations

where fitting is done accurately and areas of wrong predictions or high errors. The next tree is then built with adjustments to the weights with a higher weight on areas of wrong predictions and higher error and reduced weights on areas that fit well (correct predictions or lower error). The model is updated with each new tree developed in a format similar to:

$$N\left(1\right) = Tree\left(1\right)$$

$$N\left(2\right) = Tree(1) + Tree(2)$$

$$N\left(n\right) = Tree\left(1\right) + Tree\left(2\right) + \ldots + Tree\left(n-1\right) + Tree(n)$$

Gradients minimize the loss function by iteratively adjusting model hyperparameters based on the gradient of the loss function. In each iteration of the model when a new tree is added, the error rate of the model is determined by comparing the predicted values with the actual values. The gradient itself is the partial derivative, or the slope of the error function. The gradient finds the local minima in the loss function and influences the change in model hyperparameters for the next tree to further reduce the error. XGBoost$^{\text{TM}}$ utilizes second-order partial derivatives to reach the minimum of the loss function faster.

7.2 Coaxial Rotor Dataset

The dataset utilized in this work is that of a coaxial rotor system in axial flow (climb) and was generated using the model developed in chapter 5. The ultimate goal is the application of XGBoost$^{\text{TM}}$ models to a more sparsely populated data set with a higher number of harmonics M). The work presented here is a baseline investigation into the feasibility of XGBoost$^{\text{TM}}$ for predicting the velocity across the lower rotor disk. Therefore, only results from a three blade per rotor helicopter with three harmonics are analyzed. In this case we are looking

at variations in a limited number of parameters that include nondimensional radial location on the disk ($\bar{r}$) and the following system parameters: rotor spacing (d), rotor solidity (σ), and Lock Number (γ). The range of the parameters are as follows: $\bar{r} = 0 - 1$ (step size $\Delta \bar{r} = 0.01$), $d = 0.1 - 2$ (step size $\Delta d = 0.1$), $\sigma = 0.05 - 0.15$(step size $\Delta \sigma = 0.01$), and γ = 5-8 (step size $\Delta \gamma = 0.5$). Overall, the data set contained over 150,000 data points but was trimmed down with different train-test splits in order to illustrate performance of future sparsely populated data sets, and to illustrate how different parameters react to the size of the dataset. The different dataset parameters versus the velocity on the rotor are shown in Fig. 7-1. Despite the appearance of poor correlation between γ and the velocity on the lower rotor, early investigations illustrated improved model performance with the inclusion of γ. The primary focus here is to determine model accuracy for variations in $\bar{r}$ because it has one of the more unique variations across its range and can further be adapted for higher harmonic cases.
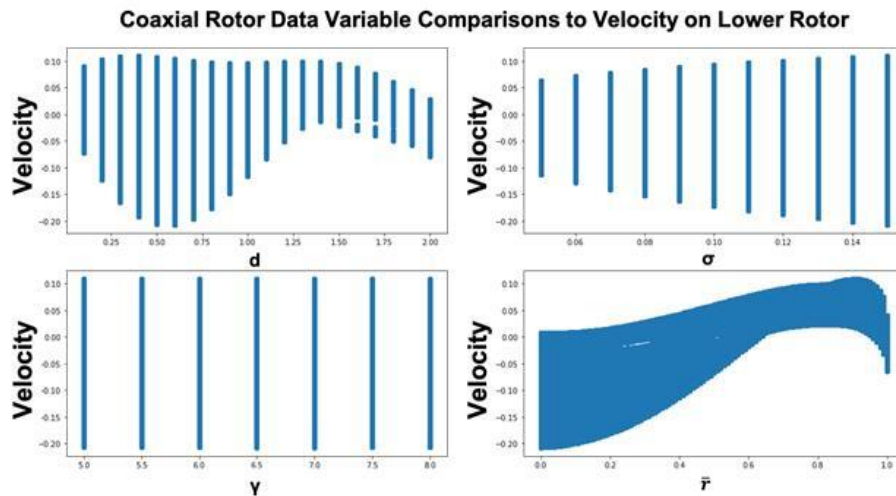
Figure 7-1: Comparison of coaxial rotor variables to velocity on lower rotor

7.3   XGBoost$^\text{TM}$ Parameters

Within XGBoost$^\text{TM}$, there are several hyperparameters that adjust how the trees are formed and perform. This work focuses on the hyperparameters that impact the number of trees (NT), depth of trees (MD), and how fast the model fits (LR). In addition, the size of data withheld for testing was varied. Several thousand combinations of these hyperparameters are tested to determine the best sets for fitting the data and make sure that the model is not overfit. It is necessary to initially utilize a wider range of hyperparameters in order to determine the best performing ranges for each within the dataset. A description of the function of the utilized hyperparameters is detailed in the following sections.

7.3.1   Number of Trees

The number of trees in a model denotes the number of weak learners the model contains and therefore the number of iterations of the model. In gradient boosted trees, each model iteration is inclusive of the previous model plus the newest tree from that iteration. By increasing the number of trees, a more detailed model can be developed.

The number of trees needed in a model is correlated to other XGBoost$^\text{TM}$ hyperparameters such as the maximum depth of each tree and the learning rate. A deeper tree would result in more terminal nodes and therefore more decision points, resulting in a need for less trees. In addition, a higher learning rate would mean the model learns faster and therefore it would take a lesser number of trees for the model to reach its best performance. A deeper tree or higher learning rate does not necessarily lead to a faster and more accurate solution.

7.3.2 Maximum Tree Depth

The maximum tree depth is how many decision layers a tree has and therefore how many terminal nodes exist in a tree. A tree of depth 1 has two terminal nodes and is often referred to as a stump. A system of stumps can be effective in that it is a slower learning model with each tree having a smaller impact on the overall system. Stumps require more trees to reach a satisfactory fit. Models with deeper trees require a lesser number of trees, and generally fit faster, but are often prone to over-fitting (a model that fits too well to the training data and has significantly lower performance on testing data). The size of the dataset and the number of variables to fit to can also dictate the tree depth. A smaller data set would likely benefit more from smaller trees.

7.3.3 Learning Rate

In simple terms, learning rate is how fast the model fits to the data. Learning rate is the step size taken between each model iteration towards finding the loss function local minima. For a higher learning rate, the model will likely fit in a smaller number of trees, generally resulting in a less accurate model because it will miss the local minima. A lower learning rate increases the probability that the model will reach the local minima, but it generally requires more model iterations to do so. Utilizing a learning rate that is too small will take the model an excessive amount of time to reach the optimal fit and does not guarantee the best fit will be reached.

7.3.4 Regularization Terms

Regularization is important in machine learning to help reduce error while avoiding overfitting the model to the training data. To accomplish this, regularization terms are added to

the loss function. XGBoost$^{\text{TM}}$ contains terms for L1 regularization and L2 regularization. L1 regularization is not impacted as significantly by outliers in the data and is able to adjust the model more appropriately when outliers exist. L2 regularization is highly influenced by outliers and performs poorly if there are many outliers.

The dataset in this work does not contain outliers, which result in testing L2 regularization adjustments with XGBoost$^{\text{TM}}$. After several hundred iterations of testing different L2 regularization values, it was determined that there was little to no effect on varying sets of model hyperparameters. It is believed that this is the case because the data was generated using finite-state inflow models and therefore any minor variations that may exist will have little influence. In this work, we used L2 norm as our error metric to further illustrate how close the models fit to the data.

7.3.5 Overfitting, Underfitting, and the Art of Hyperparameter Tuning

One of the biggest concerns with hyperparameter tuning is overfitting the model to the training data and reducing the performance on the testing data. Overfitting occurs when a model learns and fits to the noise in its training data; this subsequently has a negative impact on the performance of the model on new data. If the model learns the noise in the training data, it is unable to generalize the with new data. Overfitting is more likely to occur in nonlinear and nonparametric models because they are more flexible and likely incorporate outliers. Increasing the complexity of a model through hyperparameter tuning, such as the addition of more trees or deeper trees, are common causes of overfitting. Figure 7-2 shows an example of overfitting where the model hyperparameters have fit to the outlier points.

On the other end of the spectrum, an underfit model is one that does not model the training or testing data well. Underfitting is generally easier to detect and can be mitigated through fine tuning of the hyperparameters outlined above. Figure 7-3 provides an example of underfitting where the model does not fit the data well in several regions. This model is splitting at the wrong point in the $r = 0 - 0.15$ region and later in the $r = 0.7 - 0.9$ region. In addition, there are not enough split points in the middle of the profile, leading to a small region of under predicted values. This model can be improved by adjusting the regularization terms and tuning the learning rate, depth, and number of trees.
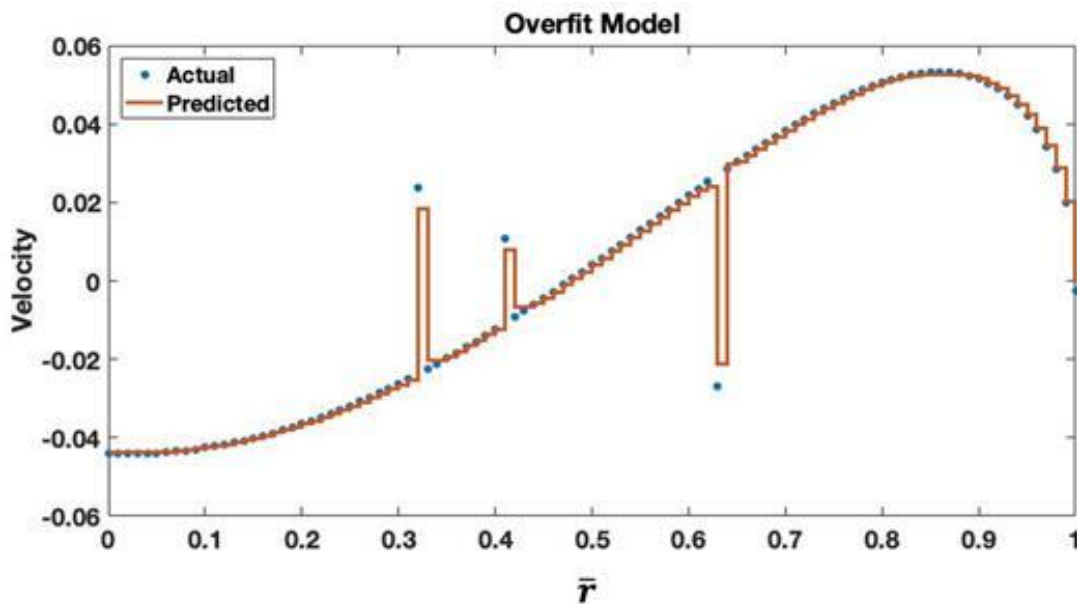
Figure 7-2: Example of an overfit model that fits to outliers in the data
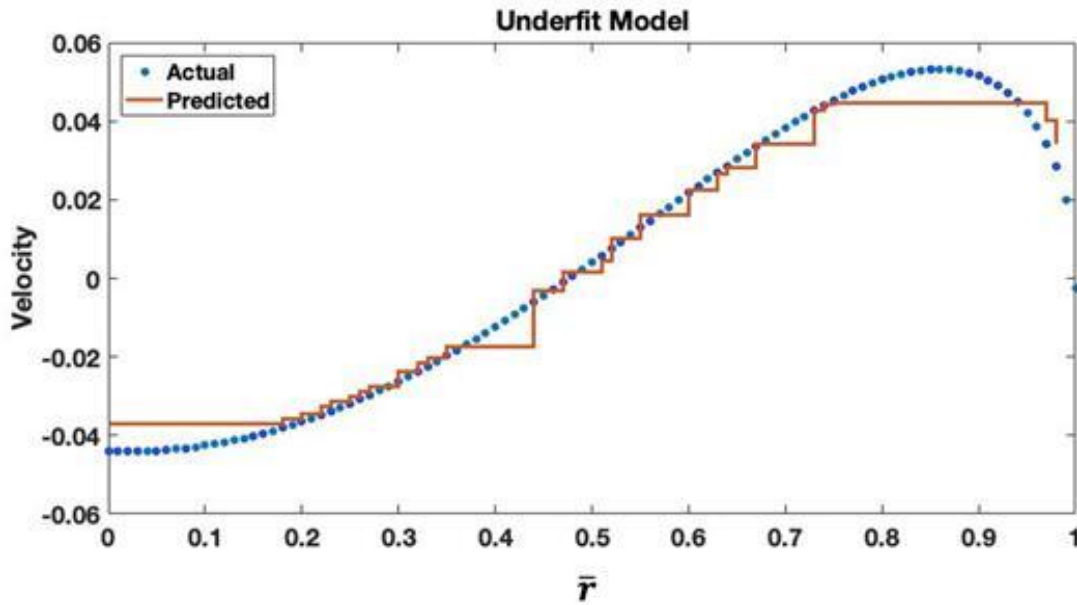
Figure 7-3: Example of an underfit model that needs more break points

Given that our dataset was developed through finite-state inflow models, there is no noise or scatter in the data like what would be found in experimental work. For this reason, it is difficult to overfit a model in the traditional sense, especially because this is a densely populated dataset. However, the model could overfit in the sense that an excess number of trees can be fit to the model and the overall error remains the same (or display exceptionally small change). Underfitting is more prevalent because it simply takes a bad set of hyperparameters to underfit a model. A broad evaluation of overfitting and underfitting for this work is shown in Fig. 7-4. Figure 7-4a shows that for a test size of 20% of the data, the baseline range of L2 norm error is 0.3-667. In this plot any set of hyperparameters that is not represented with a dark blue dot would be a severely poor fit. This is the case all models with a learning rate of 0.001 and shows somewhat uniform performance across the varied max depths. If these models were able to further improve, more trees would be needed, and potential tuning of regularization terms.

201

Figures 7-4b-d illustrate a trimmed L2 norm error scale range to 0.3-1 for the same set of hyperparameters with test sizes of 20%, 50%, and 80% to help identify the best fit models. The non-blue data points seen do not necessarily indicate an underfit model, but the error is larger than the better performing hyperparameter combinations. Rows or columns of data points that change from yellow to blue demonstrate model improvement with the respective hyperparameter. However, a row of data that illustrates successive data points of dark blue, such as the row with a learning rate of 0.05 and max depth of 10 in Fig. 7-4c, are indicative of a model that is being given too many trees and fit with a few trees. Further investigations indicated that the best fit in the row of data was for 200 trees with more trees providing the same or slightly worse performance. Comparing performance for between the different test sizes, it should be noted that many of the best performing sets of hyperparameters are the same for all the 20%, 50%, and 80% groupings. This is attributed to size of the data set and the lack of outliers within it. The relationship of performance with test size is addressed in the results section. From these plots the best performing hyperparameter combinations were determined to be *MD = 10, LR = 0.05, NT = 200* for the 20% test size and *MD = 10, LR = 0.05, NT = 1000* for the 50% and 80% test sizes. These two combinations along with two others shown in Table 7-1 are further investigated throughout this work. Hyperparameter set 1 was utilized to show what fits looked like for a poorer performing model. Hyperparameter set 2 was selected because it had relatively good performance and utilized shallower trees.
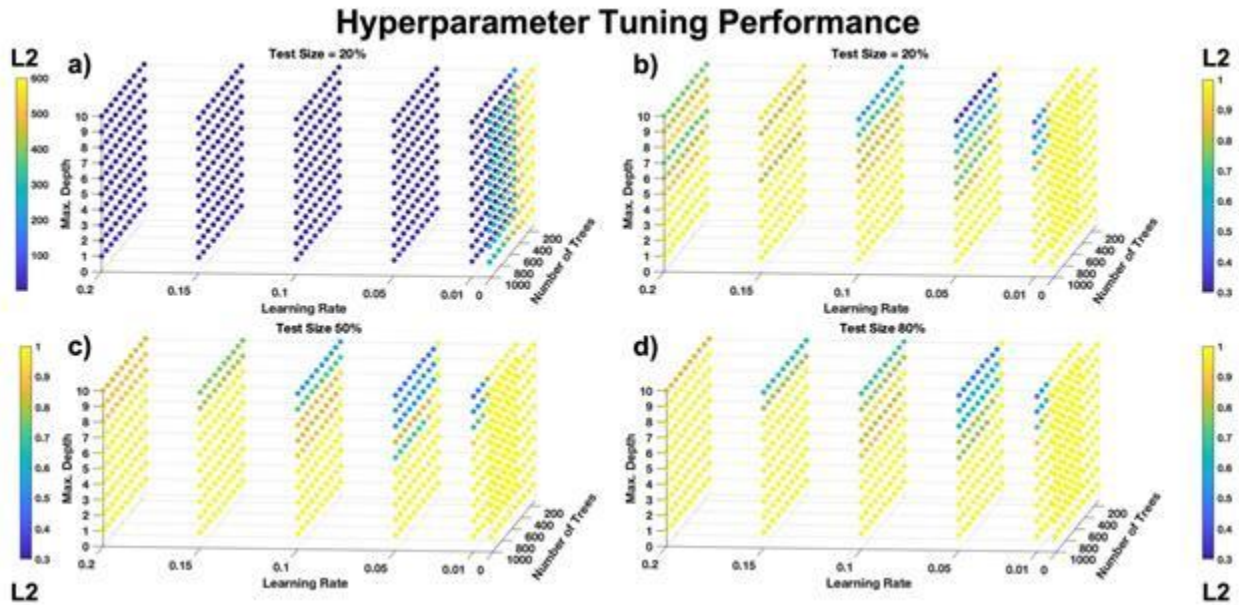
Figure 7-4: Performance of XGBoost$^{\text{TM}}$ regression models over different sets of parameters

Table 7-1: Hyperparameter sets used in analysis and associated L2 norm error.

Hyperparameter Set No.	MD	LR	NT	L2 Norm (20, 50, 80)
1	2	0.15	1000	8.28, 8.04, 8.95
2	5	0.05	1000	0.86, 1.27, 1.05
3	10	0.01	1000	0.45, 0.44, 0.48
4	10	0.05	200	0.33, 0.46, 0.49

7.4   Results

Two separate approaches to studying the feasibility of XGBoost$^{\text{TM}}$ are implemented in this work. The first approach is to evaluate different train-test split ratios to dictate the amount of data being withheld for testing. This illustrates the amount of data needed to accurately develop a model for fitting within the bounds of the helicopter properties. In order to further understand the capabilities of XGBoost$^{\text{TM}}$ to determine values within the domain, the

second approach only trains on limited data for every $\Delta \bar{r}$ in the range of 0-1. For example, if $\Delta \bar{r} = 0.02$ the training data would contain all data points with $\bar{r} = 0,\ 0.02,\ 0.04, \ldots,\ 0.98,\ 1$. The remaining data is referred to as the intermediate values. Splitting the data this way forces the model to correlate values based on neighboring values with similar σ, γ, and d, rather than correlating the values with the neighboring values and data points of equivalent $\bar{r}$ and different σ, γ, and d.

7.4.1   Train-Test Split Variation

Performance of XGBoost™ Hyperparameters

The results for this work focus on the performance of the XGBoost™ hyperparameter combinations and visualization of how the models fit to the training data. The four different sets of hyperparameters in Table 7-1 are analyzed with respect to test size comparisons before focusing on how performance develops with variations in *MD* and *LR*. In Fig. 7-5 the *MD* and *LR* in the four sets of hyperparameters were tested across test sizes of 10-90% of the full data for varying *NT* values. For the four sets of hyperparameters the 10% test size tends to perform better than the other test sizes, but not significantly better in some cases. In addition, the models tend to perform well for 40% test size, but again not significantly better. The models all consistently have their worst performance with a test size of 70%. However, the overall performance of the models is relatively similar across the 20-90% test sizes, especially for the cases with larger *NT*, which are generally the better performing models. The exceptions to this trend are sets 2 and 4 in Figs. 7-5b and 7-5d, respectively. In Fig. 7-5b, the profiles for *NT = 500* and *NT = 700* are buried beneath the *NT = 1000* profile, which is technically the best performing set of hyperparameters, however, the improvement is small when considered relatively. Though it is important to note that a small change in L2 can be significant irrespective of the relative numerical improvement when compared to other

hyperparameter sets. In Fig. 7-5d, the $NT = 300, 500$, and 700 profiles are all beneath the $NT = 1000$ profile. For set 4, the best performing number of trees is for $NT = 200$. In Fig. 7-5c, the profile for $NT = 100$ is not shown because it performed so poorly that it contained L2 norm errors in the 200-250 range and skewed the plot significantly. The $NT = 700$ and 1000 profiles in set 3 performed significantly better than the others and are better illustrated in Fig. 7-6, which shrinks the scale of Figs. 7-5c and 7-5d to show the better performing models. The results of this rescaling serve to echo the results of other hyperparameter sets in terms of the general trends described above on a much smaller scale, particularly in Figure 7-6a. Figure 7-6b reinforces this idea, noting that the greater variation in the curve is due to the more extreme rescaling which led to a higher distortion of relative L2 norm values.

In Fig. 7-7, the performance of the hyperparameter sets in Table 7-1 are illustrated for test sizes of 20%, 50%, and 80%. All of these plots reiterate how close the performance is between different test sizes with the model. The first set of hyperparameters in Fig. 7-7a are poorly fit and bottom out at L2 norm error near 8. The other three sets reach much better fits near or below L2 norm error of 1. Figure 7-7c does not show values below 700 trees because the error in earlier profiles exceeded 200. The high rate of development is common with a low learning rate and deep trees. For set 4 in Fig. 7-7d, the model quickly reaches peak performance at 200 trees which is due to the combination of deep trees and a higher learning rate. Ultimately variation between different test sizes is small, though hyperparameter development and convergence are impacted by more than just test size.

To better illustrate why the performance of the models appears to be independent of the train-test split (i.e. the relative percent of the data withheld for testing) Fig. 7-8 shows the spread of the training data when only 2% of the entire data set is used for training. The spread and amount of data points available within 2% is significant and provides confidence

in the model performance when a majority of the data is withheld for testing. In other words, there is still a significant amount of data to train on despite the small train split. This allows the model to have considerably deep trees using a comparatively sparse data set. This provides confidence in further expansion to higher harmonic cases that are less densely populated

To better visualize how the XGBoost$^{\text{TM}}$ model performance develops with variations in hyperparameters, *MD* is held constant in Fig. 7-9 and *LR* and *NT* are varied. Figure 7-9a shows a model with *MD = 5* and demonstrates how the learning rate impacts how quickly the model reaches is peak performance. In addition, the selection of *LR* is important for reaching peak performance. The smallest learning rate takes longer to reach its lowest L2 norm error, but also does not come close to the performance of other learning rates. In Fig. 7-9b for models with *MD = 10*, higher learning rate models reached their lowest L2 norm values with the initial simulation of *NT=100*. However, the performance of these models is also worse than the cases with *LR = 0.01* and *LR = 0.05*. For this dataset, the *MD = 10* models fit better than the *MD = 5* models.

Next *LR* is held constant and MD is varied along with *NT* in Fig. 7-10. Figure 7-10a shows models with *LR = 0.05* and it is easy to conclude that for this dataset a $MD \geq 5$ provides a significantly better performance. This trend is also true for models with *LR = 0.1* in Fig. 7-10b. Together, Figs. 7-9 and 7-10 demonstrate the importance of testing a range of hyperparameters for a new dataset to determine how the model fits the data and then further tune the model to reach peak performance.
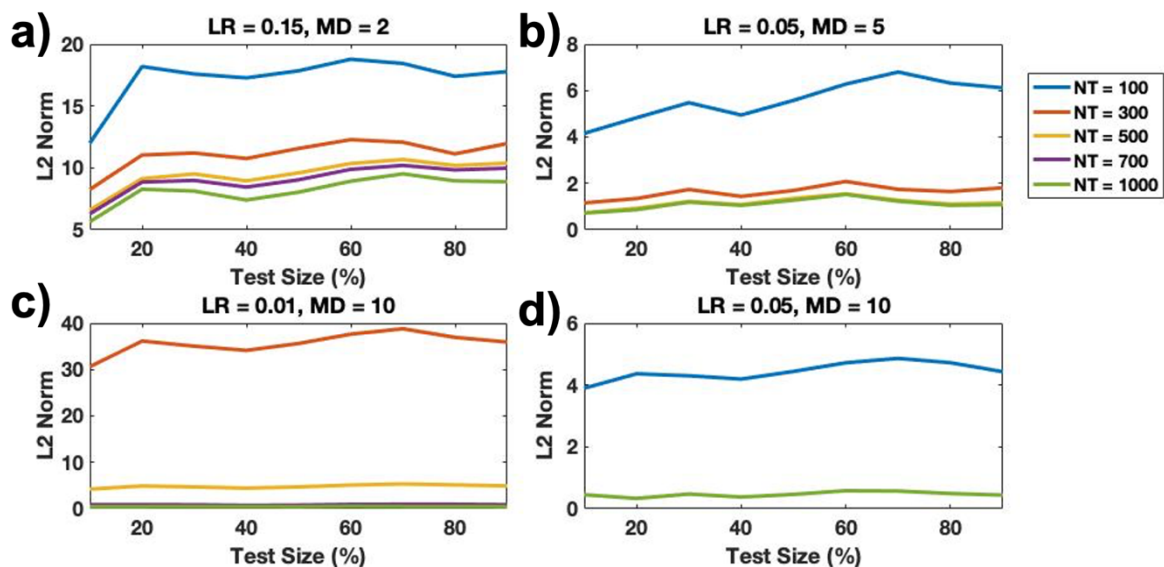
Figure 7-5: Comparison of hyperparameter performance over varying train-test split sizes
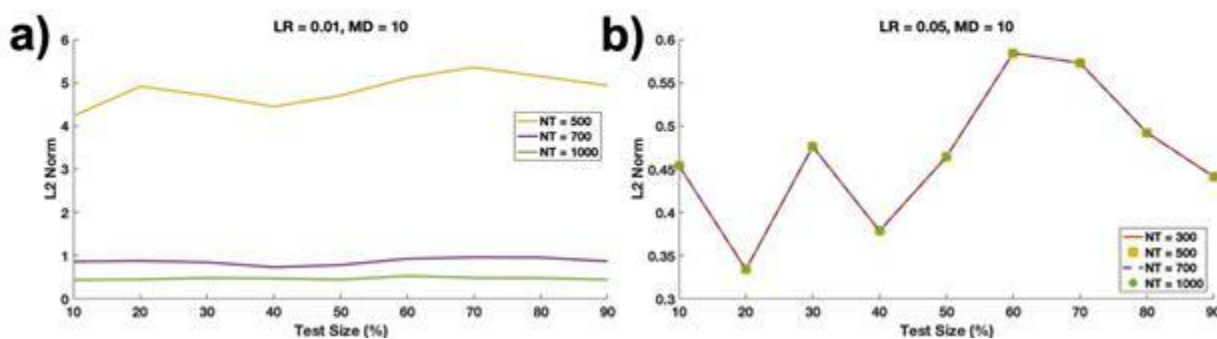
Figure 7-6: Performance of hyperparameter sets 3 and 4 over varying train-test split sizes
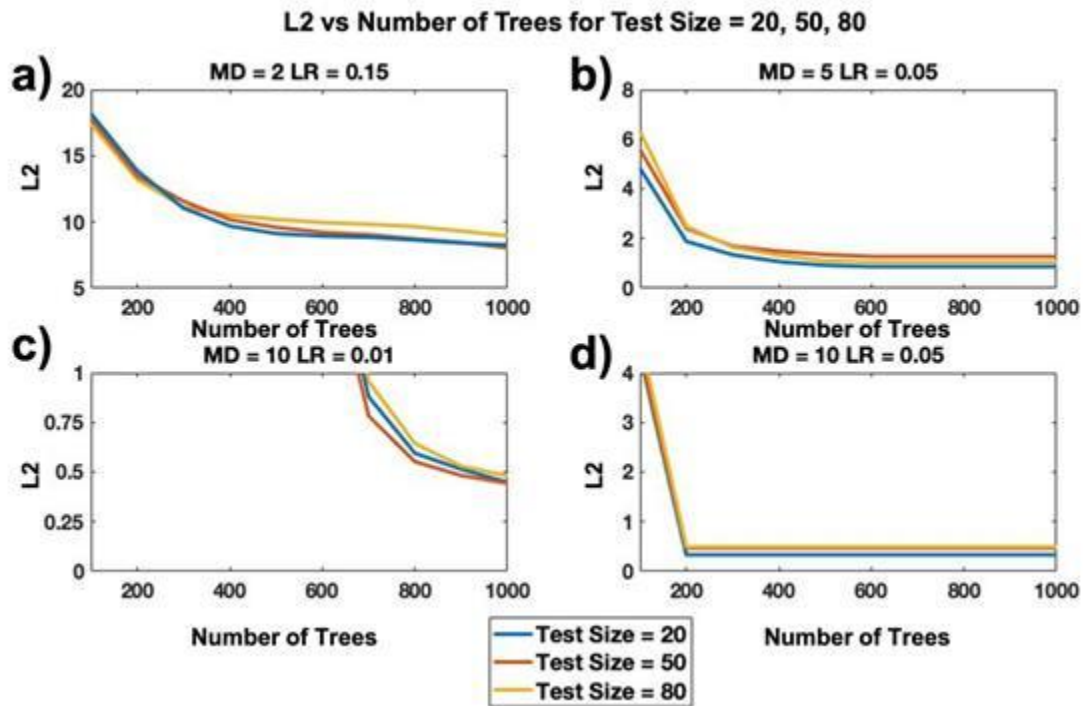
Figure 7-7: Influence of number of trees for the four hyperparameter sets with test sizes of 20%,50%, and 80%
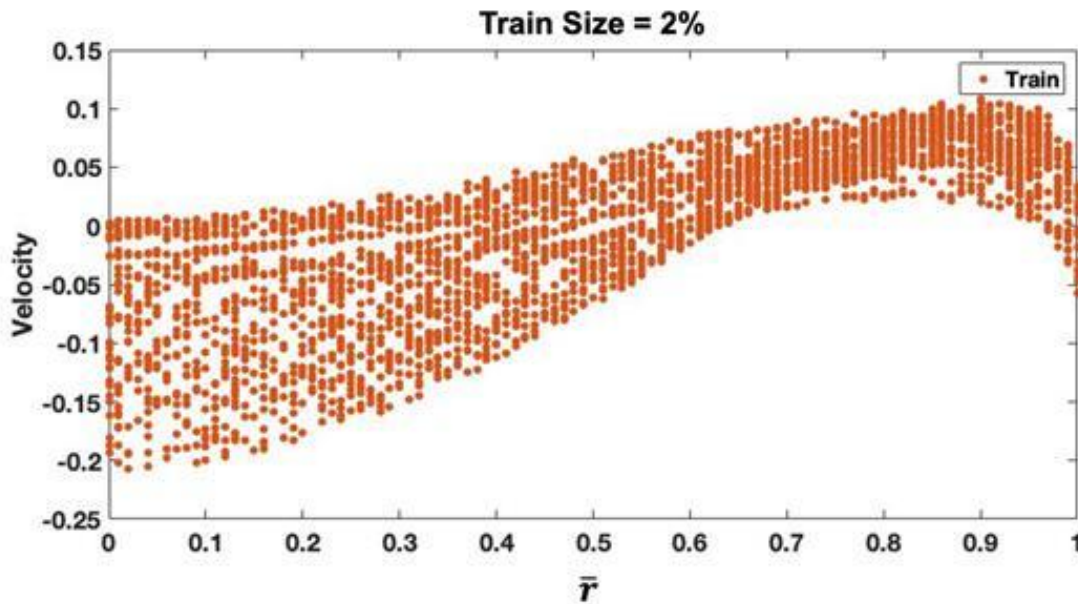
Figure 7-8: Example of data spread for a training size of 2% of entire dataset
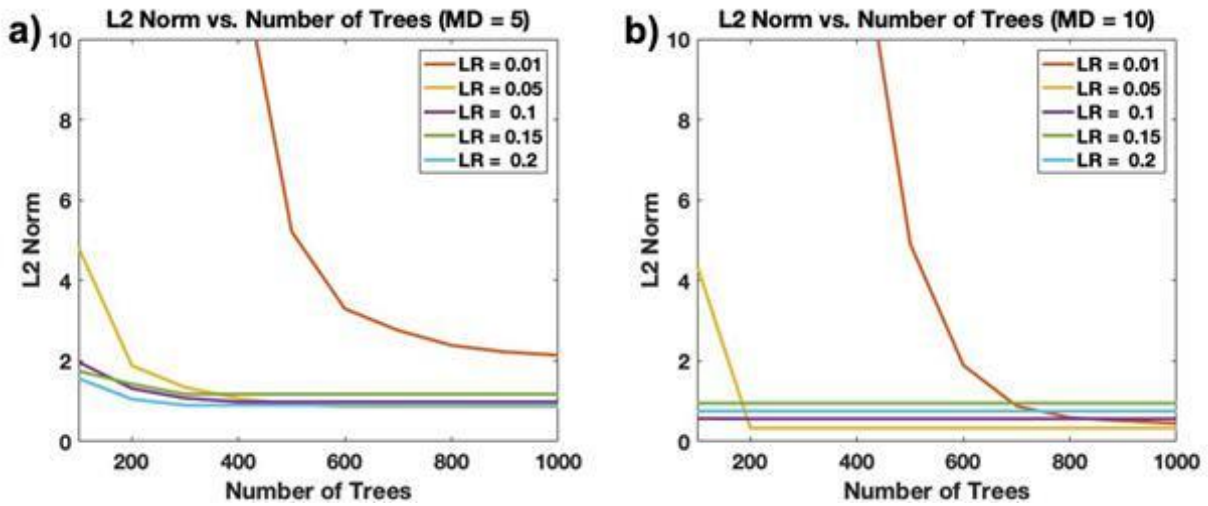
Figure 7-9: Impact of variation of *LR* and *NT* with fixed MD
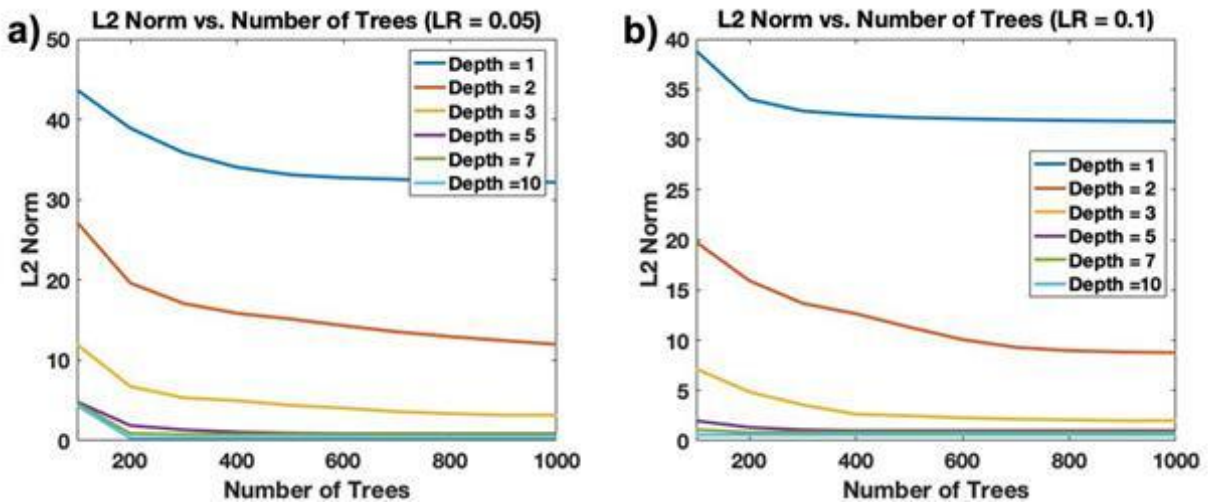
Figure 7-10: Impact of variation of *MD* and *NT* with fixed *LR*

XGBoost™ Model Fits

The next phase of the analysis sought to better analyze how the model fit the data and to look for any obvious outliers in the performance. The first analysis compares how well the predicted velocity values aligned with the actual velocity values in Fig. 7-11. This analysis is completed for the four sets of XGBoost™ hyperparameters in Table 7-1 for test sizes of

20%, 50%, and 80%. This gives insight to whether the model tends to predict values above or below the actual value, how tight the predicted values fit to the correct prediction, and if certain velocity value regions are fitting better or worse than others. For the first set of hyperparameters in the first row of Fig. 7-11, the models do not fit as tight to the actual velocity fit line, which is the result of an underfit model. From the three plots, it appears that some of the smallest values near -0.2 are predicted to be larger than they actually are. In addition, the velocities around zero are predicted to be less than what the actual values are. The other three sets of hyperparameters have a tighter fit to the actual velocity line and do not display trends like this.

Figure 7-12 shows a broad layout of the actual test data values and predicted test data values for the first hyperparameter set. This layout shows early values that are predicted to be higher than the actual and velocity values near zero that are predicted to be lower than actual. Both of these line up with the trends outlined in Fig. 7-11, though it is not possible to correlate the predicted value with its corresponding actual value. It is evident from this figure that the model is underfit. In Fig. 7-13, the actual and predicted values for the fourth set of hyperparameters demonstrate a much better correlation with no obvious outliers.

To better visualize how well the models fit, a single set of helicopter parameters are used to compare the actual and predicted values with each other. The parameters are $d = 0.2$, $\gamma = 5$, and $\sigma = 0.1$. These fits also give a form of preliminary inspection to ensure that the profiles are fitting well and go along with the L2 norm error. Figures 7-14 to 7-16 show fits for the first set of hyperparameters for test sizes of 20%, 50%, and 80%. The 20% test size case in Fig. 7-14 shows a decent fit comparison of fits between the actual and predicted values. The values are slightly off which is due to a model that has either not fully reached its best performance and would benefit from more splits in the model fitting. The influence

of larger test sizes can be seen in Figs. 7-15 and 7-16 as the predicted values tend to stray farther from the actual values. Moreover, the influence of an underlying step function is more prevalent with several clear sections of constant velocity over a range of $\bar{r}$. These profiles also better illustrate the underlying splits made in the model and that the model would benefit from either more splits or better split locations. The fit of the second hyperparameter set is illustrated in Fig. 7-17 for a test size of 20%. The predicted values are closer than the first hyperparameter set but are still slightly off for the early values ($\bar{r} < 0.4$). The final two hyperparameter sets (Figs. 7-18 and 7-19), which had the lowest L2 norm errors clearly demonstrate a well fit model with differences between the actual and predicted velocity terms that are not visible in the plot.
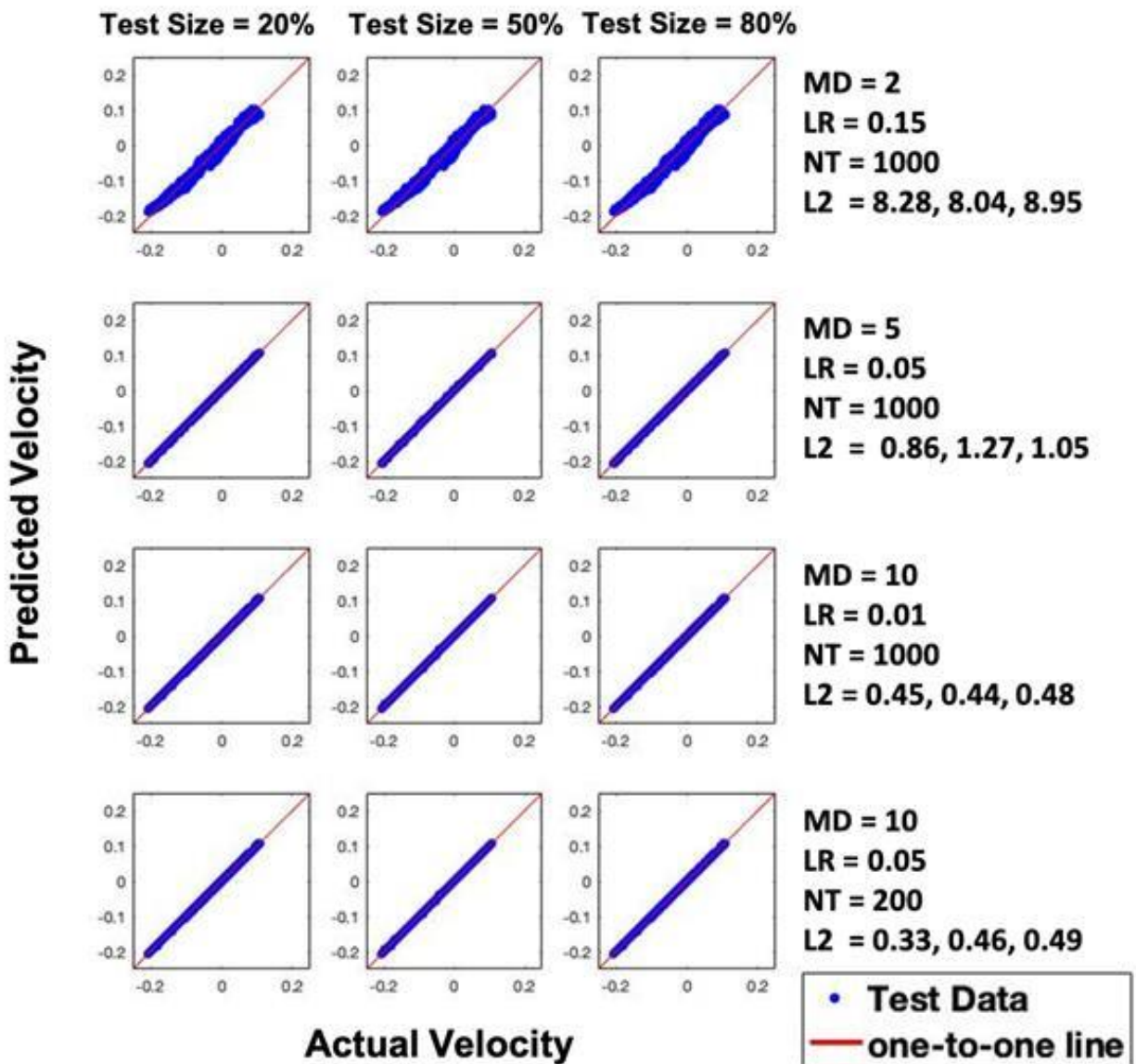
Figure 7-11: Comparison of predicted velocity and actual velocity for the four different hyperparameter sets
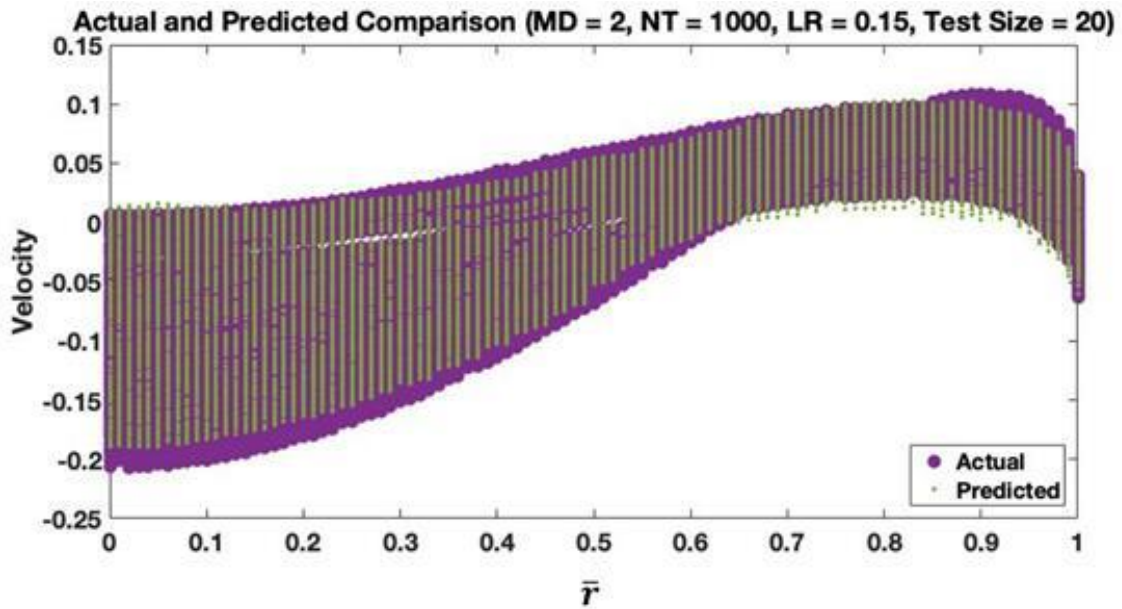
Figure 7-12: Comparison of actual and predicted velocities across the rotor for hyperparameter set 1
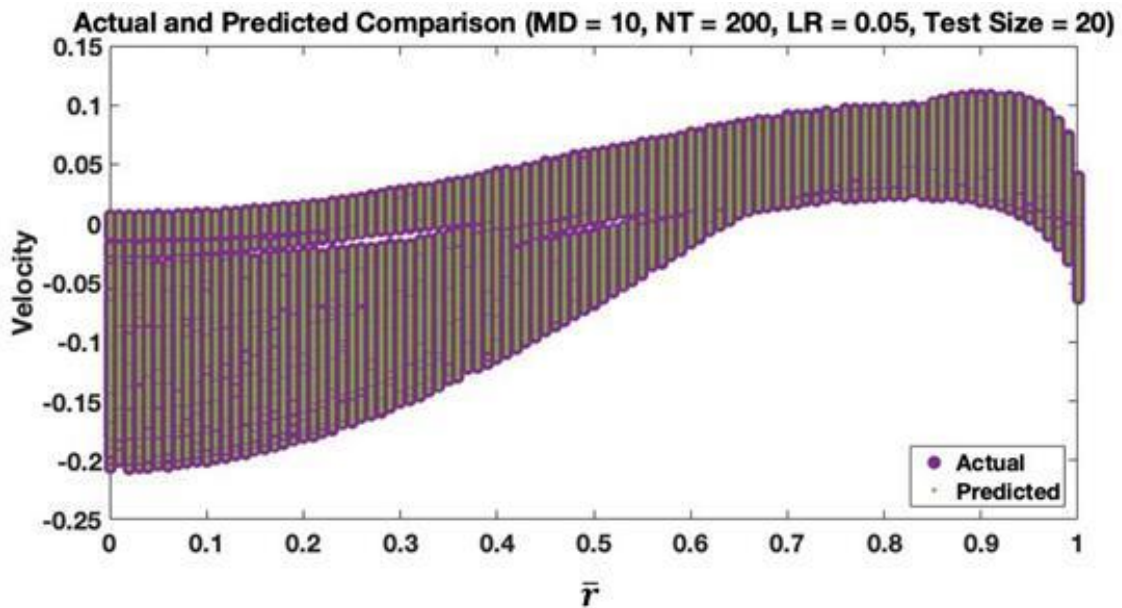
Figure 7-13: Comparison of actual and predicted velocities across the rotor for hyperparameter set 4
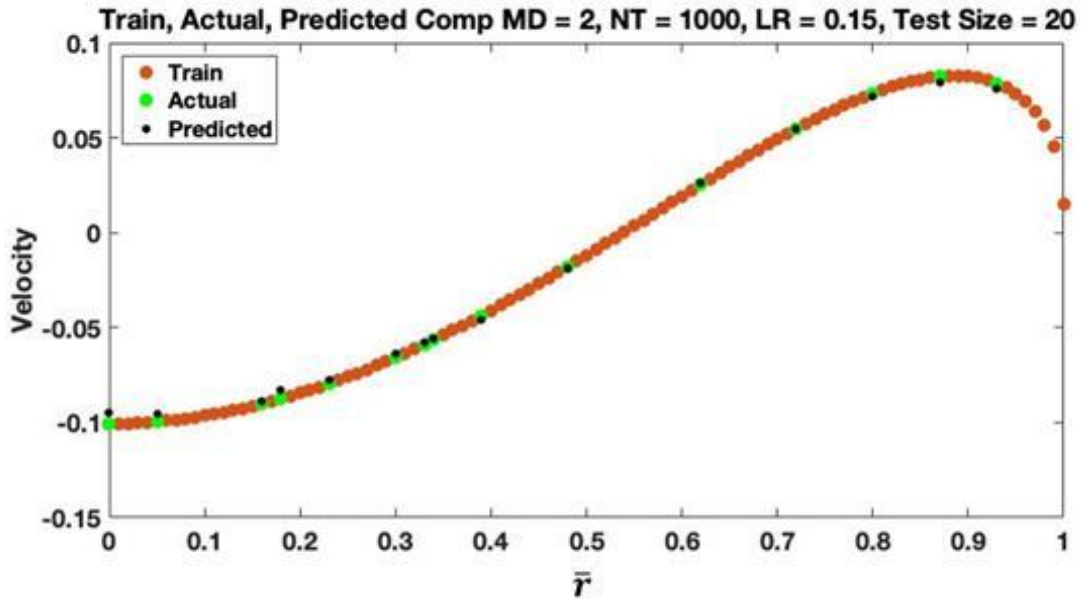
Figure 7-14: Performance of hyperparameter set 1 for a test size of 20% with helicopter parameters $d = 0.2$, $\gamma = 5$ and $\sigma = 0.1$
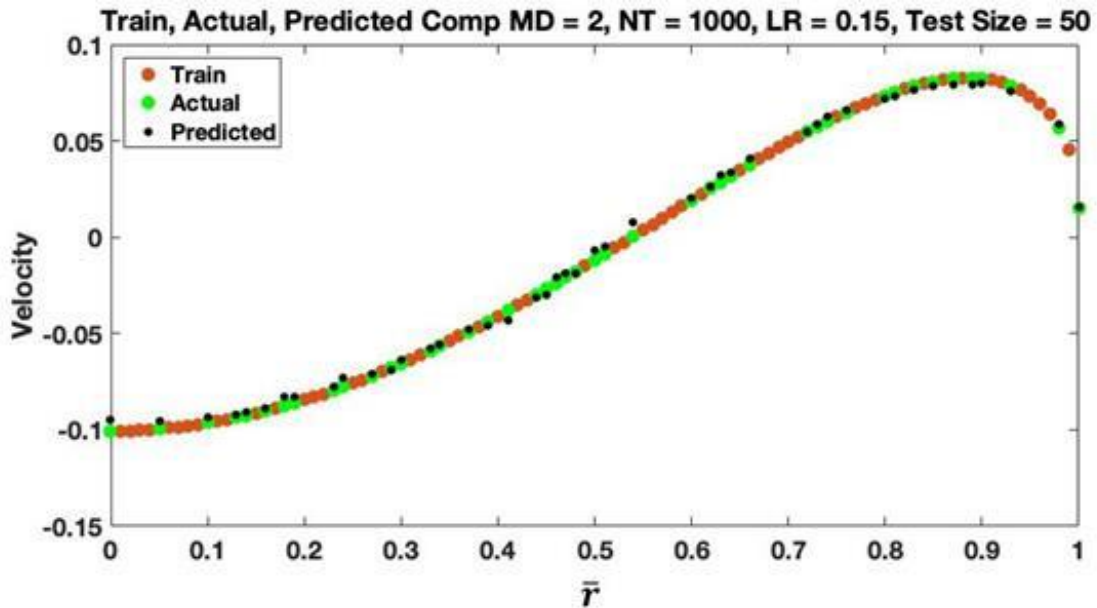
Figure 7-15: Performance of hyperparameter set 1 for a test size of 50% with helicopter parameters $d = 0.2$, $\gamma = 5$, and $\sigma = 0.1$
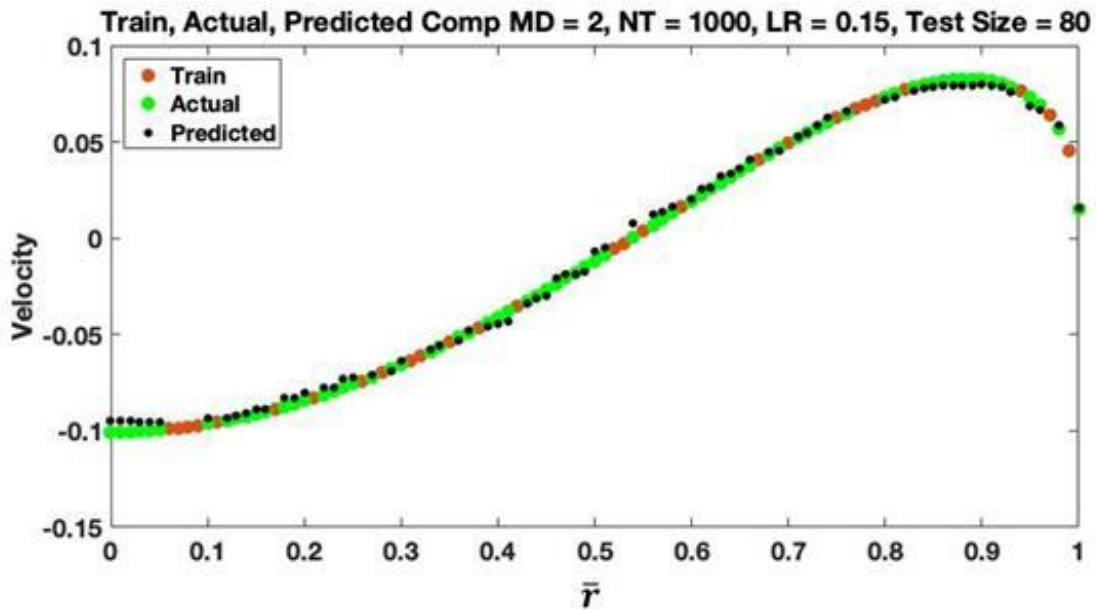
Figure 7-16: Performance of hyperparameter set 1 for a test size of 80% with helicopter parameters $d = 0.2$, $\gamma = 5$, and $\sigma = 0.1$
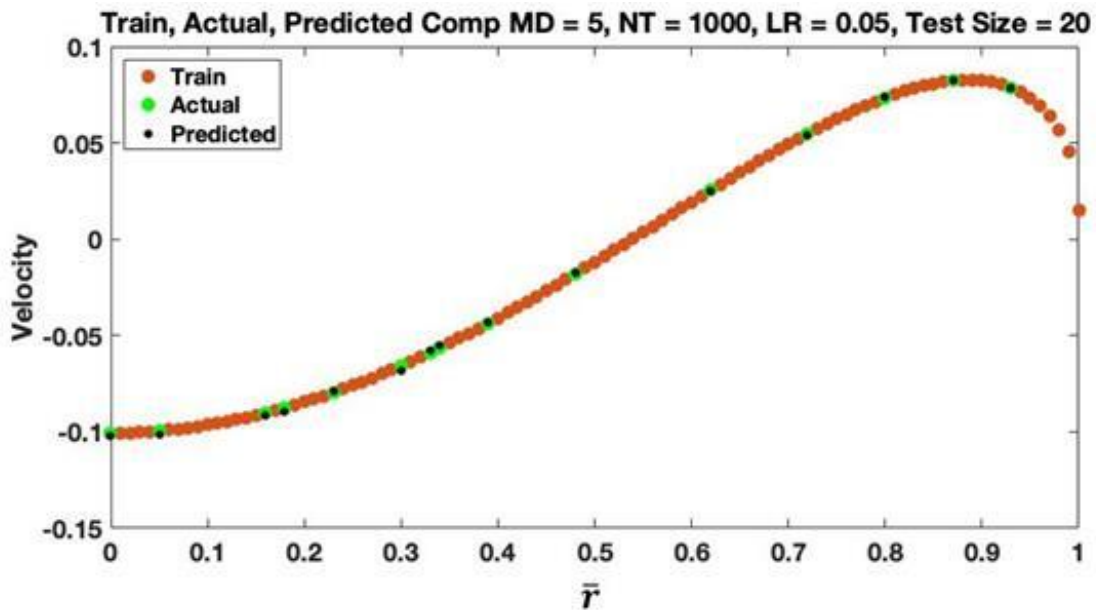
Figure 7-17: Performance of hyperparameter set 2 for a test size of 20% with helicopter parameters $d = 0.2$, $\gamma = 5$, and $\sigma = 0.1$
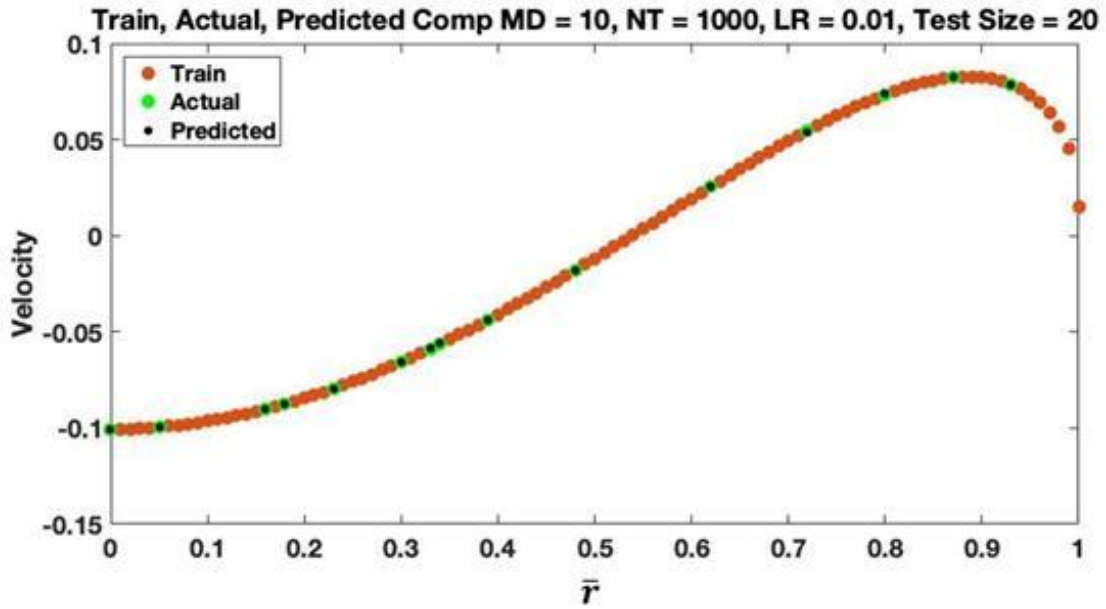
Figure 7-18: Performance of hyperparameter set 3 for a test size of 20% with helicopter parameters $d = 0.2$, $\gamma = 5$, and $\sigma = 0.1$
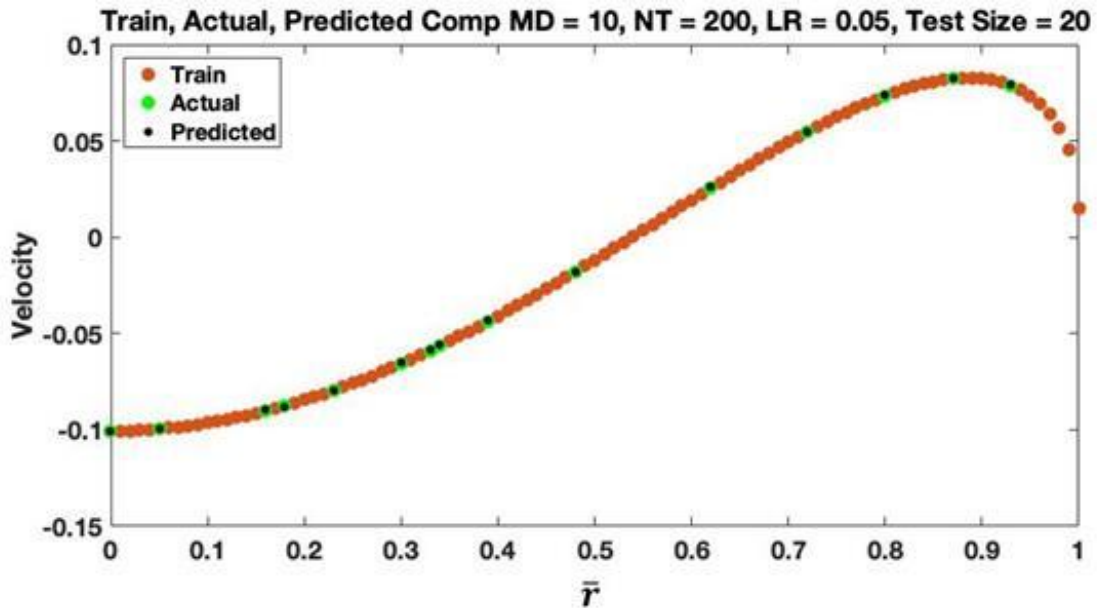
Figure 7-19: Performance of hyperparameter set 4 for a test size of 20% with helicopter parameters $d = 0.2$, $\gamma = 5$, and $\sigma = 0.1$

7.4.2 Evaluation of Intermediate Values

For investigations into predicting the intermediate values the data step size was defined as $\Delta \bar{r} = 0.02$. Prior to analyzing the intermediate values, the model still needs to be validated for performance within the training data. Therefore, 20% of the training data was withheld for testing the model. Figure 7-20 shows that many of the best performing parameters for this model are the same as for the full dataset. Given the similarities, the same four sets of hyperparameters from Table 7-1 are utilized for the results in this section. Figure 7-21 demonstrates the performance of the models for the intermediate values and illustrates a much larger L2 norm error. In addition, a wider range of hyperparameters provide performance near the best L2 norm of $\sim$7.5. The best performing of these set of hyperparameters was a set 3 from Table 7-1.

Figure 7-22 validates the predicted and actual velocities of the testing data for hyperparameter set 3. The predicted values fit close to the line and show little visible error, which is the case for the full data set with the same hyperparameters. Next, Figure 7-23 illustrates an underfit model for hyperparameter set 1 and Fig. 7-24 shows a better fit model for set 3. These are presented to further illustrate that the model is fitting well with the training data. Figures 7-25 to 7-28 illustrate model fit for a single set of helicopter parameters ($d = 0.2$, $\gamma = 5$, and $\sigma = 0.1$), which show similar performance to the previous tests of the full models.

Now that the model fitting has been validated for the training portion of the dataset, the intermediate values are evaluated to determine where the models are fitting poorly and rationalizing why. Figure 7-29 shows a comparison of the predicted and actual velocity terms for the intermediate values for a model with hyperparameter set 3. The region in the red circle in Fig. 7-29 is a group of underpredicted velocities for the model. In Fig. 7-30, the XGBoost$^{\text{TM}}$ model using parameter set 1 shows significant widespread variations between

the actual velocity values and predicted velocity values across the rotor disk. This was a poor performing model during training and was not expected to do well. Figure 7-31 shows the same comparison using hyperparameter set 3 and only illustrates significant issues between the predicted and actual intermediate values near the tip of the rotor blade ($\bar{r} = 0.95 - 0.99$). Upon further investigation, it was revealed that these values accounted for all of the circled underpredicted values in Fig. 7-29. Due to the large drop in velocity near the tip, more datapoints would be needed to obtain a better fit in this region. It was also determined that the L2 norm of the better performing models dropped down to as low as 2.95 when the values from $\bar{r} = 0.91 - 1$ were removed. Refitting the model for an $\bar{r}$ range of $0 - 0.9$ did not significantly change the way the model fit to the data and therefore, this avenue was not further pursued.

To gain better understanding of where the error existed in the models, the same single set of helicopter parameters (d $= 0.2$, $\gamma = 5$, and $\sigma = 0.1$) are evaluated for the intermediate values with all four hyperparameter sets. In Fig. 7-32, hyperparameter set 1 had issues reaching a tight fit with the predicted values pretty much across the entire profile. Outside of near the tip, the area with the poorest fit was from $\bar{r} = 0.7 - 0.9$. For hyperparameter set 2 in Fig. 7-33, the model did a better job of fitting close to the data, especially in the $\bar{r} = 0 - 0.2$ and $\bar{r} = 0.7 - 0.9$ regions. The region in between these two illustrated consistent minor errors. The final two hyperparameter sets performed similarly, as is shown in Figs. 7-34 and 7-35. These two sets had a tighter fit in the $\bar{r} = 0.2 - 0.7$ than hyperparameter set 2, but still did contain consistent minor errors. Observing the predicted values closely, it is noticeable that many of them have the same velocity value as the datapoints immediately on either side of them. This illustrates that the model is closely following the splits that form and are struggling with the intermediate values. Given that the data points are close together, the resultant error is low. However, if $\Delta\bar{r}$ was instead 0.05 (training on every fifth data point),

as was the case in Fig. 7-36, the predictions are much worse. This case better illustrates the underlying step functions that are forming in the model development.

Testing of the intermediate values provided insight into how XGBoost$^{\text{TM}}$ works with our current approach for fitting to data. At this point we could make a case for creating a large dataset spanning several harmonics and feel confident of predicting values within the domain with considerable accuracy. However, more work needs to be done in the refinement of our approach to better evaluate intermediate values.
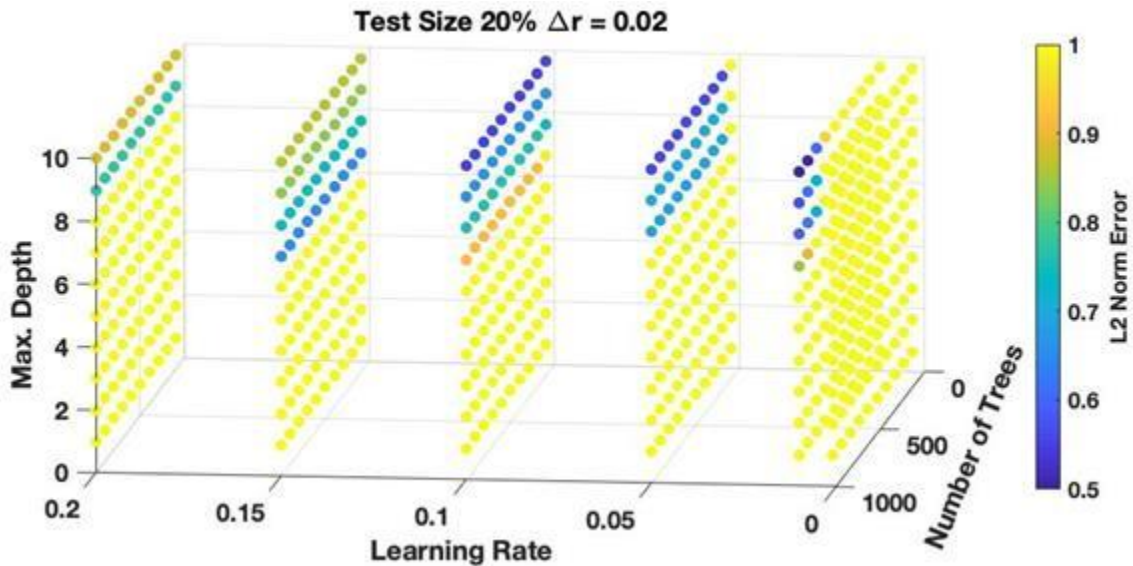
Figure 7-20: Performance of test data from training set
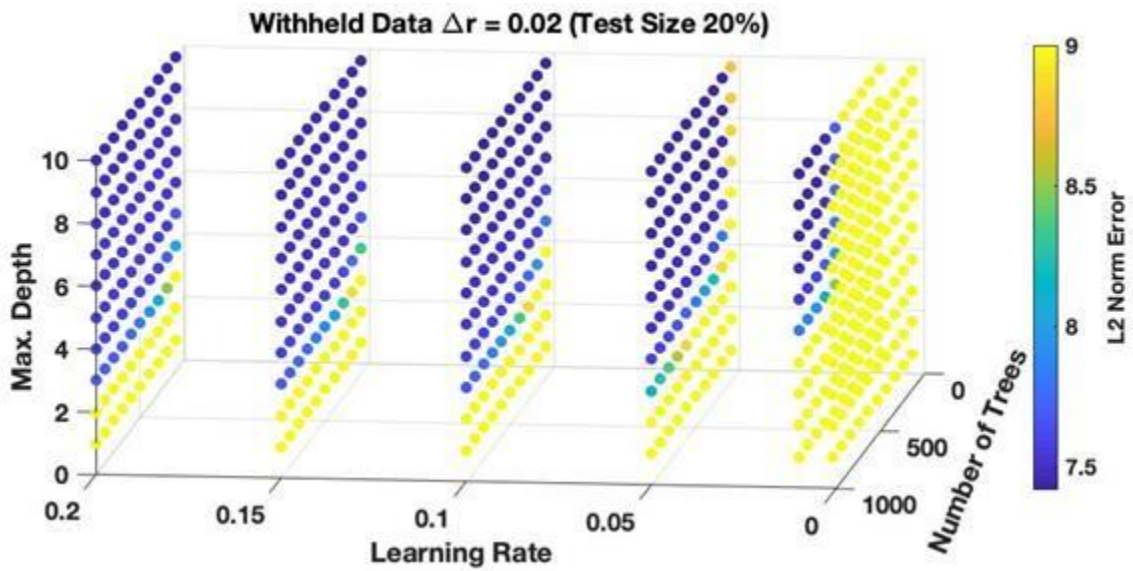
Figure 7-21: Performance of intermediate values with $\Delta \bar{r} = 0.02$
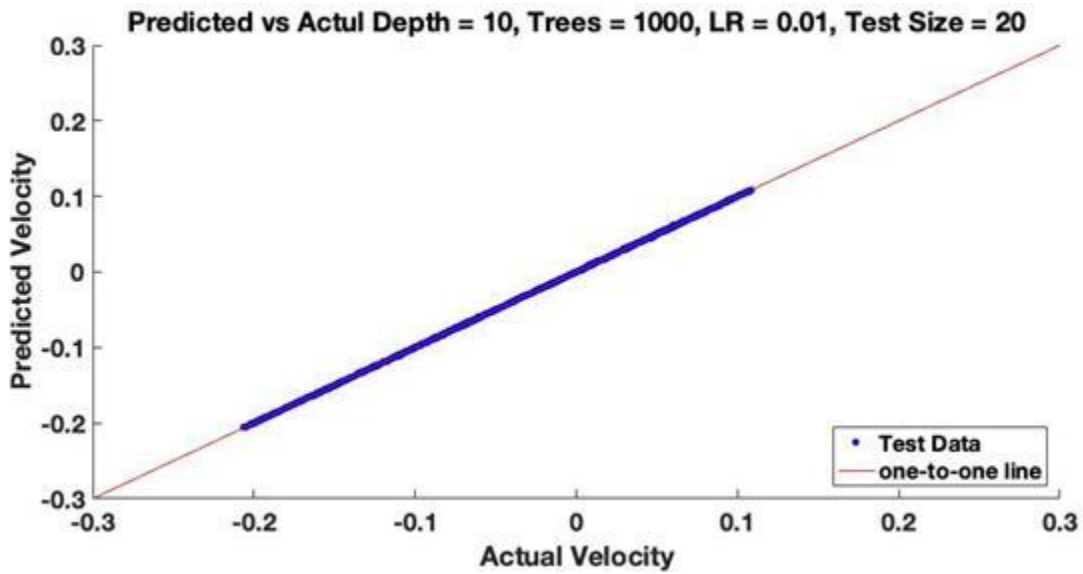
Figure 7-22: Comparison of predicted velocity and actual velocity for test data from training set for hyperparameter set 3
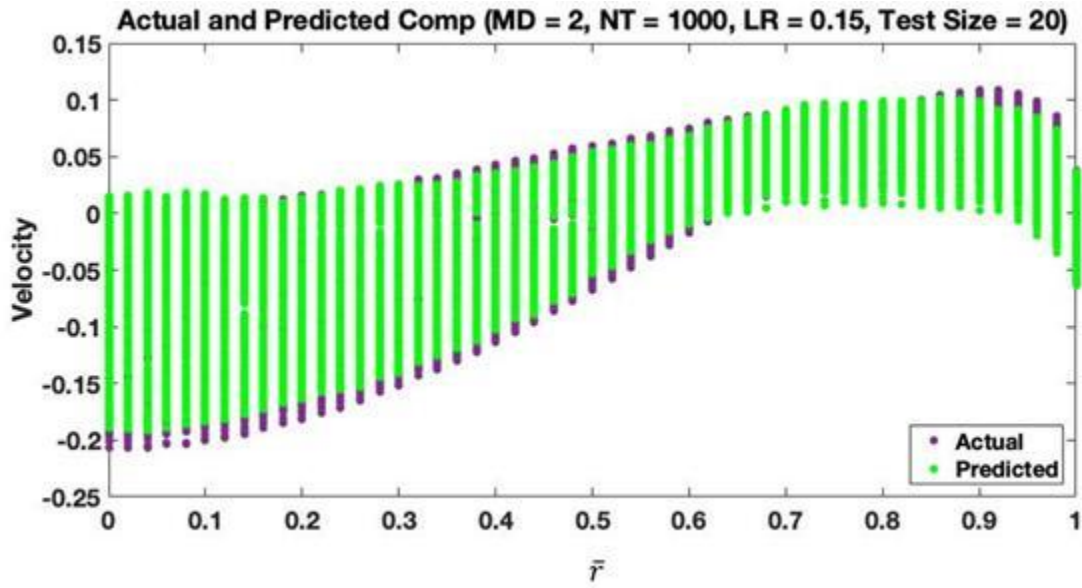
Figure 7-23: Comparison of actual and predicted velocities across the rotor for test data from training set hyperparameter set 1
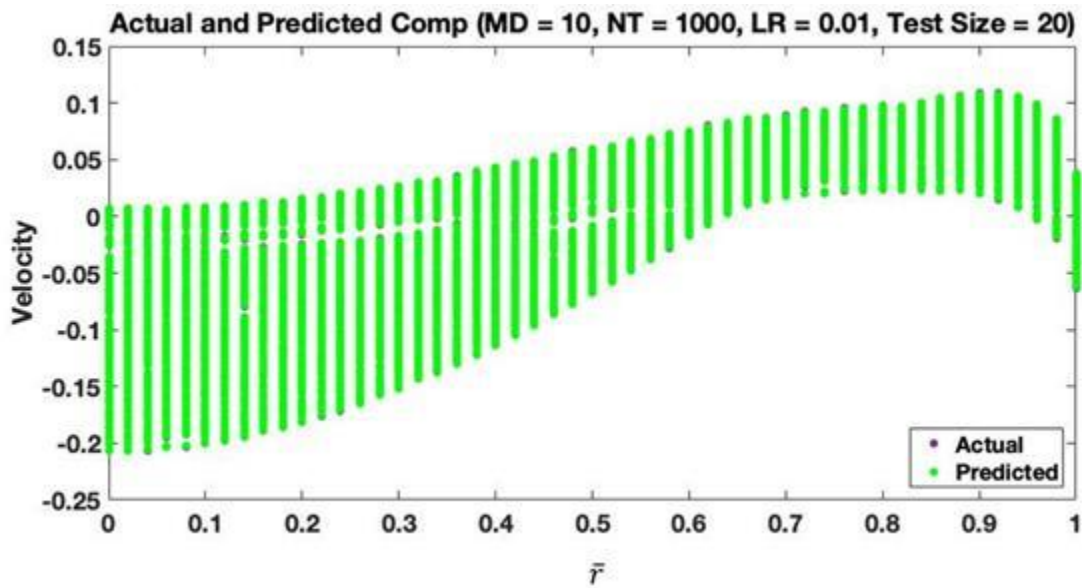
Figure 7-24: Comparison of actual and predicted velocities across the rotor for test data from training set hyperparameter set 3
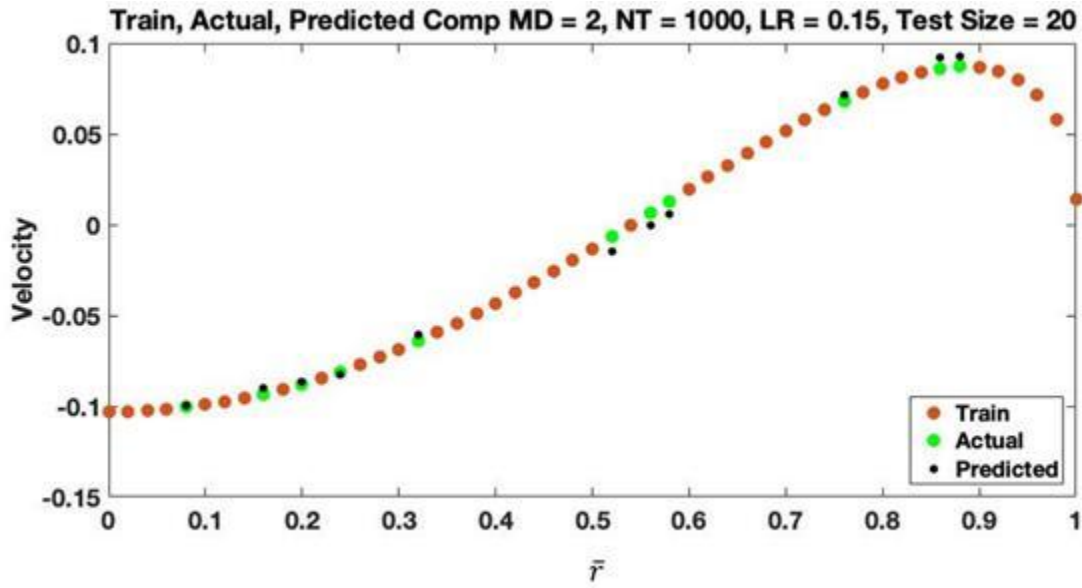
Figure 7-25: Performance of hyperparameter set 1 for a test data from training set with helicopter parameters $d = 0.2$, $\gamma = 5$, and $\sigma = 0.1$
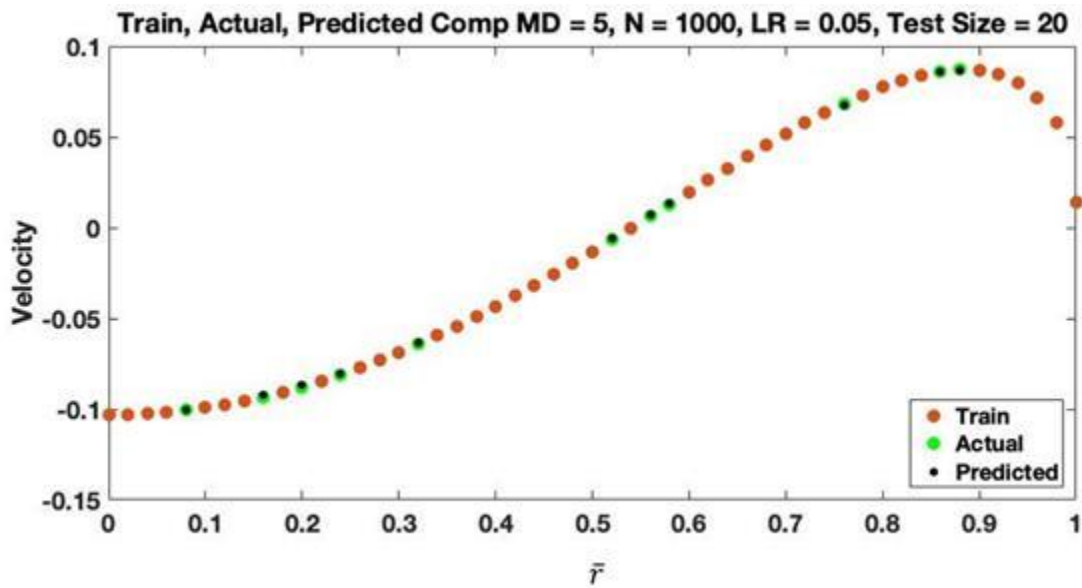
Figure 7-26: Performance of hyperparameter set 2for a test data from training set with helicopter parameters $d = 0.2$, $\gamma = 5$, and $\sigma = 0.1$
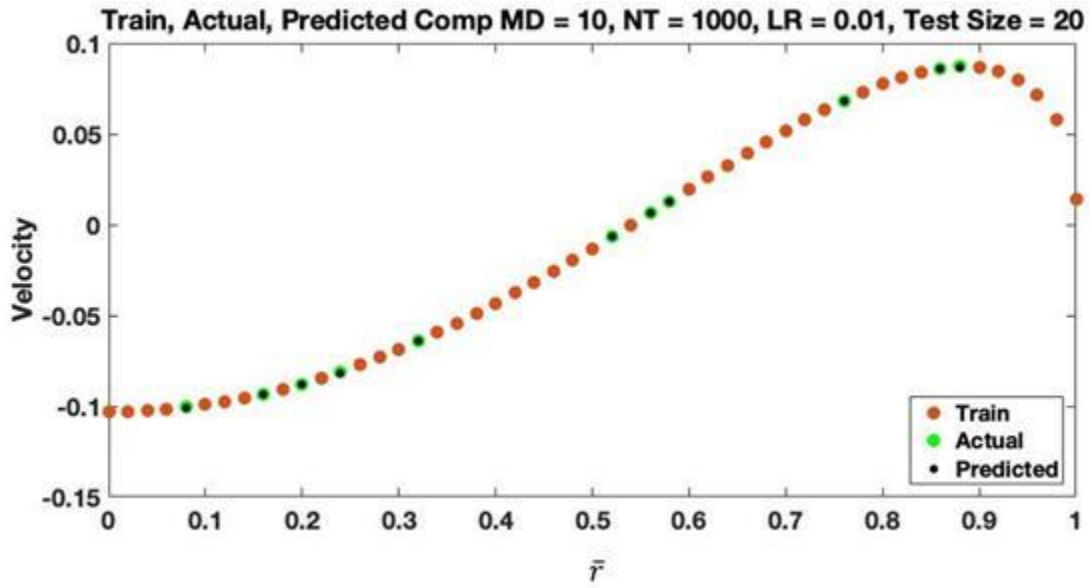
Figure 7-27: Performance of hyperparameter set 3 for a test data from training set with helicopter parameters $d = 0.2$, $\gamma = 5$, and $\sigma = 0.1$
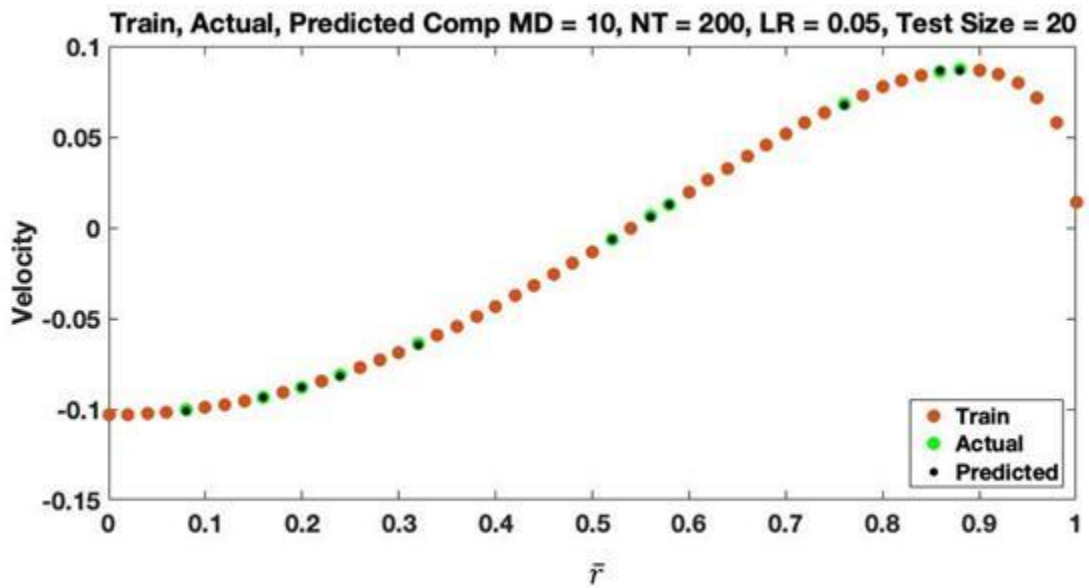
Figure 7-28: Performance of hyperparameter set 4 for a test data from training set with helicopter parameters $d = 0.2$, $\gamma = 5$, and $\sigma = 0.1$
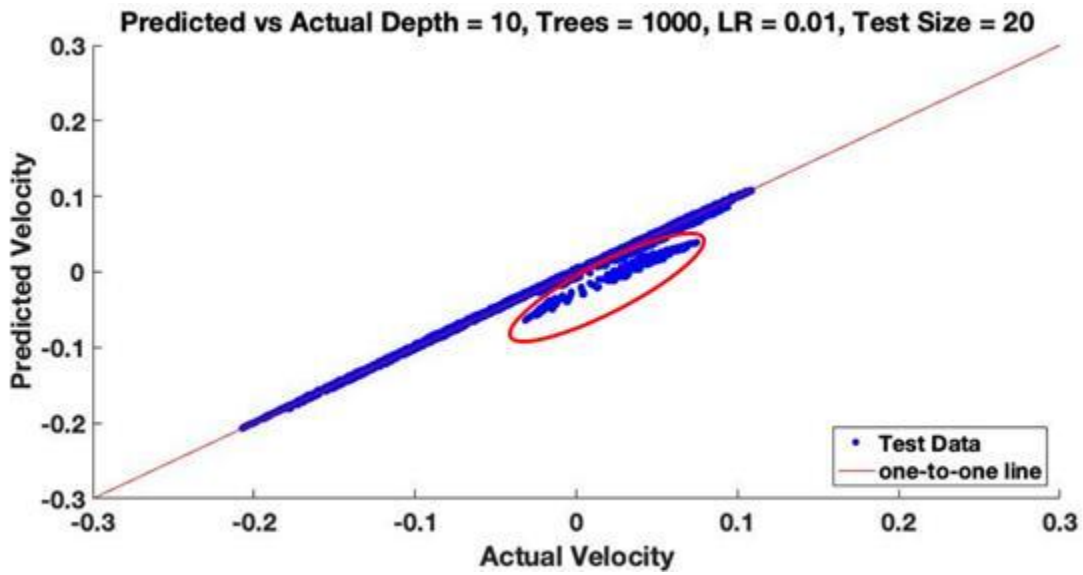
Figure 7-29: Comparison of predicted velocity and actual velocity for intermediate values with hyperparameter set 3
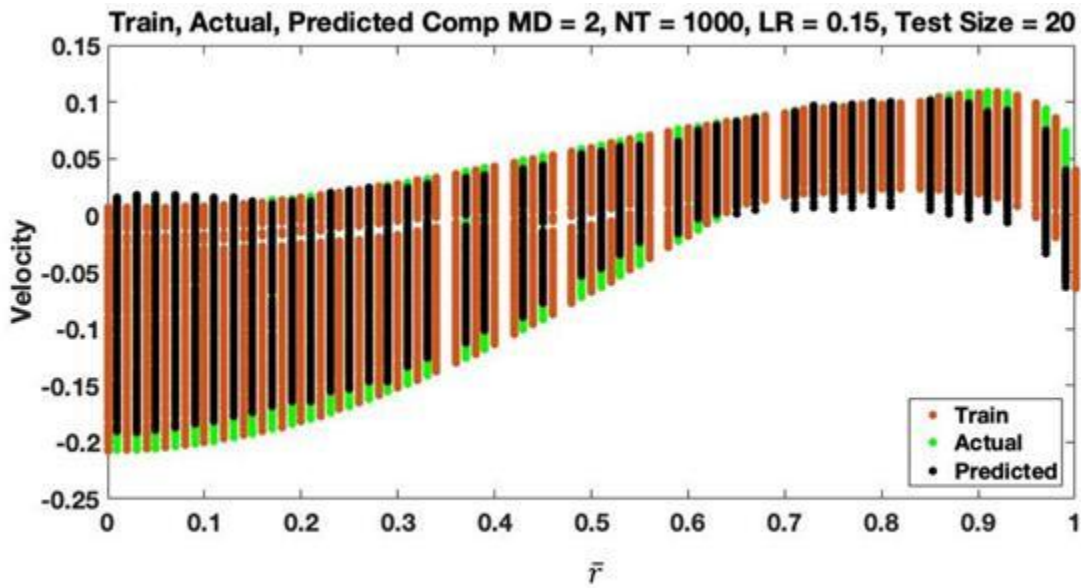
Figure 7-30: Comparison of actual and predicted velocities across the rotor for intermediate values with $\Delta\bar{r} = 0.02$ and hyperparameter set 1
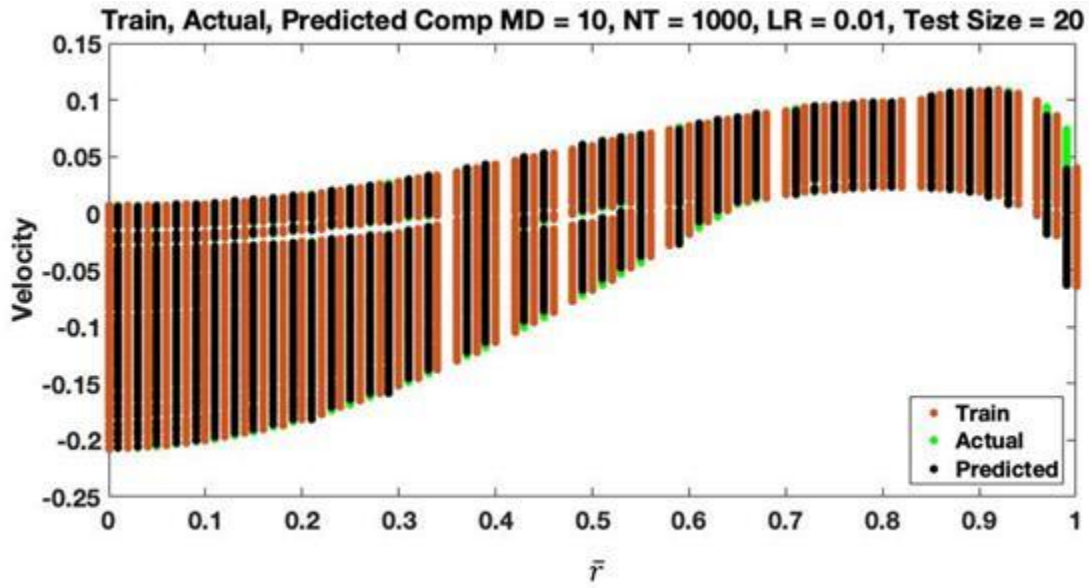
Figure 7-31: Comparison of actual and predicted velocities across the rotor for intermediate values with $\Delta\bar{r} = 0.02$ and hyperparameter set 3
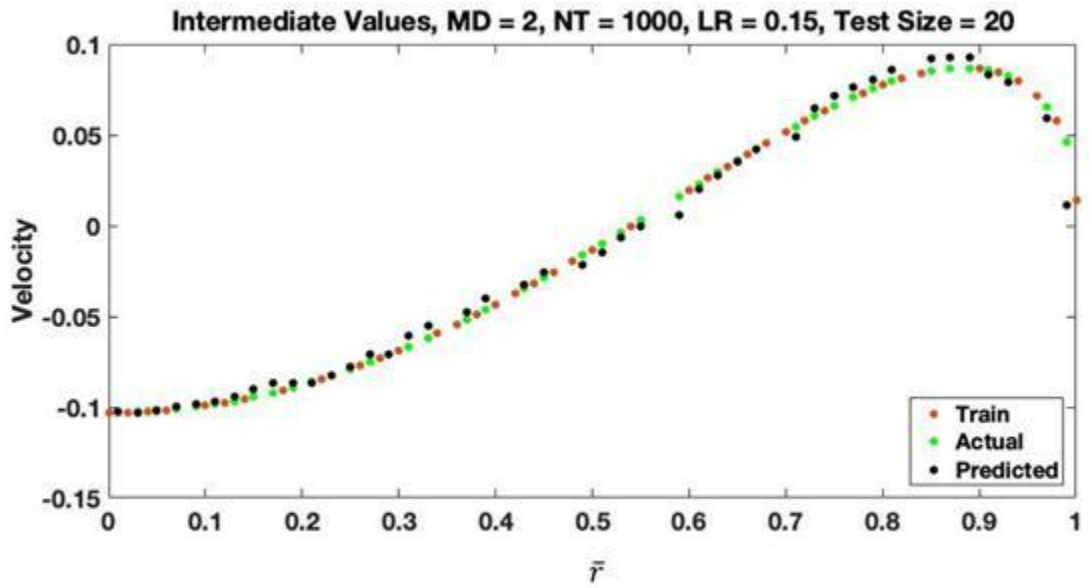
Figure 7-32: Performance of hyperparameter set 1 for intermediate values with $\Delta\bar{r} = 0.02$ and helicopter parameters $d = 0.2$, $\gamma = 5$, and $\sigma = 0.1$
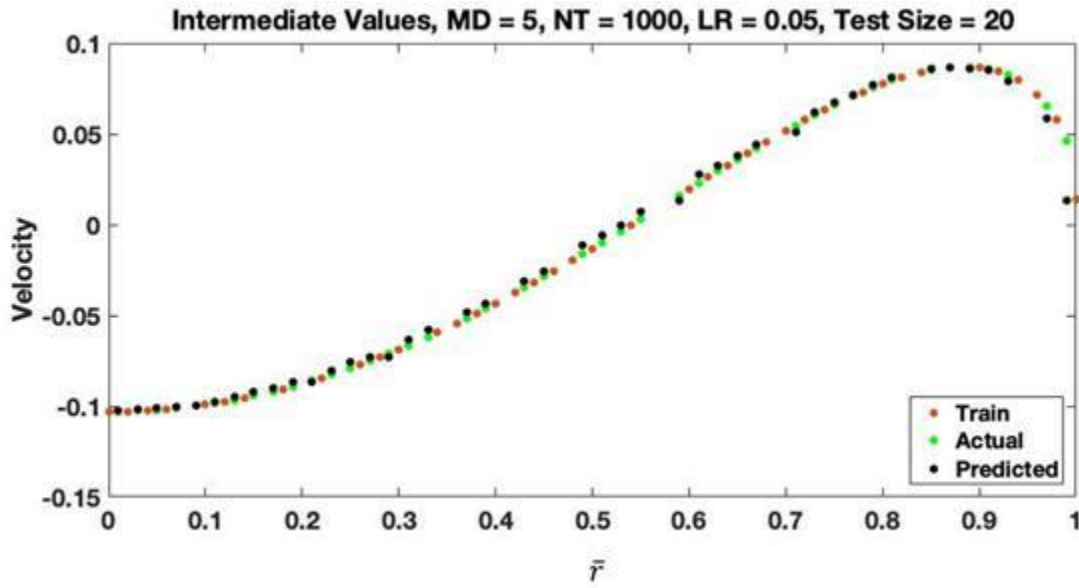
Figure 7-33: Performance of hyperparameter set 2 for intermediate values with $\Delta\bar{r} = 0.02$ and helicopter parameters $d = 0.2$, $\gamma = 5$, and $\sigma = 0.1$
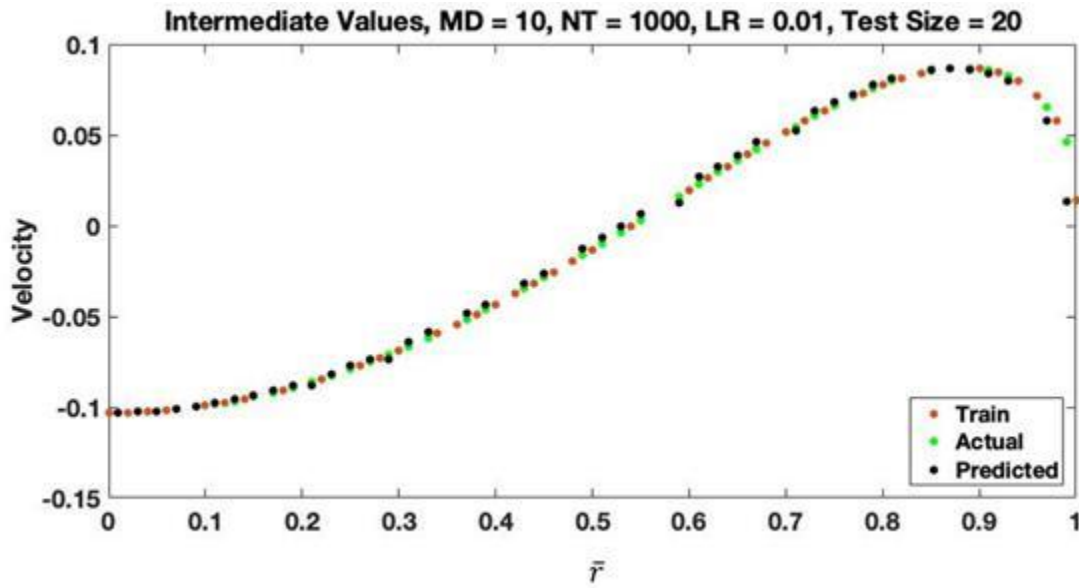
Figure 7-34: Performance of hyperparameter set 3 for intermediate values with $\Delta\bar{r} = 0.02$ and helicopter parameters $d = 0.2$, $\gamma = 5$, and $\sigma = 0.1$
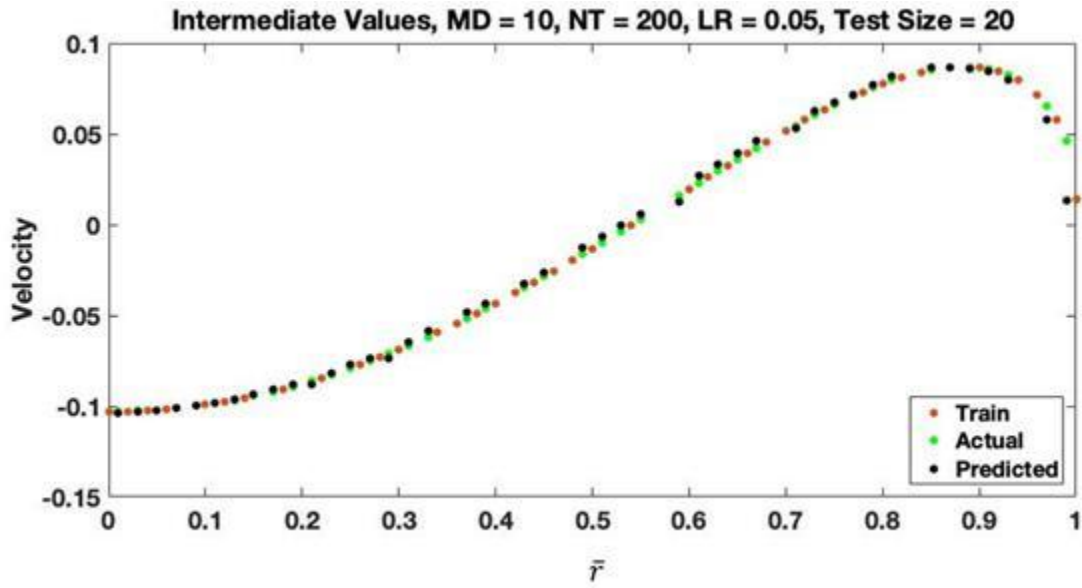
Figure 7-35: Performance of hyperparameter set 1 for intermediate values with $\Delta \bar{r} = 0.02$ and helicopter parameters $d = 0.2$, $\gamma = 5$, and $\sigma = 0.1$
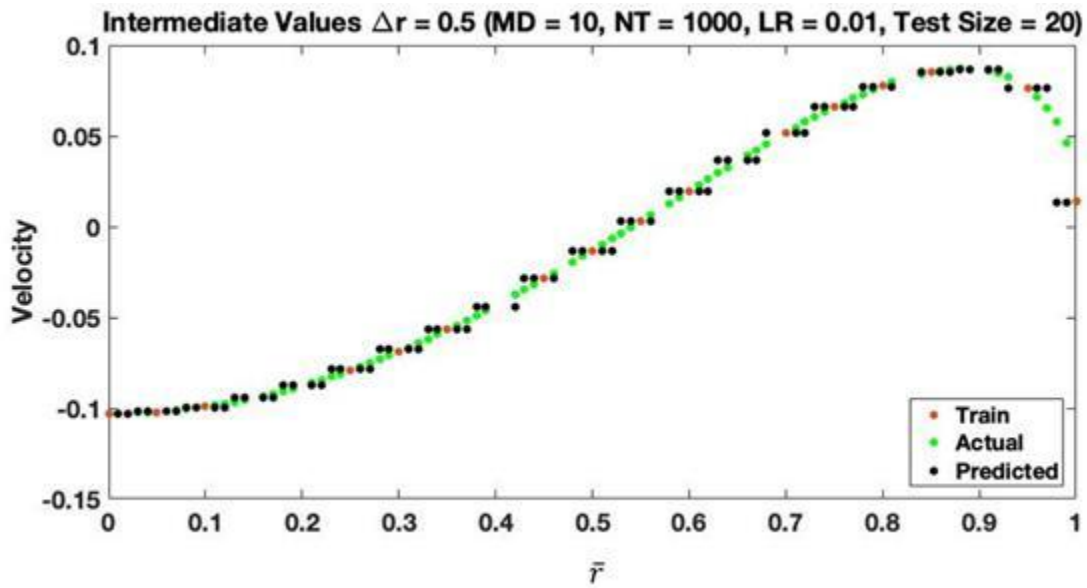
Figure 7-36: Performance of hyperparameter set 3 for intermediate values with $\Delta \bar{r} = 0.05$ and helicopter parameters $d = 0.2$, $\gamma = 5$, and $\sigma = 0.1$

Chapter 8

Summary, Conclusions, and Future Work

8.1 Summary and Conclusions

In the first part of this work, a simple proof of concept is formulated to verify the applicability of a solution process for a coupled system with time delays and adjoint variables. The proof-of-concept model provides a simple model with which to develop solution methods that utilize reverse time marching or convolution integrals. It is shown that either solution method provides an accurate solution. Therefore, only the time-marching solution process is carried out in the remainder of the work. The consideration of load sharing is also developed in this model to evenly distribute the total system load between the two rotors. It is also demonstrated in the proof-of-concept model that the solution of the velocity field is independent of the terminal conditions for the co-states. Therefore, the terminal conditions can be any value; but there is an advantage to setting them equal to either zero (for ease of use) or the steady-state value (for faster convergence to steady-state). Ultimately, the proof-of-concept model was able to demonstrate the model development processes for coupled systems with time delays and adjoint variables.

In the second part of this work, the proof of concept is expanded to develop a multiple inflow-state solution for a coupled coaxial rotor system with the pressure coefficients of Morillo. In this section, more rigorous equations are derived based on Fei's work with the adjoint theorem. The new model is at first simplified under the assumption of an infinite number of blades. Consequently, only the 0th harmonic is involved in the solution. On-disk, off-disk, and pitch- angle-coupling matrices are developed for the coupled system. The off-disk matrix and the state variables for the second rotor (which include time-delayed terms) are the new elements of the model developed here.

The third part of this work extends the infinite-blade model to solve for a finite number of blades. The finite-blade model can include an arbitrary number of blades and an arbitrary number of harmonics, as defined by the user. In addition to a finite number of blades, a rigorous treatment of the angle of attack due to climb is also added to the model. On-disk, off-disk, and blade coupling dynamic matrices are derived for this case. The finite-blade model is able to provide a more accurate dynamic solution for the system and is able to illustrate blade passage and vortex sheets from the upper rotor hitting the lower rotor.

In section 4 of this work, the finite-blade model is adapted for wind turbines. The purpose of this adaptation is to display the capabilities of the model for other applications. In the wind turbine case, the model is no longer considered lightly loaded; and, therefore, the angle of attack due to induced flow is factored into the calculation of thrust coefficient and pitch angle. For wind turbine applications, the inflow velocities are of different magnitudes than they were for the applications to lightly-loaded rotors. This changes the time delay and the distance between the vortex sheets, which leads to the off-disk velocity doubling at a smaller distance downstream. The wind-turbine model successfully illustrates similar rotor interactions for wind energy applications.

Finally, data from the model developed in the third part of this work is used to develop gradient boosted tree models as a feasibility study for potential future applications with higher harmonic models. The gradient boosted tree models are trained with different sets of hyperparameters to determine the best fit for the dataset. In addition, intermediate values are tested to determine how well the model performs with data points of unseen parameters. Overall, the use of gradient boosted trees is a probable approach for higher harmonic solutions, but more work needs to be done with predicting intermediate values.

The key conclusions from this work are:

1. Adjoint variables and time delays can be used in a dynamic analysis of coupled rotor inflow systems. The dynamics of these systems are interesting and fundamentally different from systems without adjoint variables and time delays.

2. The number of harmonics used depends on the purposes of the results and can vary from just a few (for handling qualities and flight dynamics) to dozens (for blade loads and clarity of shed vorticity).

3. Rotor spacing impacts the velocity on the upper and lower rotor disk planes differently. As spacing increases, the velocity on the lower rotor increases, but velocity on the upper rotor decreases.

4. The rotor spacing and number of harmonics have only a minor impact on the upper rotor blade dynamics. For the lower rotor, blade dynamics are significantly impacted by the rotor spacing but show only minor variations for systems with more than 6 harmonics.

5. The spacing of vortex sheets impacts how the time-delay dynamics develop and when they occur.

6. The machine learning applications illustrated the ability to model a well populated and sparsely populated dataset, but struggled with reaching the same tight prediction capabilities for intermediate values.

8.2   Future Work

In this work, all of the applications and results are for a coaxial rotor system in axial flow. This leads to two areas for potential future work, 1) development of the dynamics of coaxial rotors in skewed flow and 2) further development of the model for tandem rotor systems in both axial and skewed flow. The model developed in this work provides a framework for both skewed flow and tandem rotor development. A majority of the updates needed to expand to either of these models involve applications of the ellipsoidal coordinates into the integrals. This will in turn modify the coupled matrices and time delay, thus altering the coupled dynamics.

Another area of future work is to further investigate the how the dynamics on the rotor vary in relation to location of vortex sheets hitting both the lower rotor and the blades on the lower rotor. Several variations in dynamics were illustrated in this work, but a better understanding of how system parameters (rotor spacing, number of blades, freestream flow, etc.) impact the dynamics in the system is needed.

Future work with gradient boosted trees and XGBoost^{TM} first should focus on developing models that better fit to the intermediate values. This could be done through use of additional model parameters, different loss functions, or a different machine learning algorithm. Following this development, higher harmonic terms should be investigated for flow across the rotor to determine if a smaller sampling of higher harmonic solutions can be coupled with a

231

dense population of lower harmonic solutions to accurately predict intermediate higher harmonic solutions. Finally, this work should be expanded to the nondimensional time domain to attempt to fit the model across a more complex domain and ideally be able to develop in real time for flight simulator applications.

Appendix A

Ellipsoidal Coordinate System

The ellipsoidal coordinate system $\left(\nu, \eta, \bar{\psi}\right)$ is defined as:

$$x = -\sqrt{1 - \nu^2}\sqrt{1 + \eta^2}\cos\left(\bar{\psi}\right) \tag{A.1}$$

$$y = \sqrt{1 - \nu^2}\sqrt{1 + \eta^2}\sin\left(\bar{\psi}\right) \tag{A.2}$$

$$z = -\nu\eta \tag{A.3}$$

where the coordinates ν, η, and $\bar{\psi}$ are restricted to the following range:

$$-1 \leq \nu \leq 1 \tag{A.4}$$

$$0 \leq \eta \leq \infty \tag{A.5}$$

$$0 \leq \bar{\psi} \leq 2\pi \tag{A.6}$$

Figure A1-1 shows the ellipsoidal coordinate system viewed in the xz plane. The surfaces for $\nu =$ constant are hyperboloids and the surfaces for $\eta =$ constant are ellipsoids. For the special case, $\eta = 0$ represents the flat circular plane, and ν is anti-symmetric along the plane which contains the $\eta = 0$ circular plane. $\bar{\psi}$ is the azimuth angle measured from the negative x axis, with counterclockwise direction viewed along the positive z axis.

The nondimensional radial position with the ellipsoidal coordinates are obtained from equations (A.1), (A.2) and (A.3):

$$\bar{r}^2 = x^2 + y^2 + z^2 = \left(1 + \eta^2\right)\left(1 - \nu^2\right) + \nu^2\eta^2 \tag{A.7}$$

Similarly, from equations (A.1), (A.2) and (A.3), the ellipsoidal coordinates ν, η and $\bar{\psi}$ can be expressed in terms of x, y and z as:

$$\nu = \frac{-sign\,(z)}{\sqrt{2}}\sqrt{1 - \bar{S} + \sqrt{\left(\bar{S} - 1\right)^2 + 4z^2}} \tag{A.8}$$

$$\eta = \frac{1}{\sqrt{2}}\sqrt{\bar{S} - 1 + \sqrt{\left(\bar{S} - 1\right)^2 + 4z^2}} \tag{A.9}$$

$$\bar{\psi} = \tan^{-1}\left(\frac{-y}{x}\right) \tag{A.10}$$

where $\bar{S}$ is:

$$\bar{S} = x^2 + y^2 + z^2 \tag{A.11}$$
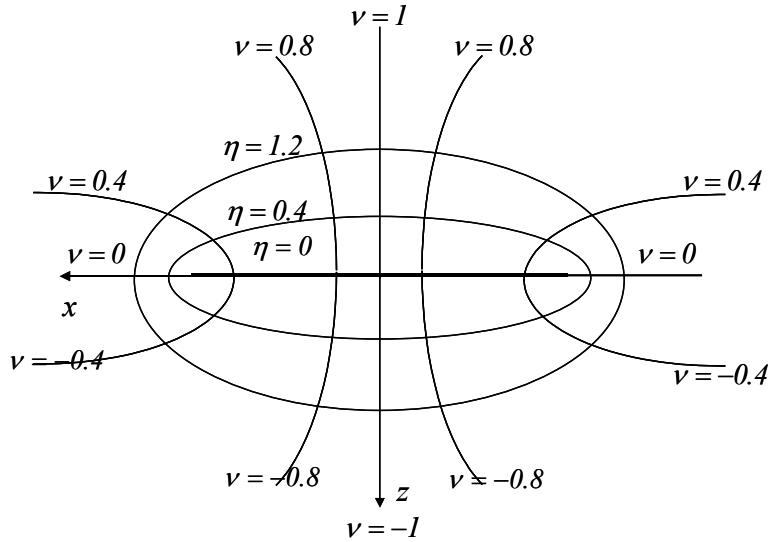
Figure A-1: Ellipsoidal coordinate system

234

Appendix B

Normalized Associated Legendre Functions

In the ellipsoidal coordinate system defined in Appendix A, the Laplace's equation takes the form:

$$\frac{\partial}{\partial \nu}\left[\left(1-\nu^2\right)\frac{\partial \Phi}{\partial \nu}\right] + \frac{\partial}{\partial \eta}\left[\left(1+\eta^2\right)\frac{\partial \Phi}{\partial \eta}\right] + \frac{\partial}{\partial \bar{\psi}}\left[\frac{\left(\nu^2+\eta^2\right)}{\left(1-\nu^2\right)\left(1+\eta^2\right)}\frac{\partial \Phi}{\partial \bar{\psi}}\right] = 0 \qquad \text{(B.1)}$$

Using the principle of separation of variables to solve equation (B.1), the Laplace equation is expressed by a multiplication of three separated parts which are only functions of ν, η and $\bar{\psi}$ respectively.

$$\Phi\left(\nu, \eta, \bar{\psi}\right) = \Phi_1\left(\nu\right)\Phi_2\left(\eta\right)\Phi_3\left(\bar{\psi}\right) \qquad \text{(B.2)}$$

Applying equation (B.2) to equation (B.1), the Laplace equation can be separated into the following three equations:

$$\frac{d^2\Phi_3}{d\bar{\psi}^2} + m^2\Phi_3 = 0 \qquad \text{(B.3)}$$

$$\frac{d}{d\nu}\left[\left(1-\nu^2\right)\frac{d\Phi_1}{d\nu}\right] + \left[-\frac{m^2}{1-\nu^2} + n\left(n+1\right)\right]\Phi_1 = 0 \qquad \text{(B.4)}$$

$$\frac{d}{d\eta}\left[\left(1+\eta^2\right)\frac{d\Phi_2}{d\eta}\right] + \left[\frac{m^2}{1+\eta^2} - n\left(n+1\right)\right]\Phi_2 = 0 \tag{B.5}$$

where m and n are the constant of separation.

Equations (B.4) and (B.5) are Legendre's associated differential equations, and the solutions to which are the associated Legendre Functions of the first kind and the second kind ($P_n^m\left(\nu\right)$, $P_n^m\left(i\nu\right)$, $Q_n^m\left(\eta\right)$ and $Q_n^m\left(i\eta\right)$). Since $P_n^m\left(i\nu\right)$ and $Q_n^m\left(\eta\right)$ will yield an infinite pressure in the flow field, they are omitted.

For the purpose of this research, the associated Legendre functions of the first and second kind are normalized as:

$$\bar{P}_n^m = (-1)^m \frac{P_n^m\left(\nu\right)}{\rho_n^m} \tag{B.6}$$

$$\bar{Q}_n^m = \frac{Q_n^m\left(i\eta\right)}{Q_n^m\left(i0\right)} \tag{B.7}$$

where ρ_n^m is:

$$\left(\rho_n^m\right)^2 = \int_0^1 \left(P_n^m\left(\nu\right)\right)^2 d\nu = \frac{1}{2n+1}\frac{(n+m)!}{(n-m)!} \tag{B.8}$$

$$Q_n^m\left(i0\right) = \begin{cases} \frac{\pi}{2}(-1)^{m+n+1}(i)^{n+1}\frac{(n+m-1)!!}{(n-m)!!}, & m+n = even \\ (-1)^{m+n+1}(i)^{n+1}\frac{(n+m-1)!!}{(n-m)!!}, & m+n = odd \end{cases} \tag{B.9}$$

In this research, numerical codes are developed to compute all the required values of $\bar{P}_n^m\left(\nu\right)$ and $\bar{Q}_n^m\left(i\eta\right)$ based on the following recurrence relations:

$$\bar{P}_{n+1}^m\left(\nu\right) = \sqrt{\frac{\left(2n+3\right)\left(2n+1\right)}{\left(n+1\right)^2 - m^2}}\left[\nu\bar{P}_n^m\left(\nu\right) - \sqrt{\frac{n^2-m^2}{4n^2-1}}\bar{P}_{n-1}^m\left(\nu\right)\right] \tag{B.10}$$

236

$$\bar{P}_{n+1}^m (\nu) = \sqrt{\frac{(2n+3)}{(n+m+1)(n+m)}} \left[\sqrt{\frac{(n-m+1)(n-m)}{2n-1}} \bar{P}_{n-1}^m (\nu) \right.$$
$$\left. + \sqrt{1-\nu^2}\sqrt{2n+1}\bar{P}_n^{m-1} (\nu) \right]$$

(B.11)

$$\bar{P}_n^{m+1} (\nu) = \frac{1}{\sqrt{1-\nu^2}} \left[\sqrt{\frac{(2n+1)(n+m)}{(2n-1)(n+m+1)}} \bar{P}_{n-1}^m (\nu) \right.$$
$$\left. - \frac{(n-m)}{\sqrt{(n+m+1)(n-m)}} \nu \bar{P}_n^m (\nu) \right]$$

(B.12)

$$\bar{Q}_{n+1}^m (i\eta) = \bar{Q}_{n-1}^m (i\eta) - (2n+1) K_n^m \eta \bar{Q}_n^m (i\eta)$$

(B.13)

$$\bar{Q}_n^{m+1} (i\eta) = \frac{1}{\sqrt{1+\eta^2}} \left[\bar{Q}_{n-1}^m (i\eta) - (n-m) K_n^m \eta \bar{Q}_n^m (i\eta) \right]$$

(B.14)

where K_n^m is:

$$K_n^m = \left(\frac{\pi}{2} \right)^{(-1)^{n+m}} H_n^m$$

(B.15)

$$H_n^m = \frac{(n+m-1)!!\,(n-m-1)!!}{(n+m)!!\,(n-m)!!}$$

(B.16)

$$(n)!! = \begin{cases} (n)(n-2)(n-4)\ldots(2) & for\ n\ even \\ (n)(n-2)(n-4)\ldots(1) & for\ n\ odd \end{cases}$$

(B.17)

$$(0)!! = 1, \ (-1)!! = 1, \ (-2)!! = \infty, \ (-3)!! = -1$$

In order to calculate to the derivation of $\bar{P}_n^m (\nu)$ and $\bar{Q}_n^m (i\eta)$, the recurrence relations are given by:

$$\left(1-\nu^2\right) \frac{dP_n^m (\nu)}{d\nu} = \sqrt{\frac{(2n+1)(n^2-m^2)}{(2n-1)}} \bar{P}_{n-1}^m (\nu) - n\nu \bar{P}_n^m (\nu)$$

(B.18)

$$\left(1-\nu^2\right) \frac{d\bar{P}_n^m (\nu)}{d\nu} = \sqrt{(n+m+1)(n-m)}\sqrt{1-\nu^2}\bar{P}_n^{m+1} (\nu) - m\nu \bar{P}_n^m (\nu)$$

(B.19)

$$\left(1+\eta^2\right)\frac{d\bar{Q}_n^m\left(i\eta\right)}{d\eta} = -\left[\frac{1}{K_n^m}\bar{Q}_{n+1}^m\left(i\eta\right) + \left(n+1\right)\eta\bar{Q}_n^m\left(i\eta\right)\right] \tag{B.20}$$

$$\left(1+\eta^2\right)\frac{d\bar{Q}_n^m\left(i\eta\right)}{d\eta} = \sqrt{1+\eta^2}\frac{Q_n^{m+1}\left(i0\right)}{Q_n^m\left(i0\right)}\bar{Q}_n^{m+1}\left(i\eta\right) + m\eta\bar{Q}_n^m\left(i\eta\right) \tag{B.21}$$

where K_n^m (A2.15).

B.1   Orthogonality Integrals

$$\int_0^1 \bar{P}_j^m\left(\nu\right)\bar{P}_n^m\left(\nu\right)d\nu = \begin{cases} \delta_{jn}, & n+m=odd, j+m=odd \\[2mm] \delta_{jn}, & n+m=even, j+m=even \\[2mm] U_{jn}^m, & n+m=even, j+m=odd \end{cases} \tag{B.22}$$

$$U_{jn}^m = \sqrt{\frac{H_n^m}{H_j^m}}\frac{\sqrt{\left(2j+1\right)\left(2n+1\right)}}{\left(j+n+1\right)\left(j-n\right)}\left(-1\right)^{\frac{j+n-2m-1}{2}} \tag{B.23}$$

B.2   Area Integrals

$$\int_0^1 \bar{P}_n^m\left(\nu\right)\bar{P}_j^m\left(\nu\right)\nu d\nu = \begin{cases} A_{jn}^m, & j+m=odd, n+m=odd \\[2mm] G_{jn}^m, & j+m=even, n+m=even \\[2mm] D_{jn}^m, & j+m=odd, n+m=even \end{cases} \tag{B.24}$$

where A_{jn}^m, G_{jn}^m, and D_{jn}^m are defined as:

$$A_{jn}^m = \frac{2}{\sqrt{H_n^m H_j^m}}\frac{\sqrt{\left(2n+1\right)\left(2j+1\right)}}{\left(n+j+2\right)\left(n+j\right)}\frac{\left(-1\right)^{\frac{n+j-2m}{2}}}{\left(\left(j-n\right)^2-1\right)} \tag{B.25}$$

238

$$G_{jn}^{m} = \begin{cases} \sqrt{H_j^m H_n^m} \sqrt{(2j+1)(2n+1)} \dfrac{\left(2m^2 - n^2 - j^2 - n - j\right)}{(n+j+2)(n+j)} \dfrac{(-1)^{\frac{n+j-2m}{2}}}{\left((n-j)^2 - 1\right)}; \\[2ex] \qquad\qquad\qquad\qquad j \neq 0;\ n \neq 0;\ m \neq 0 \\[2ex] \qquad G_{00}^0 = \frac{1}{2} \quad j = n = m = 0 \end{cases} \tag{B.26}$$

$$D_{jn}^{m} = \begin{cases} \sqrt{\dfrac{1}{H_j^m H_n^m}} \dfrac{1}{\sqrt{(2j+1)(2n+1)}}, j = n \pm 1 \\[2ex] \qquad 0, j \neq n \pm 1 \end{cases} \tag{B.27}$$

239

Appendix C

Galerkin Method, Damping, Mass, and Influence Matrices

In order to transform the momentum equation into a set of ordinary differential equations, the Galerkin Method is adopted here in which velocities are expanded in terms of the prime potentials. The test functions for the Galerkin method are chosen to be the same Laplace solutions that are used as expansions for the pressure potentials. Since the velocity potentials are only defined in the upper hemisphere, the integrations will be done in the upper hemisphere, and all boundary conditions are matched. As the integration is only considered over the upper hemisphere, the velocity solution will only be valid above the disk.

After substitution of the proper expansions of pressure potentials, velocity potentials, and the expression of velocity into the momentum equation, volume integration is taken on both sides of the momentum equations. With the divergence theorem, we can then transfer the volume integral into a surface integral, which vanishes at $r \to \infty$. By the method shown in Ref. [5], the surface integral in the plane of the rotor is transformed to integrals on the rotor disk, itself, which have closed-form representations. This leads to a set of ordinary differential equations. The cosine and sine functions completely separate into two uncoupled

sets during this procedure. For the cosine parts, the Galerkin method gives:

$$
\begin{bmatrix} \left[\tilde{L}^c\right]_{o,o} & \left[\tilde{L}^c\right]_{o,e} \\ \left[\tilde{L}^c\right]_{e,o} & \left[\tilde{L}^c\right]_{e,e} \end{bmatrix} \left\{ \begin{array}{c} \{\overset{*}{\hat{a}}{}^m_n\}_o \\ \{\overset{*}{\hat{a}}{}^m_n\}_e \end{array} \right\} + \begin{bmatrix} [D]^c_{o,o} & [D]^c_{o,e} \\ [D]^c_{e,o} & [D]^c_{e,e} \end{bmatrix} \left\{ \begin{array}{c} \{\hat{a}^m_n\}_o \\ \{\hat{a}^m_n\}_e \end{array} \right\}
$$
$$
= \begin{bmatrix} [D]^c_{o,o} & [D]^c_{o,e} \\ [D]^c_{e,o} & [D]^c_{e,e} \end{bmatrix} \left\{ \begin{array}{c} \{\tau^{mc}_n\}_o \\ \{\tau^{mc}_n\}_e \end{array} \right\} \tag{C.1}
$$

where

$$
\left[\tilde{L}^c\right] = \left[\iint_s \frac{\partial \Phi^{rc}_j}{\partial z} \left(\int_0^\infty \Phi^{mc}_n d\xi \right) ds \right] = \left[\iint_s \Phi^{rc}_j \frac{\partial}{\partial z} \left(\int_0^\infty \Phi^{mc}_n d\xi \right) ds \right] \tag{C.2}
$$

$$
\left[D^c\right] = \left[\iint_s \frac{\partial \Phi^{rc}_j}{\partial z} \Phi^{mc}_n ds \right] = \left[\iint_s \Phi^{rc}_j \frac{\partial \Phi^{mc}_n}{\partial z} ds \right] \tag{C.3}
$$

The sine components are similar to equation (C.1). Note that the subscript notation "o" stands for the terms with $m + n = odd$ and "e" is for the terms with $m + n = even$. For the cosine terms, $m = 0, 1, 2, 3, \ldots$ and for the sine terms $m = 1, 2, 3, \ldots$. The sine terms begin at $m = 1$ because the pressure potential:

$$
\Phi^{ms}_n = \bar{P}^{ms}_n (\nu) \, \bar{Q}^{ms}_n (i\eta) \sin \left(m\bar{\psi} \right) \tag{C.4}
$$

implies that when $m = 0$, $\Phi^{ms}_n = 0$. In either the case of sine terms or cosine terms, $n = m, m + 2, m + 4, \ldots$ or $n = m + 1, m + 3, m + 5, \ldots$ depending on the subscript of the partition is "e" or "o". The $[D]$ matrix is as follows for both cosine and sine case:

$$
D^{rm}_{jn} = \frac{1}{K^m_n} \delta_{jn} \delta_{rm}
$$
$$
j + r = odd; \qquad n + m = odd \tag{C.5}
$$
$$
j + r = even; \qquad n + m = even
$$

$$D_{jn}^{rm} = \frac{2\delta_{nm}}{\pi \sqrt{H_n^m H_j^m}} \frac{\sqrt{(2j+1)(2n+1)}}{(j+n+1)(j-n)} (-1)^{\frac{j+3n-1}{2}}$$

$$j + r = odd; \qquad n + m = even \tag{C.6}$$

$$j + r = even; \qquad n + m = odd$$

And the $\left[\tilde{L}\right]$ matrix is given by

$$\left[\tilde{L}_{jn}^{0m}\right]^c = X^m \Gamma_{jn}^{0m} \tag{C.7}$$

$$\left[\tilde{L}_{jn}^{rm}\right]^c = \left[X^{|m-r|} + (-1)^l X^{|m-r|}\right] \Gamma_{jn}^{rm} \tag{C.8}$$

$$\left[\tilde{L}_{jn}^{rm}\right]^s = \left[X^{|m-r|} - (-1)^l X^{|m-r|}\right] \Gamma_{jn}^{rm} \tag{C.9}$$

where

$$X = \tan\left(\chi/2\right), \qquad l = \min\left(r, m\right) \tag{C.10}$$

$$\Gamma_{jn}^{rm} = \frac{sign(r-m)}{\sqrt{K_n^m K_j^r} \sqrt{(2n+1)(2j+1)}} \delta_{j,n\pm1}$$

$$r + m = odd; \qquad j + r = odd; \qquad n + m = odd \tag{C.11}$$

$$r + m = odd; \qquad j + r = even; \qquad n + m = even$$

$$\Gamma_{jn}^{rm} = \frac{(-1)^{\frac{n+j-2r}{2}} (2) \sqrt{(2n+1)(2j+1)}}{\sqrt{H_n^m H_j^r}(n+j)(n+j+2)\left[(n-j)^2-1\right]}$$

$$r + m = even; \qquad j + r = odd; \qquad n + m = odd \tag{C.12}$$

$$\Gamma_{jn}^{rm} = \frac{(-1)^{\frac{n+j-2r+2}{2}} (8) \sqrt{(2n+1)(2j+1)}}{\pi^2 \sqrt{H_n^m H_j^r}(n+j)(n+j+2)\left[(n-j)^2-1\right]}$$

$$r + m = even; \qquad j + r = even; \qquad n + m = even \tag{C.13}$$

$$\Gamma_{jn}^{rm} = \frac{(-1)^{\frac{3n+j+2m-2r}{2}} (4)sign(r-m) \sqrt{(2n+1)(2j+1)}}{\pi \sqrt{H_n^m H_j^r}(n+j)(n+j+2)\left[(n-j)^2-1\right]}$$

$$r + m = odd; \qquad j + r = odd; \qquad n + m = even \tag{C.14}$$

$$r + m = odd; \qquad j + r = even; \qquad n + m = odd$$

$$\Gamma^{rm}_{jn} = \frac{1}{\sqrt{H^m_n H^r_j}\sqrt{(2n+1)(2j+1)}}\delta_{j,n\pm1}$$

$$j + m = even; \qquad j + r = odd; \qquad n + m = even \qquad (C.15)$$

$$j + m = even; \qquad j + r = even; \qquad n + m = odd$$

The potential for $m = n = 0$, has a logarithmic term, so the integral for Γ is formally infinite for the case of $m = r = n = j = 0$. However, based on [6], we can express this integral as a finite series that approaches infinity as the number of terms approaches infinity.

$$\Gamma^{00}_{00} = \left(\frac{4}{\pi^2}\sum_{n=1}^{N_{max}}\frac{1}{n}\right) + \frac{1}{2} \qquad (C.16)$$

where N_{max} is the largest harmonic number. In this way, the integral is finite for a truncated approximation. This also allows a solution with a finite number of terms that provides formal convergence to the exact answer.

Appendix D

Load Sharing

Load sharing in a coaxial system is an approach to ensure that both rotors are contributing equally to the total lift within the system. Many helicopters contain a tail rotor which serves the purpose of countering the torque that is generated by the lifting rotor and preventing the body of the helicopter from rotating continuously. Coaxial rotor helicopters do not contain a tail rotor and obtain a net zero torque within the system by balancing the load shared by each lifting rotor. As will be shown in the following two sections, load sharing does not occur until the system has stabilized which leaves a small amount of time where the system is not balanced. In general, a coaxial rotor must be such that the torque of each rotor is equal to the other so that the craft will not yaw. We are not computing torque here. However, as a first-approximation to balanced torque, one can assume balance lift. If the lift (i.e., the torque) is not balanced, the rotorcraft would yaw due to the net torque on fuselage.

D.1   Load Sharing for Single Inflow State

For a system with a single inflow state, the load sharing considerations are more simple, but provide a solid foundation for further expansion to the system with multiple inflow states.

It has previously been shown that

$$\overset{*}{\alpha}_U + \lambda \alpha_U = \lambda F_U \tag{D.1}$$

$$\overset{*}{\delta}_U + \lambda \delta_U = \lambda F_U \tag{D.2}$$

$$F_U = \theta_U - k\alpha_U - q\alpha_L \tag{D.3}$$

Assuming that h $=$ k (and therefore $q = ke^{-\lambda d}$) and that convergence of the state and co-state variables has been achieved as $t \to \infty$. When convergence occurs the first order terms become zero such that

$$\lambda \alpha_U = \lambda F_U \tag{D.4}$$

$$\lambda \delta_U = \lambda F_U \tag{D.5}$$

and therefore, we find that

$$\alpha_U = \delta_U = F_U \tag{D.6}$$

Similarly, for the lower rotor it is shown that when convergence is achieved, the first order terms are zero.

$$\overset{*}{\alpha}_L + \lambda \alpha_L = \lambda F_L \tag{D.7}$$

$$F_L = \theta_L - k\alpha_L - k\alpha_U \left(\bar{t} - \bar{d} \right) - k\delta_U \left(\bar{t} - \bar{d} \right) - q\delta_U \tag{D.8}$$

$$\alpha_L = F_L \tag{D.9}$$

In a system where $\bar{t} \to \infty$, the time-delayed terms are assumed to be equivalent to the non-time delayed counterparts where

$$\alpha_U = \alpha_U \left(\bar{t} - \bar{d} \right) \tag{D.10}$$

$$\delta_U = \delta_U \left(\bar{t} - \bar{d} \right) \tag{D.11}$$

245

This results in the revision of the F_L

$$F_L = \theta_L - k\alpha_L - k\alpha_U - k\delta_U - q\delta_U \tag{D.12}$$

For shared lift between the upper and lower rotor

$$F_U + F_L = F_{Total} \tag{D.13}$$

the lift of each rotor is equal such that

$$F_U = F_L = \frac{1}{2}F_{Total} \tag{D.14}$$

Therefore, it is shown that

$$\alpha_U = \delta_U = F_U = \alpha_L = F_L \tag{D.15}$$

Looking at the equations for the force of each rotor, it is noticeable that the input functions θ_U and θ_L have not yet been defined for load sharing like the other variables. Rearranging the force equations above and substituting F_{Total} in for all variables it is shown that

$$\theta_U = \frac{1}{2}F_{Total}[1 + k + q] \tag{D.16}$$

$$\theta_L = \frac{1}{2}F_{Total}[1 + 3k + q] \tag{D.17}$$

θ_U and θ_L are functions of the magnitude of total lift in the system, the inflow feedback (k), and cross-flow feedback (h).

In this work, the inflow feedback, cross-flow feedback, rotor spacing, and total lifting force in the system are user defined and the input functions θ_U and θ_L are determined as a result of the user defined values. Normally, this work utilizes a system of unit normal load (F_{Total} = 1) and varies the spacing and feedback parameters. In general terms for a unit normal

246

load, θ_U and θ_L are modeled as

$$\theta_U = \frac{1}{2}\left[1 + k + q\right] \tag{D.18}$$

$$\theta_L = \frac{1}{2}\left[1 + 3k + q\right] \tag{D.19}$$

D.2   Load Sharing for Multiple Inflow States

Determination of load sharing for multiple inflow states is achieved in a similar manner as that of the single inflow state process, but as one would expect is more complex. The process also varies slightly based on final conditions of δ_U. At this point only the process for the converged final conditions will be presented because the zero final conditions process is currently incomplete.

To begin this process, we will again assume that the system is observed at time $t = \infty$ such that the system has reached a converged state. Therefore, the first order derivative terms are zero and the time delayed terms are equivalent to their non-time-delayed forms. We are again able to show that

$$\alpha_{nU}^m = \tau_{nU}^m \tag{D.20}$$

$$\alpha_{nL}^m = \tau_{nL}^m \tag{D.21}$$

$$\delta_{nU}^m = \tau_{nU}^m \tag{D.22}$$

Apply the converged final conditions, it can be further demonstrated that

$$\tau_{nU}^m = \alpha_{nU}^m = \delta_{nU}^m = \alpha_{nU}^m\left(\bar{t} - \bar{d}\right) = \delta_{nU}^m\left(\bar{t} - \bar{d}\right) \tag{D.23}$$

It should be noted that unlike the single inflow state case, the terms related to the upper rotor (τ_{nU}^m, α_{nU}^m, δ_{nU}^m) are not equivalent to the terms related to the lower rotor (α_{nL}^m, τ_{nL}^m).

The exception to this is for the first odd inflow state ($m = 0, n = 1$) where

$$\tau_{1U}^0 = \tau_{1L}^0 = \frac{\sqrt{3}}{4} C_T \tag{D.24}$$

This relationship is critical for load sharing and will be further explained below. The pressure potentials for load sharing with multiple inflow states are taken from equations

$$\left\{\tau_n^{0c}\right\}_U = \frac{\sigma a}{8} \left[\{A\}\, \theta_U - [B]\{\alpha_{nU}^m\left(\bar{t}\right)\} - [C]\left\{\alpha_{nL}^m\left(\bar{t}\right)\right\} \right] \tag{D.25}$$

$$\left\{\tau_n^{0c}\right\}_L = \frac{\sigma a}{8} \left(\{A\}\theta_L - [B]\left\{\alpha_{nL}^m\left(\bar{t}\right)\right\} - [B]\left\{\alpha_{nU}^m\left(\bar{t} - \bar{d}\right)\right\} \right.$$
$$\left. - [B]\left\{\delta_{nU}^m\left(\bar{t} - \bar{d}\right)\right\} + [C]\left\{\delta_{nU}^m\left(\bar{t}\right)\right\} \right) \tag{D.26}$$

Understanding from the previous section that our unknown terms for load sharing are the pitch angles of the rotors θ_U and θ_L. We can then solve for the θ_U and θ_L using Eqs. E.25 and E.26 by first applying the equivalencies in Eqs. E5.23 and E.21, respectively.

$$\left\{\tau_n^{0c}\right\}_U = \frac{\sigma a}{8} \left[\{A\}\, \theta_U - [B]\{\tau_{nU}^m\} - [C]\left\{\tau_{nL}^m\right\} \right] \tag{D.27}$$

$$\left\{\tau_n^{0c}\right\}_L = \frac{\sigma a}{8} \left[\{A\}\theta_L - [B]\left\{\tau_{nL}^m\right\} - [B]\left\{\tau_{nU}^m\right\} - [B]\left\{\tau_{nU}^m\right\} + [C]\left\{\tau_{nU}^m\right\} \right] \tag{D.28}$$

which is further simplified to:

$$\left\{\tau_n^{0c}\right\}_L = \frac{\sigma a}{8} \left[\{A\}\, \theta_L - [B]\left\{\tau_{nL}^m\right\} - [2B - C]\left\{\tau_{nU}^m\right\} \right] \tag{D.29}$$

These equations can be combined into:

$$\left\{ \begin{array}{c} \{\tau_{nU}^m\} \\ \{\tau_{nL}^m\} \end{array} \right\} = \frac{\sigma a}{8} \left[\begin{array}{cc} \{A\} & 0 \\ 0 & \{A\} \end{array} \right] - \frac{\sigma a}{8} \left[\begin{array}{cc} [B] & [C] \\ 2[B] - [C] & [B] \end{array} \right] \tag{D.30}$$

Isolating the pitch angles, we find

$$
\begin{bmatrix} I + \frac{\sigma a}{8}[B] & \frac{\sigma a}{8}[C] \\ 2\frac{\sigma a}{8}[B] - \frac{\sigma a}{8}[C] & I + \frac{\sigma a}{8}[B] \end{bmatrix} \begin{Bmatrix} \tau_{nU}^m \\ \tau_{nL}^m \end{Bmatrix} = \begin{bmatrix} \frac{\sigma a}{8}\{A\} & 0 \\ 0 & \frac{\sigma a}{8}\{A\} \end{bmatrix} \begin{Bmatrix} \theta_U \\ \theta_L \end{Bmatrix} \tag{D.31}
$$

For simplicity, we define the matrices as

$$
[F] = \begin{bmatrix} I + \frac{\sigma a}{8}[B] & \frac{\sigma a}{8}[C] \\ 2\frac{\sigma a}{8}[B] - \frac{\sigma a}{8}[C] & I + \frac{\sigma a}{8}[B] \end{bmatrix} \tag{D.32}
$$

$$
[G] = \begin{bmatrix} \frac{\sigma a}{8}\{A\} & 0 \\ 0 & \frac{\sigma a}{8}\{A\} \end{bmatrix} \tag{D.33}
$$

Therefore, obtaining

$$
\begin{Bmatrix} \tau_{nU}^m \\ \tau_{nL}^m \end{Bmatrix} = [F]^{-1}[G] \begin{Bmatrix} \theta_U \\ \theta_L \end{Bmatrix} \tag{D.34}
$$

As mentioned earlier, only the first odd state for the pressure distributions are equal, such that

$$
\alpha_{1U}^0 = \alpha_{1L}^0 = \delta_{1U}^0 = \tau_{1U}^0 = \tau_{1L}^0 = \frac{\sqrt{3}}{4}C_T \tag{D.35}
$$

where C_T is user defined. Load sharing within the system is accomplished by adjusting the magnitudes of the pitch angles, θ_U and θ_L. The magnitudes of the pitch angles are dependent on the number of inflow states within the system. To solve we adjust the previous equation

to develop the system a system that results in two solutions, θ_U and θ_L.

$$\begin{Bmatrix} \tau_{1U}^0 \\ \tau_{1L}^0 \end{Bmatrix} = \begin{bmatrix} \begin{Bmatrix} 1 \\ 0 \\ \vdots \\ 0 \\ 0 \\ 0 \\ \vdots \\ 0 \end{Bmatrix} & \begin{Bmatrix} 0 \\ 0 \\ \vdots \\ 0 \\ 1 \\ 0 \\ \vdots \\ 0 \end{Bmatrix} \end{bmatrix}^T [F]^{-1}[G] \begin{Bmatrix} \theta_U \\ \theta_L \end{Bmatrix} \tag{D.36}$$

In this equation, the column vectors are $1xN$ in size, where N is the number of inflow states.

To again simplify the equation, we elected to state that

$$[H] = \begin{bmatrix} \begin{Bmatrix} 1 \\ 0 \\ \vdots \\ 0 \\ 0 \\ 0 \\ \vdots \\ 0 \end{Bmatrix} & \begin{Bmatrix} 0 \\ 0 \\ \vdots \\ 0 \\ 1 \\ 0 \\ \vdots \\ 0 \end{Bmatrix} \end{bmatrix}^T [F]^{-1}[G] \tag{D.37}$$

Finally, solving for the pitch angles we obtain:

$$\begin{Bmatrix} \theta_U \\ \theta_L \end{Bmatrix} = [H]^{-1} \begin{Bmatrix} \tau_{1U}^0 \\ \tau_{1L}^0 \end{Bmatrix} \tag{D.38}$$

or

$$\left\{ \begin{array}{c} \theta_U \\ \theta_L \end{array} \right\} = [H]^{-1} \left\{ \begin{array}{c} \frac{\sqrt{3}}{4} C_T \\ \frac{\sqrt{3}}{4} C_T \end{array} \right\} \tag{D.39}$$

It should be noted that this process varies slightly for the case where the final conditions for the co-state variable are set to zero, but the overall solution will remain the same.

References

[1] Johnson, Wayne. "Wake Geometry," Rotorcraft Aeromechanics, Chap. 9, Cambridge Univ. Press, 2013, pp. 326–335.

[2] Peters, David A. "How dynamic inflow survives in the competitive world of rotorcraft aerodynamics," Journal of the American Helicopter Society, vol. 54, no. 1, 2009.

[3] Fei, Zhongyang. "A Rigorous Solution for Finite-State Inflow Throughout The Flowfield," May 2013. Washington University in St. Louis, PhD dissertation.

[4] Fei, Zhongyang and David A. Peters. "A Rigorous Solution for Finite-state Inflow throughout the Flowfield," Proceedings from The 30th AIAA Applied Aero-dynamics Conference, New Orleans, 2012.

[5] Pitt, Dale M. and David A. Peters. "Theoretical Prediction of Dynamic-Inflow Derivatives," Vertica, vol. 5, no. 1, pp. 21-34, March 1981.

[6] Mangler, K. W., and B. Squire. "Calculation of the induced velocity field of a rotor." Royal Aircraft Establishment, Rept. Aero 2247 (1948).

[7] Gaonkar, Gopal H. and David A. Peters. "Effectiveness of Current Dynamic-Inflow Models in Hover and Forward Flight," Journal of the American Helicopter Society, vol. 31, no. 2, pp. 47-57, April 1986.

[8] Peters, David A., David Doug Boyd, and Cheng Jian He. "A Finite-State Induced-Flow Model for Rotors in Hover and Forward Flight," Journal of the American Helicopter Society, vol. 34, no. 4, pp. 5-17, October 1989.

[9] Peters, David A., and Cheng Jian He. "Correlation of Measured Induced Velocities with a Finite-State Wake Model," Journal of the American Helicopter Society, vol. 36, no. 3, pp. 59-70, July 1991.

[10] Peters, David A., and Wenming Cao, "Off-Rotor Induced Flow by a Finite-State Wake Model," Proceedings in 37th AIAA SDM Conference, Salt Lake City, April 15-17, 1996.

[11] Morillo, Jorge A., and David A. Peters, "Velocity Field above a Rotor Disk by a New Dynamic Inflow Model," Journal of Aircraft, vol. 39, no. 5, pp. 731-738, September-October 2002.

[12] Hsieh, Mong-Che A., "A Complete Finite-State Model for Rotors in Axial Flow," August 2006. Washington University in St. Louis, PhD dissertation.

[13] Peters, David A., Mong-Che A. Hsieh, and Cristina Garcia-Duffy, "A Complete Finite-State Inflow Theory from the Potential Flow Equations". 3rd International Basic Research Conference on Rotorcraft Technology, Nanjing, China. 2009.

[14] Fei, Zhongyang, and David A. Peters, "Inflow below the Rotor Disk for Skewed Flow by the Finite-State, Adjoint Method," Proceedings in The 38th European Rotorcraft Forum, Amsterdam, 2012.

[15] Chen, Po-Wei, Lakshmi N. Sankar, J. V. R. Prasad, Natasha L. Schatzman, and R. Ganesh Rajagopalan, (2019). "Extraction of Dynamic Inflow Models for Coaxial and Tandem Rotors from CFD Simulations," Proceedings from VFS 75th Annual Forum and Technical Display, Philadelphia, PA May 13-16, 2019.

[16] Lakshminarayan, Vinod K., and James D. Baeder. "Computational investigation of microscale coaxial-rotor aerodynamics in hover." Journal of aircraft 47.3 (2010): 940-955.

[17] Rajmohan, Nischint, Jinggen Zhao, and Chengjian He. "A coupled vortex particle/CFD methodology for studying coaxial rotor configurations." Fifth Decennial AHS Aeromechanics Specialists' Conference, San Francisco, California. 2014.

[18] Singh, Puneet, and Peretz P. Friedmann. "A Computational Fluid Dynamics–Based Viscous Vortex Particle Method for Coaxial Rotor Interaction Calculations in Hover." Journal of the American Helicopter Society, Oct. 2018, doi:10.4050/jahs.63.042002.

[19] Singh, Puneet, and Peretz P. Friedmann. "Application of Vortex Methods to Coaxial Rotor Wake and Load Calculations in Hover," Journal of Aircraft, Vol. 55, No. 1, August 2017, pp. 373-381.

[20] He, Chengjian, and Jinggen Zhao. "Modeling rotor wake dynamics with viscous vortex particle method." AIAA journal 47.4 (2009): 902-915.

[21] Zhao, Jinggen, and Chengjian He. "A Finite State Dynamic Wake Model Enhanced with Vortex Particle Method–Derived Modeling Parameters for Coaxial Rotor Simulation and Analysis." Journal of the American Helicopter Society, 61(2), 1-9.

[22] Prasad, J. V. R., Morgan Nowak, and Hong Xin. "Finite state inflow models for a coaxial rotor in hover." Proceedings of the 38th European Rotorcraft Forum, Amsterdam, Netherlands, September 4-7, 2012.

[23] Prasad, J.V.R., Yong-Boon Kong, and David A. Peters. "Analytical Methods for Modeling Inflow Dynamics of a Coaxial Rotor System," Proceedings of the 42nd European Rotorcraft Forum, Lille, France, September 5-8, 2016.

[24] Prasad, J.V.R., Yong-Boon Kong, and David A. Peters. "Development of a Finite-State Dynamic Inflow Model for Coaxial Rotor using Analytical Methods," Proceedings of the 73rd Annual National Forum of AHS International, Ft. Worth, Texas, May 9-11, 2017.

[25] Cardito, Felice, Riccardo Gori, Giovanni Bernardini, Jacopo Serafini, and Massimo Gennaretti. "Identification of coaxial-rotors dynamic wake inflow for flight dynamics and aeroelastic applications," Proceedings of the 42nd European Rotorcraft Forum, Lille, France, September 5-8, 2016.

[26] Cardito, Felice, Riccardo Gori, Giovanni Bernardini, Jacopo Serafini, and Massimo Gennaretti. "State-space coaxial rotors inflow modelling derived from high-fidelity aerodynamic simulations." CEAS Aeronautical Journal 9.4 (2018): 587-606.

[27] Juhasz, Ondrej, Monica Syal, Roberto Celi, Vladimir Khromov, Omri Rand, Gene C. Ruzicka, and Roger C. Strawn. "Comparison of three coaxial aerodynamic prediction methods including validation with model test data." Journal of the American Helicopter Society 59.3 (2014): 1-14.

[28] Obayashi, Nana, Chong Zhou, Lakshmi Sankar and JVR Prasad. "Viscous flow simulations of coaxial rotors," Proceedings of the 42nd European Rotorcraft Forum, Lille, France, September 5-8, 2016.

[29] Silwal, Lokesh, and Vrishank Raghav. "Preliminary study of the near wake vortex interactions of a coaxial rotor in hover." AIAA Scitech 2020 Forum. 2020.

[30] Tsushima, Natsuki, and Weihua Su. "Modeling of highly flexible multifunctional wings for energy harvesting." Journal of Aircraft 53.4 (2016): 1033-1044.

[31] Henriksen, Lars Christian, Morten Hartvig Hansen, and Niels Kjølstad Poulsen. "A simplified dynamic inflow model and its effect on the performance of free mean wind speed estimation." Wind Energy 16.8 (2013): 1213-1224.

[32] Koppejan, Rogier, and Shimon Whiteson. "Neuroevolutionary Reinforcement Learning for Generalized Helicopter Control." Proceedings of the 11th Annual Conference on Genetic and Evolutionary Computation - GECCO '09, July 2009.

[33] Bagnell, J. Andrew, and Jeff G. Schneider. "Autonomous Helicopter Control Using Reinforcement Learning Policy Search Methods." Proceedings 2001 ICRA. IEEE International Conference on Robotics and Automation (Cat. No.01CH37164), May 2001.

[34] Dracopoulos, Dimitris C., and Dimitrios Effraimidis. "Genetic programming for generalised helicopter hovering control." European Conference on Genetic Programming. Springer, Berlin, Heidelberg, 2012.

[35] Abbeel, Pieter, Adam Coates, and Andrew Y. Ng. "Autonomous helicopter aerobatics through apprenticeship learning." The International Journal of Robotics Research Vol. 29, (13), 2010, pp. 1608-1639.

[36] Abbeel, Pieter, Adam Coates, Morgan Quigley, and Andrew Y. Ng. "An application of reinforcement learning to aerobatic helicopter flight." NIPS'06 Proceedings of the 19th International Conference on Neural Information Processing Systems, December 2006.

[37] Pawar, Prashant M., and Sung Nam Jung. "Support vector machine based online composite helicopter rotor blade damage detection system." Journal of Intelligent Material Systems and Structures Vol. 19,(10), 2008, pp. 1217-1228.

[38] Kumar, Anil, and Pinhas Ben-Tzvi. "Extraction of Impact of Wind Turbulence on RC Helicopters Using Machine Learning." Volume 5A: 40th Mechanisms and Robotics Conference, 5 Dec. 2016, doi:10.1115/detc2016-59384.

[39] Chen, Tianqi, and Carlos Guestrin. "XGBoost." Proceedings of the 22nd ACM SIGKDD International Conference on Knowledge Discovery and Data Mining - KDD '16, Aug. 2016, doi:10.1145/2939672.2939785.

[40] Zheng, Huiting, Jiabin Yuan, and Long Chen. "Short-term Load Forecasting Using EMD-LSTM Neural Networks with a XGBoost Algorithm for Feature Importance Evaluation." Energies Vol. 10, (8), 2017, pp. 1168.

[41] Abbasi, Raza Abid, Nadeem Javaid, Muhammad Nauman Javid Ghuman, Zahoor Ali Khan, and Shujat Ur Rehman. "Short Term Load Forecasting Using XGBoost." Workshops of the International Conference on Advanced Information Networking and Applications. Springer, Cham, 2019.

[42] Gumus, Mesut, and Mustafa S. Kiran. "Crude Oil Price Forecasting Using XGBoost." 2017 International Conference on Computer Science and Engineering (UBMK). IEEE.

[43] Ren, Xudie, Haonan Guo, Shenghong Li, Shilin Wang, and Jianhua Li. "A Novel Image Classification Method with CNN-XGBoost Model." International Workshop on Digital Watermarking. Springer, Cham, 2017.

[44] White, Frank M. "Fundamental Equations of Compressible Viscous Flow," in Viscous Fluid Flow, New York, NY: McGraw-Hill, 2011, pp. 59-92.

[45] Garcia-Duffy, Cristina. "Applying Dynamic Wake Models to induced Power Calculations For an Optimum Rotor," August 2009. Washington University in St. Louis, PhD dissertation.

[46] Meyers, Johan, and Charles Meneveau. "Optimal turbine spacing in fully developed wind farm boundary layers." Wind Energy 15.2 (2012): 305-317.

Vita

Cory Seidel

Degrees   B.S. Magna Cum Laude, Mechanical Engineering, May 2015
M.S. Mechanical Engineering, December 2016
Ph.D. Mechanical Engineering, August 2020

Professional   Vertical Flight Society (VFS)
Societies   American Institute of Aeronuatics and Astronautics (AIAA)

Publications   Seidel, C. A., Peters, D. A. "Simple Inflow and Structural Dynamics of a Coaxial Rotor with Time Delays and Adjoint Variables," Proceedings of the VFS 75th Annual Forum and Technology Display, Philadelphia, PA, May 13-16, 2019.

Seidel, C. A., Peters, D. A. "Coupled Inflow and Structural Dynamics of a Coaxial Rotor with Time Delays and Adjoint Variables Including Multiple Inflow States," Proceedings of the 2020 Transformative Vertical Flight Meeting, San Jose, CA, January 21-23, 2020.

Seidel, C. A., Genter, E. Peters,D. A. "Performance of Gradient-Boosted Trees for Prediction of Coaxial Inflow Models with XG-Boost", Proceedings of the VFS 76th Annual Forum and Technology Display, Virginia Beach, VA, October 6-8, 2020.

Seidel, C. A., Peters, D. A. "Theoretical Underpinnings of Applications of Adjoint Variables with Time Delays to Rotor-Inflow Dynamics," *Journal of the American Helicopter Society.* In preparation.

August 2020

Coaxial Rotor Inflow Dynamics, Seidel, Ph.D. 2020